Panagiotis Karampelas
Lambros Ekonomou *Editors*

Electricity Distribution

Intelligent Solutions for Electricity Transmission and Distribution Networks

Springer

Energy Systems

Series editor

Panos M. Pardalos, Gainesville, USA

Panagiotis Karampelas · Lambros Ekonomou
Editors

Electricity Distribution

Intelligent Solutions for Electricity
Transmission and Distribution Networks

Springer

Editors
Panagiotis Karampelas
Department of Informatics and Computers
Hellenic Air Force Academy
Dekelia, Attica
Greece

Lambros Ekonomou
Department of Electrical and Electronic
  Engineering
City University London
London
UK

Printed on acid-free paper

Preface

Strategic research agendas worldwide on electricity transmission and distribution networks emphasize that by 2030, electricity networks will continue to function in a manner that optimizes cost and environmental performance without giving up traditionally high security and quality of supply, while hosting very large and further increasing penetration of renewable and distributed (dispersed) generation. Stimulation of local production of renewable energy requires the emergence of more intelligent transmission and distribution networks with a view to accommodate variable generation from multiple sources and a growing demand for renewable energy. Electricity wholesale competition and the deregulation of retail electricity markets with the energy value chain becoming bidirectional are models that have been internationally adopted in an effort to achieve the maximum economic benefits and energy savings. Finally, energy efficiency is by far the greatest opportunity for the power industry in the current energy market, with all the electricity market participants trying to approach it in the most effective way in order to achieve significant competitive advantages.

Taking into consideration the important changes and the reformation of the power industry that are carried out today, as previously described, the current book provides intelligent and innovative solutions that can be applied on electricity transmission and distribution networks to support these changes. Throughout the book readers have the chance to be informed: on a novel, efficient and user friendly software tool for power systems studies, on issues related to distributed (dispersed) generation and the correlation between renewable generation and electricity demand, on new methodologies which handle grid stability and control problems, on transmission and distribution networks' safety and protection issues, on energy storage and power quality, on the application of embedded systems on the transmission and distribution networks and finally on issues related to the economics of the power industry.

We express our gratitude to all the reviewers and contributing authors for offering their expertise and for providing valuable material used to compose this book. We also thank Springer for the opportunity to make a contribution to advancing and sharing the state-of-the-art research in modern electricity transmission and distribution networks.

Contents

A Methodology for Web-Based Power Systems Simulation and Analysis Using PHP Programming

Simon Agamah and Lambros Ekonomou

Abstract A methodology for carrying out web-based power systems simulations using PHP programming for the simulation engine is described in this chapter. Power system simulation is essential for planning and studying how an electrical network system will operate over time without physically assembling it. The methodology is implemented in a modular object-oriented PHP application that computes the power flow solution of electrical networks using the Newton-Raphson method. A key difference between this solution and existing web-based power systems simulation applications is in the architecture; other solutions use a 3-tier structure: web browser, web server scripts and simulation engine while this has the simulation engine running in the web server scripts thereby creating a slimmer 2-tier structure. This 2-tier structure and the choice of PHP has considerable implications in terms of server resources required to execute the solution, which is increasingly important in this era of cloud computing, Software-as-a-Service (SaaS) and smart electricity networks. The methodology covers the more recent features of PHP that make it possible to carry out such analysis which were not present in previous versions of the language. It also covers how additional classes required to provide mathematical functionality not present in the language core can be used to build the simulation engine. The methodology provides a viable option for carrying out fundamental power systems studies using open source software.

S. Agamah (✉) · L. Ekonomou
Department of Electrical and Electronic Engineering, City University London,
London EC1V 0HB, UK
e-mail: simon.agamah.1@city.ac.uk

L. Ekonomou
e-mail: lambros.ekonomou.1@city.ac.uk

1 Introduction

Web-based simulation (WBS), analysis and remote control via a web browser interface such as Microsoft Internet Explorer™, Google Chrome™, Mozilla Firefox™ is increasingly becoming relevant and even necessary in some cases with the rise of cloud computing, Software-as-a-Service (SaaS) and smart grid technologies [1, 2]. The information and communications technology infrastructure that enable this service oriented architecture of software have evolved over time, and so have the programming languages that are used to develop these applications [3, 4].

The context of web-based simulation that is presented in this methodology is defined by [5] as the use of resources and technologies offered by the world-wide-web (WWW) for interaction with client (web browser) and server (remote computer) modelling and simulation tools. Furthermore the definition excludes simulation packages that are downloaded from a server to a local computer and executed independent of the web browser, emphasizing that a browser always has to play an active role in the modelling or simulation process, either as a graphical interface or, additionally, as a container for the simulation numerical engine [5].

Several detailed reviews such as [1, 5–7] cover the programming languages, structures and techniques that are being used to perform web-based simulations that do not require an application package to be installed and run on a local computer independent of the web browser. The advantages and disadvantages of such methods are also well documented in them.

The structure of such WBS applications usually consists of 3 or more tiers as shown in Fig. 1. The front end tier or client side is the web browser located on the user's computer or other device for user input and displaying results, the middle tier
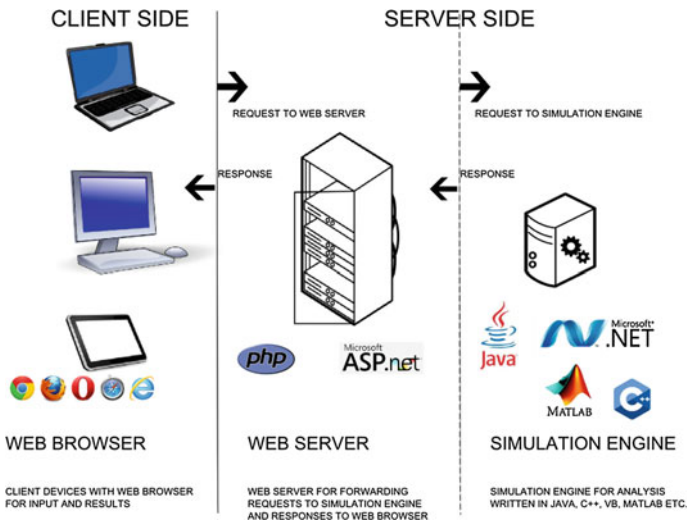
Fig. 1 3-tier architecture implemented by existing web based power systems simulators

is the remote web-server which runs software written in a web programming language such as ASP.NET, PHP:Hypertext Pre-processor (PHP), CGI scripts or Perl scripts that receives the Hypertext Transfer Protocol (HTTP) requests from the web browser, processes it and passes it on the simulation engine which either resides on the same back-end server computer or on a remote server. The simulation engine, which is an application such as MATLAB, NEPLAN, ExtendSIM receives the requests to perform a simulation and it returns the result to the user on the web browser via the program on the web server [5]. This is how the vast majority of WBS in different disciplines is operated. The simulation engine is usually written in a programming language such as Java, C#, Visual Basic, C, or C++ which are used for desktop and server applications. Essentially the web versions provide a "window" to access the functions of these traditionally desktop-based software packages through a component that facilitates this interaction.

Programs written in Java are compiled into Java Byte Code which the Java Virtual Machine compiles into native machine code to achieve platform independence [6]. On the other hand, according to Bryne et al. in [5] the Microsoft .NET Framework allows supported programming languages including Visual Basic, C# and others to be compiled into an Intermediate Language (IL) and then to a platform specific Common Language Runtime (CLR) to achieve platform independence and language interoperability. Full support for the .NET runtime is currently only available on Windows, meaning that some features are only available to be run on the Windows platform [7]. The multiple-platform, single-language support of Java is compared against the single-platform, multiple-language support of the .NET framework by programmers [5]. Furthermore, the .NET framework enables web support using ASP. NET which is integrated into it, while web support for Java is achieved through the use of additional components or Java Applets that are downloaded and run in a separate process on the Java Virtual Machine but shown in the web browser [8].

The main benefit of using this 3+ tier approach shown in Fig. 1 is that programmers can focus on writing only a business logic layer to provide interaction with the web server technologies and leave the base functionality intact. This reduces the amount of modules of the software that must be rebuilt from ground-up specifically for web use. The web server application therefore acts as a data transport layer between the front-end web browser and the main processing in the program running on a back-end server.

A different approach which has not been used previously is to develop a slimmer 2-tiered structure for the simulation application as illustrated in Fig. 2. Instead of using the web server only as a transport layer, a 2-tiered approach which has the simulation engine written in a web programming language and all or most of the processing carried out on the web server is proposed.

There are several reasons why this approach has not been used in the past including the recent maturity and re-emergence of web programming languages such as PHP [3] and JavaScript into general programming languages which wasn't the case previously. Furthermore the existing desktop simulation applications had access to a solution for web access while remaining in their native code by using the 3-tiered approach described earlier, and so there hasn't been a pressing demand for
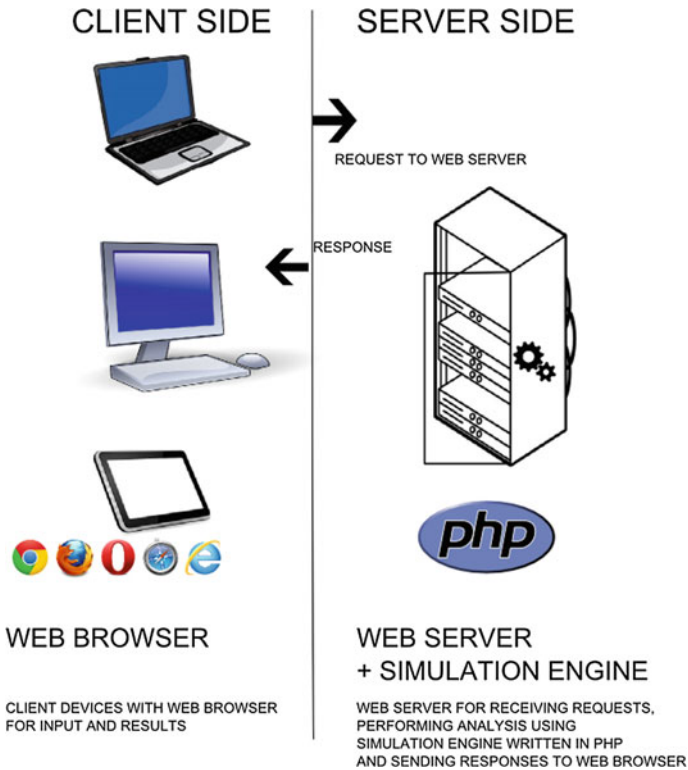
Fig. 2 2-tier architecture implemented with simulation engine written in PHP language

this approach yet. The benefits offered by such a 2+ tier approach include a reduction in the points of failure, a leaner and simpler application which reduces the amount of dependencies required for it to run on a server to achieve similar results as a 3 tier approach, and even a reduction or elimination of licensing costs if it is built with an open source solution such as PHP.

The focus of this chapter is Web based Power Systems Simulation (PSS) and Analysis for network planning and Active Network operation. The IEEE Power & Energy Society (PES), Power System Analysis, Computing, and Economics (PSACE) Committee have created a taskforce on Open source software and maintain a list of open source PSS packages with a summary of their features in chronological order [9]. The languages that have been used to develop these applications and others in the past include FORTRAN, C, C++, JAVA, Visual basic [10] and are all versatile languages. As at the time of this writing, no Power Systems Simulation and Analysis application has been developed using the most popular [11] open source web programming tool PHP. The most recent versions of PHP support Object Oriented Programming (OOP) [4] and features that can be found in general purpose programming languages and which greatly enhance simulation application architecture.

Some Web-based solutions have been implemented using the 3-tiered approach, using ASP.NET and Java. Furthermore, some of the commercial Power Systems Simulation packages including NEPLAN (via NEPLAN 360), MATLAB (via MATLAB Web deployment) and DigSilent (via PSSe + Django) now have web access. InterPSS, a free package based on using a preprogramed spreadsheet, is also available for use on the internet [12].

This Introduction has presented a background of the existing WBS solutions which involve 3 or more tiers and proposed a different 2-tiered approach specifically for Power Systems Simulation, Analysis and Network Management using PHP simulation engine. The rest of the chapter will review some of the previous research and implementations carried out in Web-based Power Systems simulation, and will give the benefits and challenges offered by a PHP solution. The methodology for the implementation of the Web based PHP simulation engine is also described, including the design of the application and the interaction between different components and the parameters that will be inspected to provide performance benchmarks. The results obtained from simulations carried out using the PHP power systems simulation engine are included in this chapter and finally conclusions from the results obtained are presented and areas for further research and potential improvements on the solution are discussed.

2 Web-Based Power Systems Simulation Software

2.1 Commercial and Open Source Web-Based Power Systems Simulation Software

The most common commercial and open source Power Systems Simulations software packages are listed by Open Electrical in [10]. The IEEE PSACE also sponsors a Taskforce for Open Source Software for Power Systems [9]. The packages in these detailed lists that explicitly have Web-based interfaces or a module that can allow web access are InterPSS and NEPLAN 360 from Neplan AG [13]. SimPowerSystems from MathWorks extends MATLAB's Simulink and MatPower, which was developed by members of the Power Systems Engineering Research Centre of the Cornell University, is a set of MATLAB files with Power Systems analysis functions [14]. MATLAB programs can now be deployed as web applications [15], hence it follows that MatPower and SimPowerSystems solutions can also be deployed online and may be classified as a Web-based solution. An overview of the web related characteristics of each of these packages is as follows:

2.1.1 InterPSS

InterPSS stands for Internet Technology Based Power Systems Simulator. It was developed using Java, XML and the Eclipse IDE. The web-access is available in
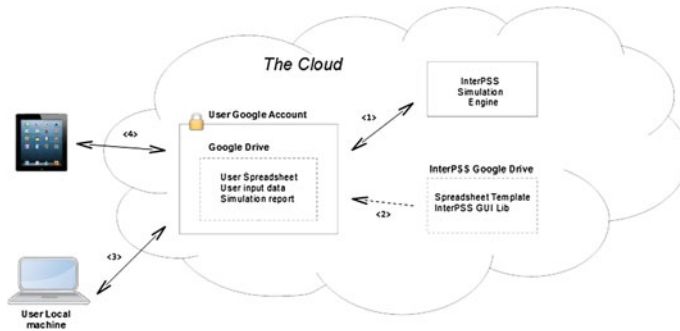
Fig. 3 InterPSS high level architecture [12]

InterPSS 2.0 which is completely cloud based [12]. Data input and results output are implemented using a Google Drive™ spreadsheet template and a set of common shared libraries hosted on the InterPSS account which the users can copy to their Google Drive™ Accounts, open and edit in a Web browser. The simulation engine runs in on a cloud server and receives a simulation request via a Google App Script (based on JavaScript) embedded in the spreadsheet, carries out the processing and sends the result back to the spreadsheet where it can be stored. The High Level Application diagram is as shown in Fig. 3 [12].

It is a 3+ tier System with a Java Program as the Simulation Engine, and the Google App Script and Google Drive™ Spreadsheet as the data transport tier via a Google Web Service, and the web browser for user interaction via the spreadsheet.

2.1.2 NEPLAN 360

NEPLAN 360 is a power system analysis tool that can be operated from inside a web browser and is licensed by Neplan AG. According to the NEPLAN 360 website it is the first fully browser based power system analysis tool on the market and offers therefore all advantages of cloud computing [13]. The calculation modules have the same characteristics as the ones in the desktop version of NEPLAN and it handles AC and DC networks in the same manner as the desktop version [13]. It also provides a similar Graphical User Interface (GUI) and can also be accessed without a web browser by using Web Services to build networks and access the results of calculations.

2.1.3 MATLAB Based Systems: SimPowerSystems and MATPOWER

The Web implementation of these solutions is inferred from the capability of MATLAB files to be run from Web Applications. This is possible as MATLAB running on a server can be invoked as an Automation server from any language that

supports Component Object Model (COM), so Web applications can use ASP.NET [16], VBScript and JavaScript [15] (can only be deployed from MATLAB running on a web browser locally on a computer and not remotely on a web server). This is also a 3-tier methodology with the MATLAB application residing on a server being called from an intermediate language such as PHP or ASP.NET on a web server or in the web browser [16].

2.2 Web-Based Power Systems Simulation in Previous Research Work

There have been implementations of Web-based PSS in previous research work, perhaps not as many as one would expect given the ubiquitous nature of Web-based systems recently.

Leou and Gaing in [17] use Active Server Pages (ASP), which is a web programming language similar to PHP and a predecessor of ASP.NET, to call functions in modules programmed in Visual Basic programming; therefore implementing a 3-tier architecture as previously described.

In [18] Chen and Lu describe a system based on a Model-View-Controller framework (MVC) that uses a Java 2 Platform Enterprise Edition (J2EE) architecture to connect to an existing legacy system by using Java Server Pages (JSP) in the server, applets in the web browser and Fortran based simulation routines as the Simulation engine in a 3+ multi-tier system with the web server acting as a gateway.

Yang, Lin and Fu implement a .NET framework system for micro power system design [19]. The application layer uses the C# based assemblies and Dynamic Link Libraries (DLLs) for the simulations and ASP.NET for serving results to the web browser.

Shaoqiong Tan et al. also implement a Web-based simulator using a stack comprising ASP.NET for the web server programming and C# language for the simulation engine in [20]. They also indicate that C# is an evolution of C and C++, which is designed for building a wide range of enterprise applications that run on the .NET Framework.

Finally Hong Chen et al. use Java programming for a SCADA system over Local Area Networks and Internet, with a Java Applet for a GUI [21]. This system isn't web browser based therefore runs on a different platform from the simulation package described in this chapter.

2.3 Advantages and Disadvantages of Using a PHP Simulation Engine for Power Systems Simulation

The merits and demerits of PHP are discussed widely on the internet in detail [22, 23]. As with any other programming language, the purpose determines what counts

as an advantage or disadvantage. In relation to a web based simulation engine, the main advantages and disadvantages of using PHP for power systems analysis are as follows:

Advantages:

   i. Platform Flexibility
      Because PHP can be used on multiple platforms including Windows and UNIX based systems such as Linux, the operating system or computing system does not affect the development of the simulation tool [23].
  ii. Reduction in Server Resources Required for Some Operations and Reduced Pricing
      Because the PHP simulation engine results in a thinner application, the server processing power and memory requirements are less, leading also to reduced expenditure on the server and cloud computing resources. PHP was designed to be run on open source web servers and platforms, which means any application developed using PHP is well suited for students, schools and SMEs with budget limitations. Furthermore, power systems studies will benefit from having more free alternatives to the premium packages that dominate the market which usually have limits on network size.
 iii. Suitability for Smart Networks
      With the introduction and proliferation of smart networks [24] and devices that use TCP/IP and HTTP communications for power systems applications [25, 26], PHP which is a web programming language and is designed for use over such networks may provide more applications for consumer interaction with future electricity networks.
  iv. Database Support
      One of the strongest points of PHP is its support for a wide range of databases. By using database specific extensions, e.g., for a MySQL database or MSSQL, or using an abstraction layer like its native PHP Data Objects (PDO), PHP can use data from various sources [23]. The implication is that legacy data from existing systems can be connected to such applications with a level of ease that is not available with other languages, and without modifying that data format.
   v. Interconnectivity
      PHP has support for talking to other services using protocols such as LDAP, IMAP, SNMP, NNTP, POP3, HTTP, COM (on Windows), etc. [23]. Raw network sockets can also be opened to interact using any other protocol. PHP also has support for instantiation of Java objects and using them transparently as PHP objects [23]. This implies that applications created using other languages can be extended to be used in the power systems analysis based on the PHP platform. PHP can also execute shell commands, meaning that a fall back system to a 3-tier system is also possible when the application requires additional functions.

vi. Portability

PHP can be compiled into C++ using the Hip-hop PHP compiler (HpHpC) [27, 28]. The performance gains of C++ are combined with the rapid development paradigm of PHP using this approach. Hip-hop for PHP was developed by the creators of Facebook™ who originally used PHP to develop the popular social networking site but required some of the performance and scalability features of C++ without converting their entire codebase. The Hip-hop Virtual Machine (HHVM) is also available for use to scale PHP applications without compiling them, working like a Just-In-Time (JiT) compiler [27, 28].

vii. Results Presentation

Using PHP allows simulation results to be published in a web-based, interactive manner on the internet or a local network easier than other programs such as PowerFactory or MATLAB. PHP code can easily be embedded in Web Pages, making the integration process easier for results presentation. By using JavaScript, CSS and HTML tools, the otherwise static results may also be given aesthetic modifications unmatched by other platforms.

viii. Simplicity and Learning Curve

PHP was designed to be easy to learn and to allow beginners and less experienced programmers to build dynamic websites and achieve complex tasks easily [22, 23, 29]. By using PHP for power systems analysis, engineers with little programming experience can perform analysis and computation without the assistance of third parties and exert full control on their work. Experienced programmers in other C-style languages in general also find it easy to learn.

ix. Availability of Analytical Tools

PHP provides adequate tools for power systems analysis, such as matrix manipulation, complex number analysis, etc. The tools for Mathematical computation are provided both natively and via Math extensions [30]. Although there are packages and languages that provide more power and control to carry out functions required for the analysis of power systems, the OOP concepts available in PHP allow the creation of specific functions as required.

Disadvantages: The disadvantages and challenges that are likely to be encountered when using PHP for power systems analysis related to this work are as follows:

i. Language Flaws

The flaws of the PHP programming language itself are well documented [22, 29] with issues such as consistency, loose variable types and declarations, programming style, repetitive or obscure function names, scope, comparison operators, etc. Most of the flaws in the language are as a result of the flaws in the original versions with updates retaining some of them for compatibility

reasons. This may prove to be a pitfall when writing power systems applications in PHP.

ii. Availability of Programming Tools and Libraries for Power Systems Analysis
   Languages like C++ for Power systems analysis provide tools that make it
   easier to perform certain tasks, such as in C++ where native Templates can be
   used to declare the System admittance matrices [31]. This isn't the case in PHP
   and an extension [30] has to be used for matrix operations, or Matrix operations functions must be created by the developer. The same issues are expected
   for carrying out other forms of mathematical analysis, and it may require
   significant additional work writing functions specifically to perform these or
   the use of third party extensions. Furthermore, as no previous power simulation systems have been written in PHP, there aren't any reusable components
   apart from those developed in the simulator described in this chapter. It means
   that any other engineers or researchers will have to use these or lose time
   re-developing operational components which are already available in packages
   like MATLAB [14]. This will have to be weighed against the advantages it
   provides in making a decision to use PHP.

iii. Performance
   Since PHP is interpreted and not compiled, PHP programs must be parsed,
   interpreted, and executed each time each time they run and are therefore
   usually slower than compiled languages [28]. However virtual machines such
   as HHVM [27] described previously as well as fast web server applications
   such as NginX [32] mitigate this interpreted language inherent performance
   issue significantly.

A lot of the disadvantages and advantages of PHP may be viewed from a more
philosophical standpoint, regarding the perceived quality or maturity of PHP as a
programming language, or even if it is appropriate to refer to it as one rather than as
a scripting language.

The PHP-based solution meets the requirements for a power systems simulation
outlined in [33]. It exploits the advantages presented and can produce valid, consistent results comparable with benchmarks from other recognised packages
therefore it is a suitable candidate for the investigations.

3   Methodology

This section describes the methodology implemented in building a Web-based
Power Systems Simulation Engine using PHP programming and is essentially a
documentation of its functions. The simulation engine performs a load flow analysis
on a given network using the Newton-Raphson method according to the procedure
outlined in [34] to obtain unknown bus voltage magnitudes and angles, and also the
real and reactive power magnitudes for a given network. It also computes the line

flows by first computing line currents and then the power flowing in each line as well as its direction.

The system architecture to show the different components of the application and their interactions are outlined in this section. It will begin by showing how some concepts which are not native to PHP but required for power systems analysis are achieved and then break down the engine into its modules and how they interact.

3.1 Extending the Functionality of PHP to Handle Power Systems Simulation Concepts

The most important part of the methodology is how PHP will be extended to handle operations that are not native to it. For power systems computations matrix, complex number and vector operations are the most important to be considered. The PHP core comes with a library for general and basic mathematical operations [35]. It does not provide full native support for matrix operations, complex numbers and vectors.

To use such functions one can either install mathematical extensions [36] which will allow the programmer call functions for matrix operations as though they were native to PHP, or the programmer will have to include a PHP class file that contains methods to perform matrix, vector and complex number operations and then refer to that class each time the operation is required. The PHP group currently doesn't provide an extension for complex number operations, but have a repository for such classes using a PEAR extension. PEAR stands for PHP Extension and Application Repository and is a framework and distribution system for reusable PHP components [37].

3.1.1 Matrix Operations

A matrix may be defined in PHP as arrays of arrays, representing rectangular matrices in row major order [38, 39] so a two by two matrix [1 2; 3 4] would be

$$\$matrixArray = array(array(1,\ 2),\ array(3,\ 4))$$

An array is defined in the PHP manual as an ordered map. A map is a type that associates values to keys [40]. It is a programming concept available in most languages.

Defining a matrix as described limits the programmer to storage and retrieval of data in a particular order as well as some other ordered data operations. To allow full matrix operations such as arithmetic, vector multiplication and finding the determinant, the PEAR Math Matrix package is used in developing this simulation engine. These packages are PHP classes with matrix operations, methods and properties. Using this method is preferred to using the PHP Lapack extension [38]

that provides some of these functions for two reasons. Firstly, the Lapack extension serves a specific purpose only−the matrix and linear algebraic operations, while the PEAR extension is installed once and used for several packages with different functions. Secondly, the classes used in the PEAR extension are written purely in PHP and are only additional PHP files that are included with the application. They can therefore be modified to suit the application easily.

The matrix is instantiated as follows:

$$\$matrix = new\ Math\_Matrix(\$matrixArray);$$

Now the $matrix variable is a Matrix Object [1,2; 3,4] and has all the properties and methods of a matrix, rather than being just a multidimensional array which only stores and retrieves the data in an ordered manner.

The limitation of the Math_Matrix class is that it can only accept real numerical values. The obvious problem with this in power systems analysis is that a bus admittance matrix is made up of complex number values. To solve this problem, the complex admittance matrix is organized and manipulated using native PHP multidimensional arrays while other matrices, such as the Jacobian matrix, which consist purely of real values and require other matrix operations are formed using this matrix class.

3.1.2 Complex Number and Vector Operations

PHP also doesn't natively handle complex number operations such as conjugation, inversion and determining angles which are required for power systems analysis. The PEAR Complex number package [41] is used to enable this functionality. Some operations such as solution of linear algebraic equations involving Jacobian matrices require vector analysis; the vector in this case referring to a one-dimensional array of real and reactive power. The matrix package for example solves linear equations using an iterative error correction algorithm and requires as input the left hand side vector and a right hand side matrix. To enable this type of functionality the PEAR vector package [42] is used in this methodology as it allows the use of vector methods and properties on variables in the simulation engine.

3.2 PHP Simulation Engine Classes

The simulation engine is implemented using Object Oriented Programming (OOP). OOP creates models based on a real world environment. As such, the structure is modular and functions can be re-used or modified independently of the entire program, and the functions are less dependent on each other but rather work alongside each other as required to achieve results [4, 43]. The Classes are PHP

Table 1 Electrical network definition in PHP simulator

S/n	Class Description	Methods	Properties
1	*Network Class:* represents an electrical network with no elements. It is the main dependency for all other classes as instances of the element class are added to this class to build the network.	*InitializeNetwork*: sort buses and lines in a particular order, set slack bus, compute bus unknowns and call method to form admittance matrix for this network *addBus*: add a bus object to this network *addLine*: add a line object to this network *Bus*: returns a particular bus object in the network by number *BusRealPower, BusReactivePower*: returns the real and reactive power of a given bus *BusUnkowns*: compute unknown parameters for given bus *formAdmittanceMatrix*: forms the network admittance matrix from the lines and respective buses given *delPdelQMatrix*: returns a vector of the change in power for the linearized relationship involving change in power, voltage magnitude and angle and the Jacobian matrix	*Buses*: array of bus objects in the network *Lines*: array of line objects in the network *admittanceMatrix*: multidimensional array of line admittances *jacobianMatrix*: matrix object representing Jacobian matrix from latest iteration *slackBus*: integer of slack bus number; default is 1 *voltageControlledBuses*: array of voltage controlled buses; filled during network initialization *initialV*: initial voltage magnitude for iterations, default is 1.0 per unit *initialD*: initial voltage angle for iterations, default is 0 *solution*: array for storing power flow solution *dPdQM_network*: vector of change in real and reactive power
2	*Bus Class*: object representing a power bus, or a node in an electrical network with all its properties and methods	*__construct*: set bus number, specified voltage magnitude PU and angle both default to null *addElement*: adds an element object to this bus and update the properties of this bus according to the properties of that element object, whether it is a generator or a load	*P*: bus real power *Q*: bus reactive power *S*: bus apparent power *Type*: slack, PQ or PV *Elements*: array of elements at this bus *Unknowns*: array of bus unknowns filled during network initialization *previousV, previousD, previousP, previousQ*: variable to store previous values of voltage magnitude, angle and power during iterations

(continued)

Table 1 (continued)

S/n	Class Description	Methods	Properties
3	*Line Object*: represents a line in an electrical network	*__construct*: initialize the line, set the numbers for connected buses and value for line impedance real and imaginary parts	*From*: number of first connected bus *To*: number of second connected bus *Impedance*: complex number object with impedance value *Admittance*: complex number with admittance value *Label*: string to label this line according to from-to notation
4	*Element Object*: object representing a generic element in the network. The element may either be a generator or other active element or a load.	*__construct*: initialize element and set its properties. The properties default to null so they may be set after initialisation	*S*: a complex number object representing the apparent power. Computed from the values of real and reactive powers given or declared explicitly. Can be negative or positive depending on the flow property. *Flow*: string representing direction of power flow in or out of the network in relation to this element *P*: real power *Q*: reactive power *Name*: user defined name for the element

Objects that contain Methods (actions, functions) and Properties (descriptions of physical attributes) for each of the system components.

The classes defined in this simulation engine are based on physical elements of the power network and some classes are defined for the computation operations performed on these elements. Some of the classes are dependent on others and cannot perform any functions without input from their dependencies.

3.2.1 Network Definition in PHP Classes

The classes described in Table 1 have been developed to form an electrical network in the PHP application which is ready for any operation or computation such as power flow or short circuit analysis and using any chosen method. With the exception of the jacobianMatrix property in the Network element, these are the bare minimum required objects for any other power system analysis that may be carried

out. This structure means these classes can be easily re-used in other PHP applications.

3.2.2 Newton-Raphson Power Flow Solution in PHP Classes

The Classes described in Table 2 are used to perform a power flow using the Newton-Raphson (NR) method on a valid PHP electrical network object. The modular structure of this methodology means that any other solution may be used

Table 2 PHP classes for Newton-Raphson power flow solution

S/n	Class Description	Methods	Properties
1	*JacobianMatrix:* contains the methods for the formation of the Jacobian matrix for a given network	*delPdelD, delPdelV, delQdelD, delQdelV*: these methods form the sub matrices of the Jacobian Matrix *FormMatrix*: takes a power network object and runs the methods for the Jacobian sub-matrices on it and returns a full Jacobian matrix as a matrix object. This object is stored in the Network's JacobianMatrix variable	No properties declared as all elements can be accessed from matrix object returned on its formation
2	*lfNR (Load Flow Newton Raphson)*: computes a Newton Raphson power flow solution for a given network according to the NR algorithm.	*exec*: this executes the individual steps of the power flow by forming the Jacobian Matrix, forming the power change vector and using the Matrix Object linear equation solution to obtain a step solution *updateNetwork*: updates the buses of the network with the latest results from an Iteration step *solve*: iteration function that calls the exec function at each step and checks the tolerance of the solution before finally computing slack bus values when given convergence criteria is met or set number of steps exhausted	*maxIterations*: maximum number of Iterations, to prevent infinite iterations *e*: variable for acceptable convergence criteria *step*: current iteration step
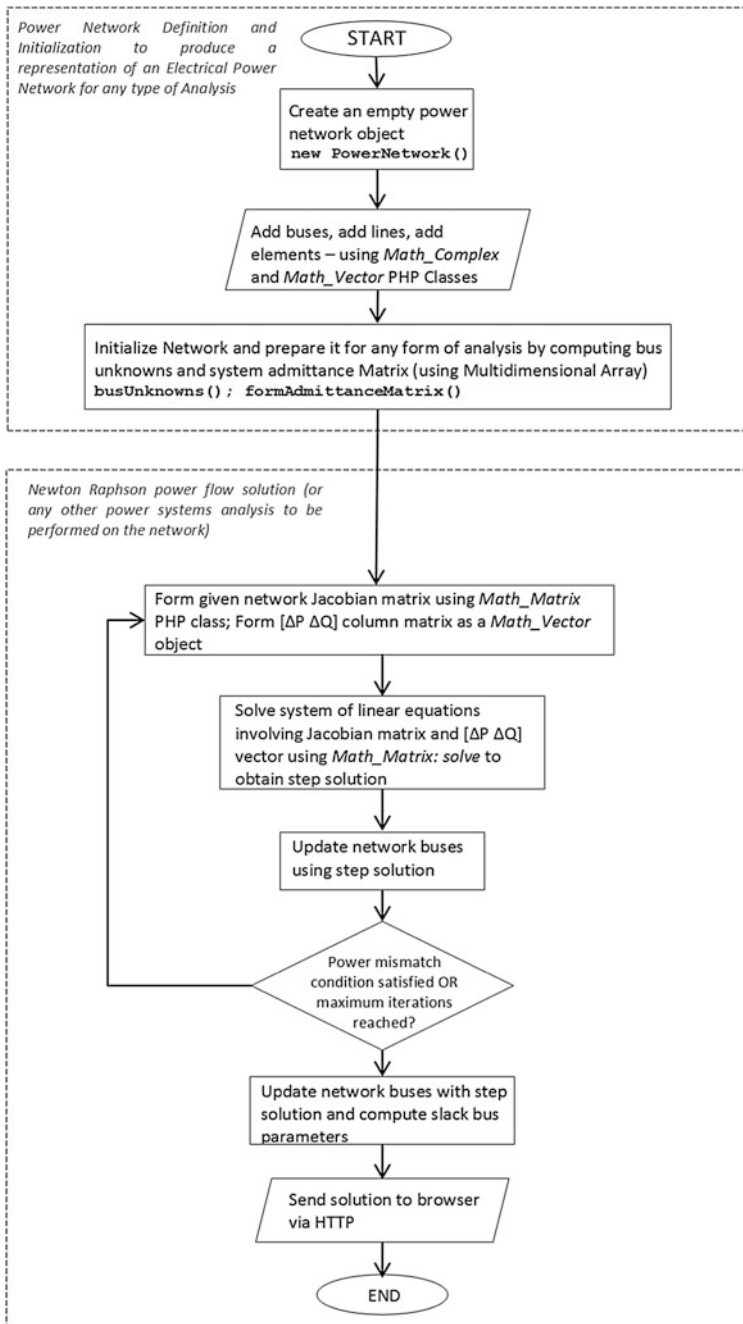
Fig. 4 Flowchart for Newton-Raphson power flow solution in PHP

alongside the NR on the same network and won't require the entire application including the network definition classes to be developed again.

3.2.3 Newton-Raphson Power Flow PHP Application Flowchart

The PHP application for computing the Power flow solution using the Newton-Raphson follows the same flow chart structure as a generic power flow using any other method described in [44]. The specific flowchart for this PHP application and methodology is shown in Fig. 4 and describes the interaction between the classes. This same structure can be incorporated into other power systems studies that require a power flow analysis to be carried out as a step, such as optimal power flow computation. The full process may also be broken into smaller processes because of the modular nature of the application. The flowchart shown in Fig. 4 is separated into two parts. The first part shows the process of creating a power network from the network data provided and is the basic requirement for the simulation. This network resides in the PHP application and can be used for any other analysis such as short circuit studies, reliability analysis, etc. The second part of the flowchart shows the process for the power flow carried out on the network, and can be replaced by another process.

4 Results and Discussion

The implementation of the methodology was tested by running a load flow analysis on different sized networks obtained from [34] and comparing with the results given. The computation of the load flow and network modelling in [34] was done using MATLAB programs.

The PHP application for these particular results was run on a shared remote web server with the software specification shown in Table 3. There are several other configuration parameters however these are the ones with some relevance to this implementation.

Table 3 PHP server software specification

	Item	Value
1	PHP version	5.2.17
2	Web server	Apache2.0.64
3	Operating system	Linux

4.1 Networks Tested and Parameters Observed

The solutions for 2-Bus, 3-Bus, 6-Bus, 26-Bus and 30-Bus networks obtained from [17, 34] were found to be consistent and accurate according to the results provided when the Newton-Raphson load flow was performed on them. The following server resource parameters were measured on the server side:

1. Execution time of functions
2. Memory usage of functions

These parameters were chosen to be observed because of the most likely applications which will involve using individual modules as part of a larger application residing on a server that receives multiple requests.

Because of the modularity of the application each of the functions (such as formation of admittance matrix, initialization of network, formation of Jacobian matrix, etc.) can be taken and used separately as part of a different application, thus the parameters were observed on a component/function basis.

The parameters observed also vary according to network size, network elements, convergence criteria and limits imposed. In this case however the number of buses in the network was used as an indicator of increasing complexity. Table 4 shows the average script execution time per iteration, and Table 5 shows the amount of memory allocated to the different operations involved.

It is important to note that these script execution times and memory requirements are not related to the specifications of the end user's computer and are not affected by the performance of the end user's computer. This means the time and memory requirements for each process on the same server will be similar for all users. The sole requirement for using the PHP power system application is access to the application server via a web browser and the performance will depend fully on the server. The centralized system also means that updates to the power systems simulation program are immediately accessible by all users. For example, electrical engineers on the field accessing the server through their devices to perform some analysis will always have the latest version of the application and will have a similar experience of the process in terms of performance. Fig. 5 shows a plot of the execution time and Fig. 6 shows a plot of the memory allocation for the individual simulation processes during the tests.

4.2 Discussion

The execution times shown serve as an indication of how much latency may be expected by including these scripts in an application. The execution time is most relevant for real-time online applications which will require quick results computation.

Based on the results, the time required for the same functions increases significantly between the relatively smaller networks (2-bus, 3-bus and 6-bus) and the

Table 4 Average script execution time per iteration (over 5 requests, in seconds)

	2-Bus network (4 Iterations)	3-Bus network (3 Iterations)	6-Bus network (4 Iterations)	26-Bus network[a] (3 Iterations)	30-Bus network[a] (4 Iterations)
Reading network data into application using XML	1.4529×10^{-3}	2.2199×10^{-3}	2.5980×10^{-3}	5.000×10^{-3}	5.0011×10^{-3}
Formation of admittance matrix	0.1640×10^{-3}	0.3569×10^{-3}	1.5819×10^{-3}	14.0011×10^{-3}	18.0020×10^{-3}
Formation of Jacobian matrix	0.2669×10^{-3}	0.3750×10^{-3}	2.1381×10^{-3}	21.0021×10^{-3}	27.0021×10^{-3}
Formation of power mismatch vector	0.089883×10^{-3}	0.1449×10^{-3}	0.5762×10^{-3}	3.9999×10^{-3}	5.0011×10^{-3}
Solution of sets of linear equations to obtain step solution (time per iteration)	0.6709×10^{-3}	1.1210×10^{-3}	12.8656×10^{-3}	570.0571×10^{-3}	930.0928×10^{-3}
Total including other functions	7.29513×10^{-3}	11.159×10^{-3}	67.9371×10^{-3}	1804.179×10^{-3}	3845.3848×10^{-3}

[a]Includes generator reactive power control

Table 5 Server memory allocation (in kB)—average for Jacobian matrix formation, power mismatch vector and step solution

	2-Bus network (4 Iterations)	3-Bus network (3 Iterations)	6-Bus network (4 Iterations)	26-Bus network[a] (3 Iterations)	30-Bus network[a] (4 Iterations)
Reading network data into application using XML	36.1171	41.3047	59.4180	207.6796	204.1953
Formation of admittance matrix	2.8555	4.5898	13.5898	245.8593	357.6406
Formation of Jacobian matrix	4.2148	5.9982	18.6299	472.2343	641.7265
Formation of power mismatch vector	1.2598	1.3164	1.9833	7.7578	8.8828
Solution of sets of linear equations to obtain step solution (time per iteration)	1.1816	1.1497	1.42678	4.9531	5.4843
Total including other functions	226.3867	233.5703	266.3398	727.8984	854.7890

[a]Includes generator reactive power control
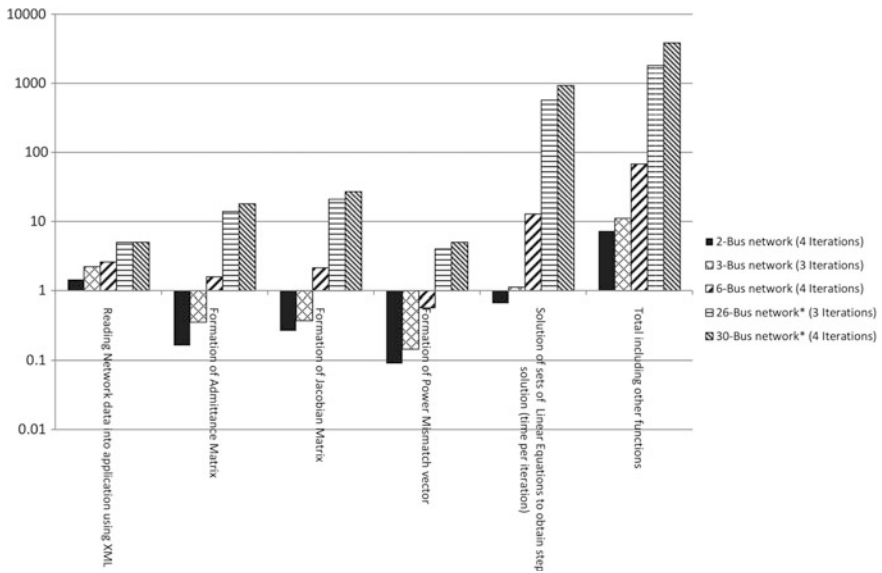
Fig. 5 Timing of power systems simulation scripts in milliseconds on a logarithmic scale in base 10
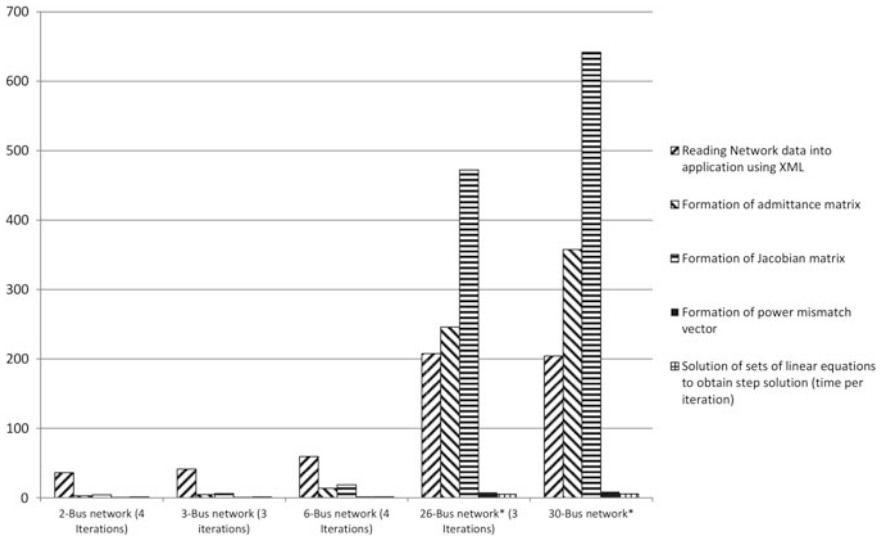
Fig. 6 Server memory allocation for functions (in kB)

larger networks (26-bus, 30-bus), such that it has to be represented on a logarithmic scale. The key areas where this jump is most visible is in the matrix operations and the vector operations which are carried out using third party classes, so this is an area which must be optimized either by rewriting the classes to improve performance or by comparison with other classes for similar functions. The generator reactive power control on the larger networks also accounts for some of the additional processing time. The relationship between the timing and size of the network may be derived by carrying out further investigations with more network sizes between the extremes.

The memory usage is relevant in cases where an application is hosted on a cloud computing platform which includes billing according to memory usage. It is also noteworthy that the memory allocation is constant for every step even in separate requests. In applications where there are multiple requests made to the server for computation, both parameters will be preferred to below.

From the results the smaller networks require the most memory for reading the network data into memory. As the size of the networks increase, the higher memory requirement comes from the matrix operations. The vector operations memory consumption remains relatively low and scales well between the network sizes.

The additional time and memory consumption from the matrix operations as the network size increases is not surprising as the matrix size does increase by up to a square with each successive dimension (2×2, 3×3, 4×4, …). Rewriting the matrix operations class with this performance improvement objective in mind or developing a PHP extension for specifically for matrix operations are some possible ways to improve the performance.

The computation speed may be improved in a number of ways without changing the structure of the code or the server machine specifications. Among the options available are changing the web server application because factors such as the transfer rate, average request time, requests handled per second and wait time for response, some of which affect the latency, vary for different web servers including Apache [45] and NginX [32] (pronounced "Engine Ex"). A virtual machine such as Hip-Hop Virtual Machine HHVM [28, 29] also improves PHP performance significantly and is increasingly being used on web application servers.

One of the advantages of an open source solution such as PHP is that a lot of third party applications exist to provide functionality or improvements that are not included in the PHP core.

Furthermore, PHP comes with shell execution functions [46, 47] which are the functions used to execute programs running on a separate simulation engine in a 3-tier framework. These functions can be triggered as a fall-back mechanism or to provide functions too complex to be derived in PHP, thereby taking advantage of its versatility.

5   Conclusion

This chapter has shown that PHP is capable of being used as a simulation engine for web-based power systems analysis and not only for results delivery from other simulation engines written in other languages, which is how web programming languages are being used currently. The methodology described the fundamental components that will be required to achieve the analysis and a modular structure for a PHP application to carry out power flow analysis using the Newton-Raphson method.

The main reason for using PHP is that it creates a new option for programming power systems simulators and in doing so creates a thinner application with fewer resource requirements, fewer points of possible failure, high compatibility and suitability for web applications and versatility. This is not to say PHP is the best solution for web-based power systems analysis, but that it is a suitable and available option.

The use of a new programming language and method to deliver solutions which are already implemented in other programming languages and methods may not be associated with any major benefits when viewed in terms of the final outcomes for the same problems. However, the possible benefits to be derived reside in the smaller details involved in the process between the problem and the solution.

The new methodology provides another viable programming option for obtaining power systems solutions which researchers and engineers will find useful in their applications, and the minor advantages derived and slight changes in the process can scale up significantly to result in major benefits and perhaps a paradigm shift in how power systems simulation is approached.

References

1. I. Bojanova and A. Samba, "Analysis of Cloud Computing Delivery Architecture Models," 2011 IEEE Work. Int. Conf. Adv. Inf. Netw. Appl. Biopolis, Singapore, pp. 453–458, Mar. 2011.
2. I. Bojanova, J. Zhang, and J. Voas, "Cloud Computing," IEEE IT Prof., vol. 15, no. 2 - March / April, pp. 12–14, 2010.
3. J. Lockhart, "The new PHP," O'Reilly Media Inc Programming Radar, 2014. [Online]. Available: http://radar.oreilly.com/2014/03/the-new-php.html. [Accessed: 15-Mar-2014].
4. D. Powers, PHP object-oriented solutions. Berkeley, CA, United States of America: Apress, 2008, pp. 3–19.
5. J. Byrne, C. Heavey, and P. J. Byrne, "A review of Web-based simulation and supporting tools," Simul. Model. Pract. Theory, vol. 18, no. 3, pp. 253–276, Mar. 2010.
6. Oracle, "Java Virtual Machine Specification," Java SE Documentation, 2011. [Online]. Available: http://docs.oracle.com/javase/specs/jvms/se7/html/jvms-1.html#jvms-1.2. [Accessed: 07-Jul-2014].
7. Microsoft, ".NET Framework Versions and Dependencies," Microsoft Developer Network, 2014. [Online]. Available: http://msdn.microsoft.com/en-us/library/bb822049(v=vs.110).aspx. [Accessed: 26-Jul-2014].
8. Oracle, "Lesson: Java Applets," The Java Tutorials. [Online]. Available: http://docs.oracle.com/javase/tutorial/deployment/applet/. [Accessed: 20-Jul-2014].
9. IEEE Open Source Software Task Force, "IEEE Open Source Software." [Online]. Available: http://ewh.ieee.org/cmte/psace/CAMS_taskforce/software.htm. [Accessed: 11-Nov-2013].
10. Open Electrical, "Power Systems Analysis Software," 2013. [Online]. Available: http://www.openelectrical.org/wiki/index.php?title=Power_Systems_Analysis_Software. [Accessed: 11-Nov-2013].
11. W3Techs: Web Technology Surveys, "Usage Statistics and Market Share of PHP for Websites, January 2014," 2014. [Online]. Available: http://w3techs.com/technologies/details/pl-php/all/all. [Accessed: 03-Jan-2014].
12. InterPSS Community, "InterPSS 2.0 Manual and Documentation." [Online]. Available: https://sites.google.com/a/interpss.org/interpss/Home/interpss-2-0. [Accessed: 28-May-2014].
13. Neplan AG, "NEPLAN 360 Overview." [Online]. Available: http://www.neplan.ch/html/e/e_PowerSystems_Properties_default_web.htm. [Accessed: 27-May-2014].
14. R. Zimmerman, C. Murillo-Sanchez, and D. Gan, "MATPOWER: A MATLAB Power System Simulation Package Documentation," 2014. [Online]. Available: http://www.pserc.cornell.edu//matpower/. [Accessed: 30-May-2014].
15. MathWorks, "Call MATLAB functions from a Web Application," MATLAB R2014a Online Manual; MATLAB COM Automation Server. [Online]. Available: http://www.mathworks.co.uk/help/matlab/matlab_external/call-matlab-functions-from-a-web-application.html. [Accessed: 27-May-2014].
16. MathWorks, "How do I leverage the MATLAB Engine to deploy my MATLAB code over the web for an ASP.NET application using MATLAB 7.3 (R2006b)," MATLAB Central: MATLAB Answers, 2012. [Online]. Available: http://www.mathworks.com/matlabcentral/answers/99541-how-do-i-leverage-the-matlab-engine-to-deploy-my-matlab-code-over-the-web-for-an-asp-net-application. [Accessed: 27-May-2014].
17. R. Leou and Z. Gaing, "A Web-based load flow simulation of power systems," IEEE Power Eng. Soc. Summer Meet. Chicago, IL, USA, pp. 1587–1591, 2002.
18. S. Chen and F. Lu, "Web-based simulations of power systems," Comput. Appl. Power, IEEE, no. January, pp. 35 – 40, 2002.
19. J. Yang, F. Lin, and Y. Fu, "Development of a Web-Based Software for Micro Power System Design," 2010 Int. Conf. Electr. Control Eng. Wuhan, China, pp. 2748–2751, Jun. 2010.

20. S. Tan and J. Yang, "Internet-based platform for power system simulating and planning," in 2011 Second International Conference on Mechanic Automation and Control Engineering, Inner Mongolia, China, 2011, pp. 2271–2274.
21. H. Chen, C. Cañizares, and A. Singh, "Web-based Computing for Power System Applications," Proc. North Am. Power Symp. (NAPS), San Luis Obispo, California,, 1999.
22. M. Alex, "PHP: a fractal of bad design," Fuzzy Notepad, 2012. [Online]. Available: http://me.veekun.com/blog/2012/04/09/php-a-fractal-of-bad-design/. [Accessed: 04-Jan-2014].
23. The PHP Group, "What is PHP?," PHP Official Website. [Online]. Available: http://www.php.net/manual/en/intro-whatis.php. [Accessed: 25-Nov-2013].
24. European Commission Directorate-General for Research; Sustainable Energy Systems, "European SmartGrids Technology Platform," Brussels, 2006.
25. X. Lu, Z. Lu, and W. Wang, "On Network Performance Evaluation toward the Smart Grid: A Case Study of DNP3 over TCP/IP," 2011 IEEE Glob. Telecommun. Conf. - GLOBECOM 2011, Houston, TX, USA, pp. 1–6, Dec. 2011.
26. R. Amiri and O. Elkeelany, "An embedded TCP/IP hard core for Smart Grid information and communication networks," Proc. 2012 44th Southeast. Symp. Syst. Theory (SSST), Jacksonville, Florida, USA, pp. 185–189, Mar. 2012.
27. Facebook, "HipHop Virtual Machine for PHP," HipHop Virtual Machine Specification. [Online]. Available: https://github.com/facebook/hhvm/wiki. [Accessed: 09-Sep-2013].
28. H. Zhao, J. Evans, S. Tu, I. Proctor, M. Yang, X. Qi, M. Williams, Q. Gao, G. Ottoni, A. Paroski, and S. MacVicar, "The HipHop compiler for PHP," Proc. ACM Int. Conf. Object oriented Program. Syst. Lang. Appl. - OOPSLA '12, Tucson, AZ, USA, p. 575, 2012.
29. A. Crane, "Experiences of Using PHP in Large Websites," UK Unix and Open Systems User Group. [Online]. Available: http://www.ukuug.org/events/linux2002/papers/html/php/index.html. [Accessed: 04-Jan-2014].
30. The PHP Group, "Math:: PEAR Packages," PEAR Packages. [Online]. Available: http://pear.php.net/packages.php?catpid=15&catname=Math. [Accessed: 09-Sep-2013].
31. M. Zhou, High Performance Computing in Power and Energy Systems: Distributed Parallel Power System Simulation. Berlin: Springer, 2013.
32. Nginx Community, "NginX." [Online]. Available: http://wiki.nginx.org/Main. [Accessed: 08-Jul-2014].
33. F. Milano, Power system modelling and scripting, First. Ciudad Real, Spain: Springer, 2010.
34. H. Saadat, Power System Analysis, Second Edi. Milwaukee: McGraw Hill, 2004.
35. The PHP Group, "PHP Manual - Mathematical Functions." [Online]. Available: http://us3.php.net/manual/en/math.installation.php. [Accessed: 17-Jun-2014].
36. The PHP Group, "PHP Manual: Mathematical Extensions." [Online]. Available: http://us3.php.net/manual/en/refs.math.php. [Accessed: 17-Jun-2014].
37. The PHP Group, "PEAR: PHP Extension and Application Repository." [Online]. Available: http://pear.php.net/. [Accessed: 17-Jun-2014].
38. The PHP Group, "PHP Manual: Lapack Class." [Online]. Available: http://us3.php.net/manual/en/class.lapack.php.
39. J. M. Castagnetto, "PEAR: Math_Matrix," PEAR Packages, 2010. [Online]. Available: http://pear.php.net/package/Math_Matrix/. [Accessed: 17-Jun-2014].
40. The PHP Group, "PHP Manual: Arrays," The PHP Manual. [Online]. Available: http://us3.php.net/manual/en/language.types.array.php. [Accessed: 17-Jun-2014].
41. J. M. Castagnetto, "PEAR: Math_Complex," PEAR Packages, 2010. [Online]. Available: http://pear.php.net/package/Math_Complex/. [Accessed: 17-Jun-2014].
42. J. M. Castagnetto, "PEAR: Math_Vector," PEAR Packages, 2010. [Online]. Available: http://pear.php.net/package/Math_Vector/docs/latest/li_Math_Vector.html. [Accessed: 17-Jun-2014].
43. Oracle, "Object-Oriented Programming Concepts," The Java Tutorials, 2013. [Online]. Available: http://docs.oracle.com/javase/tutorial/java/concepts/. [Accessed: 03-Jan-2014].
44. J. Arrillaga and C. P. Arnold, Computer Analysis of Power Systems. Christchurch, New Zealand: John Wiley & Sons, 1990.

45. The Apache Software Foundation, "Apache - HTTP Server Project." [Online]. Available: http://httpd.apache.org/. [Accessed: 08-Jul-2014].
46. The PHP Group, "PHP - Shell_Exec," PHP Official Website. [Online]. Available: http://php.net/manual/en/function.shell-exec.php. [Accessed: 08-Jul-2014].
47. The PHP Group, "PHP - Exec." [Online]. Available: http://php.net/manual/en/function.exec.php. [Accessed: 08-Jul-2014].

Integration of Dispersed Power Generation

George Seriţan, Radu Porumb, Costin Cepişcă and Sorin Grigorescu

Abstract Current paper deals with three main issues, regarding the operation of the electric power systems in the presence of distributed generation. The first issue regards the assessment of the main continuity of supply parameters, such as frequency of interruptions, duration of interruption, power not served and energy no served. This issues are the base guidelines for the network system operators' decision of building new distributed generation capacities which might be able to mitigate the electric network loss of operation. The second issue addressed was the consume variability of the various low-voltage consumers. This particularity, in conjunction with the sheer number of consumers leads to the creation of serious unbalance for the daily curve. This means that if the network system operator cannot contain the load variability, it must buy energy from intraday energy market, with a price decisively higher than the one of the reserved capacity. This issue leads to a two-fold necessity: implementing a better know-how system in order to better contain the customers load fluctuation and the necessity of distributed generation implementation, in order to help load shedding. The third issue regards general technical aspects with respect to the electrical distribution systems operation in the presence of distributed generation.

G. Seriţan (✉) · C. Cepişcă · S. Grigorescu
Faculty of Electrical Engineering, University Politehnica of Bucharest,
313 spl Independentei, sector 6, Bucharest, Romania
e-mail: george.seritan@upb.ro

C. Cepişcă
e-mail: costin.cepisca@upb.ro

R. Porumb
Faculty of Power Engineering, University Politehnica of Bucharest,
313 spl Independentei, sector 6, Bucharest, Romania
e-mail: radu.porumb@upb.ro

1 Introduction

Current transition of the current electric power system to the future smart grid is generating a turmoil of changes in the electric systems. These changes range from the electric network design, construction, analysis, operation and maintenance. The main driver of change is the ever-growing presence of distributed generation in the electric distribution systems. This situation lead to some unexpected results, such as increasing pressure on distribution systems operators to improve their services by assessing their interruption indexes, buying energy from intraday electricity markets to cover losses and turning their operation to a more business-orientated one. These three main topics were addressed in this analysis as a single framework, due to the fact that they are the causes that affects as a whole the electric distribution systems performance.

The first section is addressing the electricity distribution systems reliability indices such as frequency and duration of interruptions, power and energy not supplied. This was performed by evaluating the probability density functions (PDFs) of the of a set reliability indices. By considering the number of occurrences and duration of the interruptions as random variables (RVs), the indices become RVs and were evaluated through analytical expressions for computing their expected values and variances and with the Monte Carlo method in order to obtain the PDFs.

The second section deals with the evolution of the DSOs on the electricity market realm, where electricity suppliers need to have information on their customers' electricity consumption evolution in order to buy sufficient energy from the wholesale market to cover the hourly consumption at negotiated prices and average periods. This part proves to be particular sensitive, due to the fact that DSOs networks behaviour changes drastically, in terms of technical losses, proportionally with the presence of dispersed generation capacity into traditional electricity grid.

In the absence of such information, the service provider will be obliged to purchase the electricity wholesale market. The quantities of purchased energy may be smaller than its customer's needs—in which case, the deficit will be covered by purchasing the missing quantities in the market for next day or balancing market at higher prices. Where the supplier will buy power on the wholesale market more energy than is necessary for the customer, will be forced to sell the surplus, balancing market at a price lower than that with which the energy was purchased. Therefore, this material contains an analysis of three different customers for which DSO must refine its analysis, in order to supply with the exact amount of energy, in order to mitigate the eventual energy-level mismatches and subsequent financial losses.

The last part of the current framework shows small and medium-scale distribution generation systems as profitable solutions emerging for supplying the customers' loads in a de-centralized way. The necessity of reducing the high pollution produced by classical generation systems, the raising level of technological

solutions available and, especially, an explicit trend—in several countries—towards strong incentives for using renewable sources are among the main reasons explaining the success of the so-called distributed or dispersed generation.

2 Evaluation of the Probability Distributions of Reliability Indices in Electricity Distribution Systems Using Monte Carlo Simulation

For a distribution system with K load points, the reliability analysis takes into account two types of indices (local and global) [1]:

Local indices: are defined for each load point k = 1,…,K, and are calculated considering the frequency and duration of the states in which the point k is not supplied. Assuming the power Pk to be delivered to the point k during normal operation, the following local indices [2] are defined:

1. fk—frequency of the interruptions;
2. dk—duration of the interruptions;
3. PkNS = fkPk—power not supplied;
4. EkNS = dkPk—energy not supplied;
5. dkNS = dk/fk—average duration of the interruptions.

Global indices: are defined for the whole electrical network, representing the overall system reliability [2]:

$$\text{System Average Interruption Frequency Index} \, \text{SAIFI} = \tag{1}$$

$$\text{System Average Interruption Duration Index} \, \text{SAIDI} = \tag{2}$$

$$\text{Customer Average Interruption Duration Index} \, \text{CAIDI} = \tag{3}$$

The aim of this section is to introduce methods for calculating the analytical expressions of expected value and variance of the reliability indices, their PDFs and Cumulative Distribution Functions (CDFs).

For a better understanding of the purpose of the system analysis, we consider several parameters some of which are constant and deterministic (load power), or constant but associated to an exponential distribution (failure rate) or probabilistic, as RVs, as shown in Table 1.

		Constant	Probabilistic
Table 1 Nature of the distribution system variables	Load power (P)	×	
	Failure rate (λ)	×	
	Restoration time (τ)		×
	Number of occurrences of fault (n)		×

Also, we consider the distribution system with K load points during a given time interval [0,T]. We introduce a set Θ of the faults occurring in the distribution system and the sets Φk of the faults for which load point k is not supplied, for k = 1,…,K. A fault f Θ may require different phases of fault diagnosis and system restoration. Three types of faults are considered:

1. faults at the supply nodes, concerning the high voltage (HV) system, with a single restoration phase, due to the operations occurring on the HV system;
2. temporary faults in the distribution system, with trip of the circuit breaker, successful re-closure and final normal operation, again with single restoration phase;
3. permanent faults, requiring three different restoration phases after the trip of the circuit breaker:

   (a) remote—controlled operations, driven from the control center, to isolate the fault and restore the operation in the non-faulted part of the system;
   (b) additional manual operations, performed by the maintenance operators to isolate the fault and restore the operation in the non-faulted part of the system;
   (c) on-site repair of the fault and final service restoration.

We assume that faults are independent random events, with negligible probability of simultaneous faults.

1. The number of occurrences of a fault in a specified time interval is represented by the random value (RV) n, with Poisson distribution:

$$\Pr\{\mathbf{n}_f = N_f\} = \frac{\left(\lambda_f T\right)^{N_f}}{N_f!} e^{-\lambda_f T} \tag{4}$$

   where:

   - λ_f is the failure rate;
   - T is the length of the period of analysis;
   - N_f represents a deterministic number of occurrences of fault f.

2. The multi-phase service restoration is assumed to have a random restoration time for each phase, independent of the fault and of the restoration phase of the same fault. The RV τ is used to represent the restoration time.

Normally, we don't know a priori which is the type of distribution that emulates the behaviour of this RV. Generally speaking, there is a multitude of distribution functions which are used in calculation of τ. They are divided into two parts: one-parameter distribution functions and two-parameters distribution functions. Some other examples are shown in Table 2. The exponential PDF is sometimes used for its simplicity, but the Gamma distribution has been proven to be better to represent the real behaviour of the restoration times.

Table 2 Array of most utilized PDFs for calculating τ

	Function	Formula	Notes	Advantages
One parameter distribution functions	Exponential	$f(x) = \lambda e^{-\lambda x}$	Have limits for reality representation, due to its single parameter	Easy to calculate
	Rayleigh	$f(x) = \frac{2t}{\alpha^2} e^{\left(-t^2/\alpha^2\right)}$	Must pay attention to negative values when the variable makes sense only for positive values	
	Normal (Gaussian)	$f(x) = \frac{1}{\sigma\sqrt{2\pi}} e^{-(x-\eta)^2/2\sigma^2}$	The calculation of the parameters is iterative (assuming that mean value and variance are known)	
Two parameters distribution functions	Weibull	$f(x) = \frac{\beta t^{\beta-1}}{\alpha^{\beta}} e^{\left[-(t/\alpha)^{\beta}\right]}$	Very flexible	They characterize exhaustively the real representation
	Gamma	$f(x) = \frac{c^b x^{b-1} e^{-cx}}{\Gamma(b)}$	It is very easy to calculate (from known mean value and variance)	
	Lognormal	$f(x) = \frac{1}{x} e^{-\ln^2 x/2}$	Very flexible	

2.1 Reliability Indices

For calculating the reliability indices, it is essential to know the PDF of τ, because we must utilize the convolution without constraints. This boundary restrains the freedom of choosing PDFs, in particularly at Normal (Gaussian) and Gamma (only if they have the same scale factor).

2.1.1 Definition of the Reliability Indices

In this work, we consider the following reliability indices, defined for the time interval [0,T] [3]:

- The ***total duration of the interruptions***, represented by the RVs d_k at load point k and **d** for the whole system;

- The ***total energy not supplied***, represented by the RVs $\mathbf{w}_k$ at load point k and $\mathbf{w}$ for the whole system;
- ***The Frequency of fault occurrence*** f_k;
- ***The Power not supplied*** (P^{NS}).

We also assume that the power delivered to load point k to be P_k during normal operation. For k = 1,…,K, the classical reliability indices are then expressed in terms of the expected values of the RVs $\mathbf{d}_k$ and $\mathbf{w}_k$. For the *local indices*, we consider the expected value $E\{\mathbf{d}_k\}$ of the duration of the interruptions and the expected value $E\{\mathbf{w}_k\} = C_k\,E\{\mathbf{d}_k\}$ of the energy not supplied to load point k. The probability of the event "load point k is not supplied at a generic instant" is given by $E\{\mathbf{d}_k\}/T$. Global indices, which depend on the whole network can be build by computing a weighted average of the load point indices, using as weights the numbers of customers or the power supplied to the load points in normal conditions.

2.1.2 Expected Value of the Interruption Duration at Load Point K

The occurrence of a fault leads to a sequence of mutually exclusive fault states. Each fault state corresponds to a restoration phase, with remote-controlled or manual operations performed for restoring the service. By neglecting the simultaneous faults, it is possible to compute the duration of the service interruption during the restoration phases for any load point. We assume the service restoration after a fault $f \in \Theta$ to include a number φ_f of independent restoration phases.

The expected value $E\{\mathbf{d}_k\}$ of the duration of the service interruption during the restoration phases at load point k is computed by considering all the restoration phases in which load point k is not supplied. We introduce the binary variable $\delta_{kf}^{(m)} = 1$ if load point k is not supplied in the phase m of service restoration after the fault $f \in \Theta$, otherwise $\delta_{kf}^{(m)} = 0$ [3]. Assuming a negligible probability of simultaneous faults, in the restoration phase m = 1,…,φ_f after fault $f \in \Theta$ with failure rate λ_f, corresponding to the restoration time $\tau_f^{(m)}$, the expected value of the duration of the interruption is

$$\text{E}\{dk\} = \sum_{f \in \Theta} \sum_{m=1}^{\phi_f} \lambda_f \text{E}\left\{\tau_f^{(m)}\right\} \delta_{kf}^{(m)} \tag{5}$$

In the presence of permanent faults with multi-phase restoration, it is convenient to evaluate, for each fault $f \in \Theta$ and for all the load points k = 1,…,K, the binary variable $\delta_{kf}^{(m)}$ introduced by the fault, for m = 1,…,φ_f. For each fault at a supply node, with a single restoration phase ($\varphi_f = 1$), the variable $\delta_{kf}^{(1)}$ is equal to unity for the load points fed by the faulted supply node, zero otherwise. For each *temporary fault*, the trip of the circuit breaker isolates all the load points fed by the faulted

branch, there is again a single restoration phase ($\varphi_f = 1$) and the variable $\delta_{kf}^{(1)}$ is equal to unity for the load point fed by the faulted branch, zero otherwise. For each permanent fault, with three restoration phases ($m = 1, 2, 3$), the value of $\delta_{kf}^{(m)}$ depends on the restoration phase:

- in the first phase, $\delta_{kf}^{(1)} = 1$ if load point k is not supplied after the trip of the circuit breaker, otherwise $\delta_{kf}^{(1)} = 0$;
- in the second phase, $\delta_{kf}^{(2)} = 1$ if load point k is not supplied after the remote-controlled operations, otherwise $\delta_{kf}^{(2)} = 0$;
- in the third phase, $\delta_{kf}^{(3)} = 1$ if load point k is not supplied after the manual operations, otherwise $\delta_{kf}^{(3)} = 0$.

For any permanent fault, the evaluation of $\delta_{kf}^{(m)}$ for m = 2, 3 requires the detailed simulation of the operators performed to isolate the fault and to restore service. For this reason, we choose the backward/forward sweep analysis method (which will be presented in the next section).

2.2 Distribution System Structure and Analysis

For performing calculations as close as possible to the reality, we thought to generate a radial electrical distribution network which includes all the elements existing in a real electrical distribution network:

- Circuit breakers;
- Disconnects:
- Remotely commanded;
- Manually commanded
- Loads
- Branches (lines or transformers)

The design of the network structure was thought to be stratified into layers to simplify its numerical treatment and to facilitate the application of various calculation iterations.

2.2.1 Network Structure and Definitions

Let us consider a radial network with n + 1 nodes fed at constant voltage at the root node (node 0) as in Fig. 1. For each i-th node, let us define path(i) as the ordered list of the nodes encountered starting from the root (not included in the list) and moving
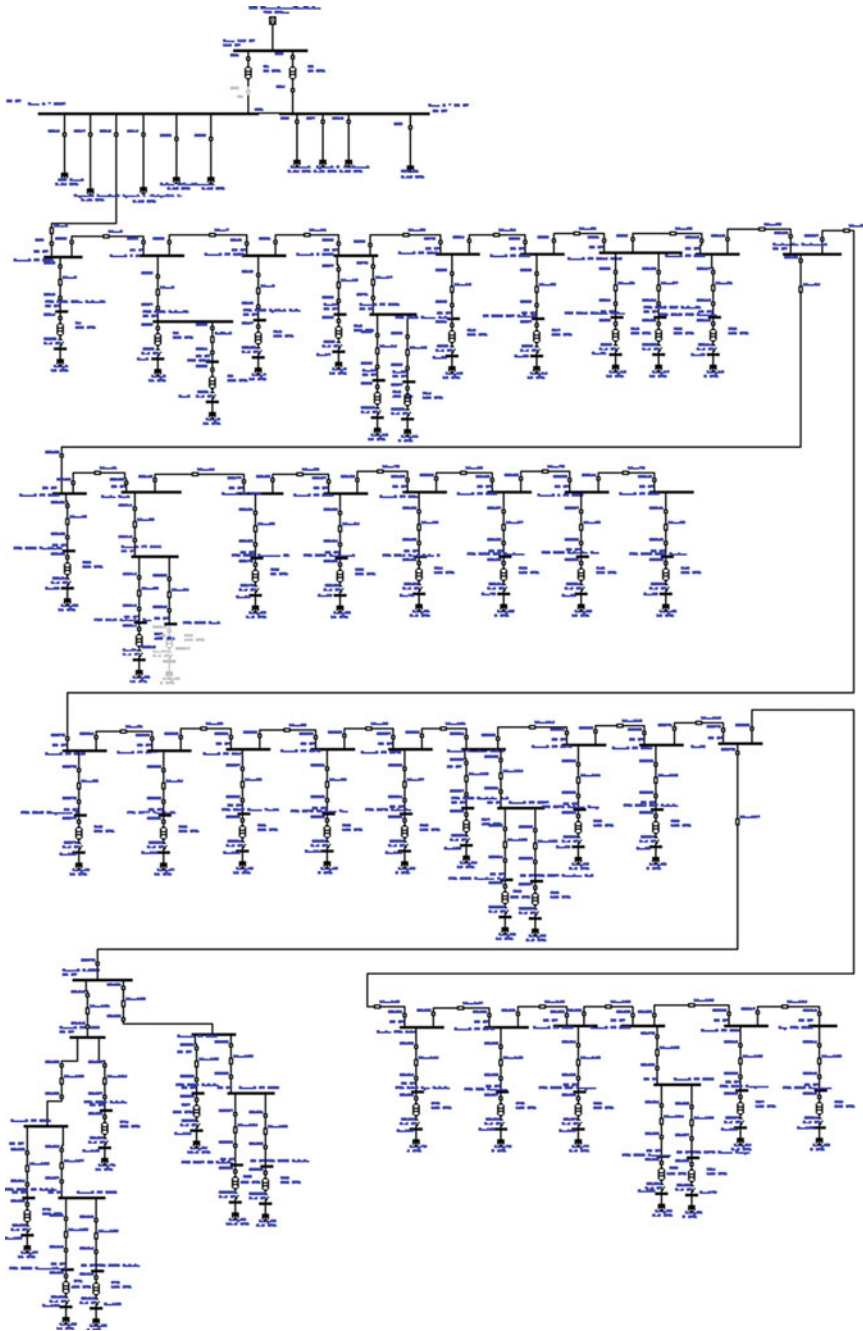
Fig. 1 The representation of the tested electrical network (ETAP 12.5)

to its i-th node [4]. Furthermore, each node belongs to a layer [5], which represents the position of the node in the network.

The following criterion is assumed for node and line numbering:

- The nodes are numbered sequentially in ascending order proceeding from layer to layer (Fig. 1), in such a way that any path from the root node to a terminal node encounters node numbers in ascending order;
- Each branch starts from the sending bus (at the root side) and is identified by the number of its (unique) ending bus.

2.2.2 Extracting L and Γ Matrices Out of the Test-Network

The above numbering leads to a particularly convenient system representation, in which both the node-to-branch incidence matrix $L \in N^{n,n}$ (root node not included) and its inverse $\Gamma = L \in N^{n,n}$ are lower triangular. Assuming for each branch a conventional value +1 for the sending bus and −1 for the ending bus, the generic component l_{ij} of the matrix $\mathbf{L}$ is

$$lij = \begin{cases} -1 & \text{if } i = j \\ 1 & \text{if } j = \text{sending bus(branch } i) \\ 0 & \text{otherwise} \end{cases} \qquad (6)$$

while the generic component γij of the matrix Γ is

$$\gamma ij = \begin{cases} -1 & \text{if j path(i)} \\ 0 & \text{otherwise} \end{cases} \qquad (7)$$

In the j-th column of the matrix $\mathbf{L}$, the rows with non-zero terms correspond to the branches having the j-th node as sending bus. In the j-th column of the matrix $\mathbf{\Gamma}$, the rows with non-zero terms correspond to the nodes belonging to the branches derived from the j-th node. In the absence of mutual coupling between branches, it is possible to build the matrix $\mathbf{\Gamma}$ directly by visual inspection, without inverting the matrix $\mathbf{L}$. The present calculation technique used largely Matlab's mathematical power. It was intended to develop a program which could include a complete view over an electrical network and calculate its different reliability indices.

So, it was implemented an algorithm which identifies a network and its mutually coupling between branches ($\mathbf{L}$ matrix) and further on, identifies the $\mathbf{\Gamma}$ matrix [4]. Its next attribute is to compute the power not supplied for temporary faults at each branch by varying m from $\delta_{kf}^{(m)}$ (see Table 3). So, for $m = 2$ the program calculates the P^{NS} after completing all the remote-controlled operations to restore the network; for $m = 3$, the program calculates the P^{NS} after completing all the remote and manual operations due to restore the network.

Table 3 Evaluation of possible fault types and corresponding load point indices

Type of fault	φ_f	m	$\delta_{kf}^{(m)}$		Explanation
Supply point	1	1	$\delta_{kf}^{(1)}$	1	Fed by the faulted branch
				0	Otherwise
Temporary	1	1	$\delta_{kf}^{(1)}$	1	Fed by the faulted branch
				0	Otherwise
	3	1	$\delta_{kf}^{(1)}$	1	Load point k is not supplied after the trip of the circuit breaker
				0	Otherwise
Permanent		2		1	Load point k is not supplied after the remote-controlled operations
				0	Otherwise
		3		1	Load point k is not supplied after the manual operations
				0	Otherwise

The results of these two iterations are used afterwards to compute the w_k for the branches affected by the fault. The advantage of this approach of the electrical network is that it gives a greater elasticity in formulating different scenarios of faulted branches.

2.3 Application of the Monte Carlo Method

2.3.1 General Hypotheses

Monte Carlo Methods (MCM) consist in experimental simulation of mathematical problems for which random numbers are used for discovering the solution.

In reliability calculations of electrical distribution networks, both analytical and simulation techniques are used. The analytical techniques are mathematical rigorous and are used to find expected value and variance. These are valuable indices for the system, but they are insufficient into give a complete view of the resulting PDF.

In our test network, the point of interest is constituted by reliability indices. It is well known the fact that MCM is a so called "blind method", which means that it has no "a priori" instrument to guide itself through the iterations for reaching an outcome. The most effective approach is to generate a random variable using a suitable probability density function that could emulate the development of the process.

So, for realizing our tests, we considered that the best type of distribution for our random numbers should be Poisson, due to the fact that its domain of definition covers the "rare event probability", and in our case (reliability indices analysis) the events (interruptions) are rare. Another motivation for our choice was that a convolution made with many discrete Poisson probability distribution functions (PDFs) has the propriety of keeping a Poisson profile.

2.3.2 The Sequential Monte Carlo Method

The sequential MCM [6–10] has been used to address the reliability indices computation. Typically, the number of faults involving a single load point is not very high, so that the load points indices exhibit unusual forms with possible multi-modal shapes. In these cases, the MCM is particularly used. Therefore, some load point indices have been computed. Global indices are less interesting for the MCM method application, since the presence at several load points make these indices very close to the Normal form.

The program is structured to run in steps, facilitating the interventions required for any modifications, also providing a better level of understanding of the algorithm.

Step 1: Read data of the electrical network matrix, composed of sending nodes, receiving nodes, type of each node (0-rigid; 1-circuit breaker; 2-remote controlled disconnect; 3-manual controlled disconnect), failure rate (λ) for each node for temporary faults, λ for each node for permanent faults, restoration time (τ) for temporary faults and τ for permanent faults; also the restoration times for Gamma-distributed temporary and permanent faults (min/year) (shape factor and scale factor) are established; the step concludes with the initialization of the indices (as permanent failure rate and temporary failure rate), and the number of years for the analysis (in our case, 10 years).

Step 2: Initialization of the parameters required for Monte Carlo (MC) simulations. There are the boundary values which delimit the acceptable values of MC simulation. Also there are the range of the classes utilized to realize MC histograms, whose limits are also determined in function of Power Not Supplied (PNS), for which two a priori values for each level were chosen and the number of classes inside the range min-max

Step 3: For a single load point a series of routines are executed to calculate:

- The Power Not Supplied (PNS),
- The Outage Time,
- Number of Interruptions,
- The Energy Not Supplied (ENS)

Step 4: Extraction of the incidence matrix Gamma out of the test-network

Step 5: An external cycle for MC calculation is generated, composed of the following subroutines:

- Creation of the random temporary fault profile;
- Creation of the random permanent fault profile;
- Another cycle is initialized for computing the reliability indices:

  - Location of the temporary faults;
  - Computation of PNS TotalInterrTime, NumberInterr, ENS for temporary faults at each branch;
  - Location of the permanent faults;
  - Computation of the PNS, TotalInterrTime, NumberInterr, ENS for permanent faults at each branch,
  - Computation of MC histograms for PNS, TotalInterrTime, NumberInterr and ENS.

The data used in the program was structured, for more convenience, into a two-dimension array, having number of rows equal with number of nodes of the test-network and number of columns equal with the number of indices needed for our iterations. In our case, the columns were formed by: *ending nodes* (of the test-network), *receiving nodes*, *type of receiving node* (0-rigid; 1-circuit breaker; 2-remote controlled disconnect; 3-manual controlled disconnect), *load* (in p.u.), *failure rate for each node for temporary faults and failure rate for each node for permanent faults*.

The output of the program looks as a series of histograms as indicated in Figs. 2, 3, 4, 5, 6, 7, 8 and 9.

Fig. 2 Histogram of PNS
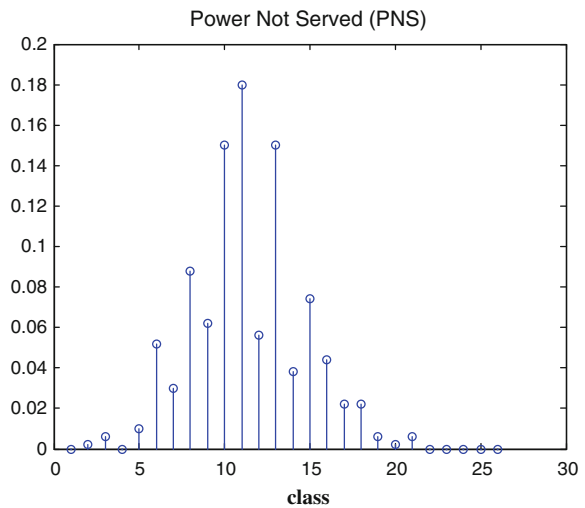
Fig. 3 Histogram of number
of interruptions
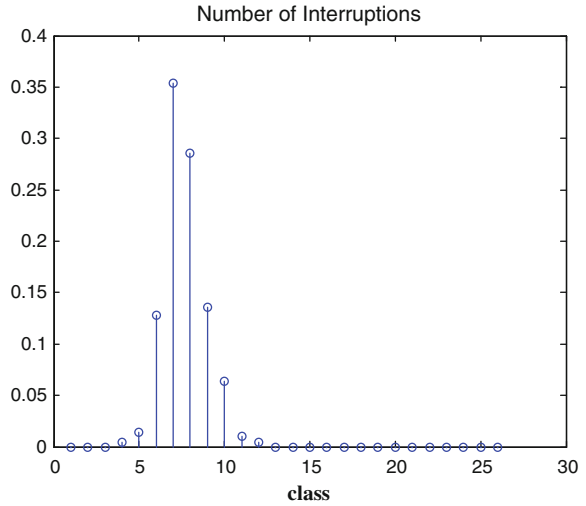
Fig. 4 Histogram of
interruption time
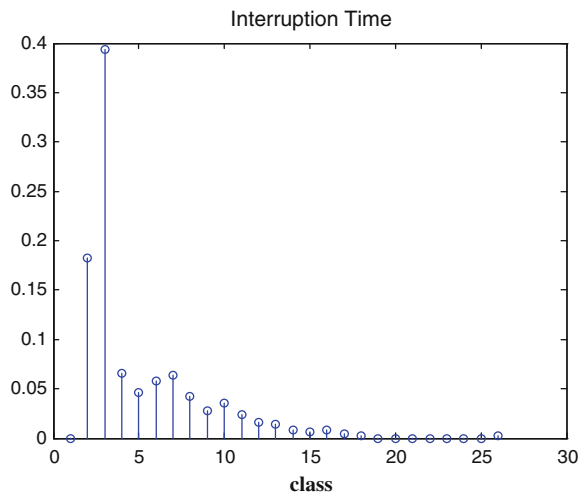
In order to further clarify the program output, a table containing principal indices of the network has been realized. It shows the variables (PNS, Interrupted Time, Number of Interruptions and ENS), differentiated upon the left (*L*) and right (*R*) part of the test-network (Tables 4, 5 and 6).

- (calculated in 500000 iterations)
- (calculated in 500000 iterations)

Fig. 5 Histogram of ENS
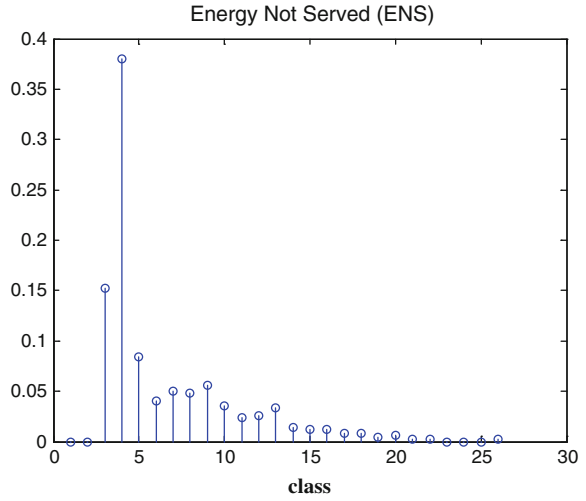
Fig. 6 Histogram of PNS
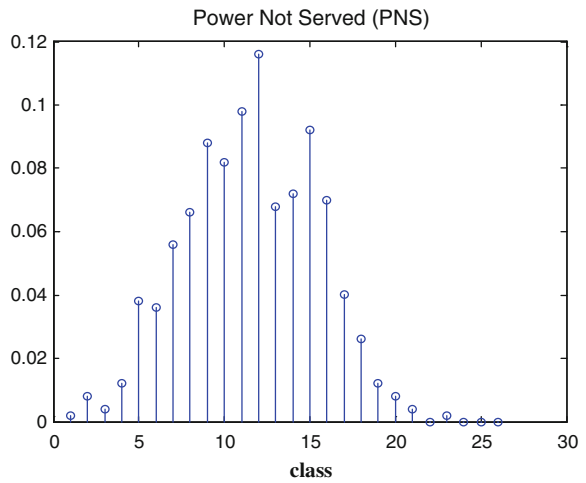
2.4 Mean Value Calculated with Analytical Methods

2.4.1 Number of Interruptions N

Represents the number of times the load point is interrupted, depending on the interruption occurred in every load point belonging to the side of the network under the same circuit breaker.

Fig. 7 Histogram of number of interruptions
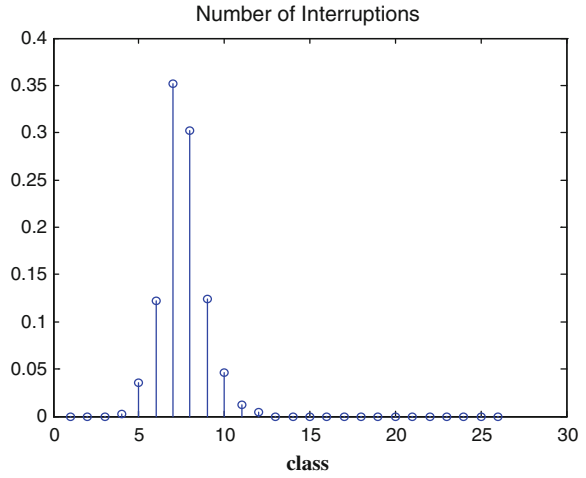
Fig. 8 Histogram of PNS
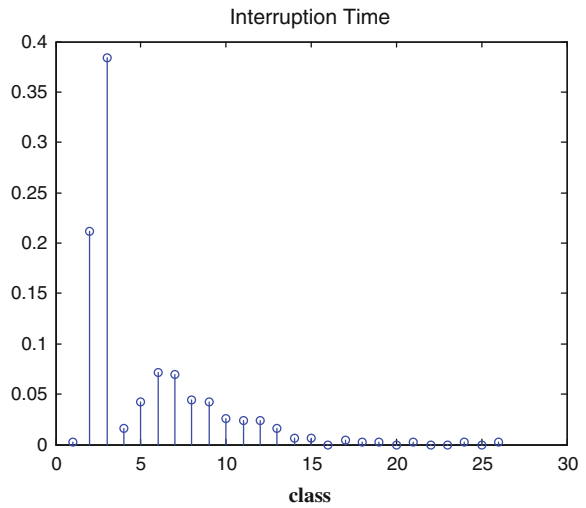
$$E\{\mathbf{n}\} = \lambda T n_{\text{branches}} \tag{8}$$

2.4.2 Power not Supplied PNS

Represents the amount of MW not supplied for every interruption at the load point in the time period under study.

Fig. 9 Histogram of number of interruptions
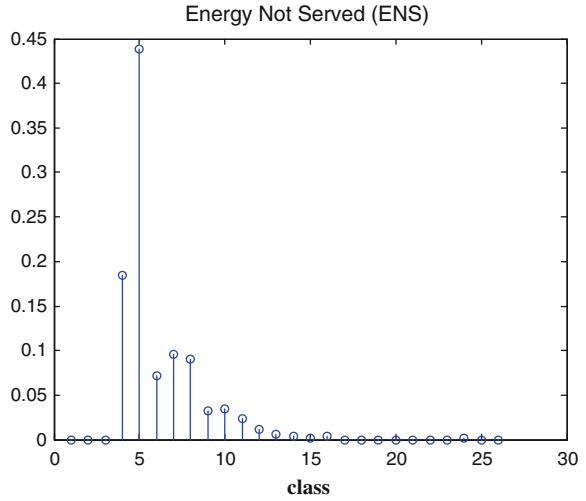
Table 4 Values for program variables, depending on the positioning on the network (L = Left; R = Right)

Variable	Network side	Min	Step	No of steps
PNS	L	10	1.6	25
	R	50	2	25
Interruption time	L	100	130.2	25
	R	100	130.2	25
Number of interruptions	L	0	4.18	25
	R	0	4.18	25
ENS	L	0	110	25
	R	0	220	25

$$E\{PNS\} = \lambda T P n_{branches} \tag{9}$$

2.4.3   Interruption Time d

Represents the total duration of interruption of the load point in the time period under study.

$$E\{\mathbf{d}\} = \lambda T n_{branches} E\{\tau_t\} \tag{10}$$

$$E\{\mathbf{d}\} = \lambda T n_{branches} E\{\tau_p\} \tag{11}$$

Table 5 Results of Monte Carlo simulation of the test-network with Matlab program

Variable	Network side	5000 iterations			500 iterations		
		Expected Value	Variance	Standard deviation	Expected Value	Variance	Standard deviation
Number of interruptions	L	27.7	630	25.1	23.3	437	20.9
	R	77.1	4941	70.3	72.8	4563	67.5
Interruption time (min)	L	664.9	664910	815.4	741.9	769965	877.4
	R	1136.1	1389866	1178.9	1131.5	1312599	1145.6
PNS (p.u.MW)	L	25.6	629	25.1	27.1	712	26.7
	R	71.1	4770	69.1	126.8	4268	65.3
ENS (p.u.MW h)	L	575.1	472067	687.1	569.5	7916910	2813.7
	R	1169.3	1525242	1235.1	1316.7	2480102	1574.8

where $E\{\tau_p\} = \alpha_p\,\beta_p$ and $E\{\tau_t\} = \alpha_t\,\beta_t$ due to the fact that we used a Gamma distribution with parameters (α_t, β_t) for the restoration time after temporary interruptions and $(\alpha p, \beta p)$ for the restoration time after permanent interruptions.

2.4.4 Interruption Time d

$$E\{ENS\} = \lambda T n_{branches} E\{\tau_t\} \tag{12}$$

$$E\{ENS\} = \lambda T n_{branches} E\{\tau_p\} \tag{13}$$

Table 7 shows that for the analysis performed upon the test-system, some discrepancies occur between the values obtained with 50000 extractions and 500000 extractions. These differences depend on the number of permanent faults occurred during the reliability simulation in the time period under study. Bolded parameters correspond to the biggest values for each parameter (column).

3 Role of Statistical Profiling for Energy Markets. Load Profiles Definition for Electricity Market

3.1 Operational and Functional Requirements for Accurate Load Profiling—Analytical Assessment

Average daily consumption which is scheduled by using weights specified in a table which contains data relating to consumer profile (differentiated for working day and non-working day) is defined from the following relations:

Table 6 Histograms of the simulated parameters PDFs'

No of extractions	P_{sel}	P_{swU}	P_{swD}	Upstream network	Downstream network
500000	0.95	0.9	0.05		
	0.05	0.05	0.05		
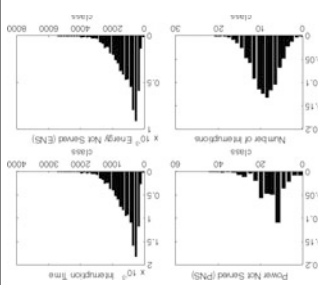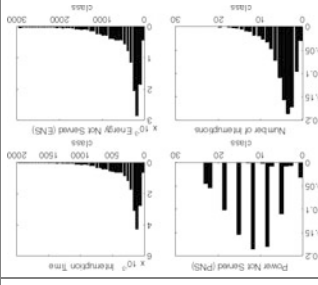
(continued)

Table 6 (continued)

No of extractions	P_{sel}	P_{swU}	P_{swD}	Upstream network	Downstream network
50000	0.95	0.9	0.9		
	0.05	0.05	0.9		

Table 6 (continued)

No of extractions	P$_{sel}$	P$_{swU}$	P$_{swD}$	Upstream network	Downstream network
	0.05	0.05	005		

Table 7 Values for program variables, depending on the positioning on the network

Extractions	P_{sel}	P_{swU}	P_{swD}	P_{NS}	N_{IN}	T_{INT}	E_{NS}
50000	0.95	0.9	0.9	9	3	10.248	40.160
				6	6	17.250	50.716
	0.05	0.9	0.9	6	6	95.884	0.038
				10.5	3	8.004	0.002
	0.95	0.05	0.9	4	6	19.390	75.985
				14	4	14.264	75.985
	0.95	0.9	0.05	12	6	**99.096**	**0.039**
				4.5	3	15.302	0.004
	0.95	0.05	0.05	10	5	48.672	190.731
				7.5	5	56.240	165.292
	0.05	0.05	0.9	0	3	22.797	89.336
				10.5	3	22.797	67.002
	0.05	0.05	0.05	12	**11**	67.679	0.027
				17.5	5	48.690	0.014
500000	0.95	0.05	0.9	16	**8**	38.011	148.954
				3	2	4.829	14.193
	0.05	0.9	0.9	0	1	3.939	15.436
				3.5	1	3.939	11.577
	0.95	0.05	0.9	10	5	16.717	21.403
				6	4	10.924	32.105
	0.95	0.9	0.05	4	2	5.076	19.891
				4.5	3	14.178	19.891
	0.95	0.05	0.05	10	5	18.512	82.185
				0	0	0.000	0.000
	0.05	0.05	0.9	0	5	15.769	61.793
				17.5	5	15.769	46.344
	0.05	0.05	0.05	14	7	19.755	77.415
				7.5	5	**62.623**	**184.051**

3.1.1 Monthly Energy Aggregation

For an average month, some using the data presented in a table that contains the results of the measurements of energy for all hourly intervals (curves, as the average consumer used to establish the data measured consumer profile):

$$\bar{Q}_{WD} = q_{WD} * N_{ZD} \tag{14}$$

$$\bar{Q}_{NWD} = q_{NWD} * N_{NWD} \tag{15}$$

$$\bar{Q}_{WD} = Q_{WD} + Q_{NWD} \tag{16}$$

where:

$\bar{Q}_{WD}$ = amount of energy distributed on working days for a month, according to the measured values;

$\bar{Q}_{NWD}$ = amount of energy distributed in non-working days for a month, according to the measured values;

q_{WD} = average daily consumption associated with any working days for a month, according to the values given in the table containing the results of the measurements of energy for all hourly intervals;

q_{NWD} = average daily consumption associated with any non-working days for a month, according to the values given in the table containing the results of the measurements of energy for all hourly intervals;

Q = energy distributed within one month according to measured values

N_{WD} = number of working days in the month;

N_{NWD} = number of non-working days in the month.

3.1.2 Evaluation of Energy Weights

$$P_{WD} = \frac{\bar{Q}_{WD}}{\bar{Q}} \tag{17}$$

$$P_{ZNL} = \frac{\bar{Q}_{NWD}}{\bar{Q}} \tag{18}$$

where:

P_{WD}, P_{NWD} is the weight of the energy distributed for one month with respect to working days/holidays, determined accordingly to the measured values which underline the consumer profile, according to the table that contains the results of the measurements of energy for all hourly intervals.

3.1.3 Monthly Energy Calculation

Energy distributed in the settlement month, differentiated according to type of day (working/nonworking) shall be established according to the following relationship:

$$\bar{Q}_{monthWD} = Q_{month} * P_{WD} \tag{19}$$

$$\bar{Q}_{monthNWD} = Q_{month} * P_{NWD} \tag{20}$$

$$\bar{Q}_{monthWD} + \bar{Q}_{monthNWDZNL} = Q_{month} \tag{21}$$

where:

Q_{month} = the amount of energy distributed in the settlement,

3.1.4 Monthly Calculation of Energy Weights

Daily quantities of energy distributed in paying month must be approved according to profile schedule (using the weights shown in a table containing data relating to consumer profile) is determined according to the relationship presented in sequel:

$$Q_{WD} = \frac{Q_{monthWD}}{N_{WD}} \tag{22}$$

$$Q_{NWD} = \frac{Q_{monthNWD}}{N_{NWD}} \tag{23}$$

3.1.5 Daily/Hourly Energy Calculation

Monthly representation of quantities of energy will be distributed on the basis of the approved profile on differentiated working days/non-working days, according to the following relationship:
working day

$$Q_{hourWD} = Q_{WD} * \gamma \tag{24}$$

where:

Q_{hourWD} = energy distributed according to a time interval for a working day;
γ = represents the percentage determined for the characteristic profile of working days, for a given time interval (according to the table containing data relating to consumer profile)

non-working day

$$Q_{hourNWD} = Q_{NWD} * \eta \tag{25}$$

where:

$Q_{hourNWD}$ = energy distributed according with a time interval for a working day;
η = is the percentage determined for the characteristic profile of working day, for a given time interval (according to the table containing the data relating to consumer profile)

Hourly quantities are expressed in, MWh with 3 decimals, so that the difference between the amount of energy distributed monthly and the sum of hourly energies to be less than 1 kWh.

3.2 System Application

The question of determining the load curve profile is very economically-efficient for small users and for users. Under these circumstances, the establishment of hourly values of energy associated with a supplier can realize, for each point of consumption for providing hourly consumption by spreading recorded on a calculation based on a consumer profile (Table 8).

3.2.1 Daily/Hourly Energy Calculation

This illustrates loading profile contributions such as lighting, cooling, ventilation and other tasks performed throughout the day. Evaluation of total energy consumption in energy will show a rapid increase during the morning because of the transitional arrangements of the receivers. Once the systems are started, the demand is relatively constant throughout the day (Fig. 10 and Tables 9 and 10).

Table 8 Types of end-users

No	User
1	Fuel stations
2	Small businesses without cooling
3	Small businesses with cooling
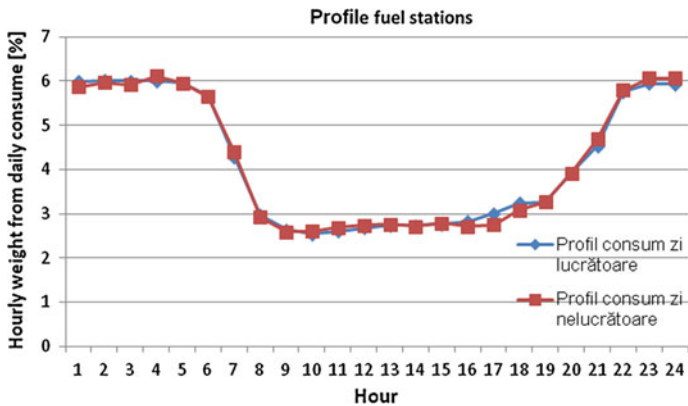
Fig. 10 Load curves for fuel stations

Table 9 Measurements results

Average consume curve (MWh)		
Interval	Interval	Interval
00:00:00	0.022172	0.0216
01:00:00	0.022233	0.021959
02:00:00	0.022206	0.021763
03:00:00	0.022228	0.022517
04:00:00	0.02201	0.021892
05:00:00	0.020953	0.020771
06:00:00	0.015875	0.016159
07:00:00	0.010996	0.010746
08:00:00	0.009761	0.00953
09:00:00	0.009384	0.009575
10:00:00	0.009638	0.009875
11:00:00	0.009911	0.010075
12:00:00	0.010116	0.010171
13:00:00	0.01013	0.009992
14:00:00	0.01024	0.010242
15:00:00	0.010442	0.01
16:00:00	0.011121	0.010105
17:00:00	0.011998	0.011334
18:00:00	0.012086	0.011996
19:00:00	0.014503	0.01443
20:00:00	0.016751	0.017271
21:00:00	0.02131	0.021321
22:00:00	0.021964	0.022321
23:00:00	0.021949	0.022325
QWD	**0.369977**	
QNWD		**0.367971**

3.2.2 Small Businesses Without Cooling

This illustrates loading profile contributions such as lighting, cooling, ventilation and other tasks performed throughout the day. Evaluation of total energy consumption in energy will show a rapid increase during the morning because of the transitional arrangements of the receivers. Once the systems are started, the demand is relatively constant throughout the day (Fig. 11).

3.2.3 Small Businesses with Cooling

Minimum and maximum limits presents a limited variation of about 2 %, which indicates the uniformity of type SBC users consumption. The load curve flattening

Table 10 Data for fuel
stations (hourly weights of
energy consume)

	Consume profile	
	Mean WD (%)	Mean NWD (%)
00:00:00	5.992922	5.87012
01:00:00	6.009401	5.967501
02:00:00	6.002037	5.914281
03:00:00	6.007807	6.119338
04:00:00	5.948917	5.949384
05:00:00	5.663411	5.644785
06:00:00	4.290759	4.391289
07:00:00	2.972176	2.920385
08:00:00	2.638239	2.589743
09:00:00	2.536494	2.602199
10:00:00	2.605032	2.683727
11:00:00	2.678725	2.738079
12:00:00	2.734215	2.764123
13:00:00	2.737945	2.715432
14:00:00	2.767672	2.783372
15:00:00	2.822449	2.717697
16:00:00	3.005845	2.746005
17:00:00	3.24298	3.080044
18:00:00	3.266598	3.260086
19:00:00	3.91999	3.92137
20:00:00	4.527673	4.693623
21:00:00	5.759701	5.794254
22:00:00	5.936602	6.066014
23:00:00	5.932409	6.067147
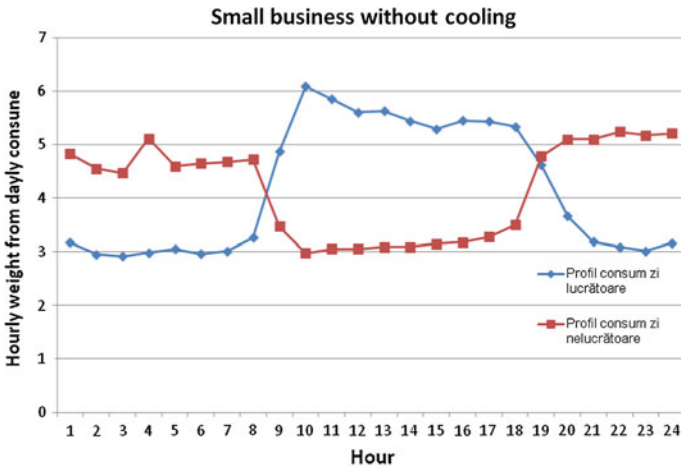
Fig. 11 Load curves for SBwC (WD and NWD)
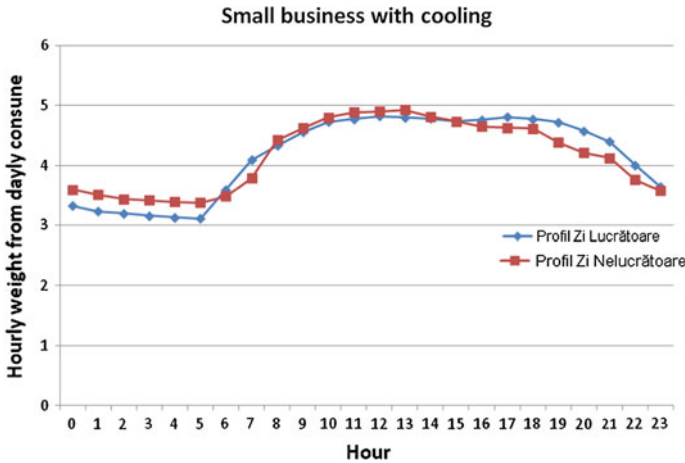
Fig. 12 Load curves for SBC (WD and NWD)

we can say that it has a high value which indicates that in the case of SBC have a flat load curve (Fig. 12).

4 Operation of Distribution Systems with Dispersed Generation

4.1 Operational Aspects of Voltage Control

An evident effect of the introduction of DG sources in the distribution system is to increase the voltage profile along the feeders. If the total power provided by the local generators does not exceed the local load, the effect is limited to reducing the currents injected in the local nodes by the distribution systems, with the beneficial effects of reduce losses and increase the voltage profile, without leading to unacceptable voltage values. In this case, the possible contribution of switchable nodal capacitors located in the distribution systems should be coordinated with the real needs of reactive power support for voltage profile improvement.

For the customers that have implemented smart metering devices [11–46] (which can record consumption at different time intervals, memorize the values and remotely transmit the information), this consumption variation is known [47–52]. For customers that have not installed such intelligent devices, it requires a method by which the total electricity consumption over a period of time to be assigned to time slots [53–56].

Typically, the issue of the load curve profile determination is posed for small users and for users. In their case, the installation of meters with registration of hourly electricity consumption is economically unjustified [57, 58].

The integration and development of local resources, owned and managed by different subjects, requires a strong effort for revising the current operation practices of the distribution systems [59–61]. In fact, well-known properties of traditional distribution systems, such as operation with radial configuration with a single generator in the root node, and the subsequent unidirectionality of real power flows and typical decreasing voltage profiles along the feeders, are no longer ensured in the presence of a non-negligible amount of distributed generation. The differences affecting the system operation are extended to the need for using new or dedicated algorithms to solve traditionally studied problems such as power flow, voltage control, fault calculation, reliability and power quality aspects, and so on.

Analyzing the DG impact on the distribution systems requires specifying the type of network used (Low Voltage—LV, or Medium Voltage—MV, in urban suburban or rural areas) and the DG technology considered, depending on the location of the system and on the voltage level. Aggregations of loads and sources used at a certain voltage level are required to analyze higher voltage levels. A key aspect is the type of interface between the DG and the network. This can be either a voltage-controllable synchronous machine/transformer group or an inverter-type connection or, considering the possibility of operating a portion of the system as a micro-grid [60], a suitable separation device allowing for re-synchronization between the separated micro-grid and the distribution system. The impact of the introduction of DG sources in the distribution system is typically analyzed by using a parameter called *penetration level*, expressed as $\chi = \gamma P_{DG}/P_L^{\max}$, where P_{DG} is the total generation installed for the local sources, $P_L^{\max}$ is the peak power demand and γ is the capacity factor, depending on the characteristics of the technologies used [61].

The last section of the paper provides a detailed discussion of the key aspects concerning the integration of local generations into the distribution systems. The focus is on voltage control and its impact on voltage profile and distribution system losses. Faults, dynamics and power quality issues are not included due to space limitations, while network islanding and reliability issues are addressed in [62]. Results showing the impact of the local generation on voltage control and losses are shown for examples on the real MV distribution system, operating in a rural area. In particular, cogeneration sources were positioned in the nodes requiring a relatively large amount of power, while groups of photovoltaic generators were located in every node.

When the amount of local generation exceeds the local load, the local sources supply part of the distribution system load. In this case, there are branches in which the current flow is inverted, leading to a voltage increase at the branch terminal far from the HV/MV substation (the root node). The subsequent increase of the voltage profile may lead to unacceptable voltages at some nodes [59, 60, 63]. The above problem is related to voltage-uncontrollable local sources. In some cases, voltage-controllable DG sources are used, typically consisting in synchronous machines interfaced with the distribution system with a local transformer. These sources can give a contribution to the overall voltage control of the distribution

system, by imposing a proper set-up voltage. However, this contribution is limited to the range in which the reactive power of the generator lies within its lower and upper bounds.

The voltage set point of the local generators interacts with the centralized voltage control at the HV/MV substation [64, 65]. Traditional methods for supporting the voltage profile in radial distribution systems include the use of under-load tap changers (ULTCs) in the HV/MV substation transformer, driven by line drop compensation (LDC), switchable capacitors at the MV node of the HV/MV substation or at some nodes of the distribution system. The recent introduction of local DG sources, generally owned and operated independently of the centralized voltage control, is leading to an increasing difficulty in performing voltage control, since the local sources are out of the control of the centralized control. Studies have been carried out for evaluating suitable techniques to modify the existing centralized voltage regulation at the HV/MV substation transformer [66–70]. The results obtained indicate that voltage monitoring at various nodes of the distribution system is required in order to take into account the variability of the voltage profile along the feeders. However, in the presence of a large penetration of DG sources, monitoring should be extended to a large number of nodes, in order to represent the effect of several scattered local sources on the voltage profile variation.

In urban distribution systems, the possibility of voltage control through DG sources is almost negligible, since distribution lines are relatively short and the contribution of the HV/MV substations prevails over the one of the local DG sources. For extra-urban or rural systems, some voltage control may be given by voltage-controllable local generators, depending on their size and reactive power limits.

In order to study the possible voltage control provided by the local generator, the *Q-V* characteristics of the generator (including the reactive power limits) and of the external system (including the local transformer) are compared. Let's consider an operating condition in which the specified real power of the local generator is P_G. The local transformer has transformation ratio t_T and the series impedance $Z_T = R_T + j\,X_T$ located at the local generator side, as shown in Fig. 3. Assuming the voltage magnitude V_L at the network side as a parameter, the reactive power output Q_G of the generator depends on voltage magnitude V_G at the generator terminals according to the nearly linear external characteristic

$$Q_G = \frac{X_T V_G^2}{Z_T^2} - \sqrt{\frac{V_G^2 V_L^2}{t_T^2 Z_T^2} - P_G^2 - \frac{V_G^4 R_T^2}{Z_T^4} + 2\frac{V_G^2 R_T}{Z_T^2} P_G} \qquad (26)$$

The external characteristics correspond to the dashed lines in Fig. 14. In order to identify the possible operating points for the generator, the reactive power/voltage curve of the generator is superposed to the external characteristic. Figure 14 shows that the generator is able to operate in the voltage support mode (PV node model) until its reactive power limits are reached. This corresponds to guarantee voltage support for a limited range of voltage magnitude values at the network side, while

Fig. 13 Model of the local generator and transformer
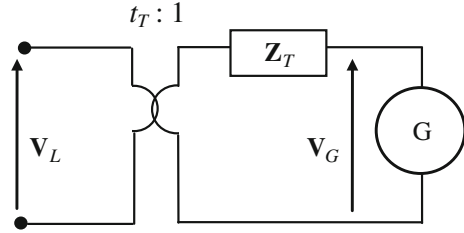
Fig. 14 Local generator and external system *Q*-*V* characteristics
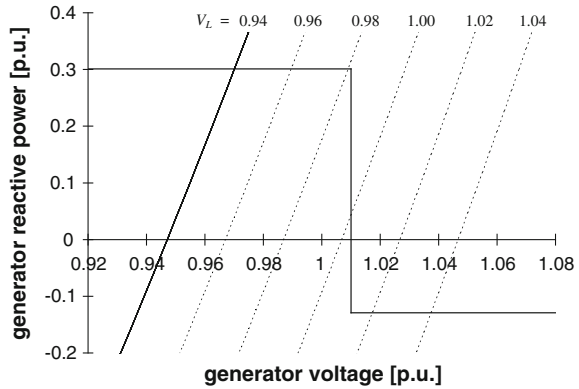
in the other operating conditions the generator operates with reactive power generation fixed at the maximum (or minimum) value and as such is no longer able to provide voltage support to the network (Fig. 13).

5 Conclusions

The increasing penetration of dispersed generation into the electricity distribution systems calls for revisiting the operation practices and the related analysis tools. In this framework, some key aspects have been analyzed, concerning voltage control, voltage profiles and losses. These topics showed a particular interest from the point of view of electricity grid evolution towards smart grid.

The approach of this section was to gather and analyze a collection of topics and phenomena, which are depicting apparent eclectic parameters of electric distribution systems, but which are among the most sensitive issues for the utilities and customers alike, due to their high impact on reliability, continuity of operation and prices.

For addressing the continuity of supply issue, a sequential MCM has been implemented to deal with the calculation of the reliability indices. The MCM method is effective to give not only the expected value and variance, but the whole

PDF of different reliability indices. The interest for the PDF is due to the possibility of computing particular information such as the tail probability, which could be useful for defining additional indicators such as the probability of exceeding a given value, important for the regulation of competitive electricity markets.

Results obtained on a test distribution system have been successfully compared to the analytical values of the reliability indices. The permanent faults have a very long restoration time, failure rate and relatively long restoration time, so that the values obtained by the MCM method vary according to the number of permanent faults occurred in the time period under study. This causes the discrepancies between analytical and simulated mean values.

Also, throughout the whole section, the authors have sought to create frameworks that can be used later by the beneficiary for mathematical models. In sequel are listed the obstacles in the face of improving energy distribution activity and the action required to be taken with a view to the removal of obstacles. The second part of the material contains a study of the power consumption curves of the electricity customers in general, with a special focus on three different customers. These customers are important, and the DSO must refine its analysis in order to supply with the exact amount of energy, in order to mitigate the eventual energy-level mismatches and subsequent financial losses.

The electricity prices and operation costs issues were addressed in the second part of this section, some key objectives were completed, such as definition of the mathematical model for calculating the hourly energy specific, identification of the three target groups for users who have developed consumer profiles, definition of the two types of significant load and assessment of the impact of using consumer profiles on users.

The analysis performed showed both the possibility of developing an exact summary of the hourly consumption, and the possible volatility of the customers' consumption profile, weighted by a set of very volatile state parameters.

The main perils for smart grids development are the lack of investment in facilities for LV, a significant proportion of the consumers having old installations with access to conductors. Also, other pitfalls are poor status of the DSO infrastructure, namely network areas with great lengths, LV overload, with inadequate insulation and ageing hardware. Another difficulty is the action to raise awareness of the extent of the economic agents who work with very low loads.

The action required in order to ease the translation from the current electric systems to smart grid is the continuance of control actions for faulty consumers of electrical energy, recovery and restoration system compulsory in secure system.

The objectives of the distributor and of the owner or manager of the local generator-transformer group are generally different. The distributor aims at maintaining an acceptable voltage profile, while the local manager is primarily interested in reducing the internal losses of the local group. Besides being antagonist, these characteristics are complementary for the electric system operation.

The three issues addressed in this section deserve to be further analysed, in order to deepen the understanding the overall impact of the DG into the existing

distribution systems, in order to develop innovative tools for assisting the distribution operators in performing efficient voltage control, suitable loss allocation and profitable use of DG resources in competitive electricity markets.

References

1. R.Billinton, "Distribution System Reliability Performance and Evaluation", Electrical Power &Energy Systems, Vol.10, No.3, pp.190-200, July 1998;
2. E.Carpaneto, G.Chicco, A.Mosso, A.Poggi and P.Ribaldone, "Tools for optimal operation and planning of urban distribution systems", Proc. CIRED 2001, Amsterdam, The Netherlands, June 18-21, 2001, paper 5_22;
3. E.Carpaneto, G.Chicco, A.Mosso and A.Ponta. "Analytical Evaluation of the Probability Distributions of Reliability Indices for Large Distribution Systems", Proc. PMAPS 2002, Naples, Italy, September, 22–26, 2002, pp.31-36;
4. E.Bompard, E.Carpaneto, G.Chicco, R.Napoli, Convergence of the backward/forward sweep method for the load-flow analysis of radial distribution systems, Electrical Power and Energy Systems 22 (2000) 521-530.
5. D Shirmohammadi, H.W.Hong, A.Semlyen, G.X.Luo, A compensation-based power flow method for weakly meshed distribution and transmission networks IEEE Transactions on Power Systems 1988; 3(2): 753-62;
6. R.Billinton, R.N.Allan, Reliability Evaluation of Engineering Systems: Concepts and techniques, Pitman Advanced Publishing Program, 1983;
7. R.Billinton, P.Wang, Teaching Distribution System Reliability Evaluation Using Monte Carlo Simulation, IEEE Transactions on Power Systems, Vol.14, No.2, May 1999;
8. Y.Ou, L.Goel, Using Monte Carlo simulation for overall distribution system reliability worth assessment, IEE Proceedings on Generation Transmission and Distribution, Vol.146, No.5, September 1999;
9. M.Postolache, Metode numerice, Editura Tehnică, 1993, pag 149-153;
10. O.Stănășilă, V.Brânzănescu, Matematici speciale, Editura ALL, 1995, pag 335-345.
11. Shijie Deng, Stochastic Models of Energy Commodity Prices and Their Applications: Mean-reversion with Jumps and Spikes, Program on Workable Energy Regulation (POWER), University of California Energy Institute, February 2000, PWP-073;
12. Trueck Stefan, Weron Rafal and Wolff Rodney, Outlier Treatment and Robust Approaches for Modeling Electricity Spot Prices, Hugo Steinhaus Center, Wroclaw University of Technology, August 2007, MPRA Paper No. 4711, posted 07. November 2007 / 04:09;
13. Adam Misiorek, Stefan Trueck and Rafal Weron, Point and Interval Forecasting of Spot Electricity Prices: Linear vs. Non-Linear Time Series Models, Nonlinear analysis of electricity prices, Volume 10, Article 2, Issue 3, 2006;
14. Michael Bierbrauer, Stefan Trück, and Rafael Weron, Modeling Electricity Prices with Regime Switching Models, M. Bubak et al. (Eds.): ICCS 2004, LNCS 3039, pp. 859–867, 2004. c Springer-Verlag Berlin Heidelberg 2004;
15. Rafał Weron, Heavy tails and electricity prices, Research Report HSC/05/2, The Deutsche Bundesbank's Annual Fall Conference (Eltville, 10-12 November 2005);
16. Ross Baldick, Sergey Kolos, Stathis Tompaidis, Interruptible Electricity Contracts from an Electricity Retailer's Point of View: Valuation and Optimal Interruption, Operations Research Vol. 54, No. 4, July–August 2006, pp. 627–642, ISSN 0030-364X, EISSN 1526-5463 -06 - 5404 -0627;
17. Min Liu and Felix F. Wu, Managing Price Risk in a Multimarket Environment, IEEE Transactions on Power Systems, Vol. 21, No. 4,pag.1512-1219, November 2006;

18. Jacob Lemming, Electricity Price Modelling for Profit at Risk Management, Systems Analysis Department Risk National Laboratory, DK-4000,Roskilde;
19. Siem Jan Koopman, Marius Ooms, M. Angeles Carnero, Periodic Seasonal Reg-ARFIMA-GARCH Models for Daily Electricity Spot Prices, TI 2005-091/4 Tinbergen Institute Discussion Paper, September 16, 2005;
20. Alvaro Cartea and Marcelo G. Figueroa, Pricing in Electricity Markets: a mean reverting jump diffusion model with seasonality, September 2, Commodities Modelling Workshop, Birkbeck College, University of London, September 2004;
21. Reinaldo C. Garcia, Javier Contreras, Marco van Akkeren and João Batista C. Garcia, A GARCH Forecasting Model to Predict Day-Ahead Electricity Prices, IEEE Transactions On Power Systems, Vol. 20, No. 2, May 2005;
22. Derek W. Bunn, Structural and Behavioural Foundations of Competitive Electricity Prices, Modelling Prices in Competitive Electricity Markets, Edited by D.W. Bunn. 2004 John Wiley & Sons, Ltd. ISBN 0-470-84860-X;
23. Terence C Mills, The economic modelling of financial time series, Second edition, Cambridge University Press, 1999;
24. Julián Barquín, Ángel Garro, Eugenio Fco. Sánchez-Úbeda, Santiago Tejero, A New Model for Electricity Price Series Modelling and Forward and Volatility Curves Computation, 8th International Conference on Probabilistic Methods Applied to Power Systems, Iowa State University, Ames, Iowa, September 12-16, 2004;
25. Eva Benz, Stefan Trück, Modeling the Price Dynamics of CO2 Emission Allowances, Preprint submitted to Elsevier Science February 20, 2008;
26. Geman, H. and Roncoroni, A., Understanding the fine structure of electricity prices, Journal of Business 79 (3) 1225-1261, 2006;
27. Svetlana Borovkova, Ferry Jaya Permana, Modelling electricity prices by the potential jump-diffusion, Stochastic Finance 2004 Autumn School & International Conference;
28. Audun Botterud, Magnus Korpas, A stochastic dynamic model for optimal timing of investments in new generation capacity in restructured power systems, Electrical Power and Energy Systems 29 (2007) 163–174;
29. Nektaria V. Karakatsani and Derek W. Bunn, Modelling the Volatility of Spot Electricity Prices, Department of Decision Sciences, London Business School, March 2004.
30. Hanjie Chen and Ross Baldick, Optimizing Short-Term Natural Gas Supply Portfolio for Electric Utility Companies, IEEE Transactions on Power Systems, Vol. 22, No. 1, February 2007;
31. Nima Amjady and Farshid Keynia, Day-Ahead Price Forecasting of Electricity Markets by Mutual Information Technique and Cascaded Neuro-Evolutionary Algorithm, IEEE Transactions On Power Systems, Vol. 24, No. 1, February 2009;
32. Work Package 5 – D5.2, Modelling electricity prices: from the State of the Art to a draft of a new proposal, Project contract no. 043363, January 2007;
33. Matt Davison, C. Lindsay Anderson, Ben Marcus, and Karen Anderson, Development of a Hybrid Model for Electrical Power Spot Prices, IEEE Transactions On Power Systems, Vol. 17, No. 2, May 2002;
34. Antonio J. Conejo, Miguel A. Plazas, Rosa Espínola, and Ana B. Molina, Day-Ahead Electricity Price Forecasting Using the Wavelet Transform and ARIMA Models, IEEE Transactions On Power Systems, Vol. 20, No. 2, May 2005;
35. Shi-Jie Deng, Wenjiang Jiang, Levy process-driven mean-reverting electricity price model: the marginal distribution analysis, Elsevier, available online 10 July 2004;
36. Terry A. Robinson, Electricity pool prices: a case study in nonlinear time-series modelling, Applied Economics, 2000, 32, 527- 532;
37. Graeme A. Guthrie and Steen Videbeck, Electricity Spot Price Dynamics: Beyond Financial Models, New Zealand Institute for the Study of Competition and Regulation, and Victoria University of Wellington December 14, 2004;
38. Ronald Huisman, Christian Huurman, Ronald Mahieu, Hourly electricity prices in day-ahead markets, Energy Economics 29 (2007) 240–248;

39. Mika Goto, G. Andrew Karolyi, Understanding Electricity Price Volatility Within and Across Markets, JEL Classification Codes: G13, August 25, 2003;

40. Helen Higgs, Andrew C. Worthington, Stochastic price modelling of high volatility, mean-reverting, spike-prone commodities: The Australian wholesale electricity market, JEL classification: C32, D40, Q40;

41. Rafal Weron, Heavy-tails and regime-switching in electricity prices, Mathematical Methods of Operations Research manuscript, 9 May 2008;

42. Thilo Meyer-Brandis, Peter Tankov, Multi-factor jump-diffusion models of electricity prices, project supported by the Europlace Institute of Finance;

43. Jan Seifert, Marliese Uhrig-Homburg, Modelling Jumps in Electricity Prices: Theory and Empirical Evidence, JEL Classification: C11, G12, G13, Q4;

44. D. C. Sansom, T. Downs and T. K .Saha, Support Vector Machine Based Electricity Price Forecasting For Electricity Markets utilising Projected Assessment of System Adequacy Data, The Sixth International Power Engineering Conference (IPEC2003), 27-29 November 2003, Singapore;

45. Stephan Schlueter, A long-term/short-term model for daily electricity prices with dynamic volatility, Energy Economics 32 (2010) 1074–1081;

46. Michel Culot, Valerie Goffin, Steve Lawford, Sebastien de Menten and Yves Smeers, An Affine Jump Diffusion Model for Electricity, Department of Mathematical Engineering and CORE, UCL, January 7, 2006;

47. Ronald Huisman, Ronald Mahieu, Regime jumps in electricity prices, Energy Economics 25 (2003) 425–434;

48. Qin Zhang and Xifan Wang, Hedge Contract Characterization and Risk-Constrained Electricity Procurement, IEEE Transactions On Power Systems, Vol. 24, No. 3, August 2009;

49. Chang R.F., Lu C.N., Load Profiling and Its Applications in Power Market, PES2003, Toronto, rap. 000686.

50. Gerbec D.ș.a.,Consumers' Load Profile Determination Based on Different Classification Methods, PES2003, Toronto, rap. 000797.

51. Gerbec G., Gubina F., Toroš Z., Actual Load Profiles of Consumers without Real Time Metering, PESGM 2005, San Francisco, rap. 000841.

52. Grigoras G.ș.a., Missing Data Treatment of the Load Profiles in Distribution Networks, IEEE PowerTech Bucharest 2009, rap.782.

53. ILIE I-S., CHICCO G., Exploiting Support Vector Clustering Techniques for Electrical Load Profiling, MPS 2008, Cluj-Napoca, III.9 Hesaminia A. - 59.pdf.

54. Ramos S., Vale Z., Data Mining Techniques to Support the Classification of MV Electricity Customers, PESGM 2008, Pittsburgh, rap.001209.

55. Salgado R.M., Ohishi T., Ballini R., Clustering Bus Load Curves, PSCE 2004, New York, rap. 000581.

56. Sousa J.C., Neves L.P., Jorge H.M., Determining typical load profiles of Low Voltage Consumers, IYCE Conference, Budapesta 2007, rap. 176.

57. EDUPERCO, Contract nr. 2 din 25.06.2008, Criterii de stabilire a profilelor de consum statistice în vederea participării la piața de energie electrică cu decontare orară, faza I, iulie 2008;

58. EDUPERCO, Contract nr. 101 din 06.06.2007, Definire si analiza profile de sarcină in vederea participarii la piata de energie electrica cu decontare orară;

59. N.Hadjsaid, J.-F.Canard and F.Dumas, "Dispersed generation impact on distribution networks", IEEE Computer Applications in Power, Vol.12, 1999, pp.22-28.

60. P.P. Barker and R.W. De Mello, "Determining the impact of distributed generation on power systems. I. Radial distribution systems", IEEE/PES Summer Meeting, 2000, Vol.3, pp.1645-1656.

61. T.Ackermann, G.Andersson and L.Söder, "Distributed Generation: a definition", Electric Power Systems Research, 57 (2001) pp.195-204.

62. B.Lasseter, "Microgrids", IEEE/PES Winter Meeting, 2001, Vol.1, pp.146-149.

63. V.H.Méndez, J,Rivier, J.I.de la Fuente, T.Gómez, J.Arceluz and J.Marin, "Impact of Distributed Generation on Distribution Losses", MedPower 2002, Athens, Greece, November 4-6, 2002.

64. E.Carpaneto, G.Chicco and R.Porumb, "Reliability aspects of distribution systems with local generation resources", CIEM 2003 Conference, Bucharest, Romania, October 23-25, 2003.

65. A.Padilha, I.F.E.D.Denis and R.M.Ciric, "Voltage regulation in distribution networks with dispersed generation", Proc. 17th CIRED, Barcelona, Spain, May 12-15, 2003, paper 4.82.

66. L.Kojovic, "Impact of DG and voltage regulator interaction on distribution system voltage regulation", Proc. 17th CIRED, Barcelona, Spain, May 12-15, 2003, paper 4.31.

67. A.Bonhomme, D.Cortinas, F.Boulanger and J.-L.Fraisse, "A new voltage control system to facilitate the connection of dispersed generation to distribution networks", Proc. 16th CIRED, Vol.4, 2001.

68. S.K.Salman, D.J. King and G.Weller, "New loss of mains detection algorithm for embedded generation using rate of change of voltage and changes in power factors", 7th International IEE Conference on Developments in Power System Protection, 2001, pp.82–85.

69. T.E. Kim and J.E.Kim, "A method for determining the introduction limit of distributed generation system in distribution system", IEEE/PES Summer Meeting, 2001, Vol.1, pp.456-461.

70. E.Bompard, E.Carpaneto, G.Chicco, R.Napoli, F.Piglione, "Computation and uses of the energy flows for the distribution system analysis over time intervals", IEEE Porto Power Tech, Porto, Portugal, September 10-13, 2001, paper PST3-238.

71. ANRE Procedură pentru definirea şi utilizarea profilului rezidual de consum- Proiect Var. II, www.anre.ro;

72. Dialynas E.N., Megaloconomos S.M., Dali V.C., Interruption cost analysis for the electrical power customers in Greece, CIRED, Amsterdam 2001, Rap. 2_20;

73. Chapman D., Introduction to Power Quality, REP 00032;

74. Chapman D., The Cost of Poor Power Quality, REP 00034;

75. Albert Hermina, Florea I., Alimentarea cu energie electrică a întreprinderilor, Editura tehnică, Bucureşti, 1987.

Islanding Detection Methods for Distributed PV Systems Overview and Experimental Study

Anastasios Kyritsis, Nick Papanikolaou, Stathis Tselepis and Christos Christodoulou

Abstract The current work presents an overview of islanding detection techniques, highlighting their advantages and disadvantages. Generally, all anti-islanding techniques detect the absence of utility-controlled generation and stop energy production. However, when the generation (from PVs) and loads within the island segment are well balanced—prior to the isolation event—it is difficult to detect the utility absence. The performed analysis indicates the fact that the islanding detection is a complicated procedure, which is affected by various parameters (load matching, quality factor, PV actual generation etc.). The islanding prevention techniques which are elaborated in this paper are limited to the case where the island segment belongs to the LV distribution grids, while remote islanding detection techniques are out of scope. Furthermore, this work presents an overview of the evaluation of the islanding detection techniques according to IEC 62116 and IEEE Std. 929-2000 standards. Finally, results from the experimental evaluation of various islanding detection techniques from different single phase inverters are presented too.

A. Kyritsis · S. Tselepis
Centre for Renewable Energy Sources and Saving (CRES), Pikermi, Greece
e-mail: kyritsis@cres.gr

S. Tselepis
e-mail: stselep@cres.gr

N. Papanikolaou
Laboratory of Electric Machines, Department of Electrical & Computer Engineering,
Democritus University of Thrace, Xanthi, Greece
e-mail: npapanik@ee.duth.gr

C. Christodoulou (✉)
Department of Electrical Engineering, Technological Educational Institution (T.E.I.)
of Central Greece, Lamia, Greece
e-mail: christod@teilam.gr

1   Introduction

Nowadays renewable energy generation systems are developing rapidly on the way
to meet future global energy demand, while reducing environmental pollution. The
successful application of these systems requires efficient power converter topolo-
gies and also advanced control functions which assure the reliability, the safety and
the power quality of the electrical grids. Although issues such as frequency devi-
ation, voltage fluctuation and harmonic distortion are faced successfully under
steady state operation, some others such as the Islanding detection and prevention
are still pending, especially at LV distribution grids where grid-connected PV
systems are the majority of renewable energy generation systems.

Islanding is the condition in which a portion of an electric power grid, containing
both load and generation, is isolated (either intentionally or not) and continues to
operate [1, 2]. The PV industry, in order to satisfy the apprehensiveness of electric
power providers in case of islanding situations, has developed several islanding
detection and prevention techniques (also called anti-islanding techniques) which
can be divided into local and remote (or communication) techniques. Moreover,
local techniques divided into passive, active and hybrid techniques are also intro-
duced. Remote islanding detection techniques are based on the communication
between the electric power providers and the renewable energy generation systems,
through supervisory control, data acquisition and power-line carrier communication
systems. These techniques may offer high reliability, but actually it is difficult to be
applicable in LV distribution grids with large amount of distributed grid-connected
PV systems, due to the system complexity, while in the meantime they are still very
expensive to be implemented [2–6].

Generally, all anti-islanding techniques detect the absence of utility-controlled
generation and stop energy production. However, when the generation (from PVs)
and loads within the island segment are well balanced -prior to the isolation event-
it is difficult to detect the utility absence; thus, customer and utility equipment can
be damaged, since the generation units (PVs) are no longer under utility voltage and
frequency control, or if the main grid re-closes into the island segment out of
synchronisation. Last but not least there is danger of shock hazard to unsuspecting
utility line-workers since the distribution lines within the island segment are
energised.

Next paragraphs present the afore-mentioned islanding detection and prevention
techniques, their advantages and disadvantages, as well as a test procedure to
evaluate their effectiveness according to IEC 62116. The islanding prevention
techniques which are elaborated in this paper are limited to the case where the
island segment belongs to the LV distribution grids, while remote islanding
detection techniques are out of scope.

2   Passive Islanding Detection Techniques

Passive islanding detection techniques typically monitor parameters such as voltage and frequency at the point of common coupling (PCC). The inverter ceases energising the grid if a remarkable change from normal voltage and frequency values occurs. The most popular passive techniques are the:

(a) Under/Over Voltage and Frequency (U/O-V&F) monitoring techniques,
(b) Voltage Phase Jump (VPJ), and
(c) Voltage Harmonics Detection (VHD).

Generally, all passive islanding detection techniques do not affect the inverter output power quality as well as their effectiveness is not affected by the parallel operation of other inverters [2–7].

2.1   The U/O-V&F Monitoring Technique

Nowadays all grid-connected PV inverters have to be equipped with U/O-V&F monitoring techniques that cease the PV energy production (even under utility-controlled generation) if voltage or frequency values at the PCC exceed the predefined thresholds. For example in Greece the voltage value at PCC (VPCC) should not exceed more than −20 or +15 % the grid voltage nominal value, while the frequency should not exceed more than ±0.5 Hz the frequency nominal value. Taking for granted that the inverter 'feeds' the grid with active power under unitary power factor (only the utility grid feeds the load reactive energy needs), the operation of U/O-V&F monitoring technique depends on real and reactive power flow balance at the PCC. In more details, if there is imbalance between the PV production and the load needs (the utility may feed the load with real or/and reactive energy), then the VPCC amplitude after the island segment "genesis" will change due to active energy unbalance and the frequency of the inverter output current will also change due to reactive energy unbalance (the load resonant frequency does not usually lie near the utility frequency). So the U/O-V&F monitoring technique detects the changes and prevents the islanding operation. On the other hand, in cases that active and reactive power balance exists within a network part, then there will not be any remarkable PCC voltage amplitude or frequency deviation after it is islanded and so the U/O-V&F monitoring technique will fail to detect the island operation.

Actually, taking into account that the U/O-V&F monitoring technique is activated only if PCC voltage amplitude and/or frequency take values outside the predefined thresholds, this implies that the afore-mentioned techniques will not detect any island operation for resistive load changes between 114 and 90 % of the pre-island segment "genesis" resistive load value (for the case of Greek utility voltage trip values). This load range is shown in Fig. 1 and is also called

Fig. 1 Non-Detection Zone (NDZ) presentation
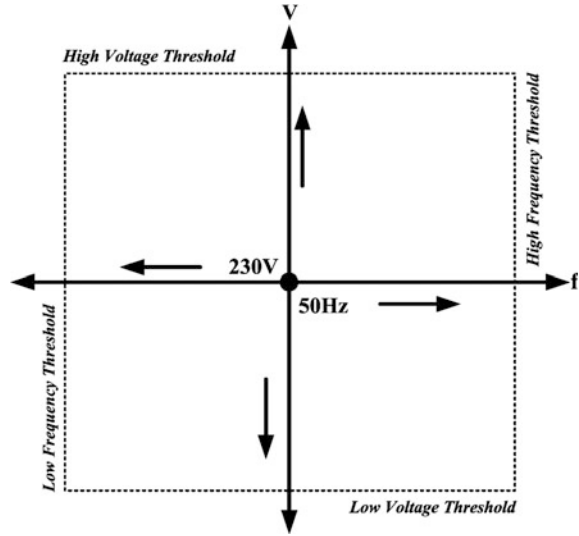
Non-Detection Zone (NDZ) for active energy unbalance and it varies according to each Distribution Operator thresholds. An additional NDZ for reactive energy unbalance can be also defined by using the appropriate reactive load equations. Nevertheless, the existence of a wide NDZ area makes U/O-V&F monitoring techniques to be considered as insufficient ones [2–7], although they can be easily implemented by software routines and so they are less expensive. It is worth mentioning that this situation worsens in cases where the Distribution Operation includes a Fault Ride Through scheme and/or Auxiliary Services (Voltage Support) for the interconnected PV systems—making so islanding detection much more complicated.

Last but not least, some others similar anti-islanding techniques [6] are based on the monitoring of the:

(a) Output power change (dP_{inv}/dt),
(b) Frequency change (df/dt), also known as the ROCOF method, and
(c) Ratio of frequency change over power (df/dP_{inv}),

where "P_{inv}" is the inverter output power and "t" is a certain duration of time (depending on the electric grid inertia).

2.2 The Voltage Phase Jump (VPJ) Monitoring Technique

The Voltage Phase Jump (VPJ) technique monitors the phase angle between the inverter output current and voltage waveforms at the point of common coupling, seeking for an unexpected phase jump; the grid-connected PV systems operate with

current-source or voltage source current control inverters which synchronise their output current with the utility voltage by using zero crossing techniques and phase-locked loops (in order to detect either the VPCC rising or falling to zero value). Thus, the inverter output current follows a fixed waveform between two consecutive PCC voltage zero crossings. Consequently, an instant after the island segment "genesis", the PCC voltage will not be under utility-control and so a sudden phase jump between the PCC current and voltage waveforms will be established. At the following PCC voltage zero crossing, if the phase divergence is higher than a predefined threshold value, the VPJ technique will command the inverter to cease energising the grid. The threshold values are difficult to be defined either if the inverter is allowed to operate under non-unitary power factor, or if among the local loads there are significant motor loads which may cause transient phase jumps (e.g. during start up). Due to the afore-mentioned thresholds there is also a Non-Detection Zone for this type of monitoring techniques. Similar islanding detection techniques can be found in literature either as Power Factor Detection, or Transient Phase Detection techniques [2–7].

2.3 The Voltage Harmonics Detection (VHD) Monitoring Technique

The Voltage Harmonics Detection (VHD) technique measures the voltage Total Harmonic Distortion (V_{THD}) at the point of common coupling and compares its THD_V value with a predefined threshold value. Before the utility disconnection the THD_V value is almost negligible, due to the presence of the strong distribution network; after the island segment "genesis" the inverter output current harmonics are feeding the load (which impedance is usually higher than the grid one) and so voltage harmonics are produced [8]. For example, the grid-connected PV inverters limit their output current THD_I value below 5 % at full rated power (although higher THD_I values emerge under partial generation conditions). So, the absence of the utility grid causes at least an equivalent for the case of pure resistive loads. The generated voltage harmonics or the THD_V value changes are detected by the VHD technique and so the inverter ceases energising the islanded segment. Unfortunately, the structure of the island segment (it is usually modelled as a parallel RLC circuit) may lead at lower THD_V values, depending on the quality factor (QF) of the equivalent circuit. Thus, the appropriate selection of the trip threshold for successful islanding detection is difficult to be defined. Additionally, for non-linear loads, the THD_V value may become too high causing faulty island detection under the electric power grid presence, while for linear loads (under island operation) the THD_V value may become too low to be detected, especially for modern PV inverters with very low THD_I. Similar islanding detection techniques can be found in the literature as Current Harmonics Detection techniques, while some of them measure only the third and the fifth current or voltage harmonics [2–7, 9].

3 Active Islanding Detection Techniques

Active islanding detection techniques are sensing the absence of utility-controlled generation by causing small scale intentional disturbances at the PCC and monitoring the network response. If a small perturbation is able distract grid operation from its normal conditions, the inverter ceases energising the grid. Active islanding detection techniques usually contain an active circuit that forces voltage, frequency or network impedance change, through positive feedback control perturbation techniques. Generally, the active techniques reduce remarkably (or even eliminate) the Non-Detection Zone. However, they may produce serious deterioration of the power quality or even cause instability problems. The most popular active techniques are the:

- (a) Impedance Measurement,
- (b) Impedance Detection at Specific Frequency (IDSF),
- (c) Slip-mode Frequency Shift (SMFS),
- (d) Active Frequency Drift (AFD),
- (e) Sandia Frequency Shift (SFS), and
- (f) Sandia Voltage Shift (SVS).

3.1 Impedance Measurement Monitoring Technique

The Impedance Measurement technique imposes variations at the inverter output current waveform (either at the amplitude, the phase angle or the frequency) and detects any impedance deviations at the inverter output stage. Thus, this technique is known as Output Variation, and Current Notching, as well as Power Shift technique. The current perturbation is usually performed through amplitude variation and the corresponding voltage perturbation depends on the utility impedance (which is supposed to be very small under grid-tied operation) and the power nominal values. If the electric power grid is disconnected, a remarkable change in PCC voltage rms value will happen due to the island segment higher impedance. The grid impedance deviations are monitored by calculating the ratio dV_{PCC}/dI_{inv}, where "I_{inv}" is the inverter rms output current. Moreover, by considering the Distribution Operator allowable voltage threshold values, it is obvious that the minimum current amplitude deviation has to be equal to the U/O-V monitoring technique full window size for successful island detection. For example in Greece the minimum current amplitude deviation has to be higher than 35 %.

The effectiveness of the Impedance Measurement technique decreases in case of parallel operation of many inverters—unless all inverters' output current perturbation are synchronised—as well on high-impedance (weak) grids. Moreover, in order to sense the utility disconnection, it is necessary to pre-estimate the utility impedance and use it as a threshold value. Last but not least, this islanding detection technique may cause grid voltage flicker and stability issues [2–7, 9].

3.2 The Impedance Detection at a Specific Frequency (IDSF) Monitoring Technique

The Impedance Detection at a Specific Frequency (IDSF) technique relies on the same operation principals with the VHD technique and so it is characterised by the same general advantages and disadvantages. Its main difference is that a specific current harmonic component is intentionally injected by the inverter to the PCC and the generated voltage harmonic value is measured. Considering that the grid impedance at the specific harmonic order is significantly lower than the islanded segment one, the amplitude of the generated voltage harmonic component depends on the presence of the utility grid as well as of the island segment impedance at the specific harmonic order. The effectiveness of the IDSF technique increases if the inverter injects to the grid a sub-harmonic current component instead of a high order one. However, if the sub-harmonic component amplitude has to remain very limited in order to avoid saturation issues to the distribution transformers [2–7].

3.3 The Slip-Mode Frequency Shift (SMFS) Monitoring Technique

Although the grid connected PV systems feed the electrical grid under (almost) unitary power factor, the Slip-mode Frequency Shift (SMFS) technique forces the phase angle between the inverter output current and the PCC voltage to change as a function of the PCC frequency, while a positive feedback technique is used in order to destabilise the PV system operation even under well balanced island conditions. The equation which describes the connection between the phase angle and the PCC frequency is given is [6]. The inverter phase angle response curve is chosen in such a way so that the inverter phase angle increases faster than the load phase angle. An instant before the island segment "genesis" the electric power grid provides a stable frequency reference, leading so to a stable phase angle value (between the inverter output current and the PCC voltage phasors) which cannot affect the electrical grid frequency. On the other hand, after the island segment formation, the positive feedback will force the new operation point to become outside the U/O-F protection threshold values and so the inverter ceases energising the grid island segment. Moreover, according to the specific anti-islanding technique reasoning, a small PV output power quality degradation is inevitable, as well as transient phenomena are possible to emerge at electrical grids with high PV penetration level and inverters with high gain positive feedback loops. Moreover, the positive feedback loop causes problems in case of noise at the reference waveform. Contrariwise, the effectiveness of the SMFS technique is not affected in case of parallel operation of many inverters [2–7, 9].

3.4   The Active Frequency Drift Monitoring Technique

According to the Active Frequency Drift technique, a time interval with zero inverter output current is imposed at the end of each utility half-cycle, aiming to cause deviations at the electrical grid frequency. If the above current waveform is applied to an island segment with pure resistive characteristics, then at the end of the first line half cycle the generated voltage frequency will be slightly higher (or smaller) compared to the grid nominal frequency. In this case, the PV inverter (assuming grid-tied operation) will increase (or decrease) the inverter output current frequency in order to eliminate the phase error. At the end of the next half line cycle, the inverter will detect a new phase error and consequently it will increase (or decrease) the output current frequency again. The continuous frequency changing process will cause the Under/Over Voltage and Frequency monitoring technique activation and so the inverter will cease energising the grid. Moreover, according to the AFD technique, the duration of every two consecutively zero inverter output current intervals have to be dissimilar. Of course, in case of non island conditions the aforementioned changes are not possible to affect the utility frequency. Like in previous anti-islanding technique, a small PV output power quality degradation is inevitable. Moreover, the effectiveness of the AFD technique decreases in case of parallel operation of many inverters -unless all inverters are synchronised to increase or decrease the output current frequency simultaneously. Last but not least, the inverter output current waveform may generate even harmonic order components to the low voltage grids.

Finally, the AFD technique Non-Detection Zone depends on the ratio of the two dead time intervals to the voltage half line duration (also called chopping fraction). It is worth mentioning that the NDZ may be affected from the combination of strong capacitive and resistive loads, or light inductive and strong resistive loads (in other words by high quality factor loads).

Similar islanding detection techniques can be found in the literature either as Frequency Bias or Frequency Shift Up/Down techniques. A noteworthy modification of the AFD technique is the Frequency Jump (FJ) technique. According to the FJ the time intervals with zero inverter output current are inserted not at every line cycle, but less periodically (e.g. every third cycle) or at sophisticated selected cycles, in order to minimise the inverter output current distortion. The effectiveness of the FJ technique decreases in case of parallel operation of many inverters -unless all the inverters' output current perturbation is synchronised [2, 6, 9].

3.5   The Sandia Frequency Shift (SFS) Monitoring Technique

The Sandia Frequency Shift technique (SFS) relies on the same operation principals with the AFD technique, with an additional positive feedback loop being applied to

the utility grid frequency measurement in order to destabilise the PV system operation under island conditions. The equation that describes the relation between the chopping fraction, he nominal voltage frequency and the generated voltage frequency deviation is given in [9]. The SFS technique detects any utility frequency deviation and tries to amplify the frequency error by applying a positive feedback. Before the island segment "genesis" the electric power grid prevents any voltage frequency alteration, while after the island segment "genesis" the SFS technique reinforces the frequency error, until the U/O-V&F monitoring technique activation. The Sandia Frequency Shift technique is characterised by the same general advantages and disadvantages of the AFD one, while the positive feedback reduces noticeably the NDZ spread. On the other hand the positive feedback causes problems in case of noise at the reference waveform. Similar islanding detection techniques can be found in the literature either as Accelerated Frequency Drift, Active Frequency Drift with Positive Feedback, or Follow the Herd techniques [2, 6, 9].

3.6   The Sandia Voltage Shift (SVS) Monitoring Technique

The Sandia Voltage Shift technique measures the PCC rms voltage value and applies a positive feedback loop to the measured value. According to this anti-islanding technique any rms voltage diviation causes an inverter output current decrease or increase according to the SVS operation principals. Thus, in case of island conditions (assuming island segment with strong resistive characteristics) a reduced (or increased) inverter output current will cause further VPCC reduction (or increase), leading finally to a remarkable PCC rms voltage value deviation that will cause the U/O-V&F monitoring technique activation. Of course, an inverter output current reduction due to a transient PCC rms voltage value decrease (under grid-tied operation) cannot affect the PCC rms voltage value. On the other hand in case of island segment, the positive feedback loop will accelerate the PCC rms voltage value reduction, leading to a very fast U/O-V&F monitoring technique activation. Although either increasing or decreasing output current operations are possible, the current reduction method is in favor in order to protect the electric installations from critical voltage levels. Moreover, many PV inverter manufactures use a combination of the two above anti-islanding techniques (SFS and SVS) in order to achieve an extremely narrow NDZ. Unluckily, the SFS technique causes a small PV output power quality degradation (that may be harmful at weak electrical grids), while it may also decrease the MPPT controller efficiency—and so the inverter electrical efficiency—due to the intentionally inverter output current reduction and the corresponding output power reduction in case of utility presence. Similar islanding detection techniques can be found in the literature either as Voltage Shift, Positive feedback on voltage, Follow the Herd or Variation of P and Q techniques [2, 6, 9].

4 Hybrid Islanding Detection Techniques

Nowadays, many PV inverter manufactures incorporate both active and passive techniques leading so to Hybrid techniques. According to these anti-islanding schemes, the active method is implemented only when the islanding mode is suspected by the passive method.

5 Islanding Detection Techniques Test Procedure According to IEC 62116

The scope of IEC 62116 standard is to provide a test procedure for the performance evaluation of the islanding prevention measures that are used in single or multi-phase utility-interconnected PV systems. Inverters that meet the requirements of this standard are considered to be non-islanding as defined in IEC 61727. According to IEC 62116 [1], a PV inverter is considered to be compatible with the anti-islanding protection demands if under any test condition—described in Table 1—the islanding detection is achieved in less than 2.0 s for over/under voltage and 1.0 s for over/under frequency (unless the Distribution Operator demands are different). The necessary test bench is shown in Fig. 2.

For test condition A, the real load and only one of the reactive load components should be adjusted to each of the load imbalance conditions shown in the shaded part of Table 2. Each cell corresponds to the active and reactive power (%) flow through S1 in Fig. 1, with positive value denoting a power flow from the Inverter to the AC power source. Actual load values should be within ±1 % of those specified. After each adjustment, an island test is being run and the run-on time is recorded. If any of the recorded run-on times is longer than the one recorded for the rated balance condition, then the non-shaded parameter combinations require also testing.

For test conditions B and C, the real load and only one of the reactive load components should be adjusted to each of the load imbalance conditions shown in Table 3. Actual load values should be within ±1 % of those specified.

Table 1 IEC 62116 test conditions

Inverter			
Condition	Inverter output power	Inverter input voltage	Inverter trip settings (Voltage—frequency)
A	Maximum	>90 % of rated	Manufacturer specified
B	50–66 % of the maximum rated	50 % ± 10 % of rated	Nominal
C	25–33 % of the maximum rated	<10 % of rated	Nominal
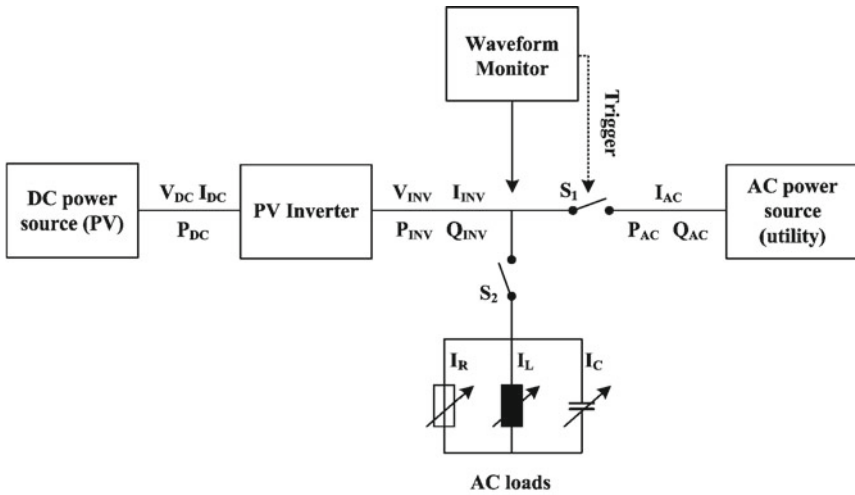
Parameters to be measured			
Symbol	Parameter	Symbol	Parameter
V_{DC}	DC voltage	I_R	Resistive load current
I_{DC}	DC current	I_L	Inductive load current
P_{DC}	DC power	I_C	Capacitive load current
V_{INV}	AC voltage	P_{AC}	Utility active power
I_{INV}	AC current	Q_{AC}	Utility reactive power
P_{INV}	Active power	I_{AC}	Utility current
Q_{INV}	Reactive power		

Fig. 2 Islanding detection techniques test bench according to IEC 62116

Table 2 IEC 62116 test condition A

Condition A				
% deviation in active and reactive load from nominal				
−10, +10	−5, +10	0, +10	+5, +10	+10, +10
−10, +5	−5, +5	0, +5	+5, +5	+10, +5
−10, 0	−5, 0		+5, 0	+10, 0
−10, −5	−5, −5	0, −5	+5, −5	+10, −5
−10, −10	−5, −10	0, −10	+5, −10	+10, −10

An additional anti-islanding frame that has to be discussed is the one that IEEE Std. 929-2000 describes [10]; according to this Standard, a PV inverter is able to pass through any islanding condition,

Table 3 IEC 62116 test condition B & C

Condition B & C
% deviation in active and reactive load from nominal
0, −5
0, −4
0, −3
0, −2
0, −1
0, 1
0, 2
0, 3
0, 4
0, 5

- if it disconnects in less than 10 line cycles in case of an islanded mode, where:
  - there is at least 50 % load—PV generation imbalance, or
  - the islanded load power factor is less than 95 % (either leading or lagging).

- if it disconnects in less than 2.0 s in case of an islanded mode, where:
  - there is up to 50 % load—PV generation imbalance, and
  - the islanded load power factor is greater than 95 % (either leading or lagging), and
 - the islanded network quality factor is less than 2.5.

6 Experimental Evaluation of Islanding Detection Techniques

In the following paragraphs the performance of several anti-islanding techniques—as they are applied in commercial PV inverters—will be experimentally studied, according to the test bench in Fig. 2. A typical example that highlights the U/O-V&F monitoring technique operation is shown in Figs. 3 and 4 for the case of a 3.0 kW commercial single phase transformerless inverter. Initially, the voltage is slowly increased and the value that causes the trip is registered. After the initial conditions restoration step voltage variation takes place from the same central point to a value above the measured high-voltage threshold. The time between the voltage step and the intervention of the protection is measured. The above procedure is inversely repeated by decreasing the voltage in order to obtain the low-voltage threshold. The same procedure is repeated to determine the high-frequency and low frequency thresholds and the time between the frequency step and the intervention of the protection is measured.
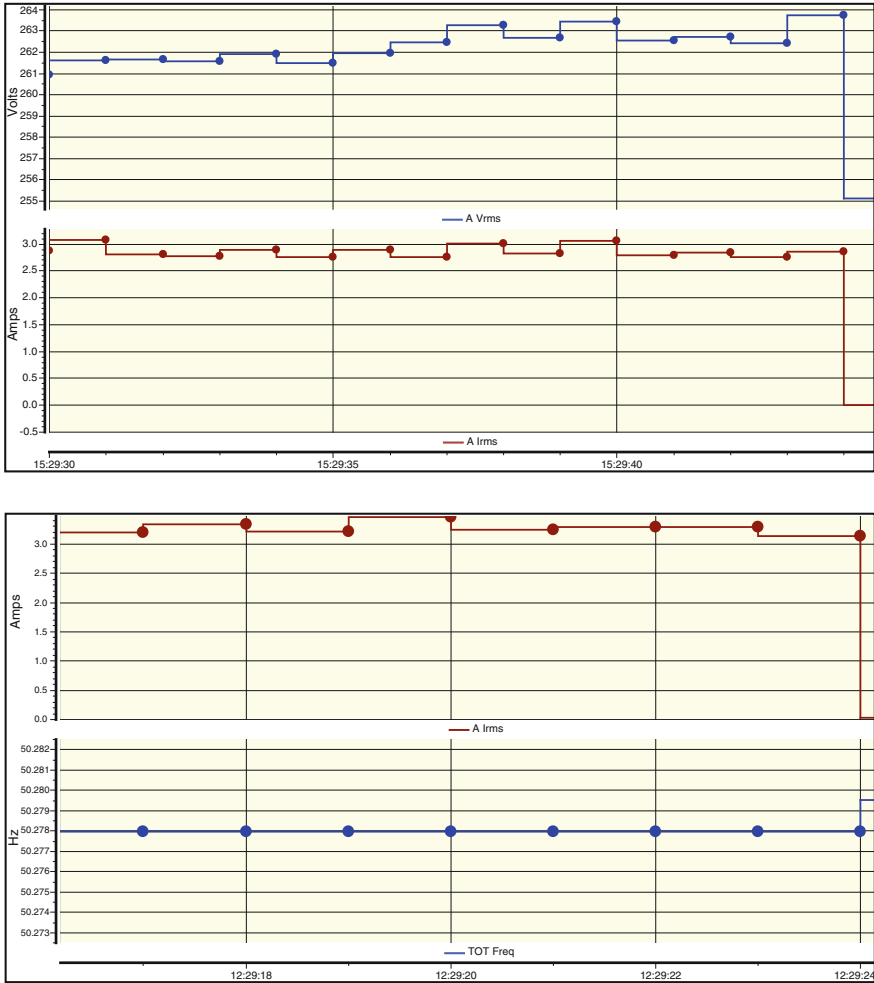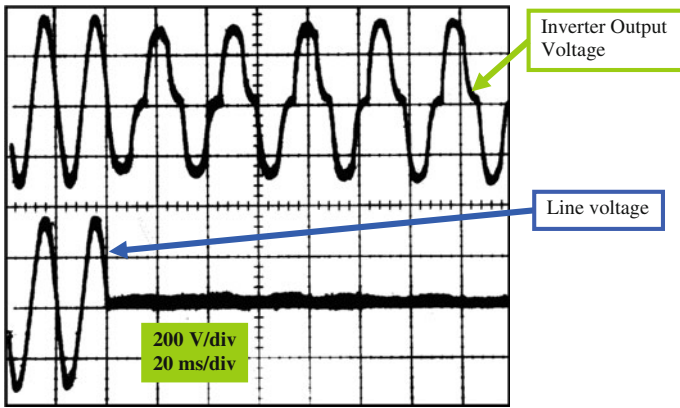
Fig. 3 The U/O-V&F monitoring technique; determination of over voltage and frequency thresholds (3.0 kW commercial single phase inverter). The *purple colour* represents the VINV and the *green colour* represents the I$_{INV}$

Additionally, Fig. 5 exhibits the inverter response in case of islanded mode under generation—consumption match and pure Ohmic load (the network quality factor is zero). This situation shows clearly the weakness of this passive monitoring technique to disconnect the inverter, due to the fact that the islanded network rms voltage remains within the Distribution Operation thresholds. It is worth mentioning that the alternative use of the passive VHD monitoring technique could be more effective—due to the distorted waveform of the islanded network voltage; however, under realistic quality factor values (between 0.05–0.25) even this monitoring technique would become ambiguous.
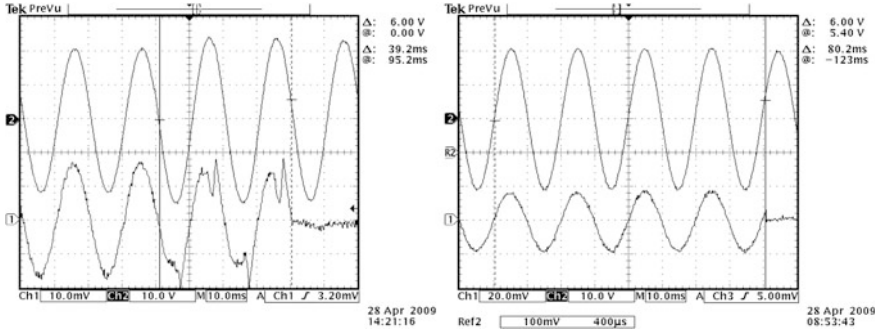
Fig. 4 The U/O-V&F monitoring technique; measuring the time interval between the voltage or frequency step and the intervention of the protection (3.0 kW commercial single phase inverter). The *purple colour* represents the V_{INV} and the *green colour* represents the I_{INV}
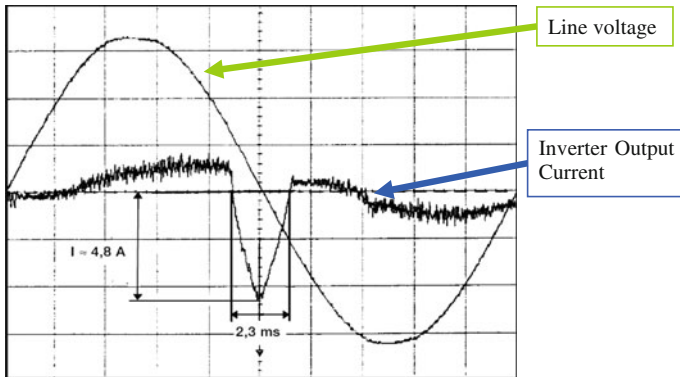

Fig. 5 The U/O-V&F monitoring technique; islanding operation under generation—consumption balance and pure Ohmic load (testing at a 4.0 kW commercial single phase inverter)

A typical example that highlights the effectiveness of active over passive islanding detection techniques in the aforementioned case of load match and realistic QF values is shown in Fig. 6; in this test a 2.0 kW single phase inverter is examined under load match and for QF = 0.125. The inverter implements the AFD monitoring technique, which manages to achieve disconnection at 380 ms. This is a satisfying response according to both the above mentioned international standards—which demand for the specific network condition a disconnection time of less than 2.0 s.

Moreover, Fig. 7 shows the implementation of the active impedance monitoring technique, performed by a 700 W single phase inverter unit; here the impedance measurement comes through a periodical current pulse injection which duration is about 2.3 ms and its peak value is comparable to the inverter nominal current
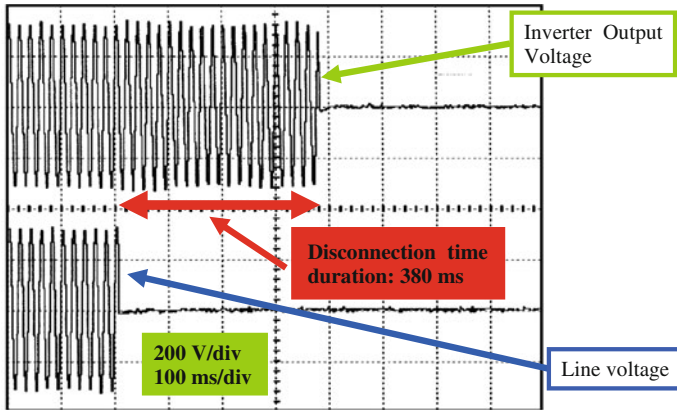
Fig. 6 The AFD monitoring technique; islanding operation under generation—consumption balance, QF = 0.125 (testing at a 2.0 kW commercial single phase inverter)

Fig. 7 The impedance monitoring technique implemented by a 0.7 kW commercial single phase inverter

amplitude. Although this method is very efficient for the detection of any islanding condition, it is obviously less attractive for high power PV systems due to the network voltage quality as well as the protection issues that it raises.

An improved impedance monitoring implementation that limits the voltage quality effects is discussed in Fig. 8; here the current pulse takes place after a dead time of 2.5 line cycles, which is enough for the detection of islanded operation (through voltage and/or frequency drop) under normal network/operation conditions. Thus, in this algorithm the current pulse is the second islanding detection stage (for cases of unusual high QF values).
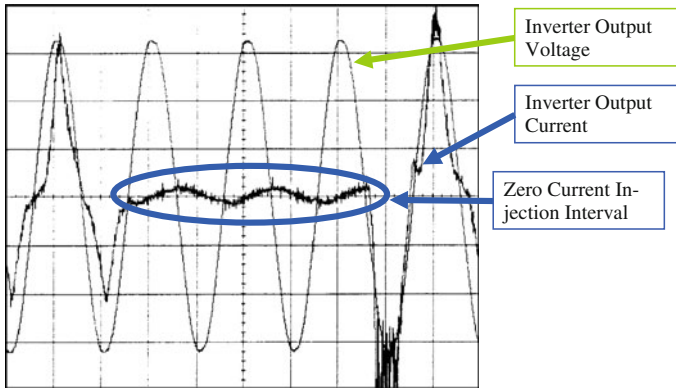
Fig. 8 The improved impedance monitoring technique implemented by a 1.0 kW commercial single phase inverter

7   Conclusions

A detailed overview along with an experimental evaluation process has been presented in this work, highlighting the fact that the islanding detection is a rather complicated work which depends on numerous factors (e.g. load matching, quality factor, PV actual generation). Moreover, this work encumbers as distributed PV generation penetration level increases due to its impact on the power quality of the supply. The experimental procedure that has been presented shows that the use of active islanding detection techniques based on positive feedback loops is the best way for PV inverters to become compatible with the IEC 62116 and the IEEE Std. 929-2000 standards and with small impact on distribution power quality. Nevertheless, it is foreseen that as penetration level increases the combination of local active and remote monitoring techniques will become obligatory—a step forward on the way to smart distribution integration.

References

1. IEC 62116 Test procedure of islanding prevention measures for utility-interconnected photovoltaic inverters.
2. Ward Bower and Michael Ropp, "Evaluation of Islanding Detection Methods for Utility-Interactive Inverters in Photovoltaic Systems", SANDIA REPORT, SAND2002-3591, Unlimited Release, Printed November 2002.
3. IEA International Energy Agency, "Evaluation of Islanding Detection Methods for Photovoltaic Utility Interactive Power systems", Report IEA PVPS T509: 2002.

4. Wei Yee Teoh, Chee Wei Tan, "An Overview of Islanding Detection Methods in Photovoltaic Systems" 58 International Conference of World Axademy of Science, Engineering and Technology, WASET 2011, Bali (INDONESIA), 26-28 October 2011, pp. 674-682.
5. T. Funabashi, K. Koyanagi R. Yokoyama, "A Review of Islanding Detection Methods for Distributed Resources" IEEE Power Tech Conference Proceedings, Bologna (Italy) 23-26 June 2003, vol. 2, 6 pp.
6. P. Mahat, Z. Chen, and B. Bak-Jensen, "Review of islanding detection methods for distributed generation," in Proc. 3rd Int. Conf. Electr. Utility Deregulation Restructuring Power Technol., 2008, pp. 2743–2748.
7. Ropp, M.E., Begovic, M., Rohatgi, A., "Determining the Relative Effectiveness of Islanding Prevention Techniques Using Phase Criteria and Non-detection Zones," IEEE Transactions on Energy Conversion vol. 15 no. 3, Sep 2000, p. 290-296.
8. EN 50160: "Voltage characteristics of electricity supplied by public distribution systems", CENELEC 1999.
9. D. Velasco, C.L. Trujillo, G. Garcera´, E. Figueres, "Review of anti-islanding techniques in distributed generators", Renewable and Sustainable Energy Reviews, 2010. 14(6): p. 1608-1614.
10. IEEE Std. 929-2000 – IEEE Recommended Practice for Utility Interface of Photovoltaic (PV) Systems.

The Use of PLC Technology for Smart Grid Applications Over the MV Grid: The DG Paradigm

G. Chatzis, S. Livieratos and P.G. Cottis

Abstract As the Smart Grid has the potential to bring significant value to the various stakeholders of the electricity market, a methodology for the evaluation of the smart grid benefits related to distributed generation is required to facilitate decision making. This chapter proposes a generic framework to assess these benefits using as a study case an autonomous distributed photovoltaic generation system in a Greek island that employs powerline communications technology.

1 Introduction

The rapid development of information telecommunications and technologies (ICT) has made feasible the distributed control of power systems as well as the real time power management and power flow control. The smart grid can be regarded as an ICT-enabled electric power network which can intelligently integrate/incorporate the actions of generators, distributors and consumers of energy, aiming at delivering electrical power in a sustainable, economic and secure way [1, 2]. The term smart grid (SG) refers to the introduction of intelligence to the electric power grid based on data transfer between grid nodes and central controlling entities that make decisions to enhance the operation and performance of the power network.

G. Chatzis (✉) · P.G. Cottis
School of Electrical and Computer Engineering, National Technical University of Athens, Iroon Polytechniou 9, Athens 15780, Greece
e-mail: georgios.chatzis@alumni.ethz.ch

P.G. Cottis
e-mail: pcottis@central.ntua.gr

S. Livieratos
School of Pedagogical and Technological Education,
Department of Electrical and Electronic Engineering Educators,
Heraklion, Athens 14121, Greece
e-mail: slivieratos@aspete.gr

The smart grid moves through and processes data in order to make preventive or corrective actions at local level. By incorporating smart metering and machine to machine (M2M) technologies to monitor the power grid, additional significant benefits will be offered, leading to intelligent power network operation.

The significant penetration of distributed generation (DG) of electric power expected in the near future necessitates speeding up the transition from the existing one-way power flow model, from large generation plants towards the consumption side, to a two-way power flow model, where power may flow between any nodes across the power grid. This decisive change the generation, distribution and transmission of energy makes the interaction between the power network and its nodes imperative, though quite complex. Drastic changes are needed with regard to the operation, control and protection of the power grid. In the context of transforming the traditional power grid into the smart grid, a hybrid Wireless-Power Line Communications (W-PLC) approach seems suitable for transferring SG data over the Medium Voltage (MV) grid. The main objective of a W-PLC SG communications (SGC) system is to transfer IP (internet protocol) data packets from/to any node over the power grid. In addition to offering an IP-based communications platform, the W-PLC option may offer additional benefits to the power grid such as self-diagnosis and self-healing or the capability of embedding intelligence wherever necessary.

This chapter comprises four sections aiming at:

- Demonstrating the importance of information flow throughout the SG and describing how to collect, move through and process SG data employing as an indicative study case the distributed photovoltaic (PV) generation in an island.
- Establishing PLC technology as a candidate solution suitable for the implementation of the SGC infrastructure over the MV grid.

2 Smart Grid and Distributed Generation

2.1 The Smart Grid

The smart grid utilizes ICT to achieve two-way communication aiming at controlling and optimizing the operation of the various parts of the power network energies. Among the main objectives of the smart grid are to save energy, reduce operation and maintenance costs, increase reliability and enhance customer care [3]. The smart grid includes intelligent systems to monitor and control the power flow and the overall network operation. It is based on a communication infrastructure capable of supporting fast and reliable two-way transfer of information across the power network as well as to/from related entities responsible for its monitoring and control. Smart metering is expected to enable the real time transfer of all the information necessary to monitor the power flow and the grid condition. The

effective operation of the smart grid is dependent on direct and reliable communication of the various network nodes, such as substations and smart meters, with the corresponding controlling entities. Given the span of the power network and the immense number of its nodes, it is expected that the volume of information moving through the SG will be huge, giving rise to new "big data" engineering challenges.

Moreover, the smart grid must support the optimal operation and control of the power network and the integration of dynamic systems to manage the energy value chain incorporating power generation, transmission and distribution. Key features related to the transmission and management of energy in the smart grid are:

- The nodes and the overall infrastructure of the power network are or can be monitored by intelligent electronic devices (IEDs) compatible with the IP protocol.
- The SGC infrastructure allows IEDs to communicate securely and reliably either with the controlling entities or with each other, if necessary.
- The data from the SG nodes and from any related data source should be transferred following specific protocols and be convertible into usable information where necessary.
- Computational tools incorporating the operational tactics and business policies enable decision-making by the utilities or by the users either automatically or through human intervention.

A large part of the assets of the transmission and distribution networks are encountered in the substations. In the distribution network, particularly, there is a large area between substations and consumers that includes many network assets whose status becomes known only after a scheduled inspection or a failure. An important objective of the smart grid is to enhance the observability, and consequently, the necessary level of controllability of the network assets. This will result in better system operation and considerable reduction of the relevant maintenance cost.

The basic SG functions can be classified into real-time and non-real-time. The former are functions enabled by sensors and measuring devices distributed over the power network. Proper communication and control of such distributed devices will: (i) enhance the observability of critical network nodes and subsystems, (ii) enhance power flow and quality, (iii) enable fault detection and restoration, and (iv) offer physical surveillance of the power network. The latter category encompasses SG activities related to the integration of any information necessary for day-to-day operation which is available to the databases of the utilities or of the power providers.

The electric companies have the necessary vertical structure to process the collected data, but it is difficult to dynamically combine such data with operational data acquired in real-time. Therefore, it is essential to formulate a common mode of hierarchical/selective presentation of information and enable secure and reliable two-way data transmission. Although some characteristics of the smart grid have already been implemented, the transformation of the traditional power network into the smart grid necessitates: (i) new types of equipment and new computational tools

(ii) complete re-engineering of the electric power companies that goes beyond simple monitoring of some operation and performance indicators.

2.1.1 The Communication Infrastructure of the Smart Grid

The smart grid requires two-way communication between various parts of the power network and the relevant stakeholders. The SGC infrastructure must have the following features:

- Ubiquitous presence
- High availability and reliability
- Secure data transfer
- Capability of providing multiple service classes

The communication infrastructure of the SG must also support the integration either of various network functions, such as supervisory control and data acquisition (SCADA), automated operation of transmission and distribution systems, operation and maintenance, or of business functions, such as customer care, market monitoring, etc. The communication networks implementing the smart grid may be classified into:

i. The last-mile access network: The corresponding SG nodes are residential users or small and medium enterprises (SMEs) that are connected to the Low Voltage (LV) network. The local access networks (LANs) formed employ short range wireless technologies (Wi-Fi, Bluetooth, Zigbee) or wired technologies such as PLC or Ethernet.

ii. The intermediate access network: The corresponding SG nodes are installed directly on the MV power network. This SGC category encompasses industrial customers, independent DG producers and concentrators/gateways of information acquired from various network nodes. The intermediate access network is deployed over the MV grid and may employ metropolitan access network (MAN) technologies such as 4G/Wimax, 3G/Wi-Fi, microwave links or Broadband PLC (BB-PLC), Narrowband PLC (NB-PLC) or hybrid W-PLC. In extreme cases, remote DG units, such as wind turbines located in islands or in remote mountainous areas, may communicate with the relevant controlling entities via satellite.

iii. The backbone network: The corresponding nodes are: (a) aggregators of information encountered in the intermediate access network, (b) operational and business units of the utilities, energy producers or alternative providers and (c) other energy market stakeholders, such as the regulatory authorities. These nodes can be connected to the backbone via the Internet. As the related communication technologies must provide high capacity, optical fiber or VDSL (Very-high-bit-rate Digital Subscriber Line) are preferred. In most cases, the power generation plants are connected to the backbone via dedicated fiber optic links.

Table 1 Overview of SG communication options

	Coverage—availability	Quality of service (QoS)	Cost
Optical fiber	Urban areas	Very good	High
GSM/3G	Urban and particular rural areas	Moderate (low reliability)	Low
4G/WiMax	Urban and rural areas	Good	Moderate
Satellite communications	Anywhere	Very good	Very high
Wireless-BB PLC	Anywhere	Very good	Moderate

Table 1 outlines the available networking technologies for the SG operation with regard to availability, QoS (stability and reliability) and cost.

2.1.2 The Hybrid Wireless-BB PLC

PLC systems operate in the 1–34 MHz frequency band and may offer high transmission rates and make feasible a variety of SG applications and services [4]. The new IEEE P1901 standard aims at meeting the QoS requirements related to broadband applications, both indoor, employing the LV network (especially for multimedia applications), and outdoor, employing the MV network (especially for SG services). Also, compliance with the international ElectroMagnetic Compatibility (EMC) regulations ensures that PLC systems can coexist with primary wireless services and operate without causing harmful interference.

The hybrid wireless PLC (W-PLC) technology combines PLC transmission with wireless transmission (usually Wi-Fi) in order to create a reliable, high-capacity and low-cost intermediate access network that may be installed over the MV grid. W-PLC allows data transmission over the MV grid offering monitoring, control, management, and surveillance of its critical parts and operations. The main advantage of W-PLC is its immediate applicability without requiring the installation of an additional communication infrastructure. It may offer last mile access employing either small range-low power wireless tecnologiesor PLC via the LV grid. The benefits of installing a W-PLC infrastructure over the MV grid are:

- Due to its ubiquitous presence, the installation of a hybrid W-PLC network on the MV grid for providing broadband SG data transmission is immediate, affordable and scalable.
- As Distribution System Operators (DSOs) own the SGC infrastructure they are fully responsible for the acquisition, transmission and processing of SG data. This minimizes the cost for SGC services and ensures secure and reliable processing of the SG data.
- The average transmission delay and error rate are kept at acceptable levels.

- The PLC units are usually capable of integrating many SG services, in a direct and selectively scalable way.
- Diagnosing the status of the powerlines is feasible by processing specific noise patterns and signals superimposed on the PLC signals.
- The various alternative technologies employed in the implementation of the smart grid can offer only a part of the services required. W-PLC can easily be made compatible with almost any ICT technology in the attempt either to enhance its communication capabilities or to cooperate either with alternative communication technologies or with existing or future automation technologies.

Overhead MV powerlines can transfer communication signals at transmission rates currently exceeding 200 Mbps at the physical layer. The transmission rates feasible by PLC can significantly exceed 200 Mbps, if proper measures are taken to overcome the very low power injection levels dictated by current EMC regulations. Given that the volume of many kinds of SG data can be quite low, the NB-PLC technology, which exhibits significantly lower ranges compared to BB-PLC, might be a reliable and cost effective alternative for low rate SG communications over the MV grid.

The capability of real-time monitoring the power network, which constitutes a fundamental SG service, will render the DSOs operation more flexible and adaptable to the dynamic behavior of the power network by supporting the energy control centers (ECCs) in monitoring, analyzing and managing the power generation, transmission and distribution.

There are two kinds of areas related to SG operation: local areas of variable geographical extent around the SG nodes and wide areas requiring communication between the SG local areas and the ECCs. The primary specifications related to SG operation concern the transmission rates and the aggregate throughput required the service availability and coverage, and the QoS with regard to reliability and delay.

2.2 Distributed Generation

Several definitions of DG are based either on the voltage level at which the DG interconnection is done or on the size of the DG power plants connected. DG units are relatively small power generation plants which can supply residential, commercial or even industrial users with electric power using either renewable energy sources (RES) or even fossil fuel plants of small size [5]. In general, DG can be defined as small-scale electric energy generated at various points across the power grid. In general, DG units are more frequently encountered in areas located closer to the end-user side. The re-engineering of the power system together with the evolution in building small-scale power plants have led to a rapid development of DG. The re-engineering of the power grid in order to incorporate DG is a complex issue. Reconfiguring the traditional power grid to create an enhanced smart-power grid

differs significantly from the traditional power grid planning since the existing distribution grids have been traditionally designed as passive systems of radial topology.

The general characteristics of DG systems are:

- As the implementation of DG plants reflects mainly the business initiatives of various private investors in the energy sector, DG is not planned and developed by the utilities or by the independent power transmission operators (IPTOs).
- No central operation plan of DG units is done by the IPTO.
- The nominal power of DG units varies between several hundreds of kW and several MW.
- The DG units are connected directly either to the distribution grid or to the transmission grid.

Many factors determine the DG suitability for a particular area. Among them are which locations are suitable to install, what are the operational loads and the distribution areas, the technology used, how the environment will be affected, etc. Significant technological innovations and changes in the economic and regulatory environment during the last decade have pushed forward DG. The primary reasons that contributed to the evolution of DG are:

- The development of efficient DG technologies.
- The technical and economic restrictions related to building new transmission networks or extending existing ones.
- The increasing demand for highly reliable electric power.
- The liberalization of the electric energy market.
- Severe environmental measures and restrictions.

The integration of DG into the traditional power grid changes the mode of operation of the power network and creates new challenges related to power quality and reliability, network stability, and grid safety. Such integration is not an easy task due to various operational and regulatory issues. The most important technical issues are related to the voltage and current at the output of DG installations and to the power quality. Therefore, appropriate procedures are required, which must be widely acceptable and easily applicable in order to make feasible and accelerate the DG integration without affecting the current operation and stability of existing power networks.

2.2.1 DG Technologies

The various DG technologies are depicted in Fig. 1. There are two major DG groups: (i) technologies using fossil fuels and (ii) technologies using RES.

The main DG technologies currently employed in residential areas are: PV generators, low-power wind turbines (WT) and fuel cells having a nominal power ranging from 2 to 5 KW. In addition to the preceding technologies, some other options are commercially available such as reciprocating engines, micro-turbines,
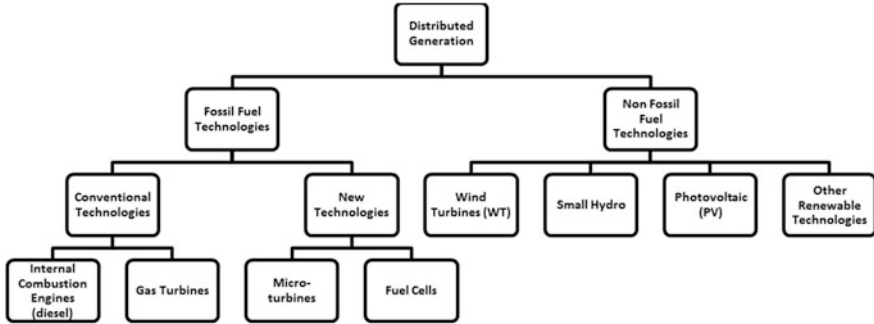
Fig. 1 DG technologies

diesel generators, conventional coal generators, biomass and small hydro with nominal power ranging from 10 KW, e.g. for PV, up to 1.500 KW, e.g. for biomass. An increasing trend towards the use of RES has emerged worldwide over the last decade by the environmental measures aiming at reducing CO_2 emissions and the continually rising prices of fossil fuels.

2.2.2 DG Advantages and Disadvantages

DG is expected to significantly enhance power quality and reliability and be better customized to the end-users needs. The potential benefits from DG are [6]:

- Combined heat and power (CHP) systems are expected to enhance the aggregate energy efficiency of power systems.
- Local power generation employing RES or non-conventional energy sources is more cost-effective for customers who are located far from the traditional power generation.
- By been connected during peak periods, DG can reduce "demand" charges by the local utilities.
- Distributed generators, capable either of being connected to the power grid or of operating standalone, can feed supply loads of high priority during long outages of the main utility.
- Employing sophisticated power electronic interfaces, the distributed generators are capable of providing high-quality power with regard to voltage and frequency stability.

The advantages offered by DG are numerous and significant. The most important is the peak load reduction which contributes to balancing both the individual and the average demand profiles. Dispersed RES can defer power generation, thus lowering the costs for system upgrading. Furthermore, as DG is usually installed near consumption, it reduces both the transmission losses and the cost of energy transport. Also, it is much easier to acquire sites for RES plants compared to those

destined for the installation of large scale generation plants. Technical benefits associated with improved power quality and reliability are offered as DG can either relieve the existing power network or be used for backup during non predictable power outages or voltage dips. Equally important are the environmental benefits offered by DG as the enhanced RES penetration is expected to significantly reduce the use of fossil fuels and, consequently, CO_2 emissions.

On the other hand, high DG penetration can cause serious technical problems to the power grid operation, and, consequent adverse economic effects. The variable energy production due to intermittent RES operation restrains the percentage of energy demand that can be satisfied by transforming wind or solar energy to electric. Hence, as, so far, the maximum RES penetration remains rather limited, high levels of conventional power generation are still required.

2.2.3 DG Interconnection with the Power Grid

DG changes the traditional one-way power flow from High Voltage (HV) to MV and next to LV. So far, distribution systems have been designed to passively transfer electric power from generation to the end users. As DG dictates a bidirectional power flow model, DSOs have to deal with new issues that require different handling of the power grid. These new issues related to DG are [7]:

- Congestion and power capacity reduction: DG connection close to consumption side does not generally lead to an increase of congestion events, but possibly to their reduction. The positioning of DG points of interconnection (POIs) are of high importance.
- Losses: Depending on the DG type and location and the grid technology and configuration, DG may either reduce or increase the distribution network losses. Low DG penetration is expected to reduce energy losses, whereas high DG penetration is expected to increase them.
- Short circuits: DG connection to the distribution system increases the short circuit currents which causes problems to various system components such as line conductors, breakers and switches. The crucial POIs are those where the short circuit currents may take maximum values, that is, at the lines stemming from the primary substations.
- Voltage profile: The range of voltage fluctuations depends on the nominal power of the DG units connected and the corresponding POI positions as well as on the power factor and the local grid topology.
- System instability: a DG unit should be able to remain connected to the distribution grid after a fault.
- Islanding: Problems may arise when a DG unit continues to supply power to a part of the distribution network which has been electrically isolated from the rest of the system.

- System unbalance: Large reserve capacities are necessary to mitigate the fluctuations in DG production as the power produced each time must be equal to the sum of the power consumed and the power lost.
- Power quality: DG connection may aggravate the power quality by causing voltage fluctuations and distortion, endangering the normal operation of certain electric devices.

Before analyzing the above issues, several definitions must be given. The demarcation point of an electrical installation is the point at which it is connected to another installation or to the public network. The Point of Common Coupling (PCC) of a power supply network is the electrically nearest point to a particular load, where other loads are, or may be, connected. These loads can be devices, equipment or systems, or distinct customer installations. The PCC is the reference point for determining the effects caused to the network due to a specific installation. In addition to the PCC, POIs are defined as the points, either on the LV or on the MV grid, where the producer's facilities are connected to the grid. Metering units for both the energy injected to the grid and the energy supplied by the grid are also installed at various POIs. There are also automatic interconnection switches implementing connection/disconnection of the generator to/from the network. To connect the generation facilities to the power supply network, various network components such as substations, transformers and powerlines are involved. When the existing infrastructure is inadequate or causes severe voltage fluctuations, appropriate measures must be taken such as direct connection to the MV buses of the HV or MV substation HV via a dedicated power line, or installation of a new HV/MV transformer.

3 DG Integration into the Autonomous Power Grid of an Island

3.1 PV Penetration in an Autonomous Island Grid. A Study Case

The Greek power grid is interconnected with those of neighboring countries and serves the mainland of the country as well as several connected islands. However, many Greek islands are autonomously powered employing diesel generators at a very high cost. Introducing RES, particularly PV ones, in the power generation mix of the autonomous grids in Greek islands is of great importance. The integration of PV energy production into the local power grids can be implemented either at the transmission or at the distribution level, depending on the size of the generation. Distributed PV units of small size are generally connected to the main grid at the primary or secondary distribution level, giving rise to several issues that should be addressed by the smart grid.

3.1.1 Autonomous Grids

Autonomous Grids (AGs) installed in the Greek islands are not interconnected with the power system of the mainland; hence, they must be capable of autonomously responding to power demand, both reliably and safely. This causes several problems such as:

- Operational redundancy: The severe fluctuations in power demand do not allow the complete withdrawal of fossil fuel generation, thus limiting the RES penetration.
- High cost of spinning reserve: The operational plan of conventional production stations foresees spinning reserve, i.e. the nominal power of diesel generators in operation should be higher than their operational output power, rendering them capable of delivering additional power, when required. The total spinning reserve is determined by the reserve necessary to cover the intermittent DG operation.
- Large frequency, voltage and current fluctuations due to the low inertia of the AG or the low short circuit power.
- The severely adverse effect of load fluctuations to the quality of the electric energy provided.
- High production costs.
- Geographic dispersion of DG units that severely affects the AG security.
- Severe system instability.
- The continually growing energy demand and the strict environmental regulations for the development of renewable generation and transmission projects, especially in economies with high touristic development.

The total installed power of wind PV plants in certain Greek islands is shown [8] in Table 2.

3.1.2 Interconnection Issues When PV Systems Are Integrated into the MV Grids of Greek Islands

The interconnection issues concerning the interaction of PV systems with the main grid are related to several factors and parameters [9] such as the voltage profile, the active and reactive power flow, the thermal (current) loading of power network elements, the transient stability (preservation of synchronism), the voltage stability and reactive power control and the frequency control [10].

The utilities are concerned about the quality of the electric power offered by DG integration into the grid affected by the harmonics, voltage dips, voltage flicker and overvoltage caused. Several studies have led to the development of guidelines concerning DG integration into the MV grid. The most important functional requirements concerning the integration of dispersed PV units into the MV grid are:

Table 2 Wind and PV plants in several Greek islands

Island systems	Wind power PPC (KW)	Wind power individuals (KW)	Total wind power (KW)	Solar power (KW)
CRETE	16800	88971.2	105772	489
KOS-KALYMNOS-LEROS-LIPSI	0	8000	8000	0
LIMNOS	1140	0	1140	0
MYTILINI	2025	9825	11850	1
MILOS-KIMOLOS	0	2050	2050	0
AMORGOS	0	0	0	0
MYKONOS	0	300	300	0
CHIOS-PSARA	5500	3050	8550	0
SYROS	0	2790	2790	0
IKARIA	385	600	985	0
PAROS-NAXOS-IOS	0	1800	1800	0
SAMOS	2925	2950	5875	0
SKYROS	0	0	0	0
SIMI	0	0	0	0
SANTORINI-THIRESIA	0	0	0	0
RHODES-CHALKI	0	12075	12075	0
KARPATHOS-KASOS	275	950	1225	0
SIFNOS	0	0	0	0
PATMOS	0	0	0	0
KITHNOS	500	0	500	0

- If voltage fluctuations exceed the limits allowed for longer than a specified period, usually taken equal to 1 s, the PV unit must be disconnected from the grid for security reasons. Fast voltage recovery is recommended after an outage or other abnormal conditions. The same considerations apply for frequency fluctuations that deviate from the relevant nominal value for longer than a specified period, typically equal to 1 s.
- Similarly to all devices incorporating power electronics, PV systems should not cause harmonic distortion signals and electromagnetic interference beyond acceptable levels.
- In case of short circuit within PV units, the latter should be disconnected from the grid.
- In case of short circuit in the power network, the PV unit involved must be disconnected.
- When a part of the main grid is isolated, not due to a short circuit, there is the possibility that the affected section is fed only by the associated PV units with voltage and frequency within acceptable limits (islanding).

3.1.3 Voltage Fluctuations

The percentage voltage fluctuation at the POIs of PV units to the MV grid is given by [11]

$$\varepsilon(\%) = \frac{100}{V_n^2} (R_\kappa \cdot P + X_\kappa \cdot Q) \tag{1}$$

where $\tilde{Z}_\kappa = R_\kappa + jX_\kappa$ is the equivalent impedance of the MV at the POIs. P and Q represents the flow of active and reactive power as in

$$P = P_{DG} - P_L \tag{2}$$

$$Q = Q_{DG} - Q_L \tag{3}$$

P_{DG}, Q_{DG} are the active and reactive power of the PV units and P_L, Q_L the active and reactive power loads respectively. The sign of Q_{DG} depends on the power factor. If ε_{max} is the maximum allowed level of voltage fluctuations, then

$$\left| \frac{100}{V_n^2} (R_\kappa \cdot (P_{DG} - P_L) + X_\kappa \cdot (Q_{DG} - Q_L)) \right| \leq \varepsilon_{max} \tag{4}$$

The following DG and PV measures can be calculated from (4). The aggregate active power, the adjustment of the reactive power of each unit and, consequently, of the power factor of the whole PV installation, provided that the active power does not change.

3.1.4 Power Factor at the MV Bus

As to the operation of generators having power factors within a specified range, maintaining a fixed aggregate power factor sensed by the grid is imperative. The MV bus is defined as the part of the grid where several MV lines are connected to. In the absence of DG units, the power flows from the MV bus to the connected lines. When DG units are connected to the MV grid, the total active and reactive power of the MV bus is the sum of the active and reactive power of the DG units and loads. In this context, it is the aggregate power factor at the MV bus that must lie within the specified limits.

$$pf_{bus} = \frac{P_{DG} - P_L}{\sqrt{(P_{DG} - P_L)^2 + (Q_{DG} - Q_L)^2}} \tag{5}$$

The reactive power Q_C, which is injected into the grid as a result of a compensation mechanism for both voltage and power factor fluctuations, must be taken into account in the calculations of the total reactive power.

3.2   Autonomous Power Grids in Islands

The first step for the deployment of an autonomous smart grid based on PLC technology in an island is to specify the requirements concerning the necessary data transfer. Subsequently, the corresponding features of the SGC network must be defined.

The demand side can be estimated based on historical data. However, as the smart grid allows monitoring of the demand side in almost real time, any kind of statistical estimation applies only during the first steps of the analysis and does not constitute an objective of the present work. The intensity of solar radiation and temperature should be continuously monitored as they determine the power generation levels. Due to their importance, inverters should also be monitored continuously. Their critical features are the DC input voltage/current, the AC output voltage/current, the output power, the power factor and the harmonics. By monitoring these features, (i) the inverters efficiency can be determined (ii) possible points of failures can be identified.

As to the data acquired from individual PV units, there is a distributed architecture based on Ethernet, or on FDDI (Fiber Distributed Data Interface) technology or on PLC systems applied on the LV grid with small coverage (of radius less than 500 m). The data are dynamically exchanged with the distributed databases. The remote terminal units (RTUs) distributed over the PV systems exchange information and receive commands through the LAN connecting them to the DACs (Data Acquisition and Control) of the PV units. The LAN nodes perform the following functions:

- Receiving-sending data, interfacing the administrator with the PV units.
- Implementing local control functions.

The information from the nodes of a specific PV system is collected at its DAC, which is located at the POI of the PV system to the MV grid. The various DAC nodes communicate with each other and with auxiliary control systems via a WAN. The DAC nodes either uplink their data to a central entity located at the ECC or receive commands downlinked from the ECC via the backhauling network, and, subsequently, via the LANs.

Independent power producers (IPPs) install RTUs at their premises for remote monitoring and control of their PV units in order to become capable of providing any information required by the ECC. So do the corporate customers. IPPs should also provide ECC with signals related to their output power (MW, MVAR) and voltage, status of the interconnection breakers, etc. Finally, smart meters collect and forward data from/to consumers and energy producers, and manage the energy loads locally.

The ECC coordinates the various system components and the overall operation of the local power grid. In this framework, it coordinates the connection of the conventional generation units, manages the RES/PV generation and connection, and integrates storage facilities. The ECC processes data acquired from RTUs dispersed across the power grid, particularly from RTUs installed at substations and at the POIs of PV systems.

4 Mathematical Formulation of the Study Case

The problem addressed in the present chapter refers to an MV line supporting an indicative Autonomous System (AS) of a Greek island. The main MV line stems from the bus of the AS generation plant. The remaining MV lines are regarded as loads connected to the buses. The impedance (per unit length) of the ACSR-95 power-lines assumed is [11]:

$$Z_0 = R + jX = 0.22 + j0.33 \ \Omega/\text{km} \tag{6}$$

4.1 AS Generation Plant Bus

The MV bus voltage V_0 of the indicative AS plant is adjusted by the AS generators in order to vary from a minimum value of 15.3 kV (this value corresponds to a percentage 15.3/15 * 100 % = 102 %) to a peak value of 16.05 kV (which corresponds to a percentage 16.05/15 * 100 % = 107 %) assuming an MV nominal value equal to $V_n = 15 \text{kV}$. The voltage adjustment is dependent on the total complex power S_{tot} produced ($V_0 = V_{min}$ when $S_{tot} = S_{min}$ and $V_0 = V_{max}$ when $S_{tot} = S_{max}$). The relationship between V_0 and S_{tot} is assumed to be linear, that is

$$V_0 = aS_{tot} + b \tag{7}$$

where the coefficients a and b are determined applying linear regression to the simulation results.

The AS loads are residential, commercial or industrial and are either directly connected to the generation plant (directly connected loads) or dispersed across the grid (dispersed loads). The nominal characteristics of the various loads, denoted by the n index, are:

$$P_{\text{load}_n} = \begin{cases} 15 \, \text{MW}, & \text{directly connected loads} \\ 1.2 \, \text{MW}, & \text{dispersed loads} \end{cases} \tag{8}$$

MV line ASCR-95
Total distance: 40 km
Distance between successive nodes: 5 km
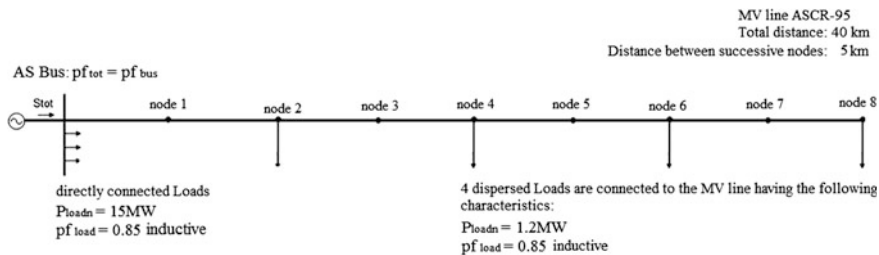
Fig. 2 Indicative MV topology in a Greek island

An inductive power factor common for all the loads is assumed, i.e.

$$pf_n = pf_{load} = \cos\varphi = 0.85 \tag{9}$$

The indicative grid topology is depicted in Fig. 2, where an ACSR-95 MV line with dispersed loads is connected to the AS bus (MV bus). Loads of 15 MW are also connected directly to the AS bus.

The active power absorbed by a load connected to node i at time t is evaluated taking into account the demand, Demand(t) and the nominal load value of node i P_{load_n}:

$$P_{load}(i, t) = -P_{load_n}(i) \cdot Demand(t) \tag{10}$$

The negative sign in the right hand side of (5) denotes power absorption. The annual demand in an AS of a Greek island is plotted as a function of time in Fig. 3.

The demand values plotted in Fig. 3 are percentages with respect to maximum demand. An increase in demand is readily observed during the summer months due to tourism and increased needs for air conditioning.

In addition to the active power, the reactive power consumed is also of interest. The reactive power absorbed by a load connected to the MV grid at node i at time t is

$$Q_{load}(i, t) = P_{load}(i, t) \cdot \tan\varphi \tag{11}$$

The reactive power of the various loads is negative since their power factor is inductive, i.e. power is absorbed by the grid.

4.2 PV Units

The PV units connected to the MV grid of the island under consideration have nominal output power $P_{PVn} = 0.5$ MW and nominal power factor equal to 1, i.e.
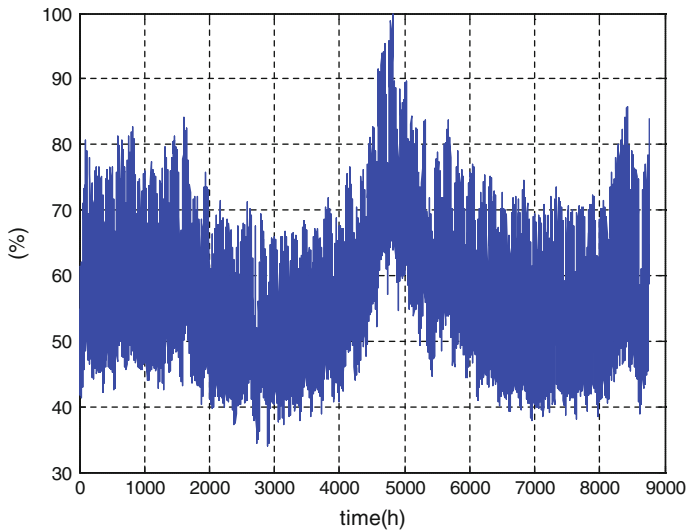
Fig. 3 Annual demand in a Greek island [12]

$pf_{PV} = 1$. The various parameters related to the operation of the PV units are denoted as follows:

- Total panel surface A (m^2)
- Panel efficiency coefficient at STC (Standard Test Condition) n_{STC} (%)
- Panel temperature NOCT (Nominal Operating Cell Temperature) T_{NOCT} (°C)
- Solar radiation intensity G(t) (W/m^2)
- Ambient temperature T_{amb}(t) (°C)

The solar radiation intensity G(t) and the ambient temperature T_{amb}(t) vary with time as shown in Figs. 4 and 5, respectively.

Taking into account the high solar radiation intensity and ambient temperature, the PV units are capable of injecting active power to the MV grid which is equal to

$$P_{PV}(i, t) = S_{ac}(i, t) * pf_{PV} \tag{12}$$

where S_{ac}(i,t) is the complex power injected to the MV grid.

The corresponding reactive power is

$$Q_{PV}(i, t) = P_{PV}(i, t) * \tan(\cos^{-1} pf_{PV}) \tag{13}$$

The sign of the reactive power depends on pf_{PV} being positive for capacitive pf_{PV} and negative for inductive pf_{PV}.
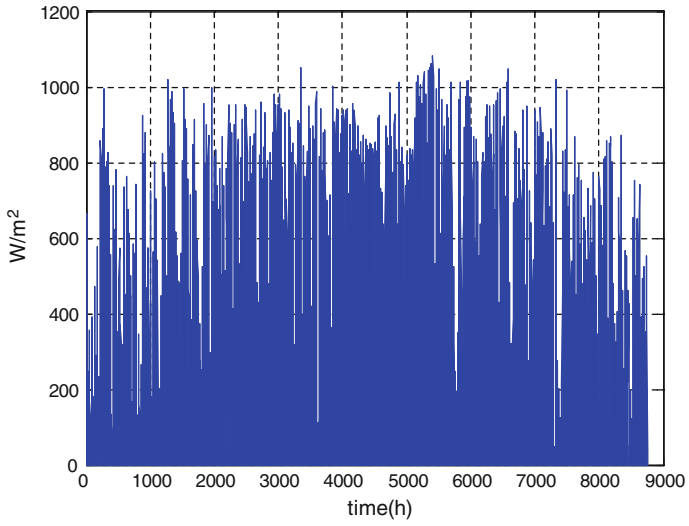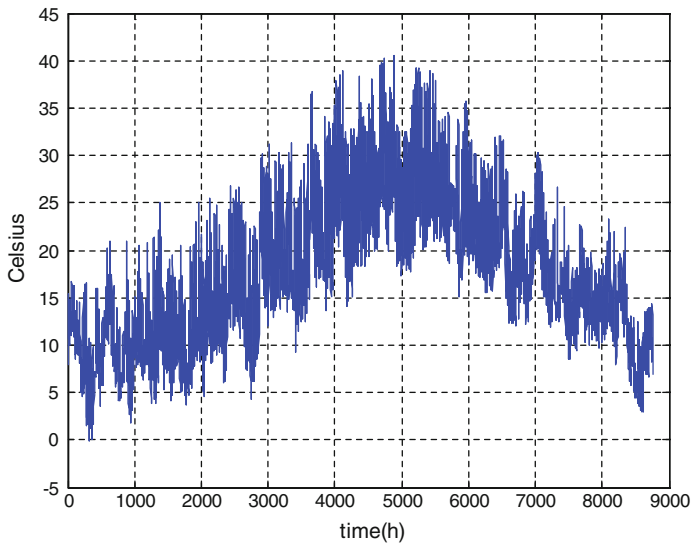
Fig. 4 Annual solar radiation intensity

Fig. 5 Annual temperature intensity

The input-output relationship is given by the following equations:

$$Sac(i,t) = A \cdot n_{STC} \cdot (1 - \Delta_{nG}(t) - \Delta_{nT}(t)) \cdot G(t) \tag{14}$$

In (14), $\Delta_{nG}(t)$ is the radiation change related to the solar radiation intensity via

$$\Delta_{nG}(t) = -0.04 \cdot \ln(G(t)/1000) \tag{15}$$

The actual temperature of the solar panel is related to the radiation G(t) and the ambient temperature $T_{panel}(t)$ via

$$T_{panel}(t) = T_{amb}(t) + \left(\frac{G(t)}{800}\right)(T_{NOCT} - 20) \tag{16}$$

The performance change $\Delta_{nT}(t)$ is related to the panel temperature via

$$\Delta_{nT}(t) = -0.0045 \cdot (25 - T_{panel}(t)) \tag{17}$$

Typical values for the parameters of the 0.5 MW PV units considered in the framework of the study case examined in this chapter are:

- A = 3500 m^2
- n$_{STC}$ = 14.5 %
- T$_{NOCT}$ = 45 °C
- 0 < G (t) < 1.100 W/m^2
- 0 ≤ T$_{amb}$ ≤ 45 °C

4.3 Energy and Power Calculations

The primary metrics determining the performance of an MV line in the current chapter are the total power factor pf$_{total}$ at the bus, which should be as close to 1 as possible, and the acceptable range of voltage fluctuations at the various nodes of the MV line, which should not exceed the specified limits. The total complex power and the power factor at the bus at time t are given, respectively, by [13]

$$S_{total}(t) = \sqrt{\left(P_{PV_{total}}(t) + P_{load_{total}}(t)\right)^2 + \left(Q_{PV_{total}}(t) + Q_{load_{total}}(t)\right)^2} \tag{18}$$

$$pf_{total}(t) = abs\left[\frac{P_{PV_{total}}(t) + P_{load_{total}}(t)}{S_{total}(t)}\right] \cdot sign\left[Q_{PV_{total}}(t) + Q_{load_{total}}(t)\right] \tag{19}$$

where $P_{PV_{total}}(t)$ is the aggregate power injected by the PV units and $P_{load_{total}}(t)$ is the aggregate active power consumed by the loads of the AS. $P_{load_{total}}(t)$ enters into (18)

and (19) with a negative sign. On the other hand, $Q_{PV_{total}}(t)$ is the aggregate reactive power absorbed or injected by the PV units (dependent on the value of pf_{PV} that determines its sign) and $Q_{load_{total}}(t)$ is the aggregate reactive power absorbed by the loads. The following equations hold:

$$P_{PV_{total}}(t) = \sum_{i=0}^{N} P_{PV}(i, t) \tag{20}$$

$$Q_{PV_{total}}(t) = \sum_{i=0}^{N} Q_{PV}(i, t) \tag{21}$$

$$P_{load_{total}}(t) = \sum_{i=0}^{N} P_{load}(i, t) \tag{22}$$

$$Q_{load_{total}}(t) = \sum_{i=0}^{N} Q_{load}(i, t) \tag{23}$$

where N is the number of POIs where the PV units are connected to the main MV powerline. When there is no energy generated by the PV units, the expressions (18) and (19) are modified yielding

$$S_{total}(t) = \sqrt{(P_{load_{total}}(t))^2 + (Q_{load_{total}}(t))^2} \tag{24}$$

$$\begin{aligned} pf_{total}(t) &= abs\left[\frac{P_{load_{total}}(t)}{S_{total}(t)}\right] \cdot sign(Q_{load_{total}}(t)) \Rightarrow \\ pf_{total}(t) &= -abs\left(\frac{P_{load_{total}}(t)}{S_{load_{total}}(t)}\right) = pf_{load} = -0.85 = 0.85\,\text{inductive} \end{aligned} \tag{25}$$

To bring the power factor closer to 1 a reactive compensating power Q_C must be injected at the bus, whose value has been evaluated as 1.758 Mvar under zero PV production. The absolute values of the aggregate complex power and power factor are given by:

$$S_{total}(t) = \sqrt{(P_{PV_{total}}(t) + P_{load_{total}}(t))^2 + (Q_{PV_{total}}(t) + Q_{load_{total}}(t) + Q_c)^2} \tag{26}$$

$$pf_{total}(t) = abs\left[\frac{P_{PV_{total}}(t) + P_{load_{total}}(t)}{S_{total}(t)}\right] \cdot sign\left[Q_{PV_{total}}(t) + Q_{load_{total}}(t) + Q_c\right] \tag{27}$$

Practically, the voltage at the various nodes of the line is allowed to vary within a range ±5 % of its 15 kV nominal value. If no PV units are connected to the MV line, the voltage ranges for most of the time from 14.25 kV up to 15.75 kV corresponding to 95 and 105 % of the nominal value, respectively.

Assigning i = 0 to the POI of the AS generator, the voltage at the bus $V_0(t)$ is known at any time t. The following equations hold for the active and reactive power values

$$P_0(t) = P_{PV_{total}}(t) + P_{load_{total}}(t) \tag{28}$$

$$Q_0(t) = Q_{PV_{total}}(t) + Q_c + Q_{load_{total}}(t) \tag{29}$$

At any node i, the voltage at time t is determined from

$$V(i, t) = V(i - 1, t) + \varepsilon(i, t) \tag{30}$$

$$\varepsilon(i, t) = \frac{100}{V_n^2} (R(i) \cdot P(i, t) + X(i) \cdot Q(i, t)) \tag{31}$$

where ε (i, t) is the percentage of the voltage fluctuations.

The following equations hold at the bus of the AS generator (i = 0)

$$V(0, t) = V_0(t) \tag{32}$$

$$P(0, t) = P_0(t) \tag{33}$$

$$Q(0, t) = Q_0(t) \tag{34}$$

The input impedance $\tilde{Z}(i) = R(i) + jX(i)$ at node i is determined from

$$R(i) = 0.22 \frac{\Omega}{km} * D(i) \tag{35}$$

$$X(i) = 0.33 \frac{\Omega}{km} * D(i) \tag{36}$$

where D(i) is the distance between nodes i and i − 1 in km. The active and reactive power at node i at time t are determined from:

$$P(i, t) = P(i - 1, t) - P_{PV}(i - 1, t) - P_{load}(i - 1, t) \tag{37}$$

$$Q(i, t) = Q(i - 1, t) - Q_{PV}(i - 1, t) - Q_{load}(i - 1, t) \tag{38}$$

All the above time varying quantities, quantifying the technical problem under consideration, are examined on a per hour basis over the year of reference. The relevant graphs depict their hourly variation taking into account that 1 year contains 8760 h. From the SGC perspective, the information related to the above quantities is transmitted every hour. Hence, the ECC receives measurements and forwards possible control commands on an hourly basis too.

If PV generation enhances the AS of an island, both the annual energy produced (in MWh) by the PV units and the corresponding capacity factor, which is basically

the utilization rate, should be determined. The annual energy production by the PV unis is given from [14]

$$E_{PV} = \sum_{t=1}^{8760} P_{PV_{total}}(t) \tag{39}$$

where $P_{PV_{total}}(t)$ is the aggregate power produced by the PV units within an hour. The annual PV utilization ratio is defined as the ratio of the energy actually produced in the year of reference to the energy that would be produced if the PV units were operating at their nominal level all the time for the whole year [14], i.e.

$$CF = \frac{E_{PV}}{8760 \cdot N \cdot P_{PV}} \tag{40}$$

5 Numerical Simulations

In the numerical simulations, the voltage fluctuations are calculated on an hourly basis and are plotted for an annual system operation. The aggregate power factor pf_{tot} at the AS bus is also calculated and the relevant percentages are plotted too.

5.1 MV Line Without Any PV Units Connected

In the first simulation scenario—which constitutes the reference scenario—depicted in Fig. 6, there are no PV units connected to the main MV line:

At the AS bus a compensating reactive power Q_C, equal to 1.758 Mvar, is injected. In the first simulation scenario the main MV line is connected only to loads. The corresponding simulation results are plotted in the following Figs. 7 and 8.

Figure 7 shows the hourly values of the power factor at the bus of the AS, whereas Fig. 8 shows the corresponding annual percentages. As deduced from
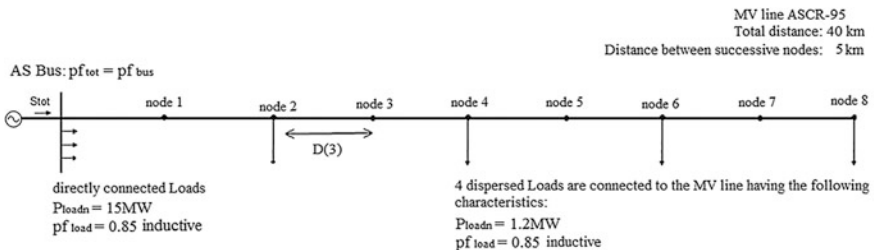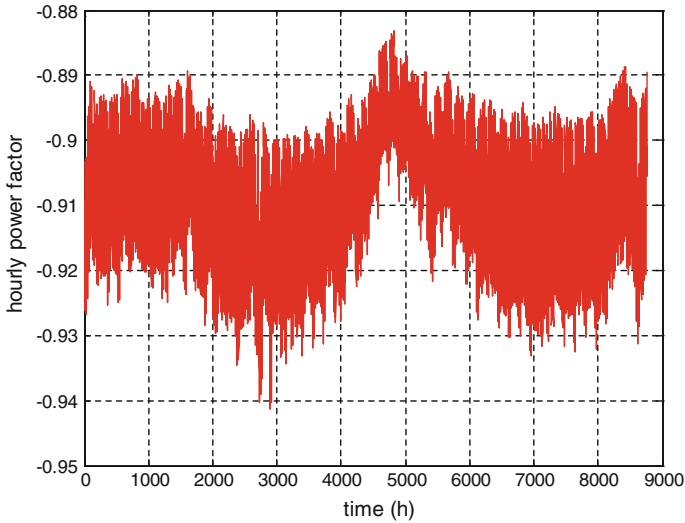

Fig. 6 MV line without PV units

Fig. 7 Hourly power factor values in the MV line without PV units connected
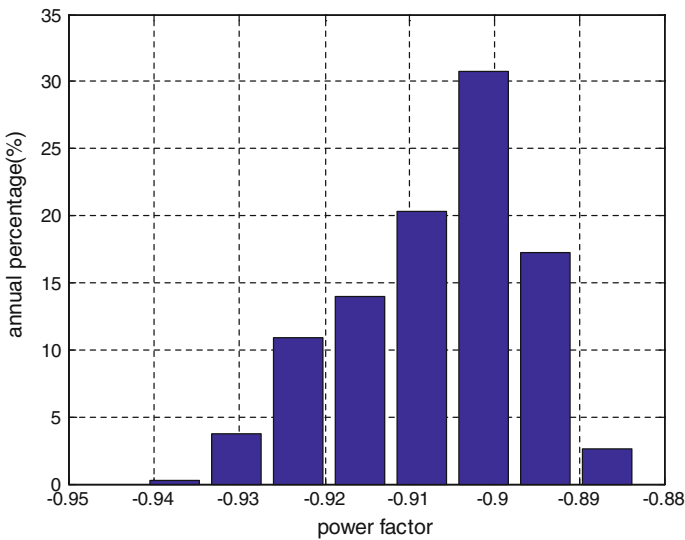

Fig. 8 Annual percentage of power factor values in the MV line without PV units connected

Fig. 7, the aggregate power factor pft_{otal} (t) ranges from 0.8832 (inductive) to 0.9413 (inductive). The value of pf_{total} (t) is concentrated around 0.90 (inductive) since, for approximately 70 % on a year basis, the power factor ranges from 0.89 to 0.91 exhibiting an average value of 0.9068.

Simulation results concerning the voltage fluctuations at various nodes are given in Figs. 9, 10 and 11. Figure 12 shows the annual time percentages during which the voltage fluctuations at the critical nodes of the MV line exceed the specified limits.
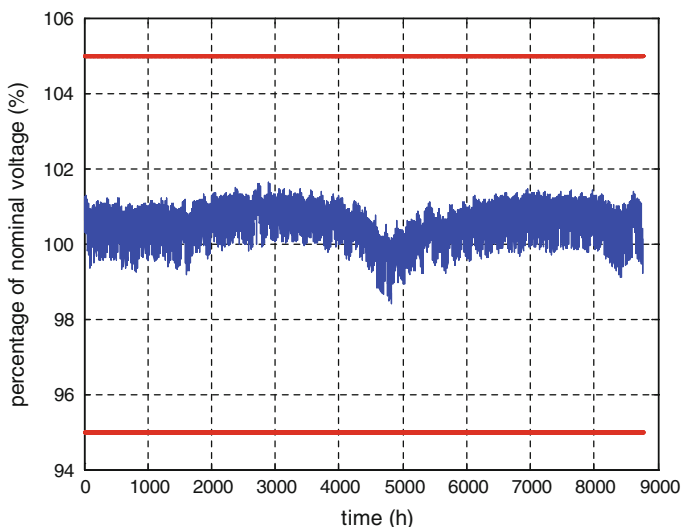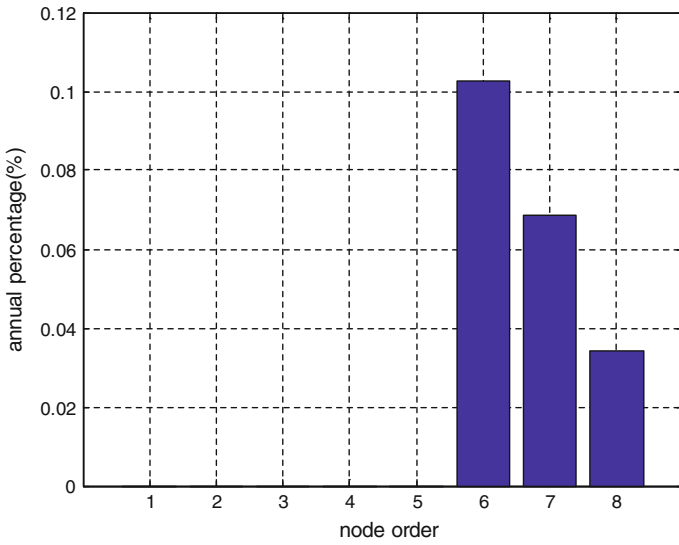

Fig. 9 Voltage fluctuations at node 3 of the MV line without PV units connected
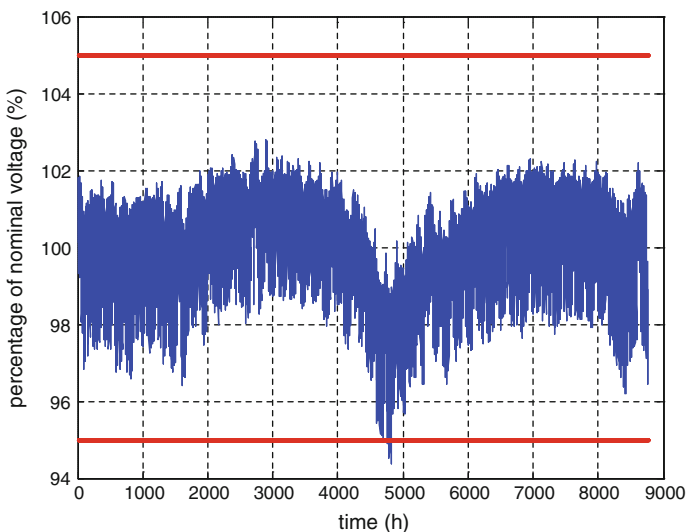
Fig. 10 Voltage fluctuations at node 6 of the MV line without PV units connected
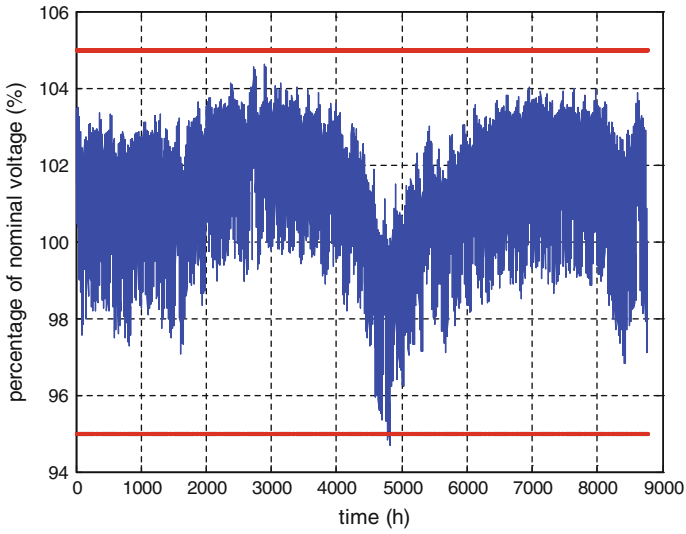
Fig. 11 Voltage fluctuations at node 8 of the MV line without PV units connected

Fig. 12 Annual time percentages during which the voltage at the nodes of the MV line exceeds the specified limits without PV units connected

Concluding, at nodes 0, 1, 2, 3, 4, 5 the voltage fluctuations never exceed the specified ±5 % limits, whereas at nodes 6, 7, 8 these limits are exceeded for very small annual percentages.

5.2 MV Line Enhanced with Eight PV Units Without Control

In this simulation scenario, eight PV units are connected to the MV line at nodes 1 to 8. The MV line configuration is illustrated in Fig. 13.

This scenario examines how the incorporation of the PV units affects the operation and performance of the main MV line. The relevant simulation results concerning the power factor at the bus of the AS are given in Figs. 14 and 15.

As observed from Fig. 14, the power factor at the bus of the AS ranges from 0.8222 (inductive) to 0.9404 (inductive). Figure 15 shows that pf_{total} (t) experiences greater variance, possibly due to the active power injected by the PV units, as the reactive power of PV units is zero. The average power factor is evaluated 0.8942 (inductive). The voltage fluctuation results at three indicative nodes are also evaluated under the reference scenario and are plotted in Figs. 16, 17 and 18. Figure 19 shows the annual time percentages during which the voltage at each node of the MV line ranges outside the specified limits.

As readily observed from the indicative Figs. 16, 17 and 18 and summarized for all the nodes in Fig. 19, the voltage fluctuations at nodes 3, 4, 5, 6, 7, 8 exceed the acceptable limits. As observed from Figs. 16, 17 and 18, the 105 % threshold is significantly exceeded, whereas, as observed from Fig. 19, the relevant annual percentages are quite high. In general, incorporating PV generation can deteriorate the power factor at the bus, increasing both its range and variance. More importantly, the voltage fluctuations at the POIs of the PV units exceed the specified limits for quite high annual percentages.
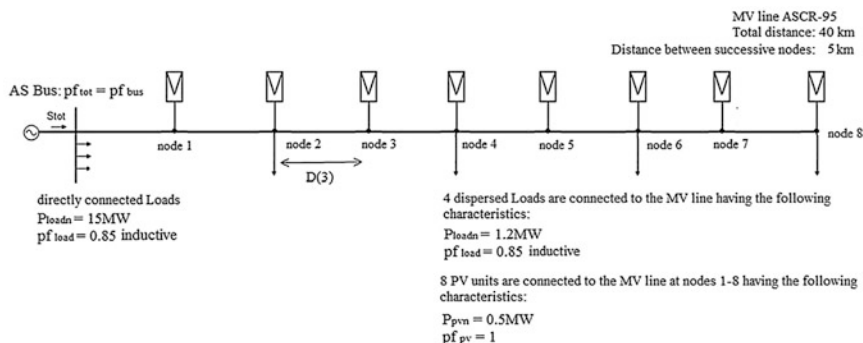

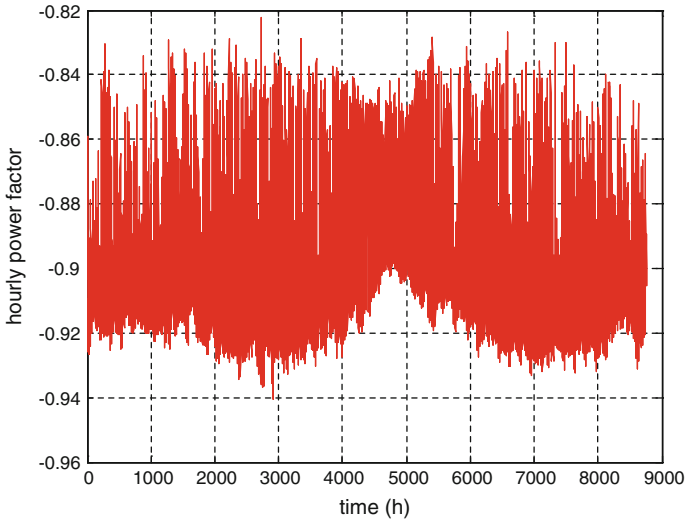**Fig. 13** MV line with 8 PV units without control

Fig. 14 Hourly power factor values in the MV line with 8 PV units connected without control
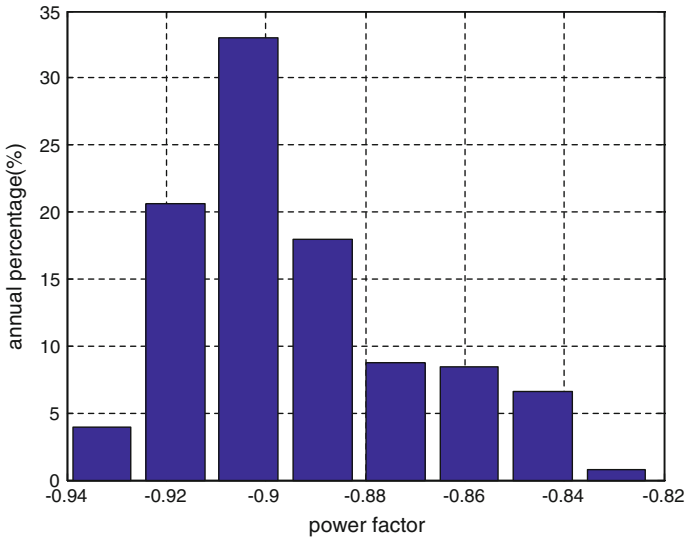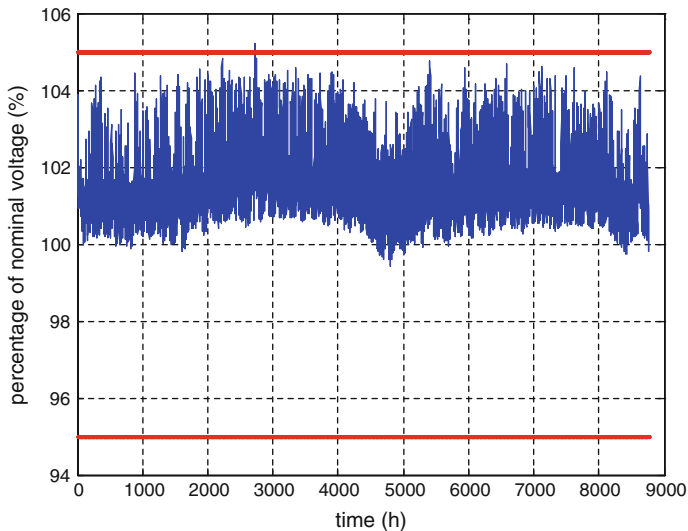

Fig. 15 Annual percentage of power factor values in the MV line with 8 PV units connected without control

Fig. 16 Voltage fluctuations at node 3 of the MV line with 8 PV units connected without control
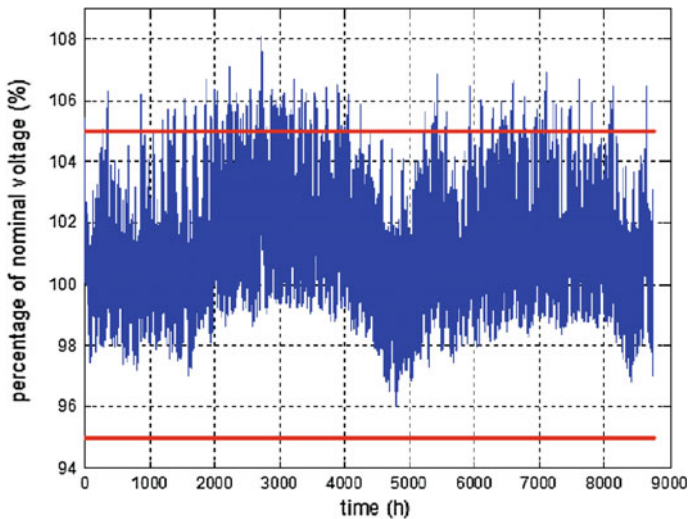
Fig. 17 Voltage fluctuations at node 6 of the MV line when 8 PV units are connected without control

Fig. 18 Voltage fluctuations at node 8 of the MV line with 8 PV units connected without control

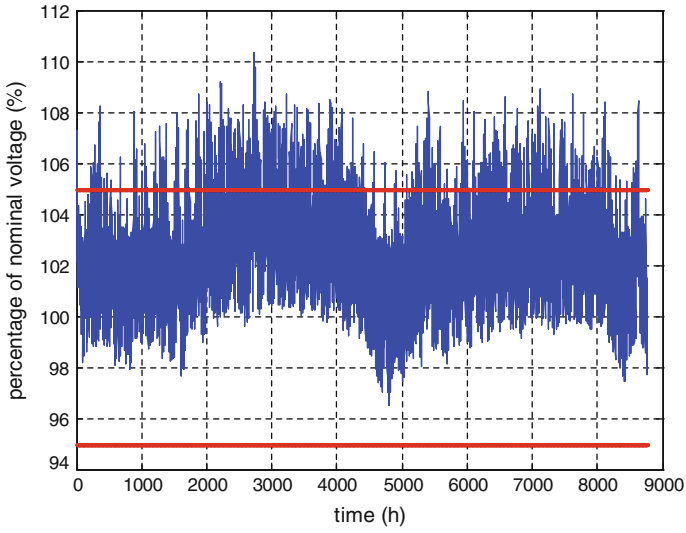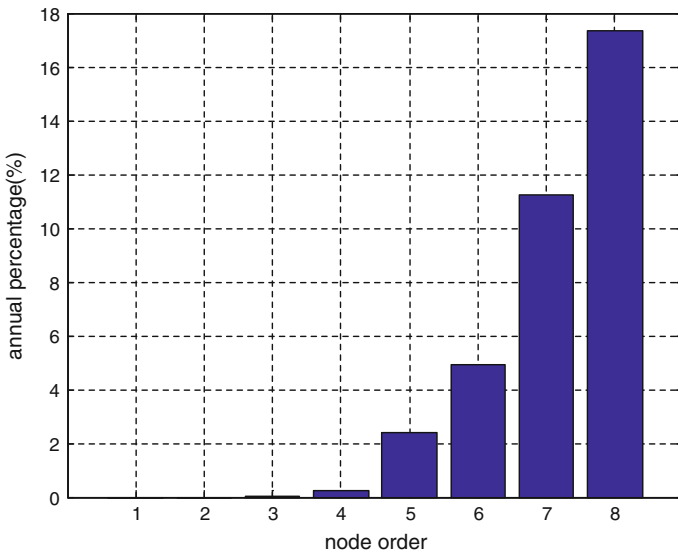**Fig. 19** Annual time percentages during which the voltage at the nodes of the MV line exceeds the specified limits with 8 PV units connected without control

The aggregate annual energy generation of the PV units is

$$E_{PV} = \sum_{t=1}^{8760} P_{PV_{total}}(t) = 6.4511 \cdot 10^3 \, MWh \tag{41}$$

whereas the corresponding annual PV utilization ratio is

$$CF = \frac{E_{PV}}{8760 \cdot N \cdot P_{PV}} = \frac{6.4511 \cdot 10^3 \, MWh}{8760 \cdot 8 \cdot 0.5 \, MW} = 18.41\,\% \tag{42}$$

5.3 Monitored and Managed MV Line with Eight PV Units Connected

Two important issues have arisen from the previous simulation scenarios. The first one concerns the power factor pf_{total} (t) at the bus, which should not, in general, deviate significantly from 1. pf_{total} (t) is variable and can be either inductive or capacitive. This depends on whether the reactive power is injected or consumed. Negative pf_{total} (t) values correspond to an overall inductive behavior of the line (the line consumes reactive power), whereas positive pf_{total} (t) values correspond to an overall capacitive behavior of the line (the line produces reactive power). The sign of pf_{total} (t) is the same to that of the total reactive power of the MV line. The second one concerns the voltage fluctuations levels at the POIs of the PVs to the MV line which should not exceed the specified limits, i.e. ±5 % in the scenarios examined.

These issues can be addressed by simultaneously regulating both the compensating power Q_C and the power factor of the PV units, pf_{PV}, which is assumed common for all of them. As Q_C increases, the aggregate reactive power at the bus is reduced and the aggregate power factor is improved, whereas the voltage at the POIs of the PV units becomes higher. To reduce such voltage variations, both Q_C and pf_{PV} should be combinedly adjusted.

The method proposed in the current chapter to deal with the above issues by properly managing the related quantities is based on information acquired from all the critical nodes of the MV segment considered, comprising, among others, the POIs of the PVs and the POI of the conventional power generator. The relevant data must be collected by the ECC. PLC is proposed as the communication technology to transfer this data between the critical nodes of the MV grid and the ECC. In this framework, DAC units are installed at these nodes, equipped with RTUs to transfer the required data. All measurements are transferred to the ECC, which, in turn, performs the computations, determines the relevant parameters and controls accordingly the nodes of the grid by transferring the relevant commands via the PLC network. A central controlling entity is expected to perform better as it monitors the MV grid status in real time and responds by accordingly controlling the operation of its critical nodes. In the indicative SG scenario examined in

Sect. 4.3, the topology is the same as the topology depicted in Fig. 13. But, in this case, a monitoring and control procedure is applied to the critical system nodes. The necessary monitoring and control data are transferred through the MV segment employing PLC. The simulation results for the aggregate power factor at the bus and the voltage fluctuations at several critical nodes of the MV grid are given in the following figures:

Figure 20 shows that the power factor at the bus of the AS ranges from 0.7512 (inductive) to 0.9404 (inductive), whereas Fig. 21 shows that pf_{total} (t) is concentrated around 0.90 (inductive) with an estimated average value 0.8906 (inductive). The simulation results plotted in Figs. 22, 23 and 24 show that the monitoring and control procedure enabled employing PLC data transfer across the MV segment leads to an almost complete confinement of the voltage fluctuations within the specified limits, in contrast to the previous operational scenario, where the PV incorporation to the MV grid was not monitored nor controlled. Figure 25 shows the annual time percentages during which the voltage at the POIs of the PVs to the MV line exceeds the specified limits.

It is readily observed from Fig. 25 that the voltage fluctuations at nodes 2, 3, 4, 5, 6 lie always within the specified limits, whereas at nodes 1, 7, 8 they are not. Comparing these simulation results with the relevant ones when neither power factor control nor voltage control were done, it is readily deduced that monitoring and control of the PV units, enabled exploiting the PLC transmission of data acquired from the critical nodes, results in a significant improvement in the operation and the performance of the MV segment considered. In fact, the voltage fluctuations at nodes 1 and 7 exceed the specified limits for a practically insignificant annual percentage and only the voltage at node 8 exhibits severe fluctuations.
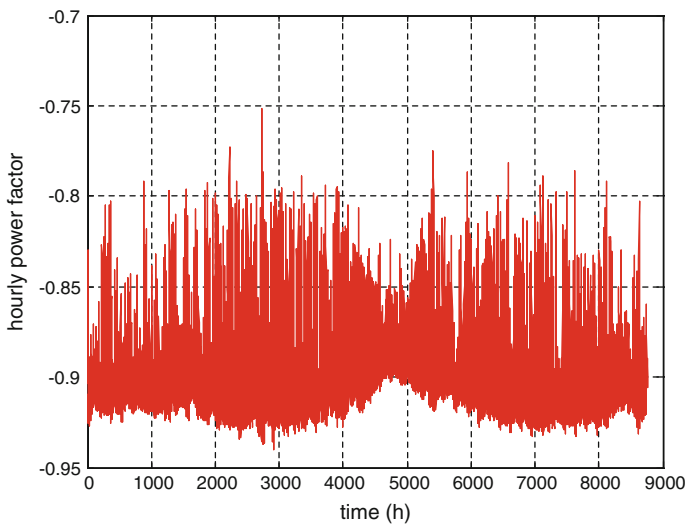
Fig. 20 Hourly power factor values in the MV line with 8 PV units connected with control
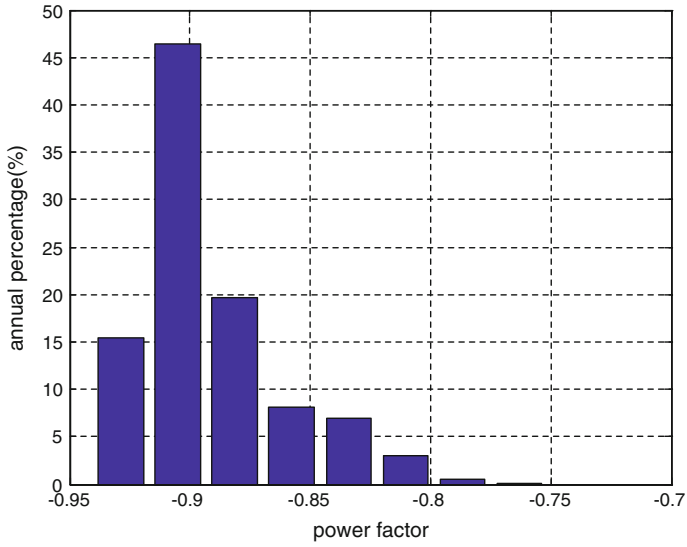
Fig. 21 Time Percentages of the power factor in the MV line with 8 PV units connected with control

Fig. 22 Voltage fluctuations at node 3 of the MV line with 8 PV units connected with control
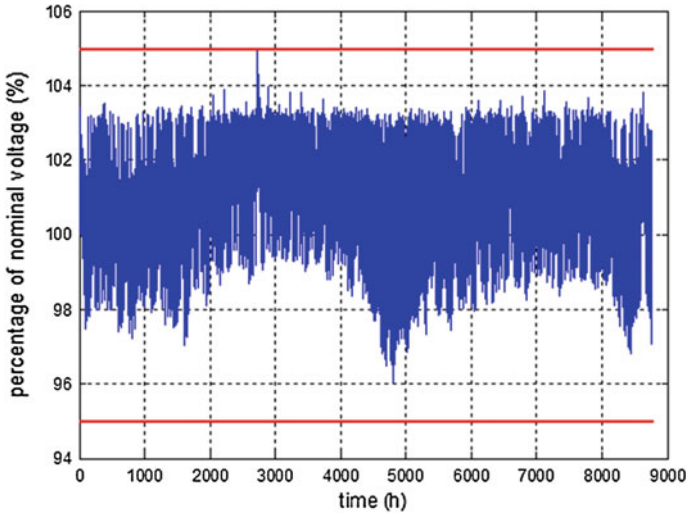
Fig. 23 Voltage fluctuations at node 6 of the MV line with 8 PV units connected with control
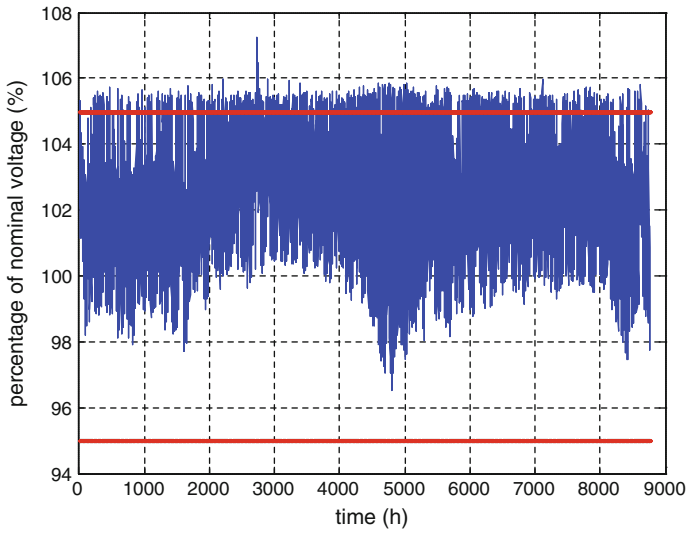
Fig. 24 Voltage fluctuations at node 8 of the MV line with 8 PV units connected with control
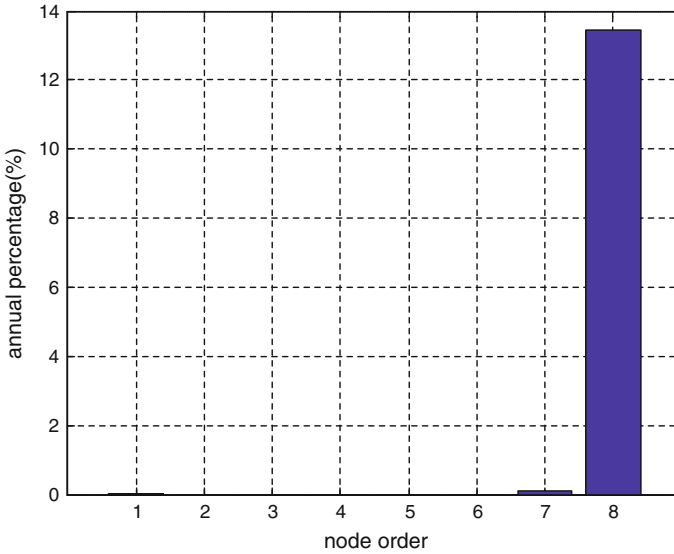
Fig. 25 Annual time percentages during which the voltage at the nodes of the MV line exceeds the specified limits with 8 PV units connected with control
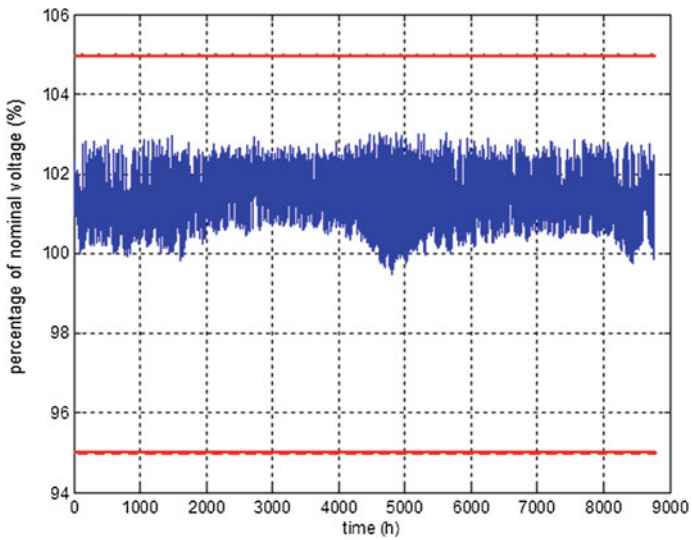
The annual PV generation under this scenario is

$$E_{PV} = \sum_{t=1}^{8760} P_{PV_{total}}(t) = 5.9415 \cdot 10^3 \, \text{MWh} \tag{43}$$

whereas the corresponding annual PV utilization ratio is

$$CF = \frac{E_{PV}}{8760 \cdot N \cdot P_{PV}} = \frac{5.9415 \cdot 10^3 \, \text{MWh}}{8760 \cdot 8 \cdot 0.5 \, \text{MW}} = 16.96\% \tag{44}$$

Both the above quantities are slightly reduced compared to the non controlled PV operation because the PV units do not operate at 100 % efficiency for certain time periods, thus reducing their output power, commanded to do so by the SG controlling mechanism.

6 Design Guidelines for the PLC Based SG Scheme to Monitor and Control the Distributed PV Units

Though any competent SGC technology could be adopted to offer the proposed monitoring and control mechanism, PLC has been chosen to move information and commands through the MV segment considered in order to monitor and control the

operation of dispersed PV units. In this framework, DACs are installed at the critical nodes, namely at the POIs of PV units and of critical loads. The RTUs that monitor the loads behavior measure the corresponding active power $P_{load}(i, t)$, reactive power $Q_{load}(i, t)$ and voltage at the relevant POIs. The RTUs employed to monitor the PV units measure the solar radiation $G(i,t)$, the ambient temperature $T_{amb}(i, t)$, the produced active power $P_{PV}(i, t)$, the reactive power $Q_{PV}(i, t)$ and the voltage V at their POIs. The relevant measurements are concentrated in the corresponding DACs, which convey them to digital data and forward them to the ECC. There the necessary calculations required to support the decision making procedures are performed. These calculations concern the aggregate power factor pf_{total} (t), the compensating power Q_C required at the bus, and the pf_{PV} at the POIs of the PV units. The updated values of pf_{PV} are sent to the DACs of the PV units. Therefore, a full duplex communication between the ECC and the dispersed DACs is required, which, in the SGC scenario adopted in the current chapter, is implemented employing PLC via the MV line. The DACs send information from the loads and the PV units to the ECC and the ECC sends the control commands to the DACs that adjust the parameters of the corresponding PV units. If convenient, the DACs may be embedded in the PLC units employed, requiring only one SG unit. For greater flexibility DACs and PLC units can be installed independently and communicate employing a short range wireless technology. This gives rise to a hybrid W-PLC communication platform.

Under steady state operating conditions, the transmission rates required for monitoring and control are low, of the order of several hundreds bps per node and of few kbps for the entire PLC network. This is because the transferred data volume is low and monitoring signals are uplinked, analyzed and presented at the ECC at a low operational frequency. The data volume in the specific SG application is low since there is no need for broadband data transmission. Moreover, the relevant packet transmission delay does not create any problems.

On the other hand, when transient phenomena occur, such as short circuits or disconnection—connection events of either PV units or loads, etc., the nodes must be continuously monitored by the SGC network, so that the power system can adapt to the new conditions. The transmission rates can be higher than the previous ones, because they must adapt to a more frequent transmission of data necessary for proper monitoring. Moreover, the volume of data becomes higher than in the steady state. In the downlink transmission the situation may be substantially differentiated compared to steady state operation (e.g. exchange data with the critical nodes more frequently), while, in this case, it is critical to keep the round trip delay low to avoid congestion phenomena and keep the SGC network availability at high levels.

To determine the various communication characteristics of the SGC network, it should be taken into account that the following measurements are required at each node:

- Active power
- Reactive power
- Output voltage
- Output current

Because, in general, the MV grid is a three-phase power network, every measurement produces $3 \times 4 = 12$ numerical values. If 5 bytes are required to represent each numerical value with acceptable accuracy, 60 bytes per measurement are required. Assuming that, due to the small packet size, the network layer introduces a 100 % overhead, the overall traffic created per measurement is 120 bytes. Assuming additional overhead due to encryption, error-control and data link layer operation, the total traffic created per measurement is of the order of few hundred bytes. Assuming a sampling rate of the order of one measurement every 15 min, a 1–3 Kbps link can reasonably transfer that kind of information to the ECC in less than 1 s, which is a delay acceptable for applications such as the connection of PV units to the MV power grid. It should be noted that the computations required at the ECC by the control mechanism may take tens of seconds to complete. In the worst operational scenario, that is when all the PLC nodes send their data simultaneously to the ECC, an MV line, comprising 5–15 nodes, requires a PLC transmission link with capacity ranging from 10 to 30 Kbps. Such simultaneous node communication with the ECC is needed when all the nodes exceed the specified operational limits and the ECC must apply the control procedure to all of them. The latter analysis concerns the uplink.

The most critical requirement from an SG monitoring and control scheme is to ensure high availability. In Fig. 18 the most severely affected node, namely node 8, in the absence of control, exceeds the specified limits for approximately 18 % of time on an annual basis. This exceedance is significantly reduced, becoming approximately 13 %, due to the employment of SG. Similarly, the deviation from the specified limits concerning the operation of the other affected nodes, namely node 4, 5, 6 and 7, is almost fully compensated by the SG employment

7   Conclusions

The present chapter presents a generic framework to assess the benefits of introducing smart grid PLC technologies for the incorporation of PV generation units in the autonomous system of an island. In the study case analyzed it is assumed that the main MV line of the island under consideration is fed by more PV units than it can support without control. If such a system is enhanced by PV power generation without been enhanced by an SG mechanism to monitor and control the distributedly connected PV units, serious problems may arise affecting the operation of the entire power network. Since, the most critical requirement from a SG monitoring and

control scheme is to ensure high availability, the present study confirms that PLC enabled smart grid can enhance both the availability of the main MV line and the penetration of PV generation into the autonomous system of an island.

References

1. Kumar, R.; Ray, P.D.; Reed, C. Smart Grid: An Electricity Market Perspective. In Proceedings of IEEE Power and Energy Society (PES) Conference on Innovative Smart Grid Technologies (ISGT 2011), Anaheim, CA, USA, 17–19 January 2011.
2. Fang, X.; Misra, S.; Xue, G.; Yang, D. Smart Grid—The New and Improved Power Grid: A Survey. IEEE Commun. Surv. Tutor. 2012, 14, 944–980.
3. Livieratos, S.; Vogiatzaki, V.E.; Cottis, P.; A generic framework for the evaluation of the benefits expected from the Smart Grid, Energies 2013, 6, 988-1008; doi:10.3390/en6020988.
4. Sarafi, A.M.; Tsiropoulos, G.I.; Cottis, P.G. Hybrid Wireless-Broadband over Power Lines: A Promising Broadband Solution in Rural Areas. IEEE Commun. Mag. 2009, 47, 140–147.
5. Willis, H.L.;Power Distribution Planning Reference Book 2nd edition, Marcel Dekker, ISBN 0-8247-4875-1, 2004.
6. Chowdhury, S.; Chowdhury, S.P.; Crossley, P.; Microgrids and Active Distribution Networks, ISBN 978-1-84919-014-5, Institution of Engineering and Technology, London, UK, 2009.
7. L'Abbate, A.; Fulli, A.; Starr, F,; Peteves, S.; Distributed Power Generation in Europe: technical issues for further integration, ISBN 978-92-79-08222-1, JRC Scientific and Technical Report, 2008.
8. www.rae.gr.
9. Schwabe, U.K.W.; Jansson, P.; Streamlining large scale photovoltaic arrays for utility interconnection, Power Tech, 2009, IEEE Budapest.
10. Kundur, P., 1994. Power System Stability and Control. USA: McGraw-Hill, Inc.
11. Papathanassiou, S. A., 2007. A Technical Evaluation Framework for the Connection of DG to the Distribution Network, Electric Power Systems Research, 77(1), pp. 24-34.
12. http://www.admie.gr/en.
13. Bergen, A. R. & Vittal, V., 2000. Power System Analysis. 2nd ed. New Jersey: Prentice Hall.
14. Papathanassiou, S. & Boulaxis, N., 2006. Power limitations and energy yield evaluation for wind farms operating in island systems, Renewable Energy, 31(4), pp. 457-479.

The Correlation Between Renewable Generation and Electricity Demand: A Case Study of Portugal

P.J.F. Torres, L. Ekonomou and P. Karampelas

Abstract This chapter identifies the correlation between renewable electricity generation and electricity demand using as a case study Portugal. It presents the Portuguese current electric system, the installed generation capacity, and the electricity demand pattern for the year 2012. It also presents the 2020 national strategy for this sector, namely the Renewables Plan of Action, its targets and challenges. It focuses on the three main natural resources that exist in the country and describes their technology as well as the technical challenges for the integration of renewable generation in the electric system. Through this study the effectiveness of hydro, solar and wind power to meet electricity demand in Portugal is investigated. Statistical data regarding the seasonal and daily availability of the three main resources, relating them with the electricity generated from those sources and their correspondent capacity factors are presented. In addition, comparative analyses are performed between the electricity demand curve, both seasonal and daily, and statistical data related to the electricity generation from the renewable sources using both the Pearson product-moment correlation coefficient and graphical illustrations. The results obtained confirm a correlation between the renewables availability, namely, hydro and wind power, and electricity demand during a typical year. They also suggest no correlation between demand and a solar/wind combination during a 24-h period, however, they reveal a complementarity between solar and wind power availability during a typical day, highlighting the need and advantages of energy

P.J.F. Torres (✉) · L. Ekonomou
City University London, Northampton Square, London EC1V 0HB, UK
e-mail: paulo.torres.1@city.ac.uk

L. Ekonomou
e-mail: lambros.ekonomou.1@city.ac.uk

P. Karampelas
Department of Informatics and Computers, Hellenic Air Force Academy,
Dekelia Air Base, Dekelia, Greece
e-mail: pkarampelas.hafa@haf.gr

storage systems and "smart grid" technologies, to adjust electricity generation curves to demand load curves. The authors strongly believe that this study can be useful to the development of national strategies for the modern electric power systems.

1 Introduction

The development of sustainable systems to address the world energy needs has gone up in the agenda in the past few decades. The causes for this rise were several, and can be separated in three different dimensions as suggested by World Energy Council in its understanding of a Sustainable future: Energy Security, Social Equity and Environmental Impact Mitigation. The fact that a large share of the world's fossil resources is concentrated in political instable countries, its inevitable scarcity in the long-term and the expected increase in world's population (specially in emerging countries) and subsequent energy consumption poses as a security challenge for governments to deal with. The second dimension refers to the level of uncertainty concerning the affordability of these resources, i.e., the volatility of fossil fuel prices. The circumstances following the oil crisis in 1973 or more recently in 2008, when crude oil prices reached a maximum record, showed how vulnerable, and dependable, economies across the world are from these resources. In 2010, 81.1 % of the primary energy supply came from fossil fuels, and several studies indicate a close correlation between GDP and energy consumption [1]. Concerning the environmental impacts from burning fossil fuels, they are well studied and identified. In some cases, such as 'acid rains' or pollutants emissions from transport and power sector, improved technology has helped mitigating part of the impacts, but still far from addressing all. In addition, Global Warming has highlighted concerns regarding GHG emissions and all the potential consequences associated with a climate change. Whether one consider it as a scientific certainty (some would argue inevitability) or not, the fact is that it has driven governments and policy makers around the world and is having a fundamental impact in society, namely the Kyoto Protocol to the United Nations Framework Convention on Climate Change in 1997, which is currently in the second phase (2012–2020) and more recently the European Directive "20-20-20" with binding implications at national level (EU countries).

The shift from fossil fuels to alternative resources, particularly renewable sources, is widely seen as the most sustainable and effective way to address future energy needs. On one hand, they are abundant at a global scale, do not have fuel costs associated and have reduced environmental impacts (even taking into consideration the entire life-cycle of the systems), on the other hand, they are extremely location specific and, both technology and its market are still under development, making them financially less attractive for investors without support mechanisms. The Electric Power Sector, as one of the most carbon intensive sectors, has been the object of several policies in order to increase the penetration of renewable sources

in the electric systems. In 2010, the share of electricity in total primary energy consumption was 17.7 %, from which 67.4 % was generated from fossil fuels and only 19.7 % from renewables (16 % from Hydro and 3.7 % from the remaining) [1]. Portugal in particular, does not have any noteworthy fossil fuels resources, however, it possesses significant renewable resources and has clearly invested in its harnessing in recent years. In 2012, the share of renewable electricity was 37 % [2], but it has the ambition of generating 60 % of the electricity from renewable sources by 2020. According to the National Energy Strategy, the main contributors to achieve this target will be Hydro, Wind and Solar Power. Besides location and cost, there are other aspects to have into consideration such as the limitations associated with renewable electricity generation, especially when dealing with high shares of penetration. The variability and intermittency of wind and solar resources poses as a risk/challenge to the management of electric systems. In order to reduce that risk, new strategies and new investment in ancillary services infrastructure is fundamental. On the other hand, Renewable Energy development in Portugal is expected to have other beneficial impacts such as creating jobs, internationalizing Portuguese companies within the sector and attract foreign investment, thus contributing for the growth of national economy.

The present work characterizes the current power sector in Portugal together with future prospects and targets concerning renewable electricity generation. It also reviews the three renewable technologies that will have the most impact in the Portuguese Electricity Mix 2020, Hydro, Wind and Solar Power, and describes the main issues regarding the integration of large shares of renewable energy in the electric system. Section 3 presents a case study where the availability of these three resources is studied and correlated with the electricity demand. The objective of this study is to investigate the effectiveness that these three resources have to supply electricity in Portugal, taking into consideration two main aspects: the seasonal and daily availability of these resources and the typical demand load curve in Portugal. In addition, this study aims to explore signs of complementarity between these sources individually or in combination with other technologies, which will allow a better management of the grid. Ultimately, this study seeks to find options to adjust the load curve of electricity production from renewable sources to electricity demand in Portugal. The results of this study intend to provide a closer knowledge regarding the patterns of renewable electricity generation in Portugal and identify optimized solutions towards a sustainable electric system in Portugal.

2 Related Work

There have been several studies investigating the penetration of Renewables in electricity grids, namely the relation between Renewable resources and Peak Demand, in particular from Wind and Solar power given their variability and intermittency. Esteban et al. [3] proposed a method to estimate the electricity output from a dual solar-wind renewable energy system in Japan by analysing the true

minimum capacity factor that can be expected from such a system, using an historical hourly estimation of the electricity produced by a given solar-wind generating mix. Hoicka and Rowlands [4] suggested that integrating wind and solar power in Ontario's electricity grid could smooth out electricity generation by levelling high and low values. In addition, increasing the number of locations of power generation from these sources results in less variability, however the study did not consider the correlation between wind and solar resources and electricity load demand. Jong et al. [5] analyse the effectiveness of wind power and solar power to supply electricity to the grid during peak demand periods in that region, by comparing the electricity load curve for a typical year and day with statistical data from wind and solar resources. In Portugal, some studies have been carried out to analyse the impacts of renewables penetration in the electricity system. Moura and Almeida [6] studied the correlation between wind, solar and hydro resources in Portugal through their capacity factors and presents a model to reduce peak demand by introducing large-scale demand-side management and demand response technologies. Pina et al. [7] present a model framework capable of optimizing the future investment in Renewable generation taking into consideration supply and demand dynamics in Portugal during the period of 2005–2050. The results demonstrate that by using that model framework, it is possible to avoid overinvestment in infrastructure and reduce the surplus of electricity generated by renewables that cannot be used by the system. Suomalainen et al. [8] conduct an analysis where the energy systems of two islands in Azores, Portugal, are simulated using a new method involving synthetic wind speed scenarios. The results show that the location of the wind turbines should be decided based on where the wind speed patterns better match demand, instead of selecting the location with the highest mean wind speed. Jerez et al. [9] present a methodology to identify ideal locations for solar and wind power. This study takes into consideration the efficiency and stability conditions necessary to counteract the natural variability and intermittency of these resources. Krajacic et al. [10] perform a study where it is presented a potential scenario for a fully renewable electrical system in Portugal, including planning and technical solutions. The analysis is based on the H2RES software model, with special focus on intermittent sources such as wind, solar and wave power.

Despite the fact of several solutions being presented in the above analyses, these studies do not take into consideration the national targets for 2020, and the weight that each technology will have in the electricity system in 2020 according to the Government National Action Plan. Instead, they provide solutions for potential optimized scenarios.

3 Electric Sector in Portugal

3.1 Evolution and Legal Framework

In 1975, due to a change in Portugal's political regime, the electric sector was nationalized. Public institutions were formed to deliver electricity across the whole territory, which lasted until the 90s. Based on the EU Directive 96/92/CE, Portugal initiated, in 1995, the liberalization process of the sector and the partial privatization of EDP (Electricity of Portugal) by redesigning the existing structure, which resulted on the coexistence of two systems: The electric system for public service, SEP (regulated) and the independent electric system, SEVN (liberalized). In this phase, the liberalized market was only for clients with higher consumptions and higher voltage levels. In addition, an independent institution was also created to regulate the electric sector, the Energy Services Regulatory Authority (ERSE).

In 2003, new directives were published to arrange the global liberalization process and inspire a joint market between Portugal and Spain (MIBEL). Competitiveness framework for the market was finally introduced, which established the 1st of July 2007 as the deadline to extend free choice of supplier to all consumers. This new integrated system included the production and supply activities, which were carried out under an open and free competition market, while the transmission and distribution activities, which were also conducted by private companies, were awarded through public service concessions by the state, to avoid duplication of networks and consequent costs [11].

3.2 Current Situation

3.2.1 Generation

Electricity production in Portugal is divided in two areas: Ordinary Status Producers (PRO), which includes production based in conventional fuels and large hydro-electric power stations, and Special Status Producers (PRE), which involves co-generation and electricity production from renewable sources. This activity operates under a liberalized and competitive market and it is open to any investor, which, through a pure market-based logic, should result in the optimization of the system and subsequent costs reduction.

Regarding the state, it preserves two main responsibilities: creating favourable conditions for the electricity market functioning and supressing market failures concerning electricity demand by monitoring closely the electric sector and intervening whenever necessary making sure that demand is met, e.g., public concessions. Producers can sell electricity to final consumers, through bilateral contracts, to licensed suppliers, through organized electricity markets such as MIBEL or, in a smaller scale, to the system operator (ancillary services necessary to maintain the

system operational). Besides these options, producers in the special regime (PRE) can also sell their electricity to the Last Resource Suppliers (CUR), which exist to guarantee that supply of electricity is available to all consumers, especially vulnerable ones. These suppliers are subject to regulation with fixed tariffs and are expected to exist until the electricity market reaches a certain state of maturation.

Finally, it is also important to refer that in order to mitigate environmental impacts from the electric sector and to meet the European targets for 2020, there are financial support mechanisms for electricity production from renewable sources, which have been the main driver for the increase of this type of generation in the past years and will be addressed later in this chapter [12].

3.2.2   Transmission

National Electric Network (REN) has the concession, in a public service regime, to explore the National Transport Network (RNT) in Portugal, which is responsible for the transmission of electricity from large power stations to the distribution network, or, in some cases, directly to large consumers due to economic and technical advantages.

This High Voltage network is also interconnected with Spain allowing electricity exchanges between both countries, which besides increasing safety and security to the operation, has the potential to result in economic benefits by promoting competition between a wider range of producers (MIBEL). REN is also responsible for the global management of the system with focus in the coordination of all infrastructures and in providing ancillary services to ensure an optimal operation of the system [13].

3.2.3   Distribution

Distribution networks, which operate at Medium and Low Voltages, transport electricity from sub-stations to the point of use, i.e., final consumers. EDP Distribution has the concession, also in a public service regime, to explore the National Distribution Network (RDT) in Portugal and their main responsibilities are the operation, maintenance and up-grade of the network ensuring safety, reliability and their efficient connection with other networks.

The recent increase of PRE's also contributes for the overall importance of these networks, since most of their production is directly connected to the distribution networks, adding reliability and safety issues to the operation. Is therefore important to monitor and control the electricity flow in the grid and ensure that PRE's have adequate connections to the network [12].

3.2.4 Supply

Suppliers are, for the majority of consumers, who presents them with the final electricity bill, which includes electricity production costs, costs associated with the several services provided by the electric sector (transmission and distribution charges), support mechanisms for PRE's, and government taxes (VAT and environmental taxes).

Suppliers' role is to buy electricity, either directly from producers or through organized markets such as MIBEL, and then sell it to the final consumers in the retail market. MIBEL, the Iberian wholesale electricity market, consists of two organized markets: the Spot Market with daily transactions and intraday adjustments, and the Futures Market for long-term contracts (Forward/Derivatives).

Concerning consumer options and protection, there are seven licensed suppliers currently operating in Portugal, and switching supplier is facilitated through legislation and based on the market principles with no extra cost to the consumer. In addition, Last Resource Suppliers (CUR), which work under a regulated framework, ensure supply of electricity to all consumers [14].

3.2.5 Regulation

Energy Services Regulatory Authority is the independent regulator that is responsible for the electric sector. The main responsibilities are: to protect the consumer's interests, especially the most vulnerable, in terms of electricity price, service quality, access to information and security of supply; promote competition between the several stakeholders acting in the electricity markets; contribute for a gradual improvement of economical and environmental conditions in the electric sector; and arbitrate and settle potential disputes between stakeholders [14].

3.3 National Energy Strategy 2020

Electricity consumption in 2012 was 49.1 TWh, which represented a decrease when compared with 2011 (53.1 TWh) and 2010 (55.0 TWh) [2]. Analysing demand in 2012 is useful to understand the future system since recent projections to 2020 indicate no substantial growth in the consumption rate, estimating to reach 52.0 TWh in 2020, making this year a fair baseline year [15]. Figure 1 shows total electricity consumption by fuel, indicating that 37 % of the consumption was supplied by renewable sources.

From Fig. 1 it is also possible to extrapolate unfavourable hydrologic conditions since 2010 by analysing the decline in generation from Hydro, which was mainly filled by coal-fired generation and imports.
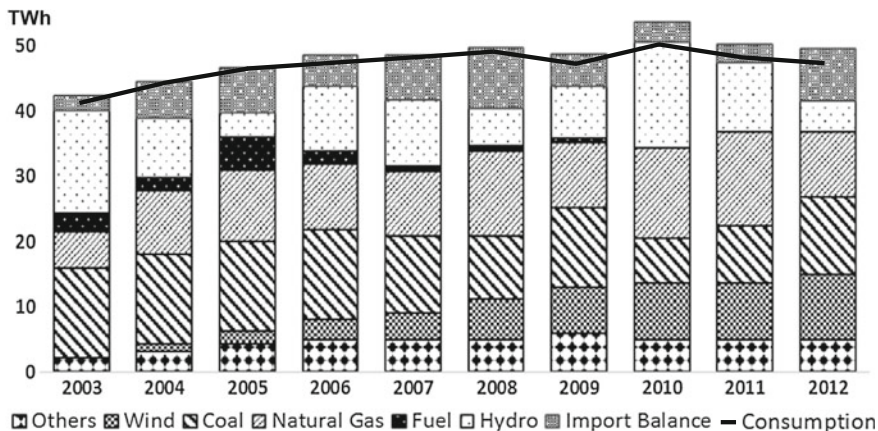
Fig. 1 Evolution of consumption in Portugal by fuel type [2]
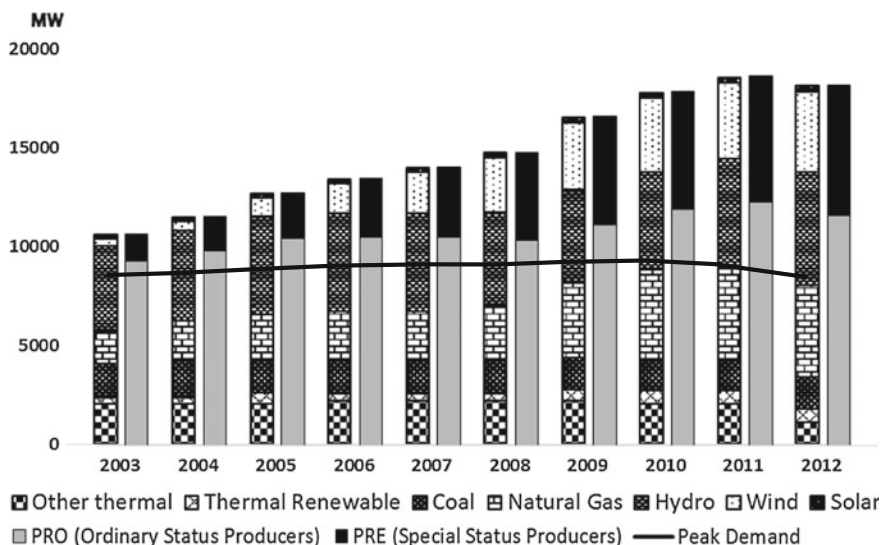
Fig. 2 Evolution of installed capacity and peak load in Portugal by fuel type [2]

Concerning peak power demand in 2012, it reached 8531 MW in February, with an annual average of 7445 MW, which has also been decreasing since 2010. Figure 2 indicates the installed capacity evolution in the last 10 years reaching to 18.546 MW in 2012 [2]. It is also interesting to see the relation between the total installed capacity evolution and the increase of Special Status Producers, which correspond mainly to capacity from renewable sources (does not include large Hydroelectric, >10 MW). There has been a substantial increase in the installed

Table 1 Solar-photovoltaic capacity factor from 2007 to 2012 in Portugal

	Installed capacity 2012 (MW)	Installed capacity 2011 (MW)	Increase (MW)	Production estimate 2020 (GWh)
Annual generation (GWh)	331	250	172	21
Average installed capacity (MW)	186	137	99	6
Capacity factor (%)	20	21	20	44

capacity to address a relatively low increase in peak demand, highlighting some of the issues involving the renewable sources, i.e., its variability and intermittency.

European Commission has defined the Portuguese targets according to the "20-20-20" European global target, which varies from country to country. Portugal is expected to reduce the primary energy consumption by 25 % through energy efficiency measures, and to have 31 % of the primary energy consumption from renewable sources and a sub-target concerning energy used for transport, which should be 10 %. In order to deliver both targets, the government introduced two programs: National Action Plan for Energy Efficiency (PNAEE) and the National Action Plan for Renewable Energy (PNAER), which have already been made legally binding.

For the electric sector, Portugal is being more ambitious setting a target of 60 % of electricity consumption from renewable sources, against the 55 % required by the European targets [16]. In order to meet this target, substantial investment is needed, which might be an obstacle given the current economical circumstances. Nevertheless, besides the investment issue, it is also important to address the availability of the natural resources in Portugal.

Table 1 shows the proposed increase of installed capacity and projected production of electricity from each type of generation [16].

From Table 1, it is possible to conclude that Portugal is hoping to meet its targets by investing mainly in three areas: Solar Power, Wind Power and Hydroelectricity.

Solar Power plays an important role in the Portuguese National Energy Strategy. The two main features of this type of Renewable energy are: the suitable resource availability in Portugal and the opportunity to decentralize electricity production thus reducing energy losses.

The expected photovoltaic installed capacity in 2020 is 1039 MW and a potential investment in 50 MW of concentrated solar, subject to developments in demonstrating the economic viability of the technology. In addiction, the R&D conditions in Portugal are excellent with some interesting initiatives such as Serpa Solar Power Plant (11 MW) or Moura Photovoltaic Power Plant (46 MW), which was at the time of commissioning (2008) the world's largest photovoltaic power plant.

Concerning Wind Power, Portugal has substantially increased the installed capacity in the last decade, from 1063 MW in 2005 to 4409 MW in 2012 [13]. By 2020, it is expected to reach to 5300 MW, from which 5273 MW is onshore generation [16]. This focus on Wind Power is part of an integrated plan to take

Table 2 Evolution of total and reversible installed capacity of hydroelectric power plants

	Installed capacity 2005 (MW)	Installed capacity 2012 (MW)	Production estimate 2020 (GWh)
Hydroelectric (total)	4816	5337	8940
Hydroelectric (reversible)	537	1088	4004

advantage of the potential complementarity between Pumped Storage Systems and Wind Power, which results in higher harnessing of wind resources and better management of the electric system. In the case of offshore generation, it is still dependant of technological development regarding deep waters. Portugal is currently testing a 2 MW turbine prototype supported by a floating structure.

Hydroelectric power stations have been an essential part of the Portuguese electric sector since early times, however, still far from reaching the entire existing potential. In 2012, the installed capacity in Portugal was 5337 MW, representing only 50 % of its potential [17]. According to the PNAER, it is expected to reach to 80 % of its potential by 2020. The other fundamental characteristic of this type of infrastructures is the possibility to integrate reversible capacity to pump water upstream and working also as an energy storage system. Table 2 shows the evolution of the reversible capacity in Hydroelectric Power Plants in Portugal [16].

Generating electricity from renewable sources in Portugal is supported by a feed-in-tariff's mechanism, meaning that producers receive a payment for each unit of electricity generated and exported to the grid, which is guaranteed by law. The payment rate is based on several factors such as the type of technology, electricity output and installed capacity, and is calculated through a complex formula. The eligible technologies are Wind, Solar, Geothermal, Hydropower and Biomass (includes Biogas), with each one having a different coefficient Z, which is defined by the government. There are also limitations regarding the duration of the contract:

- Wind energy: 15 years or until 33 GWh of electricity generated.
- Solar energy (photovoltaic): 15 years or until 21 GWh of electricity generated.
- Geothermal energy: 12 years.
- Biogas: 15 years.
- Biomass: 25 years.
- Hydro-electricity: 25 years.
- Wave energy: 15 years.

Concerning the costs associated with renewable generation, the grid operator makes the payment to the producer at an initial stage, which is then passed to final consumers through the electricity bill, according to legislation [18].

Besides this supporting mechanism, which includes all PRE's, certain specific areas need to be addressed for each type of technology in order to help Portugal

meeting the proposed European targets for 2020. These areas were identified by APREN, the Renewable Energy Association that represents Renewable Energy Producers in Portugal [19].

Regarding Solar power, the solar resource should be better characterized, especially by creating conditions to measure the direct radiation that is essential for solar thermal and concentrated solar. The lack of information regarding this resource constrains the future development of these technologies in the market. Also, the licensing process and the financial mechanisms for small-scale generation should be reviewed and simplified in order to increase the uptake of these technologies not only by the industrial and commercial sector, but also across homes in Portugal. It is seen as one way to decentralize electricity production (connected directly to distribution network), with clear benefits associated with less electricity losses and a potential reduction of investment in up-grading the existing transmission network.

Wind power faces larger challenges, since it has had a much higher penetration in the electric sector (it is expected to supply approximately a quarter of electricity consumption in 2020). Currently with 4407 MW of on-shore installed capacity, suitable locations concerning the availability of wind resource start to run short. There are two main solutions, either government starts allowing the installation of wind turbines in areas environmentally sensitive or even protected, or investment in offshore generation should be stimulated through specific mechanisms. Additionally, with such higher contribution, conditions should be provided to initiate the transition for Wind Power to be included in the electricity market. In Spain, producers have the option of either having a fixed tariff, or through a market regime combining the market price with a fixed price. United Kingdom is also planning to introduce the same principle through the Contracts for Difference (Electricity Market Reform). Finally, managing the network is also a huge challenge due to the high contribution of wind power to the electric sector. New infrastructure to support ancillary services should be provided to address the variability and intermittency associated with this resource.

The main advantage associated with Hydroelectricity and Pumped Storage systems is its complementarity with Wind power during low demand hours. With the estimated increase of renewables in the electric sector, it is vital to address this type of energy storage systems if Portugal wants to take full advantage of these resources.

3.4 Integration of Renewables into the Electric System

When increasing the renewable installed capacity for electricity generation, it is also imperative to study, develop and if necessary re-design the electricity system to cope with the specific aspects of this type of energy. High shares of renewables in the electric system result in four types of challenges: transmission requirements, distributed generation, variability and intermittency.

Electricity generation from Solar Photovoltaic and Wind Power represent major issues of potential disturbance in the electricity grid during their normal operation conditions. Since wind and sunlight availability are not under human control, integrating the electricity generated from these resources into the grid implicates managing other controllable types of generation such as Reservoir Hydroelectric plants, Pumped Storage Systems, or conventional thermal generation. These operations, which must have very low time response (second-to-minute basis), include developing new dispatch strategies for ramp mitigation (up or down), load management, ancillary services for frequency and voltage control, up-grade transmission and distribution networks, development of energy storage technologies and inclusion of advanced weather and resource forecasts in the dispatch planning operations [20].

3.4.1 Transmission Requirements

Renewable electricity generation requires a long-term planning. One important aspect is the transmission network, which must be adapted accordingly to the needs. Wind and Solar power plants are often located in remote locations far from high demand centres, such as off-shore wind, on-shore wind in mountains or solar plants in desert areas, meaning that development of new transmission lines to transport the electricity generated to points of use is essential to their integration.

Transmission planning is a complex process, since it tends to be influenced by regional politics. The possibility for a transmission line to transport electricity that was produced in one country/state, passed through another country/state, to be consumed in a third country/state makes planning a very sensitive matter, in particular to land expropriation and costs allocation.

In addition, since these new transmission lines will mainly transport electricity generated from renewable sources, characterized by being variable and intermittent, technical issues must be taken into account concerning the selection of the transmission technology to use.

3.4.2 Distributed Generation

Most of the small-scale renewable energy systems are connected directly to the distribution network. This type of generation is categorised as distributed or embedded generation and includes systems ranging from photovoltaic panels or wind turbines in buildings, which have minimal installed capacity, to plants up to 50 MW of installed capacity such as small-scale Combined Heat and Power (CHP), Wind Farms or Solar-Photovoltaic Power plants. The expected increase of this type of generation affects the vertical distribution of electricity within the grid infrastructure, i.e., instead of electricity being generated in large power plants and transported via transmission network to the distribution network and subsequently to the point of use with only one directional flow, this generation is delivered

directly to the distribution network, causing bidirectional flows disturbances, which this network is not prepared to manage since initial design did not anticipated such variations [21].

3.4.3 Variability

Wind and Solar resources variability represent the short-term variations in generating electricity from these resources, i.e., the fact that their output is not constant, which can happen because a cloud passes over a photovoltaic power plant, the wind speed drops instantly, or other similar circumstances. These situations entail particular challenges to the grid operator regarding the reliability and security of the electric system.

Grid operators must provide ancillary services to mitigate fluctuations in frequency and voltage on the network. In order to do so, operators instruct generators to inject either active or reactive power into the grid. These power injections are usually made by hydroelectric power plants or conventional thermal power plants, which results in increased wear of the equipment and higher fuel consumption for the latter. The typical ancillary services include [20]:

- Back-up and reserve capacity. Power plants that can start or stop generation within maximum 30 min (e.g. Reservoir Hydroelectric plants, Pumped Storage Systems, Conventional Thermal power plants).
- Spinning reserve. Plants that allow a prompt response for unforeseen demand variations since they can increase or decrease electricity output in a matter of seconds (e.g. Reservoir Hydroelectric plants, Pumped Storage Systems).
- Black start capability. The ability of initiating operation in a power plant without relying on the external electric network is called black start. Hydroelectric plants are usually responsible for restoring the entire network in case of complete power cut or failure.
- Regulation and frequency response. Through a continuous control and modulation of active power, plants help supporting momentarily fluctuations in load (e.g. Reservoir Hydroelectric plants, Pumped Storage Systems, Conventional Thermal power plants).
- Reactive Power compensation and voltage support. Plants that help to control reactive power, ensuring that power flows from generation to point of use, and maintaining voltage through injecting or absorbing reactive power (e.g. Reservoir Hydroelectric plants, Pumped Storage Systems, Conventional Thermal power plants).

In addition, grid operators, through close and moment-to-moment monitoring, must ensure that generation matches consumption at all times, which becomes particularly critical during times of substantial variation in demand such as early morning, when people start working, or evening, when people arrive home from work.

The provision of these services is not new, in fact, since the establishment of electricity networks that grid operators adjust frequency and voltage levels in the grid. This is because even generation from conventional and controllable plants is variable and cannot act as planned all the time. Also, electricity demand at all times is impossible to predict with 100 % certainty.

Nevertheless, high penetrations of wind and solar generation substantially increase the variability in the system, which grid operators are not used to manage at this scale, so ancillary services must be strengthen, both at the device level as at the grid operations level. Situations such as when demand variations coincide with unexpected weather conditions that affect the power output from solar and wind generation must be considered.

3.4.4 Intermittency

Intermittency, also called uncertainty, differs from variability concerning the time scale to which they refer. Intermittency relates with the hourly or daily availability of the resources, which despite of the advanced forecasting methods used nowadays, there will always be a degree of uncertainty associated. This uncertainty affects how grid operators manage the system, which is through a process called 'unit commitment' consisting in scheduling the generation of the day ahead, just a few hours in advance. When actual generation does not meet demand, the grid operator must balance the difference with reserve capacity (stand-by), which represents extra costs to the consumers. The increase of electricity generation from intermittent resources also increases the total reserve capacity necessary to cope with an eventual shift in weather conditions, thus adding cost to the process.

The 'unit commitment' process also involves estimating the necessary reserve capacity, which becomes more difficult if dealing with stochastic generation, i.e. whose output is partial uncertain and uncontrollable. The advanced forecasting methods used nowadays to predict weather conditions (wind speed and sunshine intensity) help grid operators to schedule and dispatch resources in advance, and to constantly adjust the scheduled plan, thus optimizing the available resources. Several 'advanced unit commitment methods' are used to support the grid operator in this process, which can be classified into either heuristic (computer aided empirical methods where decisions are made accordingly to a pre-defined priority list) or mathematical programming methods (more rigorous optimization-based scheduling programmes) that includes both economical and technical parameters in the decision process [22]. The outcome should be to provide the most cost-effective solution and at the same time, sufficient flexibility to the system, so that renewable resources integration neither increases the system unreliability nor an excessive reserve capacity.

3.4.5 'Smart Grid' Technologies

'Smart Grid' is a term used to describe a planned electrical network that uses information and communications technologies to operate and manage an electricity grid. It analyses supply and consumption patterns and acts in accordance, and it is not just one technology, instead it consists in a series of technologies working together to improve efficiency, reliability and security in the grid operation [23].

Nowadays, most of the systems rely on coal and gas fired power stations to balance supply and demand, however, as we move towards a low carbon future, these plants tend to be replaced by Renewable generation. 'Smart Grid' technologies will play a fundamental role in accommodating high levels of renewable generation, by mitigating the effects of variability and intermittency. This integration will rely on three main areas of 'Smart Grid' technologies: storage technology, demand side management and enhanced grid communications systems [24].

Since Renewable generation is intermittent, it is natural for periods of high production and low demand to take place. In order to take full advantage of this production, storage systems in combination with higher interconnection between countries should be in place, allowing this excess of generation during low demand to be saved and afterwards injected back to the grid during peak demand periods. The storage systems can either be centralized (e.g. pumped storage systems) or distributed (e.g. electric vehicles connected to the grid during the night).

Demand side management systems have the capacity of shifting demand during peak periods, or even reduce it, thus increasing reliability on the grid. By ensuring that electricity consumption is constantly monitored, these systems incorporate 'smart' devices in points of electricity usage (e.g. homes, offices, industry) that receive information concerning the electricity prices every given moment, allowing a choice of operating certain household appliances during low cost/low demand periods (e.g. washing machines, batteries). Another possibility is by reducing the power output of space heating/cooling equipment during peak demand. In a large-scale system, with multiple devices connected to the grid, a minor change of 2 or 3 degrees in the system's temperature (room temperature) during a peak period allows a substantial reduction in demand.

Finally, to balance supply and demand effectively, 'smart' communications systems must be in place. Such a system would communicate real time information between the various stakeholders in the network such as providing electricity prices to demand response devices across the system or reporting and repairing faults in the network. In addition, a remote centre capable of managing the entire network would allow real time response to fluctuations in the weather conditions and consequently to electricity production.

4 Case Study

4.1 Objectives

This case study intends to produce a critical analysis concerning the sustainability of the Portuguese electric system in 2020, taking into account the increasing share of Renewables. The specific goal of this research is to investigate the capability of Wind Power, Solar-Photovoltaic and Hydroelectricity to address electricity demand in Portugal, by identifying and comparing resource availability, electricity generation and electricity demand.

4.2 Methodology

This study is based on the statistical analysis of existing data to characterize the availability of natural resources, namely solar, wind and hydro and relate them with the electricity demand patterns in Portugal, both seasonal and daily. The elements used to estimate the availability of natural resources were the global solar irradiation on horizontal surface (W/m^2), the wind speed at 10 m height (m/s) and the volume of water in hydroelectric reservoirs (m^3).

The global solar irradiation data for the seasonal analysis was collected from a meteorological station located in Évora, since the National Energy Strategy favours the south of Portugal for new solar power investments, as it can easily be understood by Fig. 3a. The second location, used for the daily analysis, was Lisbon, which is more representative in terms of population with nearly 25 % of Portugal's population in only approximately 3 % of the territory. The data collected from Évora's Geophysics Centre is the daily average of the global solar irradiation recorded in the years of 2010, 2011 and 2012 from a solar radiometer with a temporal sampling of 10 min [25], while the figures from Lisbon derive from satellite hourly data and are presented as the average day of July 2005 and the average day of December 2005 [26].

The wind speed data corresponds to the year 2012 and was collected from seven meteorological stations in different locations across Portugal [28]: "Vila Real", "Viseu", "Penhas Douradas", "Monte Real", "Alverca", Sines" and "Sagres". The measurements have a temporal sampling of 3 h and the processed data is presented as the monthly average wind speed in 2012 for the seasonal analysis, and the average day of July 2012 and December 2012 for the daily analysis. These particular stations were chosen based on their location, since they correspond to areas with already existent sites of Wind Power generation, Fig. 3b.

The hydroelectric water reservoirs data, which is directly related with the levels of rainfall, was collected from the National information System for Water Resources in Portugal and is presented in volume (m^3). This institution gathers all the information related with water resources including the average levels of water
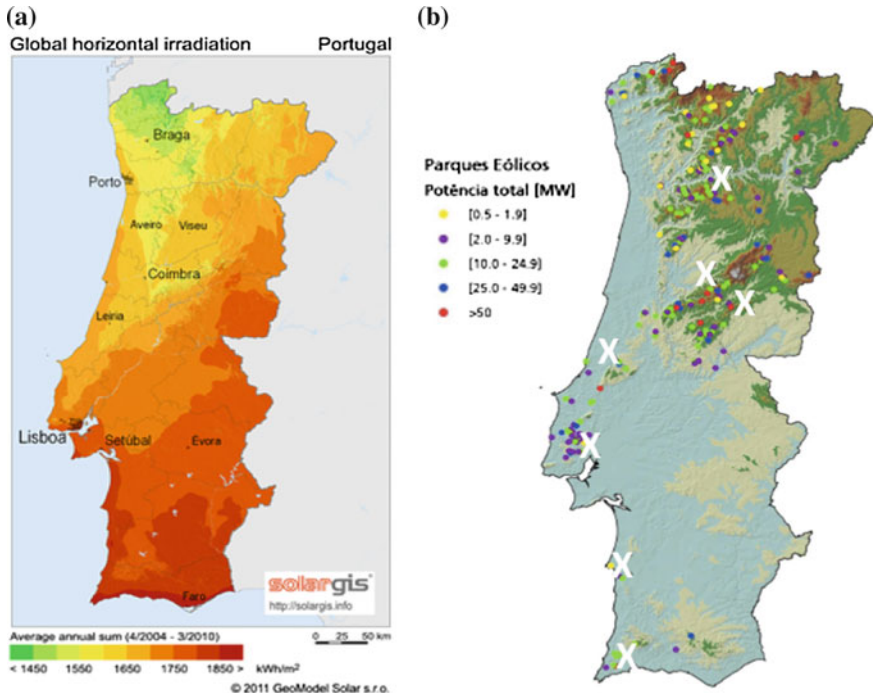
Fig. 3 **a** Annual average for global horizontal irradiation in Portugal from 2004 to 2010 [27].
b Locations (X) of the meteorological stations used for the study and the On-Shore Wind Farms in
Portugal 2008 [29]

storage in hydroelectric reservoirs and total capacity available. The data used for
this study includes 57 existent reservoirs with their average monthly storage from
1990 to 2011 [30]. In order to better characterize the potential of these resources,
data concerning the electricity generated from each resource [13] (2007–2012) is
included together with the correspondent capacity factor, which is the ratio of actual
output over a period of time to its possible output if it were operating at full time
over that period of time. The capacity factor is given by the equation:

$$Capacity\,Factor = \frac{Annual\,Generation}{Period\,of\,time\,\times\,Installed\,Capacity} \qquad (1)$$

where the Capacity Factor is in %, the Annual Generation is in MWh, the Period of
time in hours, and the Installed Capacity in MW.

Concerning electricity demand in Portugal, the data was collected from the REN
—Rede Elétrica Nacional on-line archive [13]. The data refers to the monthly load
profiles in 2012, presented in the form of consumption (GWh) and peak demand
(MW) and the daily load profiles, in winter and summer, which registered the
maximum peak demand in that year. This methodology was adapted from Jong
et al. [5], however, instead of normalizing the values of the resource availability

against their maximum value, this study uses the normalized value of electricity generation from each resource. After gathering the available data, a statistical analysis through normalized values was prepared in order to study the relations between resources availability and electricity demand during a typical year. The two methods used to establish potential correlations were the Pearson product-moment correlation coefficient and through graphical illustration, which helps to understand better the results of the first method by providing a visual component to the study. While the graphical illustration shows the seasonal and daily variation of the parameters against the demand load profile, the Pearson product-moment correlation coefficient measures the linear dependence between two chosen variables, and is given by the formula:

$$r = \frac{\sum_i (x_i - \bar{x})(y_i - \bar{y})}{\sqrt{\sum_i (x_i - \bar{x})^2}\sqrt{\sum_i (y_i - \bar{y})^2}} \tag{2}$$

the coefficient ranges from -1 to 1, where the latter indicates a positive linear correlation between the variables y and x, i.e., both variables present the same behaviour (y increases as x increases), and -1 implies a negative linear correlation, i.e., an inverse relationship (y decreases as x increases or vice versa). The value of 0 indicates no linear correlation between the variables.

In order to use this statistical tool, which only relates two variables, multiple combinations were created to study their correlation:

- Solar versus Demand
- Wind versus Demand
- Reservoir levels versus Demand
- Solar + Wind (50/50) versus Demand
- Solar + Wind (12/88) versus Demand
- Solar + Wind (50/50) versus Reservoir levels
- Solar + Wind (12/88) versus Reservoir levels
- Solar + Wind + Reservoir levels (5/35/60) versus Demand

While some of the combinations suggest an equal weight for the natural resources contribution, some combinations take into account the projected contribution of each technology/resource for electricity generation in the National Energy Strategy for 2020. This consideration was based on installed capacity. Finally, using both methods, a daily analysis is also presented to study the correlation between Solar and Wind resources and the daily demand profile, using available data to characterize a typical winter day and a typical summer day. The following combinations were used for this analysis:

- Solar versus Demand
- Wind versus Demand
- Solar + Wind (50/50) versus Demand
- Solar + Wind (12/88) versus Demand
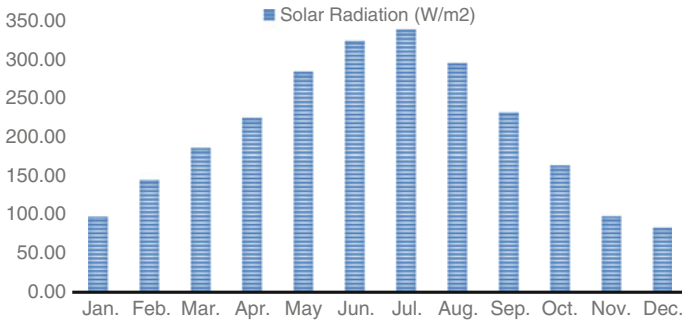
Fig. 4 Daily solar irradiation average for each month from 2010 to 2012 in Évora meteorological station

Ancillary information concerning the calculations can be found in the Appendices. It includes ancillary spreadsheets and data relevant to this study.

4.3 Availability of Resources in Portugal

4.3.1 Solar

Portugal is one of the European countries with the highest solar resources due to its location in terms of latitude, i.e., proximity to the equator. The average annual solar radiation ranges from 1450 kWh/m^2 in the extreme north to 1900 kWh/m^2 in the south of Portugal while Évora and Lisbon, which were the locations chosen for this study, have similar outputs of approximately 1750 kWh/m^2 [27]. In Fig. 4 it is possible to understand the monthly variation of the sun as a resource, enhancing the disparity between winter and summer. According to the data available from Évora meteorological station, there is a reduction of approximately 75 % of the resource from July to December.

Figure 5 shows the monthly electricity generation from Solar-Photovoltaic systems in Portugal from 2007 to 2012. It is possible to observe the continuous increase in generation every year due to the expansion of these systems in Portugal, namely the Hércules Photovoltaic power plant in Serpa with 11 MWp commissioned in 2007, and the Amareleja Photovoltaic power plant in Moura with 46 MWp commissioned in 2009. As expected, it also shows a close relation between the resource availability and electricity generation, with higher output during the summer months than winter months.

Table 3 presents the capacity factors of this technology from 2007 to 2012. The first 2 years should be disregarded from any future analysis since the sample level was reduced in terms of installed capacity, however, the following years show a consistent value approaching the 20 %, which is high when compared with other

Table 3 Solar-photovoltaic capacity factor from 2007 to 2012 in Portugal

	2012	2011	2010	2009	2008	2007
Annual generation (GWh)	331	250	172	139	30	21
Average installed capacity (MW)	186	137	99	63	31	6
Capacity factor (%)	20	21	20	25	11	44
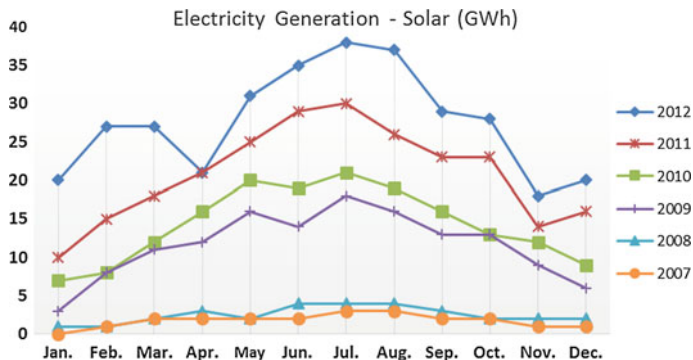
Fig. 5 Monthly electricity generation from photovoltaic systems in Portugal (2007–2012)

European countries such as UK (5.5 %) or Germany (8.8 %) in 2011 [31, 32]. Figure 6 demonstrates the daily profile of the solar resource pattern during July and December 2005. It also shows the difference in the duration of day concerning sunlight. The highest duration of daylight for a summer day is 14 h 52 min while for a winter day is 9 h 27 min [33].

4.3.2 Wind

Contrasting with solar resources, most of the Wind Power sites are located in the north of Portugal with some exceptions in the southwest coast. This study only takes into consideration on-shore wind potential since offshore is still in a development phase with few elements to characterize with accuracy the wind behaviour in the Portuguese sea. However, it is fair to assume that developments in this area will contribute for an increase of the wind potential in Portugal. Figure 7 illustrates the average wind speed per month during the year of 2012 in Portugal, considering seven strategic locations across Portugal identified as favourable sites for Wind Power generation, and the monthly electricity generation from all the Wind Farms in Portugal in the same period. Concerning the relationship between wind speed and electricity generation, one can observe that, unlike the rest of the year where generation and wind speed have a linear behaviour, the summer months have
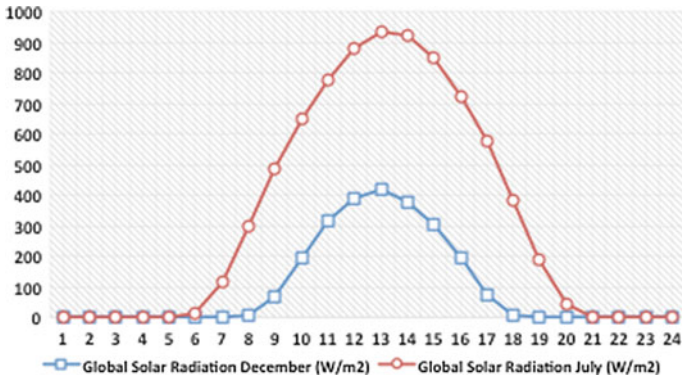
Fig. 6 Hourly solar irradiation average in Lisbon for the average day of July and December 2005
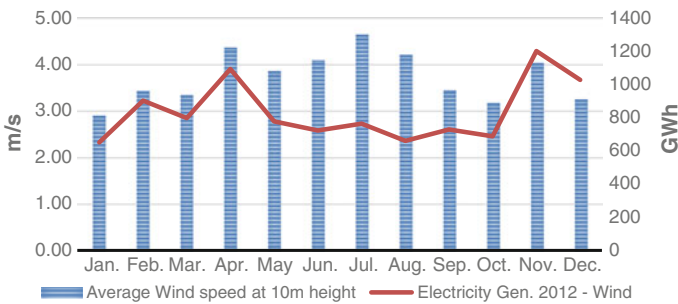

Fig. 7 Monthly Wind Speed Average for 2012, and monthly electricity generation from Wind Power in 2012

meaningful deviations in these two parameters. There are several possible reasons for this situation, one is the fact that during summer, wind distribution is highly influenced by breezes, especially in the coast, increasing the variability of wind during this season by having longer calm periods followed by high speed periods, which influence electricity output due to turbines cut-in and cut-out speeds.

Figure 8 shows the electricity generation from Wind Power in Portugal. The data relates to 6 years (2007–2012). It shows that wind as a resource, is available during the entire year, although not regular. Some discrepancies can be observed, namely in 2011, where generation plummeted from March until May, rise until July, dropped again until September, and finally rocked again reaching to its maximum output in November. This random behaviour can also be observed in the other years, however, in a more general interpretation, it is possible to register a slight increase of generation during winter rather than in summer months. Table 4 presents the capacity factor for each year, which shows a very regular annual reading
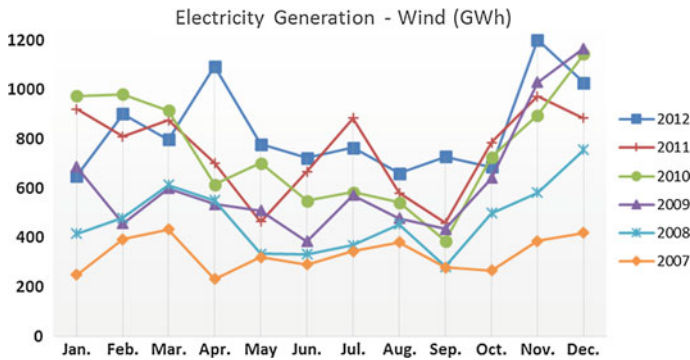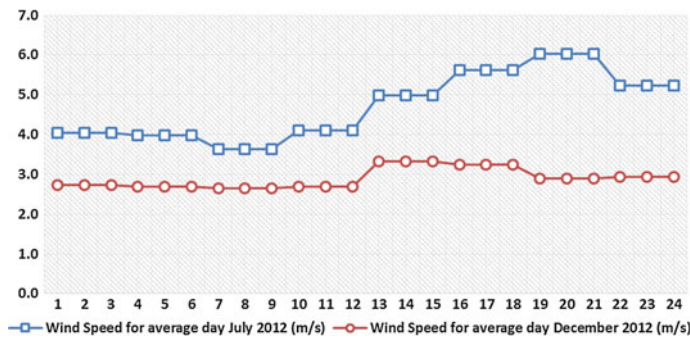
Fig. 8 Monthly electricity generation from Wind Power in Portugal 2012

Table 4 Wind power capacity factor from 2007 to 2012 in Portugal

	2012	2011	2010	2009	2008	2007
Annual generation (GWh)	10015	9008	9022	7497	5671	4002
Average installed capacity (MW)	4138	3892	3530	2991	2259	1706
Capacity factor (%)	28	26	29	29	29	27

Fig. 9 Hourly Wind Speed Average for December and July 2012

varying from 26 to 29 %, highlighting some of the aspects already referred such as the availability of the resource during the year, suggesting similar resource conditions year after year. These figures reflect the favourable conditions for Wind Power in the Portuguese territory, especially if compared with other European countries such as UK (29.8 %), one of the countries with better conditions for Wind Power, or Germany (19.3 %) in 2011 [31, 32].

Figure 9 demonstrates the daily profile of the wind resource pattern during July and December based on the data gathered from the meteorological stations.
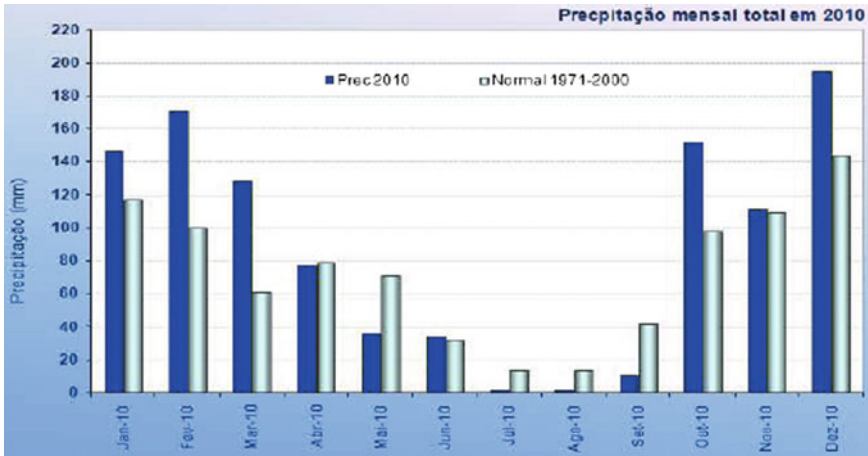
Fig. 10 Average precipitation (1971–2000) and precipitation in 2010, Portugal [35]
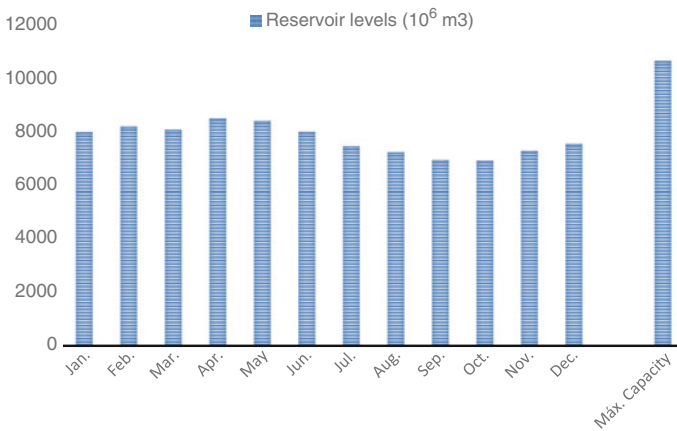

Fig. 11 Water reservoir volumes average per month from 1990 to 2011 in Portugal

4.3.3 Hydro

Rainfall is the most important feature to assess the reservoir levels and its characterized by its variability across the Portuguese territory. While in the North of Portugal, some locations can reach to 4000 mm per annum with an annual average of approximately 2200 mm, the centre and south regions range from 800 to 450 mm per annum. Another feature of the precipitation regime in Portugal is that approximately 70 % of the rainfall occurs between the months of November and April inclusive, as shown in Fig. 10.
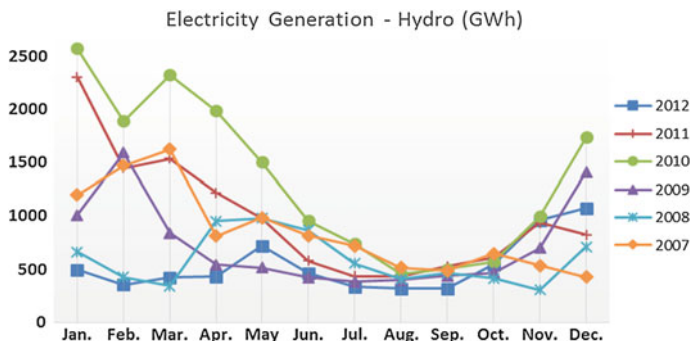
Fig. 12 Hydroelectricity generation in Portugal from 2007 to 2012

It is possible to understand the connection between the seasonal pattern of rainfall and the water availability in reservoirs (Fig. 11), i.e., a higher capacity during winter and spring. It is also important to mention that electricity production is not the only purpose of these reservoirs, which also include clean water supply for populations, agriculture, commerce, industry and supporting existing ecosystems.

In Fig. 12, it is possible to observe the electricity generation from hydroelectric plants from 2007 to 2012. It shows a fairly regular pattern with higher generation in the winter season than summer matching with the rainfall occurrence in Portugal.

Regarding the capacity factor for Hydroelectricity in Portugal, Table 5 presents very different years concerning the annual electricity generation. Unlike the other two renewable sources, which show similar resource availability throughout the studied years, i.e., similar capacity factors, Hydro outputs indicate a wide range of values varying from 47 % in 2007 to 13 % in 2012, resulting in huge differences between "wet and dry" years. In 2010 and 2007, there were very good meteorological conditions for electricity generation, while 2012 conditions resulted in the poorest year for Hydroelectricity.

Table 5 Hydroelectricity capacity factor from 2007 to 2012 in Portugal

	2012	2011	2010	2009	2008	2007
Annual generation (GWh)	6442	11832	16242	8719	7087	10240
Average installed capacity (MW)	5523	5189	4986	4970	4956	2478
Capacity factor (%)	13	26	37	20	16	47

4.4 Variation of Electricity Demand in Portugal

In 2012, the average peak demand was 7445 MW with the maximum of 8531 MW, which happened in middle February [13]. Identical to most of the European countries, there is a correlation between electricity demand and daily temperatures, with higher demand happening in the winter months. Besides showing the annual pattern of electricity peak demand, Fig. 13 also shows the consumption in 2012.

Concerning the daily profile, Fig. 14 confirms the variation between the winter and summer patterns, which can be explained by the increase of heating systems connected to the grid in the winter season, especially during the night hours where temperatures tend to drop and population is back from work to their homes, and at the beginning of the day when most of space heating systems, namely commercial and offices buildings, start operating some time before the arrival of workers.
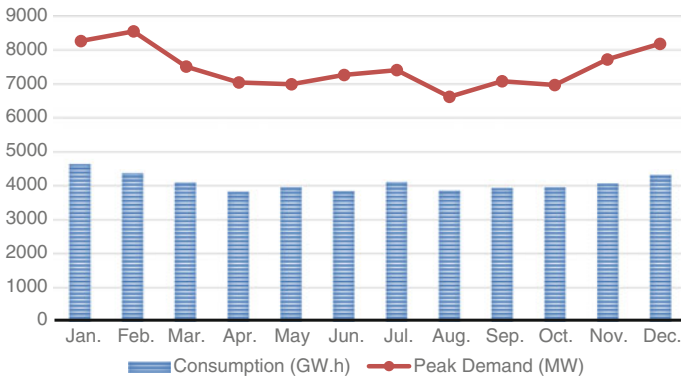

Fig. 13 Monthly electricity consumption and maximum peak demand per month in Portugal 2012
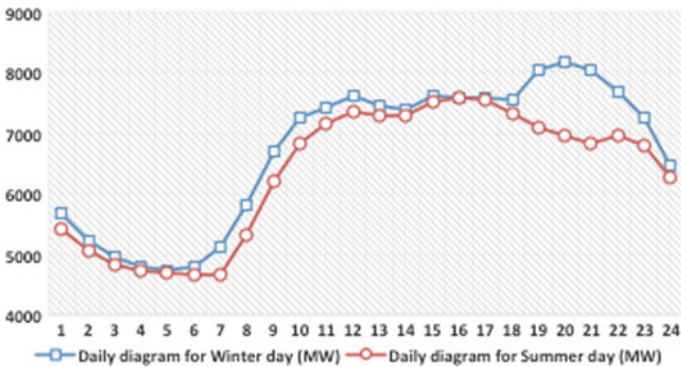

Fig. 14 Daily electricity demand profile in Portugal (23rd January and 8th July 2013)

Table 6 Results of the Pearson product-moment correlation coefficient for annual analysis

|	Pearson correlation coefficient
Solar versus Demand	−0.788
Wind versus Demand	0.623
Hydro versus Demand	0.709
Solar and Wind versus Demand (50/50)	−0.492
Solar and Wind versus Demand (12/88)	0.515
Solar and wind Versus Hydro (50/50)	−0.577
Solar and Wind versus Hydro (12/88)	0.354
Solar and Wind and Hydro versus Demand (5/35/60)	0.762

4.5 Findings and Discussion

The calculated Pearson correlation coefficients can be found in Table 6. This particular analysis shows a substantial positive correlation between both Wind power (0.623) and Hydro (0.709), and the yearly electricity demand, while Solar power has a negative correlation concerning the yearly demand pattern (−0.788). These results indicate that, individually, Wind power and Hydro availability follow the demand load curve throughout the year with higher outputs during the winter season and lower outputs during summer season, while Solar power has its maximum output during the summer season. Since Wind and Hydro are expected to supply the largest share of renewable electricity, it is also important to study their complementarity, not only concerning the operational aspect (day/night generation with storage capacity), but their resource availability. It would be beneficial if there was a negative correlation between these two sources, since they could complement each other during the year, however, for the Portuguese case, these two resources tend to co-exist during the same periods of the year, even without a significant correlation (0.354), i.e., higher availability from both during the winter than summer months. By contrast, Solar power possesses that complementarity, however, the share of this renewable source in the overall electric system is still modest to produce that desirable effect. Finally, the combination of the three resources according to their projected installed capacity in 2020 indicates a positive correlation with the demand load curve in Portugal (0.762).

In addition to the Pearson correlation coefficients, which show a fairly solid correlation between the proposed combination of renewable sources and electricity demand in Portugal, the graphical illustration (Fig. 15) allows a broader analysis by showing the variations of the four parameters during a typical year.

The Solar power availability varies approximately 70 % between July and January in a typical year, while Wind power shows a variation of approximately 50 % between its maximum (December) and minimum values (September). As stated previously, these resources could complement each other to a certain extent, i.e., if both sources contributed equally to the final electricity mix, since electricity
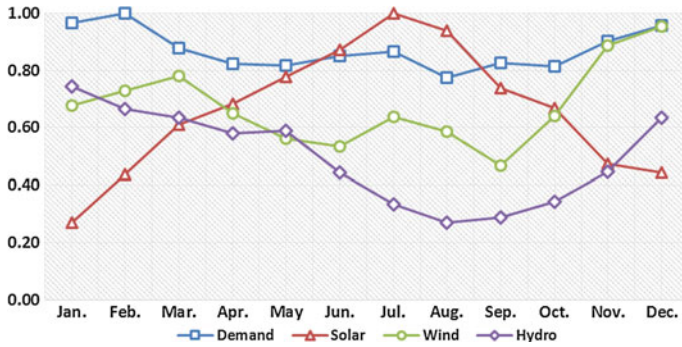
Fig. 15 Monthly variation of each resource availability normalized to their maximum value and the normalized electricity demand curve
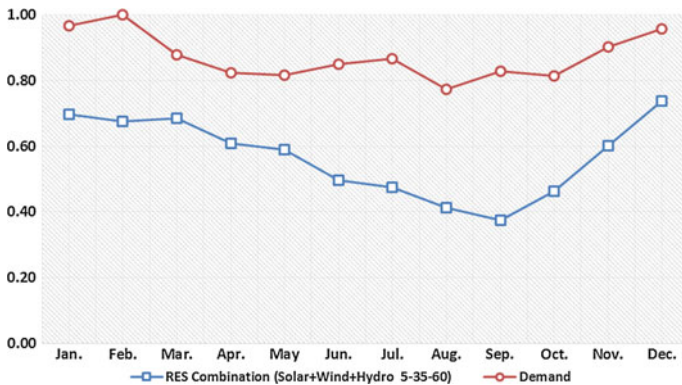
Fig. 16 Monthly variation of the renewable combination (5-35-60) normalized to their maximum value and the normalized electricity demand curve

output from Solar is higher during the summer and lower during the winter, while Wind power register the opposite pattern, i.e., lower during the summer and higher during the winter.

Hydroelectricity output varies nearly 45 % during a typical year, with January as maximum and August as minimum values, which confirms the rainfall patterns and hydro reservoir levels in Portugal.

This assessment highlights the summer season as critical with respect to electricity supply from renewable sources. Electricity demand varies around 23 % during the year reaching its lowest value in August also coinciding with the lowest value of Hydro and during the lowest period of Wind. However, the variation in demand is lower than the variation in the electricity production from these sources, which entails a potential supply deficit in this period. This phenomenon can be observed in Fig. 16, which also takes into consideration the projected installed capacity of each source.

Table 7 Results of the Pearson product-moment correlation coefficient for daily analysis

	Summer	Winter
	Pearson correlation coefficient	Pearson correlation coefficient
Solar versus Demand	0.775	0.452
Wind versus Demand	−0.566	−0.401
Solar and Wind versus Demand (50/50)	0.805	0.442
Solar and Wind versus Demand (12/88)	−0.248	−0.343

It is possible to observe a substantial decrease in the renewables contribution for this particular combination in the summer months, mainly due to a low share of Solar power (5 %). The inclusion of storage unit systems can mitigate this effect by adjusting as much as possible the production curve to the demand curve, since the ideal would be to have two curves linearly alike. Concerning the Portuguese case, the investment in pumped storage systems associated to hydroelectric reservoir plants seems natural, given the potential for these systems in Portugal. In 2020, it is expected to be in operation a total of 4004 MW of reversible capacity, which will allow a better management of the reservoirs levels taking them closer to their maximum storage capacity expressed in Fig. 11 during the high availability months, in order to increase production during the low availability months.

Concerning the daily profile analysis, the Pearson Correlation coefficients are shown in Table 7. The results indicate a positive correlation between Solar availability and electricity demand, especially during the summer (0.775), while Wind power availability has a moderate negative correlation with daily electricity demand during the entire year. In a potential combination with equal contribution from Solar and Wind sources, there would be a significant positive correlation with demand, however, with the expected contribution of these sources in 2020, there is a minor negative correlation between them and demand during the year, with coefficients of −0.248 during the summer and −0.343 during the winter.

The graphical illustration allows a better examination of the daily behaviour of these parameters. In a typical winter day (Fig. 17), the solar availability, which follows the hours of daylight, starts from 8 h, reaches the maximum output between 12 and 13 h, and ends between 18 and 19 h. The output level describes an arc-shaped curve consistent with the Sun intensity during the day, and zero during the night. On the other hand, Wind power shows opposite behaviour, with higher electricity output during the night and a considerable decrease during daytime, which enhances some complementarity between these two sources. Concerning the daily demand curve, it rises substantially from 7 to 10 h, coinciding with he beginning of the day, and maintains a constant value during daytime until 18 h, from which it peaks around 20 h and starts falling up to 40 % of the value, during night-time.
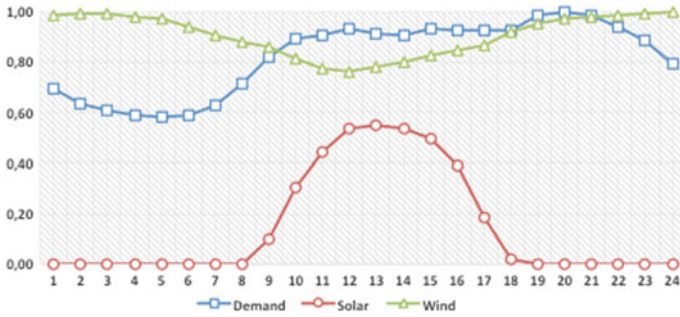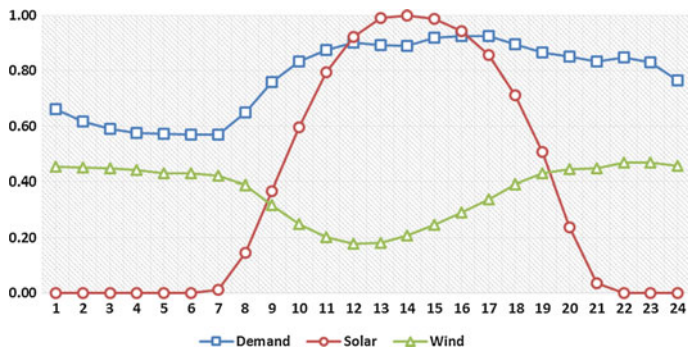
Fig. 17 Hourly variation of solar and wind power in a winter day normalized to their maximum value and the normalized electricity demand curve for the maximum peak demand in January 2013

As stated previously, Wind availability has a moderate negative correlation with demand, which can be observed in the graph, with higher levels of wind during the night when demand is lower, and when demand is higher, one can observe a reduction in availability from Wind registering its lowest point at 12 h. The exception happens during the peak period from 18 to 21 h in winter, where wind can play a fundamental role concerning demand response. In addition, Portugal has planned a proportional growth between Wind Power capacity and reversible capacity via pumped storage systems in order to make better use of the electricity produced by wind turbines during the night for later use during periods of peak demand.

Regarding Solar power availability, it coincides with daytime, which is a period of stable high demand. It provides the right curve to assist demand during daytime (between 8 and 18 h), especially the rise in demand in the morning period between 8 and 10 h. However, it cannot support the peak demand in a winter day that happens around 20 h, unless other technologies are put in place such as high capacity batteries or thermal energy storage, in order to extend the daily operational period of these systems. Besides Photovoltaic power plants, which provide electricity in larger scale, small-scale PV systems equipped with batteries can offer the appropriate solution for homes since electricity consumption is higher during the evening when people arrive from work or school, than during the day. There are also other successful examples in Solar power that can be considered for Portugal such as Concentrated Solar Power. Solana power plant in Arizona, USA, has an installed capacity of 280 MW and 6 h of molten salt thermal energy storage allowing electricity to be dispatched as needed, even during the night [34].

There is a significant variation in the three parameters from winter to summer, especially in availability levels, and not so much in the curves configuration. Figure 18 shows a substantial increase in Solar power availability either in intensity and number of hours, which goes from 7 to 21 h. In addition to this increase, demand curve also suffers some variations such as a reasonable constant reduction throughout the entire day, but especially, a considerable reduction during the period from 18 to 21 h. While peak demand in winter happens at 20 h, in the summer, it

Fig. 18 Hourly variation of solar and wind power in a summer day normalized to their maximum value and the normalized electricity demand curve for the maximum peak demand in July 2013

shifts to 16 h, making Solar power a more effective solution in this season. Wind power availability in summer suffers a large reduction when compared with winter figures, but maintains the same daily behaviour producing more electricity during the night than during the day. It registers a reduction of 29 % from its maximum point at 23 h to its minimum point at 12 h.

Wind and Solar power demonstrate the same degree of complementarity between each other, also shown in the seasonal analysis, i.e., when Solar output is maximum, Wind output is minimum (daytime), and vice versa. This situation, in particular Wind power generation, reflects the strategy developed by Portugal regarding the increase of pumped energy storage systems, which also address other concerns, namely the variability and intermittency of electricity generated from these sources. This hybrid system between Wind power and pumped energy storage systems (usually coupled to reservoir hydroelectric plants) can provide the necessary reliability and security to the electric system since Hydroelectric power plants can promptly adjust electricity generation output to meet unexpected variations on demand or back-up sudden fluctuations in Wind and Solar output, either due a Wind speed drop or clouds passing through a Solar power plant.

4.6 Limitations of the Study

Although this research was carefully prepared, there are unavoidable limitations, which are associated with the collection of data relevant to this study. The data regarding electricity production allows a reasonable understanding of patterns since it provides information concerning the last 6 years, however, the data concerning the availability of natural resources, namely solar irradiation, wind speed and rainfall have some temporal limitations, which potentially affects the final results. This situation was due, either to unavailable data to general public, or to inexistent data.

5   Conclusions

This study shows that Portugal possesses consistent renewable energy sources for electricity generation, namely Hydro, Solar and Wind Power, with high capacity factors when compared against other European countries. It also describes the typical seasonal and daily patterns of these resources availability identifying critical periods. The conditions for electricity generation in winter months are more favourable for Hydro and Wind power due to higher levels of rainfall and constant wind speed, while summer months favour Solar power. Electricity demand in Portugal is higher during the winter months than during summer time, which coincides with the resources availability, namely Wind and Hydro, the two main contributors or renewable energy in the current Portuguese system.

It is noteworthy the fact that, unlike Solar and Wind power capacity factors that are reasonable constant year after year, varying respectively, 5 and 3 % in the last 6 years, Hydroelectricity generation has much higher variations, e.g., the capacity factor in 2007 was 47 % while in 2012 was 13 %.

Moreover, on one hand, this study establishes a reasonable positive correlation between a combination of these three sources and electricity demand in Portugal during a typical year, on the other hand, the daily analysis shows no correlation between the combination of Solar/Wind power and electricity demand. Meanwhile, if the sources are studied individually, Solar power has a significant positive correlation with demand, while Wind power has a considerable negative correlation during a typical 24-h period.

Currently, Portugal already has a surplus capacity of wind power during nights, which has the tendency to increase since the national strategy foresees additional investment in this technology, and Solar power is a valid option to assist electricity demand during daytime given its load production curve, but cannot cope with demand during nigh time. These situations indicate a potential complementarity between Wind and Solar power during a typical day and require a proportional investment in energy storage systems, namely pumped storage systems or other emergent technologies such as high capacity batteries or thermal energy storage, in order to take full advantage of existent resources.

In order to address concerns regarding reliability and security of the grid, the investment in pumped storage systems should happen alongside with an increase in hydroelectric capacity, which is still at 50 % of its potential. Given the characteristics of these plants, they can work either as base load plants or peak load plants and provide the necessary ancillary services to the Grid Operator. In addition, investment and development of "smart grid" technologies will have an unquestionable positive effect in electricity consumption, i.e., providing the Grid Operator with more management options such as to adjust demand to supply instead of only the opposite.

Other studies could be performed considering the total energy storage capacity necessary to cope with the proposed 2020 electric system with 60 % of renewable

generation, and further in time, to a potential 100 % renewable electric system. Such work could also provide an estimation of the costs and level of investment associated with such a system.

References

1. International Energy Agency, "Key World Energy Statistics", Paris, France, 2012
2. Rede Energética Nacional, "Technical Data 2012", Lisbon, 2012
3. Esteban, M., Zhang Q, Utama A., Tezuka T. & Inshihara K., "Methodology to estimate the output of a dual solar-wind renewable energy system in Japan", in Energy Policy 38, pp. 7793-7802, August 2010
4. Hoicka C. & Rowlands I., "Solar and wind resource complementary: Advancing options for renewable electricity integration in Ontario, Canada", in Renewable Energy 36, pp. 97-107, June 2010
5. Jong p., Sánchez P., Esquerre K., Kalid R. & Torres E., "Solar and wind energy production in relation to the electricity load curve and hydroelectricity in the northeast region of Brazil", in Renewable and Sustainable Energy Reviews 23, pp. 526-535, January 2013
6. Moura P. & Almeida A., "Multi-objective optimization of a mixed renewable system with demand-side management", in Renewable and Sustainable Energy Reviews 14, pp. 1461-1468, January 2010
7. Pina A., Silva C. & Ferrão P., "High-resolution modelling framework for planning electricity systems with high penetration of renewables", in Applied Energy 112, pp. 215-223, May 2013
8. Suomalainen K., Silva C., Ferrão P. & Connors S., "Wind power design in isolated energy systems: Impacts of daily wind patterns", in Applied Energy 101, pp. 533-540, July 2012
9. Jerez S., Trigo R., Sarsa A., Lorente-Plazas R., Pozo-Vázquez D. & Montávez J., "Spatio-temporal complementarity between solar and wind power in the Iberian Peninsula", in Energy Procedia 40, pp. 48-57, 2013
10. Krajacic G., Duic N. & Carvalho M., "How to achieve a 100 % RES electricity supply for Portugal?", in Applied Energy 88, pp. 508-517, September 2010
11. Castro R., "National electric System characterization", Technical University, Instituto Superior Técnico, Lisbon, Portugal, 2008
12. EDP, Energias de Portugal web page [online], Available: http://www.edp.pt
13. REN, Rede Energética Nacional web page [online], Available: http://www.ren.pt
14. ERSE, Energy Services Regulatory Authority web page [online], Available: http://www.erse.pt
15. Eurelectric, "Power Statistics & Trends 2012 synopsis", Brussels, Belgium, 2012
16. Government of Portugal – Ministerial Council, "National Action Plan for Renewable Energy", in Republics Diary, 1ªserie, Nº70, Lisbon, Portugal, April 2013
17. Ministry of Agriculture, Sea, Environment and Land, "National Plan for Dams with Hydroelectric high potential", Lisbon, Portugal, 2007
18. European Commission, RES LEGAL web page [online] Available: http://www.res-legal.eu/search-by-country/portugal/single/s/res-e/t/promotion/aid/feed-in-tariff-tarifas-feed-in/lastp/179/
19. APREN Renewable Energy Association, "Renewable Energy National Route for Directive 2009/28/CE", Portugal, 2010
20. International Electrotechnical Commission, "Grid integration of large-capacity Renewable Energy sources and use of large-capacity Electrical Energy Storage" Switzerland, 2012
21. Kema Lda, "Study on the impact of Distributed Generation on the National Electricity System", ERSE, Energy Services Regulatory Authority, Lisbon, Portugal, 2011
22. Salam S., "Unit Commitment Solution Methods", in World Academy of Science, Engineering and Technology Nº 11, 2007

23. US National Institute of Standards and Technology web page [online] Available: http://www.nist.gov/smartgrid/nistandsmartgrid.cfm
24. Crossley P., Beviz A., Angulo J. & Amaltes S., "Smart energy systems: Transitioning renewables onto the grid", in Renewable Energy Focus, Volume 11, Issue 5, pp. 54-59, October 2010
25. Évora Meteorological Station, Évora's Geophysics Centre web page [online] Available: http://www.cge.uevora.pt/pt/component/cge_bd/?cge_bd_e_first=evr
26. SoDa –Solar radiation data web page [online] Available: http://www.soda-is.com/eng/services/services_radiation_free_eng.php
27. Solargis web page [online] Available: http://solargis.info
28. Weather Data, Mundomanz web page [online] Available: http://www.mundomanz.com/meteo_p/monthrep?countr=PORTUGAL&action_coun=display_coun&l=1
29. Rodrigues A., "Parques Eólicos em Portugal" (Wind Farms in Portugal), INEGI – Institute of Mechanical Engineering and Industrial Production, Portugal, 2008
30. National information System for Water Resources in Portugal web page [online] Available: http://snirh.pt/index.php?idMain=1&idItem=1.3
31. Department of Energy and Climate Change (DECC), "Digest of UK energy Statistics (DUKES), chapter 6: Renewable Sources of Energy", UK, 2013
32. Federal Ministry for the Environment, Nature Conservation and Nuclear Safety, "Development of renewable energy sources in Germany 2012", Berlin, 2012
33. Sunrise and sunset times web page [online] Available: http://www.sunrise-and-sunset.com/pt/portugal/lisbon
34. Abengoa Solar web page [online] Available: http://www.abengoasolar.com/web/en/nuestras_plantas/plantas_en_construccion/estados_unidos/#seccion_1
35. Instituto de Meteorologia I.P., "Annual Climatological Newsletter 2010", Lisbon, Portugal, 2010

A Robust Iterative Learning Control Algorithm for Uncertain Power Systems

Marina Vassilaki

Abstract Learning control is an iterative approach to the problem of output tracking for processes that are repetitive in nature and operate over fixed time intervals. The adaptability of the control law to changes of model parameters, to unmodelled dynamics and to nonlinearities of real systems has been proven valuable for applications in management and control of components of production and distribution networks. The ILC problem is converted to the design problem of the linear approximation parameters of the input function in a subspace spanned by a set of basis functions. Results on positive invariant sets of linear discrete-time systems allow for the development of a robust ILC algorithm that deals with the uncertainties in the systems model and the restriction of the input and output spaces. The method is presented in view of applications in the management and control of components of production and distribution networks such as Active Power Filters, Inverters for interfacing with renewable energies microgrids and wind turbines.

Keywords Stability · Iterative learning control · Harmonics elimination · Positive invariance

1 Introduction and Problem Statement

Learning control is an iterative approach to the problem of output tracking for processes that are repetitive in nature and operate over fixed time intervals. The adaptability of the control law to changes of model parameters, to unmodelled dynamics and nonlinearities of real systems has been proven valuable for applications in management and control of components of production and distribution networks. In the case of series connected PV inverters the control action aims at grid voltage compensation [7, 8]. The control system ensures that load voltage is auto synchro-

M. Vassilaki (✉)
Department of Electrical Engineering Educators, ASPETE,
14121 Heraklion, Athens, Greece
e-mail: mvassilaki@aspete.gr; vassilaki.m@hotmail.com

nized with the grid voltage even in the case of grid frequency variations. Essentially, this problem can be classified as the tracking of sinusoidal voltage at the load end and a problem of voltage harmonics elimination in the (micro) grid. In the case of active filters, the Iterative Learning Control algorithm is used to eliminate current harmonics of the grid and regulate current supply to the load [13, 19]. Iterative Learning Control algorithms can also be used for the control wind turbines. The control of wind turbines deals with the problem of transition between operating regions as a result of changing operating conditions and variation of model parameters and with the adjustment of operating parameters in an operating region for poorly modelized systems mainly due to the unmodelized wind behavior and to presence of nonlinearities [3, 11, 12]. The goal of the control strategy is to achieve maximal power production and limited structural fatigue of the wind turbines. The later requirement implies smooth operation of the individual turbine is also addressed by the ILC strategy [3, 18]. In all cases, the control strategy has to deal with unmodelled or unknown dynamics that can be viewed as parameter deviations of the nominal model parameters of the system. The method presented in this chapter uses a learning strategy based on the approximation of input, output and reference trajectories of a system by finite dimensional basis functions. It ensures convergence and a bounded mean square error value of the estimation when the learning parameters deviate from the nominal values and is applicable to the above mentioned problems.

The goal of the iterative learning control (ILC) methods is to achieve an output trajectory of the controlled system that matches a specified trajectory without or with minimal deviations [14]. The optimal system input is calculated through a series of iterative experiments for a finite control horizon. At the end of each of these trials the input used for the next trial is calculated via an updating law so as to minimize a convergence criterion and is executed in an open loop scheme for the next trial. Such an approach allows the achievement of good results with simple control algorithms in the face of modeling or measurement uncertainties.

In [16], it is shown that the controlled system must have either the property of passivity or bi-properness to ensure the convergence of the tracking error to 0. In order to guarantee this convergence, many ILC methods use the time derivative of the error signal to adapt the input [1, 2, 14, 15]. The dual system optimization approach is used in [1, 17]. In [9], an approach is presented that does not use the error derivative to update the control signal and is based on the use of a set of basis functions derived from a target trajectory. The input space is restricted to the prescribed finite-dimensional subspace and is updated by the projection of the error on this subspace at each experiment. The restriction of the input and output spaces introduces uncertainties in the model of the system reflected in the ILC algorithm.

In this paper an ILC method for SISO linear systems will be presented based on the property of positive invariance of polyhedral sets. Using the approach in [9] for the design of the input function, the ILC problem is converted to the design problem of the linear approximation parameters of the input function in a subspace spanned by the chosen basis functions. Results on positive invariant sets of linear discrete-time systems allow for the development of a robust ILC algorithm that deals with the uncertainties in the systems model introduced by the modeling

process and the restriction of the input and output spaces. The uncertainty constraints are supposed to be polyhedral expressing natural constraints on deviations of parameter values of the model and bounded uncertainties introduced by the restriction of input and output spaces.

The construction of the ILC algorithm is based on results on the positive invariance of linear time-invariant discrete-time systems.

The chapter is organized as follows: In Sect. 2 some results on the positively invariant sets of linear discrete-time systems that will be used in the sequel will be presented. In Sect. 3, the ILC problem will be presented and an input adaptation law from one experiment to the next will be derived. The adaptation mechanism is based on the expression of the input and output as linear combinations of a set of basis functions. The projection of the input and output signals on the subspace spanned by the basis functions and the modelling errors introduce uncertainties of the parameters of the model. An ILC algorithm tolerant of polyhedral uncertainties of the model will be presented in Sect. 4. The algorithm will be illustrated by an example presented in Sect. 6. Finally, in Sect. 7, conclusions are drawn.

2 The ILC Problem

Throughout the paper, capital letters denote real matrices, lower case letters denote column vectors or scalars, $\mathbb{N}_+$ denotes the set of nonnegative integers, $\mathbb{R}^n$ denotes the real n-space and $\mathbb{R}^{n \times m}$ the set of real $n \times m$ matrices. The superscript of the variables denotes the number of the learning iteration i.e. the trial number of the experiment and the subscript indicates the element number of a vector or a matrix. For example, $y^k(t)$ is the output of the k-th experiment at time t and x_i is the i-th element of vector x. For two vectors to $x \in \mathbb{R}^n$ and $y \in \mathbb{R}^n$, $x \leq y$ is equivalent to $x_i \leq y_i$, $i = 1, 2, \ldots n$. Finally, given a square matrix H, $\lambda(H)$ denotes its eigenvalues. I is the identity matrix and $e \in R^n$ is the n-dimensional vector with $e_i = 1, i = 1 \ldots n$.

The systems to be controlled are single input-single output, linear, continuous time and time-invariant with input $u(t)$ and output $y(t)$ where the time t variable belongs to a bounded time interval $\mathcal{T} = [0, T]$. Thus, the system to be controlled is described by a functional relation

$$y(t) = S[u(\cdot)]$$

where $u(\cdot)$ denotes the function $u : \mathcal{T} \to \mathbb{R}$ and $y(t)$ the value of the function $y : \mathcal{T} \to \mathbb{R}$ at the time instant t. Without loss of generality we assume that the system is relaxed at the time instant t=0, that is $y(t) = 0$ for all $t \in \mathcal{T}$ when $u(t) = 0$ for all $t \in \mathcal{T}$.

The Iterated Learning Control problem is formulated as follows: Given a desired output trajectory $r(\cdot)$ defined in the interval $\mathcal{T}$, determine an iterated algorithm of the form

$$u^{k+1}(\cdot) = F[u^k(\cdot), y^k(\cdot), r(\cdot)]$$

such that the resulting control input $u^k(\cdot)$ for experiment k, converges to a function $u^*(\cdot)$ and the norm $\left\|\Delta r^k(t)\right\|$ of the deviation $\Delta r^k(t) = r(t) - y^k(t)$ of the resulting output $y^k(t)$ from the desired output $r(t)$ converges to 0 as $k \to \infty$, i.e. the output converges to the reference trajectory $r(t)$.

In this paper, we consider iterated algorithms of the form

$$u^{k+1}(\cdot) = u^k(\cdot) + P(\Delta r(\cdot)) \tag{1}$$

with $K \in \mathbb{R}$.

Rather than assuming a state space representation of the system, we prefer to use the approach presented in [9] where the input and output of the system are expressed as linear combinations of sets of orthonormal functions.

We assume that the input is restricted to a set $\mathcal{U}$ spanned by n_u functions f_i which define a basis of finite dimension of this set, (i.e. $f_1, f_2, \ldots, f_{nu}, \langle f_i, f_j \rangle = \delta_{ij}$, where δ_{ij} is the Kronecker delta). An arbitrary input signal can thus be expressed as a linear combination of the functions of the basis:

$$u(t) = \sum_{i=1}^{n_u} a_i f_i(t) \tag{2}$$

Then the control input $u^k(t)$ at the k-th experiment, can be expressed as:

$$u^k(t) = \sum_{i=1}^{n_u} a_i^k f_i(t) \tag{3}$$

and we can define $a^k = [a_1^k, a_2^k, \ldots, a_{n_u}^k]^T$ where $a_i^k, i = 1, \ldots, n_u$ are the coefficients for the input $u^k(t)$.

The output $y(t)$ can be expressed as a linear combination of another set of basis functions of finite dimension that comprises the basis functions used to describe $u^k(t)$. This basis is then divided into components of $\mathcal{U}$ and $\mathcal{V}$, where $\mathcal{V}$ is a complementary set of $\mathcal{U}$. The output of the k-th trial can then be expressed as:

$$y^k(t) = \sum_{i=1}^{n_u} b_i^k f_i(t) + \sum_{i=1}^{n_m} c_i^k g_i(t) \tag{4}$$

with $g_i(t) \ i = 1, 2, \ldots, n_m, \ n_u + n_m = n_y$, where $g_i(t)$ are the elements of a finite dimension basis of $\mathcal{V}$ and $b_i^k \in \mathbb{R}, \ c_i^k \in \mathbb{R}$. If $b^k = [b_1^k, b_2^k \ldots b_{n_u}^k]^T, \ c^k = [c_1^k, c_2^k \ldots c_{n_m}^k]^T$ and the system to be controlled is linear then we can always find a matrix L_p such that:

$$\begin{bmatrix} b^T & c^T \end{bmatrix}^T = L_p a^T \tag{5}$$

Let a^* be the vector of coefficients of the optimal input $u^*(t)$ corresponding to an output equal to the reference trajectory $r(t)$ and $\begin{bmatrix} b^{*T} & c^{*T} \end{bmatrix}^T$ be the coefficient vector for $r(t)$. We define:

$$\varepsilon_u^k = a^k - a^* \tag{6}$$

and

$$\varepsilon_y^k = \begin{bmatrix} b^k \\ c^k \end{bmatrix} - \begin{bmatrix} b^* \\ c^* \end{bmatrix} \tag{7}$$

Since the functions $f_i(t)$ are the same for every input $u(t)$ the adaptation law (1) is reduced to an adaptation law of the coefficients a_i^k. We choose the ILC law for updating the coefficient vectors to be:

$$a^{k+1} = a^k + KF\varepsilon_y^k$$

with $K \in \mathbb{R}^{n_u \times n_u}$ and $F \in \mathbb{R}^{n_u \times n_y}$

Since

$$\varepsilon_y^k = L_p \varepsilon_u^k \tag{8}$$

it is easily shown that

$$\varepsilon_u^{k+1} = (I + KFL_p)\varepsilon_u^k \tag{9}$$

where I is the identity matrix. The asymptotic stability of system (9) guarantees the convergence of the solution of the ILC algorithm.

The matrix $F \in \mathbb{R}^{n_u \times n_y}$ defines the projection operator of the set of output basis functions on $\mathcal{U}$. Choosing to restrict the basis to $\mathcal{U}$ results to:

$$F = \begin{bmatrix} I_{n_u \times n_u} & 0_{n_u \times n_m} \end{bmatrix} \tag{10}$$

where the subscript of matrices denotes their size. By this choice we do not need to define the basis $g_i(t)$ and consequently c but $u^*(t) : r(t) = Pu^*(t)$ may not exist in $\mathcal{U}$. In this case, the stability of system (9) guarantees the convergence to a value u^{**} such that the norm of the error $\|\Delta r(t)\| = \|r(t) - y(t)\|$ may not attain its minimal value for $u \in \mathcal{U}$.

The matrix FL_p can be computed from the data of n_f experiments with an appropriate choice of input functions. However such a computation is not free of errors. For this reason we assume that the matrix $L_f = FL_p$ is not known but it belongs to a convex polyhedron of the $n_u \times n_u$ real space with vertices L_{fi} $i = 1, 2, \ldots, n_u$, that is

$$L_f = \sum_{i=1}^{n_u} r_i(L_{f0} + L_{fi}) \tag{11}$$

with

$$\sum_{i=1}^{n_u} r_i = 1 \quad r_i \geq 0 \quad i = 1, 2, \ldots, n_u,$$

L_{f0} being the matrix computed by a modeling approach [9]. Thus, the determination of the gain matrix K can be viewed as a robust control design problem. A solution to this problem, by taking into account constrained uncertainties as in (11), is developed in the following sections. To this end, the results of the theory of positive invariance of polyhedral sets for linear systems are used.

3   Positive Invariance of Polyhedral Sets

The theory of polyhedral positively invariant sets is used for the solution of constrained regulation problems when the aim of the designer is to confine, if possible, the trajectories of the controlled system to a set defined by linear inequalities. The problem of designing robust closed-loop controllers can be translated to such a problem if the uncertainty of the parameters is bounded by polyhedral constraints i.e. linear inequalities.

Consider a linear system described by a difference equation

$$x(k+1) = Ax(k) \tag{12}$$

with $x \in \mathbb{R}^n, A \in \mathbb{R}^{n \times n}$, and $k \in \mathbb{N}_+$.

Definition 1 A non empty subset Ω of $\mathbb{R}^n$ is said to be a positive invariant set of system (12) if all the trajectories starting from initial states in Ω remain in it for all $k \in \mathbb{N}_+$.

We consider convex polyhedral sets defined as:

$$\mathcal{P}(G, w) = \{x \in \mathbb{R}^n : Gx \leq w\} \tag{13}$$

with $G \in \mathbb{R}^{p \times n}, w \in \mathbb{R}^p, w > 0$ and $w \neq 0$.

Algebraic necessary and sufficient conditions for a polyhedral set $\mathcal{P}(G, w)$ to be positively invariant with respect to the linear system (12) are established in the following theorem [4].

Theorem 1 *The convex polyhedral set* $\mathcal{P}(G, w)$ *is a positively invariant set of system* (12), *if and only if there exists a matrix* $H \in \mathbb{R}^{p \times p}$ *with nonnegative elements such that*

$$GA - HG = 0$$

$$Hw \leq w$$

For the special case of symmetric polyhedral sets

$$\mathcal{R}(G, w) = \{x \in \mathbb{R}^n : -w \leq Gx \leq w\}$$

the following result has been established [5]:

Corollary 1 *The convex polyhedral set $\mathcal{R}(G, w)$ is a positively invariant set of system (12), if and only if there exists a matrix $H \in \mathbb{R}^{p \times p}$ with nonnegative elements such that*

$$GA - HG = 0$$

$$Hw \leq w$$

These algebraic conditions can be used for the development of control laws solving the Linear Constrained Regulation Problem, i.e. the determination of linear state feedback regulators when the state and/or input variables are subject to linear constraints and robust controllers when the uncertainty is subject to linear constraints.

Let $P(G, w)$ be the set where the linear state constraints are satisfied and

$$\mathcal{P}(D, \rho) = \{x \in \mathbb{R}^n : Du \leq \rho\}$$

the set of the constrained input.

Theorem 2 *The linear state feedback law $u = Fx$ is a solution of the LCRP if and only if the resulting closed loop system*

$$x(k+1) = (A + BF)x(k)$$

possesses a positively invariant set Ω satisfying the relations

$$\mathcal{P}(G, w) \subseteq \Omega \subseteq \mathcal{P}(DF, \rho)$$

$$\Omega \subseteq \mathcal{P}(G, w)$$

and all trajectories emanating from the set $\mathcal{P}(G, w)$ converge asymptotically to the origin.

Setting $\Omega = \mathcal{P}(G, w)$ from the above theorem we obtain the following result [6]:

Theorem 3 *The control law $u = Fx$ is a solution to the LCPR problem if there exist a matrix H and a real number β such that*

$$H \geq 0 \tag{14}$$

$$0 \leq \beta \leq 1 \tag{15}$$

$$GA + GBF = HG \tag{16}$$

$$Hw \leq \beta w \tag{17}$$

$$DFx^{(i)} \leq \rho \quad i = 1, 2, \ldots, n_v \tag{18}$$

where $x^{(i)}$ $i = 1, 2, \ldots, n_v$ are the vertices of the state constraints polyhedron $\mathcal{P}(G, w)$.

The matrix F can thus be calculated via a linear optimization problem minimising the objective function $J(F, H, \beta) = \beta$. It is worth noticing that the parameter β is a measure of the the rate of convergence of the trajectories of the resulting closed-loop system to the origin. It should also be noticed that in the case when no constraints on the input vector are imposed, then a solution to the LCRP is guaranteed if there exist a matrix H and a real number β satisfying only conditions (14)–(17).

For the special case of symmetric state constraints $-w \leq Gx \leq w$, the following result is established:

Corollary 2 *The control law $u = Fx$ is a solution to the LCPR problem if there exist a matrix H and a real number β such that*

$$0 \leq \beta \leq 1$$

$$GA + GBF = HG$$

$$|H|w \leq \beta w$$

$$DFx^{(i)} \leq \rho \quad i = 1, 2, \ldots, n_v$$

where $x^{(i)}$ $i = 1, 2, \ldots, n_v$ are the vertices of the state constraints polyhedron $\mathcal{R}(G, w)$.

An asymptotically stable linear system possesses polyhedral positively invariant sets but their complexity depends on the locus of the eigenvalues of matrix A. Necessary and sufficient conditions for the existence of polyhedral positively invariant sets of low complexity, that is with $2n$ faces are given in the following theorem: A suitable matrix H exists if the system (12) possesses polyhedral positive invariant sets of the form $\mathcal{P}(G, w)$. A sufficient condition that guaranties the existence of such positively invariant sets is presented in the next theorem [5].

Theorem 4 *The linear system (12) possesses positively invariant sets $\mathcal{R}(G, w)$ with $G \in \mathbb{R}^{n \times n}$ and rankG $= n$ if and only if the eigenvalues $\lambda_i = \mu_i \pm j\sigma_i$ of matrix A are in the open square $|\mu_i| + |\sigma_i| < 1$.*

Finally, the above results can be extended to establish conditions for the positive invariance of a polyhedral set $\mathcal{P}(G, w)$ with respect to a linear system with uncertain parameters.

Let us consider the linear system

$$x(k+1) = (A + KF)x(k) \tag{19}$$

where

$$F = \sum_{i=1}^{q} r_i F_i, \quad \sum_{i=1}^{q} r_i = 1, \quad r_i > 0 \tag{20}$$

Based on Theorem 1 the following corollary is established:

Corollary 3 *A necessary and sufficient condition for the polyhedral set $\mathcal{P}(G, w)$ to be positively invariant with respect to the system* (19) *for all matrices F given by relation* (20) *is the existence of matrices H_0 and H_i $i = 1, 2, \ldots, q$ such that*

$$G(A + KF) = H_i G \tag{21}$$

$$H_i w \leq w \tag{22}$$

$$H_i \geq 0 \tag{23}$$

Proof From (21)–(23) it follows that if there exist matrices H_0 and H_i $i = 1, 2, \ldots, q$ such that $G(A + KF_i) = H_i G$ for all F_i then by (20):

$$G(A + KF) = G(A + K \sum_{i=1}^{q} r_i F_i)$$

$$= G \sum_{i=1}^{q} r_i (A + KF_i)$$

$$= \left(\sum_{i=1}^{q} r_i H_i \right) G$$

and

$$\left(\sum_{i=1}^{q} r_i H_i \right) w = \sum_{i=1}^{q} r_i H_i w$$

$$\leq \sum_{i=1}^{q} r_i w$$

$$\leq w$$

for all $r_i \geq 0$ and $\sum_{i=1}^{q} r_i = 1$. Furthermore,

$$\sum_{i=1}^{q} r_i H_i \geq 0$$

Therefore, by virtue of Theorem 1, the polyhedral set is positively invariant with respect to system (19) for any matrix F satisfying relations (20). ∎

   The above results will be used for the derivation of an algorithm to solve the ILC problem as presented in the following section.

4   A Design Algorithm for Robust Convergence

We consider polytopic uncertainties, that is, we assume that the uncertainty matrix ΔL_p can be written as

$$\Delta L_p = r_1 L_1 + r_2 L_2 + \cdots + r_q L_q \tag{24}$$

with

$$r_1 + r_2 + \cdots + r_q = 1, \quad r_i \geq 0 \tag{25}$$

   For the ILC algorithm to converge, the system

$$\varepsilon_u^{k+1} = (I + K L_f) \varepsilon_u^k \tag{26}$$

with

$$L_f = L_0 + \Delta L_p$$

must be stable for all matrices ΔL_p satisfying relations (24) and (25).

   Based on the results of the previous section, the following iterative learning algorithm is developed:

Step 1:   Choosing an $a < 1$ reflecting the rate of convergence of ε^k to 0, and as a consequence of the convergence of parameters a^k to a^* determine a gain matrix K so that all eigenvalues of matrix $I + K L_{f0}$ are in the unity rectangle $|\sigma_i| + |\omega_i| \leq a < 1$. This is a necessary and sufficient condition for the system to have polyhedral positive invariant sets of low complexity [6]. The calculation of the gain matrix can be done by a standard eigenvalue assignment approach or by solving an LMI problem (choosing $a = \sqrt{2}/2$, for example).

Step 2: Determine the transformation matrix G transforming matrix $I + KL_{f0}$ to its real Jordan form H, that is $G(I + KL_{f0})G^{-1} = H$. In the case where the matrix $I + KL_{f0}$ has distinct real eigenvalues the lines of matrix G are the left eigenvectors of matrix $I + KL_{f0}$. Then

$$G(I + KL_{f0}) = HG \tag{27}$$

$$|H|e \le ae \tag{28}$$

Step 3: Set

$$H_0 = \begin{bmatrix} H & O_s \\ O_s & H \end{bmatrix}$$

Solve the linear programming problem

$$\min_{H_i, \beta}\{\beta\}$$
$$\begin{bmatrix} G \\ -G \end{bmatrix} KL_i = H_i \begin{bmatrix} G \\ -G \end{bmatrix}$$
$$(H_0 + H_i)\begin{bmatrix} e \\ e \end{bmatrix} \le \beta \begin{bmatrix} e \\ e \end{bmatrix} \tag{29}$$
$$H_0 + H_i \ge 0$$

for $i = 1, 2, \ldots, q$.

Then, the system (9) is stable and the corresponding iterative law guarantees the convergence of the parameters a^k of the control action $u^k(t)$ to the optimal ones a^* while admitting polytopic uncertainties, of the form (25).

Proof

$$I + K(L_{f0} + \Delta L) = I + K(L_{f0} + r_1L_1 + r_2L_2 + \cdots + r_qL_q)$$
$$= \sum_{i=1}^{q} r_i[I + K(L_{f0} + L_{fi})]$$

Therefore,

$$\begin{bmatrix} G \\ -G \end{bmatrix}[I + K(L_{f0} + \Delta L)] = \begin{bmatrix} G \\ -G \end{bmatrix} \sum_{i=1}^{q} r_i[I + K(L_{f0} + L_{fi})]$$
$$= \sum_{i=1}^{q} r_i(H_0 + H_i)\begin{bmatrix} G \\ -G \end{bmatrix}$$

and

$$\sum_{i=1}^{q} r_i (H_0 + H_i) \begin{bmatrix} e \\ e \end{bmatrix} \leq \sum_{i=1}^{q} r_i \beta \begin{bmatrix} e \\ e \end{bmatrix}$$

$$= \beta \begin{bmatrix} e \\ e \end{bmatrix}$$

which is a sufficient condition for the stability of the controlled system and the positive invariance of system

$$\varepsilon_u^{k+1} = (I + K(L_0 + \Delta L_p)\varepsilon_u^k \tag{30}$$

for any uncertainty (24)–(25). ∎

The input updating law at each iteration is:

$$u^{k+1} = u^k + P(\Delta r(t)) \tag{31}$$

where

$$P(\Delta r(t)) = [f_1(t) \quad \cdots \quad f_{nu}(t)] K L_0 \begin{bmatrix} \tilde{a}_1 \\ . \\ . \\ . \\ \tilde{a}_{n_u} \end{bmatrix}$$

Since $L_0 \tilde{a}$ is an estimation of the error $\Delta r(t)$, using the basis spanned by the functions $f_i(t)$, the coefficients $b^* = L_0 \tilde{a}_i \quad i = 1 \ldots n_u$ can be computed by applying a least squares method to achieve:

$$\min_{\tilde{a}} \int_0^T (\Delta r(t) - [f_1(t) \quad \ldots \quad f_{nu}(t)] b^*)^2$$

It should be noted that there is a trade-off between the initial choice of the eigenvalues of matrix $(I + K L_{f0})$ reflecting the rate of convergence of the parameters error to the origin and the magnitude of the uncertainty of the parameters described by ΔL reflected on the value of parameter β.

5 Constrained Iterative Learning Control

A gain matrix K resulting from the above ILC algorithm guarantees the convergence of the parameters a^k of the control action $u^k(t)$ to the optimal ones a^* but great deviations $\Delta u^k(t) \triangleq u^k(t) - u^*(t)$ are not excluded. It should be emphasized

that boundedness of parameter deviations $\varepsilon^k = a^k - a^*$ does not imply a uniform boundedness of the input error $\Delta u^k(t)$ for $t \in \mathcal{T}$. Indeed

$$\Delta u^k(t) = f^T(t)a^k - f^T(t)a^* = f^T(t)\varepsilon_u^k \tag{32}$$

and

$$\Delta u^{k+1}(t) = f^T(t)a^{k+1} - f^T(t)a^* = f^T(t)\varepsilon_u^{k+1} = f^T(t)(I + KL_f)\varepsilon_u^k$$

For

$$f^T(t)\varepsilon_u^k \leq \Delta u \tag{33}$$

to imply

$$f^T(t)(I + KL_f)\varepsilon_u^k(t) \leq \Delta u \tag{34}$$

for all $t \in \mathcal{T}$, it is necessary and sufficient [4] that there exists a scalar function $p(t)$ such that

$$f^T(t)(I + KL_f) = p(t)f^T(t) \tag{35}$$

$$0 \leq p(t) \leq 1$$

For these conditions to be satisfied it is necessary that the time-variant vector $f^T(t)$ is a left-eigenvector of the constant matrix $I + KL_f$. This condition can be satisfied only if $I + KL_f$ is the null matrix, which means that in the case when L_f is invertible, the gain matrix K must be chosen so that $K = -(L_f)^{-1}$. This however is not possible because matrix L_f is not known exactly. For this reason, only constraints on a distance between $u^k(\cdot)$ and $u^*(\cdot)$ can be considered.

5.1 Mean Value Constraints

The mean square value Δu_{rms}^k of the control input deviation $\Delta u^k(t) = u^k(t) - u^*(t)$ is defined by relation $\Delta \bar{u}_{rms}^k = \left(\frac{1}{T} \int_0^T (u^k(t) - u^*(t))^2 dt \right)^{1/2}$

Then, by virtue of (32) we get

$$(\Delta \bar{u}_{rms}^k)^2 = \frac{1}{T} \int_0^T (u^k(t) - u^*(t))^2 dt = \frac{1}{T} \int_0^T (f^T(t)\varepsilon_u^k)^2 dt \tag{36}$$

$$= \frac{1}{T} \int_0^T \varepsilon_u^{k^T} f(t) f^T(t) \varepsilon_u^k dt \tag{37}$$

$$= \varepsilon_u^{k^T} \frac{1}{T} \int_0^T f(t) f^T(t) dt \varepsilon_u^k \tag{38}$$

or

$$(\Delta \bar{u}_{rms}^k)^2 = \varepsilon_u^{k^T} \bar{F} \varepsilon_u^k \tag{39}$$

where

$$\bar{F} = \frac{1}{T} \int_0^T f(t) f^T(t) dt$$

Remark 1 In the case $f_i(t)$, $i = 1, 2, \ldots, n_u$ constitute a set of orthonormal functions then $\bar{F}$ is the identity $n_u \times n_u$ matrix.

Remark 2 A weighted mean square deviation can be defined as

$$\Delta \bar{u}_{Qrms}^k = \left(\frac{1}{T} \int_0^T (f^T(t) Q \varepsilon_u^k)^2 d \right)^{1/2} \tag{40}$$

where $Q \in \mathbb{R}^{n_u \times n_u}$, $Q = diag(q_1, q_2, \ldots, q_{n_u})$ with $q_1 \geq 0$. Then,

$$(\Delta \bar{u}_{Qrms}^k)^2 = \varepsilon_u^{k^T} Q \bar{F} Q \varepsilon_u^k$$

The weighted mean square deviation can be used if for example errors due to high frequency components (usually represented by high indexed $f_i(t)$, must be penalized.

Given an admissible mean square control deviation $\Delta u_{\max}$, the problem of mean-value constrained ILC consists in the determination of a bounded region $\mathcal{R}$

$$\mathcal{R} \subseteq \mathcal{Q}(\bar{F}, \Delta u_{\max}) \triangleq \varepsilon_u \in \mathbb{R}^{n_u} : \varepsilon_u^{k^T} \bar{F} \varepsilon_u^k < \Delta u_{\max} \tag{41}$$

such that if

$$\Delta \bar{u}_{Qrms}^k \in \mathcal{R}$$

then

$$\Delta \bar{u}_{Qrms}^{k+1} \in \mathcal{R}$$

In other words the problem is to determine a positively invariant set $\mathcal{R}$ of the iterated system (9) satisfying relation (41).

Having determined a positively invariant set $\mathcal{P}(G, e)$, a solution to this problem is obtained by determining the maximal value r^* so that

$$\mathcal{P}(G, r^* e) \subseteq Q(\bar{F}, \Delta u_{\max})$$

This can be achieved by determining the maximal value of λ such that

$$\max\{\lambda_1, \lambda_1, \ldots, \lambda_m\}$$

$$\lambda_i^2 v^{(i)^T} \bar{F} v^{(i)} \leq \Delta u_{\max} \quad i = 1, 2, \ldots, m$$

$v^{(i)}$ being the vertices of the polyhedron $\mathcal{P}(G, e)$.

6 Example

To illustrate the application of the above ILC algorithm, an example stated in [9] will be used.

Let the transfer function of the system (supposed to be unknown for the designer of the ILC algorithm) be:

$$G(s) = \frac{s + 8}{s^3 + 10s^2 + 30s + 8}$$

To approximate the input of the system we can use derivatives of the reference system and Laguerre polynomials as basis functions.

The Laguerre polynomials are generated as:

$$L_k(s) = \frac{\sqrt{2a}}{s + a} \left[\frac{s - a}{s + a}\right]^{k-1}, \quad a > 0, \quad k = 1, 2, \ldots$$

where a is a chosen parameter.

The input space $\mathcal{U}$ is determined by the choice of the orthogonal functions f_i. In this case:

$$\mathcal{U} = span\{\{r, \dot{r}, \ddot{r}\} \oplus \{L_1(s)r, \ldots, L_5(s)r\}\}$$

where $L_k(s), k = 1, .., 8$ are the Laguerre polynomials with $a = 0.3$.

The system is simulated over a time interval $[0, T]$, $\quad T = 3s$ and the sampling period is set to be $5ms$.

To determine L_{f0} the following modeling procedure based on n_u experiments. For each experiment the input is set to be $u(t) = f_i(t)$. Then $\tilde{a}_i \in \mathbb{R}^n$ with

$$\tilde{a}_i(j) = \begin{cases} 0 & if \quad j \neq i \\ 1 & if \quad j = i \end{cases}$$

and taking into account the relation

$$y_i(t) = [f_1(t) \quad f_2(t) \quad \ldots \quad f_{nu}(t)] \, L_f \tilde{a}_i \quad t \in 0, T]$$

the i-th column of matrix L_f can be computed using the least squares method.

To determine the gain matrix K an eigenvalue assignment approach is used and the desired eigenvalues are chosen such that $|\lambda_i| \leq 0.5$. Uncertainties of a magnitude less or equal to $0.03 * L_f(i,j)$ are also assumed in the L_f estimation procedure.

The reference trajectory $r(t)$ is chosen to be the step response of the system with transfer function

$$G_r(s) = \frac{1000}{(s + 10)^4}$$

and

$$u^{k+1}(t) = [f_1(t) \quad f_2(t) \quad \ldots \quad f_{nu}(t)] a^{k+1}$$

with

$$a^{k+1} = a^k - KL_{f0}\varepsilon^k$$

such that $L_{f0}\varepsilon^k$ is the least squares estimation of the error function $\Delta r^k(t) = r(t) - y^k(t)$. For the nominal model with $L_f = L_{f0}$, the reference and the systems trajectories after ten iterations are shown in Fig. 1.
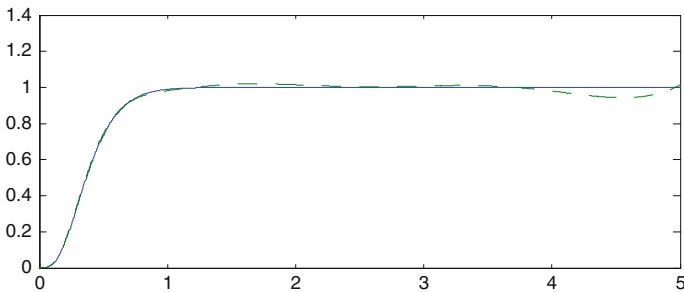
$$\nabla$$

For an L_f matrix equal to $1.3\,L_{f0}$ for $t \in [0, 5]$ of each trajectory, the same control strategy as for the nominal system is shown in Fig. 2.

For an L_i matrix greater than $1.37\,L_{f0}$ the optimization problem (29) does not have any solution.
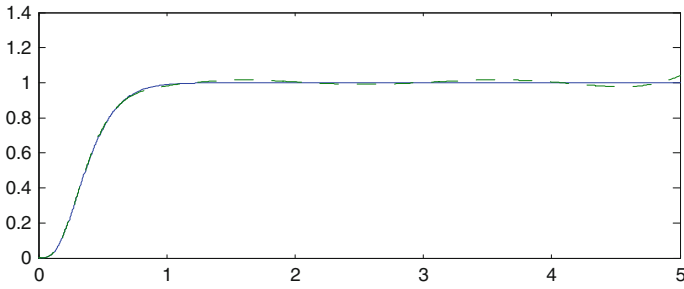
Fig. 1 The reference trajectory (-) and the output (- -) of the nominal system

Fig. 2 The reference trajectory (-) and the output (- -) of the uncertain System

7 Conclusion

In the present chapter a new robust ILC algorithm is proposed. A learning strategy based on the approximation of trajectories by finite dimensional basis functions is used. The input and output signals space is restricted to a space spanned by a finite number of functions fitting a target trajectory. Assuming polyhedral uncertainties for the model parameters, a robust ILC algorithm is presented based on the existence conditions of positive invariant polyhedral sets for the system ensuring the convergence of the learning algorithm. The algorithm is extended to provide a solution to the case where the deviation of the input function from a nominal trajectory must satisfy mean value constraints. To illustrate the design method, a numerical example has been presented. The method is presented in view of applications in the management and control of components of production and distribution networks such as Active Power Filters, inverters interfacing with renewable energies microgrids and wind turbines.

References

1. Amman N., Owens D. H.,& Rogers E. (1995), Iterative learning control for discrete time systems using optimal feedback and feedforward actions, *Proceedings of the 34th IEEE CDC*, New Orleans (pp. 1696–1701).
2. Amman N., Owens D. H.,& Rogers E. (1995), Iterative Learning Control for Discrete Time Systems with Exponential Rate of Convergence, Report Number 95/14, Center for Systems and Control Engineering.
3. Biegel B., Juelsgaard M., Kraning M., Boyd S., (2011),*Wind turbine pitch optimization*, IEEE International Conference on Control Applications (CCA), Denver CO, USA, September 28–30, (pp.1327 - 1334).
4. Bitsoris G., (1988), On the positive invariance of polyhedral sets for discrete-time systems, *Systems & Control Letters,* vol 11, (pp. 243–248).
5. Bitsoris G., (1988), Positively invariant polyhedral sets of discrete-time linear systems, International Journal of Control, vol. 47, No 6, (pp. 1713–1726).
6. Bitsoris G., and Vassilaki M., (1991), Optimization approach to the linear constrained regulation problem for discrete-time system, *International Journal of Systems Science,* vol 22, No 10 (pp. 1953–1960).
7. Dasgupta S., Sahoo S.K., Panda S.K, (2010), *Design of a Spatial Iterative Learning Controller for Single Phase Series Connected PV Module Inverter for Grid Voltage Compensation,*Power Electronics Conference (IPEC), 2010 International, Sapporo, Japan, June 21–24 (pp. 1980-1987).
8. Dasgupta S., Sahoo S.K., Panda S.K, Amaratunga G.A.J., (2011), *Single-Phase Inverter-Control Techniques for Interfacing Renewable Energy Sources With Microgrid—Part II: Series-Connected Inverter Topology to Mitigate Voltage-Related Problem Along With Active Power Flow Control,* IEEE Transactions on Power Electronics, vol. 26, no. 3, March 2011, (pp. 732–747).
9. Hammamoto K. and Sugie T., (2001), An iterative learning control algorithm with prescribed input-output subspace, *Automatica*, vol 37 (pp. 1803–1809).
10. Johnson K.E., Thomas N., (2009), *Wind farm control: Addressing the aerodynamic interaction among wind turbines*, *American Control Conference,* St. Louis, USA, June 10–12, (pp.2104 - 2109).
11. Johnson K.E., Thomas N., (2009), *Wind farm control: Addressing the aerodynamic interaction among wind turbines*, *American Control Conference,* St. Louis, USA, June 10–12, (pp. 2104 - 2109).
12. Laks J., Pao L., Alleyne A., (2011),Comparison Of Wind Turbine Operating Transitions Through the Use of Iterative Learning Control, *American Control Conference on O'Farrell Street*, San Francisco, CA, USA,June 29 - July 01, (pp. 4312–4319).
13. Luo A., Xianyong Xu, Lu Fang, Houhui Fang, Jingbing Wu, Chuanping Wu, (2010), *Feedback-Feedforward PI-Type Iterative Learning Control Strategy for Hybrid Active Power Filter With Injection Circuit,*IEEE Transactions on Industrial Electronics, vol. 57, no. 11, November 2010, (pp. 3767–3779).
14. Moore K. L., Dahleh M. & Bhattacharyya S. P., (1992). Iterative learning control: A survey and new results., *Journal of Robotic Rystems*, vol 9, No 5, (pp. 563–594).m.
15. Owens D.H., (1993),2D Systems theory and iterative learning control, *Proc. 2nd European Control Conference*, Groningen, (pp. 1506–1509).
16. Sugie T., Ono T., (1991), An iterative learning control law for dynamical systems, Automatica, vol 27, No 4, (pp. 729–732).

17. Vita V., Vassilaki M. and Chatzarakis G., (2010), Analysis and Causal Formulation Proof of an Optimal Iterative Learning Algorithm, *Intelligent Control and Automation*, vol 1, (http: // www.SciRP.org/journal/ica).

18. Weizhe Q., Panda S.K., Jian-Xin Xu, (2004),*Torque ripple minimization in PM synchronous motors using iterative learning control,* IEEE Transactions on Power Electronics,Volume:19, Issue: 2 March 2004, (pp.272 – 279).

19. Xiaoming Zha, Tao Qian, Sun Jianjun, Chen Yunping, (2002), *Development of Iterative Learning Control Strategy for Active Power Filter*, IEEE Canadian Conference on Electrical and Computer Engineering (CCEC 2002), vol 1, (pp. 240 – 245).

Damping of Power System Oscillations with Optimal Regulator

**S.J.P.S. Mariano, J.A.N. Pombo, M.R.A. Calado
and J.A.M. Felippe de Souza**

Abstract This chapter presents a study of the small signal stability applied to an electric power system, with the consideration of the Power System Stabilizer and using the optimal control theory. A new technique is proposed, which is based on pole placement using optimal state feedback for damping electromechanical oscillation under small signal. The proposed technique builds the weighting matrices of the quadratic terms for the state vector Q and control vector R in such a way that the system response also obeys conventional criteria for the system pole location. Besides, when the number of output variables is less than the order of the system, it is proposed an optimal output feedback approach, where a set of closed-loop system poles is allocated to an arbitrary position by means of a suitable output feedback. The Power Sensitivity Model is used to represent the electric power system. Information about the stability of the electric power system, when subjected to small disturbances, is illustrated by using numerical examples.

S.J.P.S.Mariano (✉) · J.A.N. Pombo · M.R.A. Calado · J.A.M.F. de Souza
University of Beira Interior, Covilhã, Portugal
e-mail: sm@ubi.pt

J.A.N. Pombo
e-mail: d1232@ubi.pt

M.R.A. Calado
e-mail: rc@ubi.pt

J.A.M.F. de Souza
e-mail: felippe@ubi.pt

S.J.P.S.Mariano · J.A.N. Pombo · M.R.A. Calado
IT—Instituto de Telecomunicações, Covilhã, Portugal

1   Introduction

The behaviour analysis of the electromechanical oscillations is fundamental to guarantee a safe and reliable operation of Electric Power Systems, thus being a topic well studied in the literature.

Along the years, different approaches for power system control have been proposed. Recent applications of Flexible AC Transmission System (FACTS), devices for evaluating system damping using various techniques, are reported in the literature [1, 2], requiring detailed information of the whole power system for the system control. It is not easy to realize this control, since the selection of appropriate feedback signals to FACTS controller is important, being the machine speed and rotor angle, without doubt, the best feedback signals to damp oscillations.

Unlike the synchronous generator stabilizer, the speed deviation and the rotor angle variables are not readily available in FACTS controller. Thus, the benefit of damping the oscillations depends on the location of FACTS controller.

Other recently employed methods combine the Automatic Voltage Regulators (AVR) with the Power System Stabilizer (PSS) [3–5]. The first controller provides simultaneously the regulation of the machine terminal voltage, to which it is attached, by the automatic voltage regulators (AVR) and the damping to local oscillations that corresponds to the PSS.

This chapter proposes two methods for the damping of power system oscillations based on pole placement.

One proposed method constructs a linear quadratic regulator with assigned closed-loop poles, and yields a solution that enables the design of an optimal regulator. However, the design of the linear quadratic regulator has one major difficulty: how to specify the weighting matrices of the quadratic terms for the state vector Q and control vector R [6–8]. To assign appropriate values for matrices Q and R in a systematic manner, avoiding the burdensome process of search by trial and error is addressed.

The other method, proposed when the number of output variables is less than the order of the system, is carried out for the optimal output feedback approach, where a set of closed-loop system poles is allocated to an arbitrary position by means of a suitable output feedback. Since the location of the poles can be arbitrary, the first step in pole assignment is to decide on their location. To choose the location of the poles, one should bear in mind that the required physical effort is dependent on the distance to the imaginary axis. Particularly, open loop zeros attract poles, and the removal of the poles near zero is very difficult. Thus, for an arbitrary location, the control vector could lead to physically or economically undesired action.

Results for small-signal stability studies of a single-machine connected to an infinite bus is also shown in the chapter; the Power Sensitivity Model (PSM) is used to represent the electric power system [9, 10], considering the Power System Stabilizers (PSS) as an additional source to damping electromechanical oscillations, and is compared with the designed optimal regulator.

This chapter is organized as follows: firstly, the main results of the optimal control theory are presented; next, both the proposed methods and the algorithms to design the optimal PSS regulators are developed; then, the power sensitivity and PSS test models are described; after, the illustration results are presented; and finally, in the conclusion, we summarize how the optimal regulators based on proposed methods yield results that are feasible, robust and accordingly to the desired performance.

2 Optimal Control Theory

In this chapter we select the most relevant issues of the Control Theory that enables us to determine controllers for linear time invariant systems represented in state equations by using optimal feedback. Particularly, we focus on methods that allow finding a solution for optimal control through state feedback, as well as through output feedback.

The state feedback needs that all the state variables can be measured with precision. In most of the cases of linear time invariant systems (LTI), only a few linear combinations of the state variable can be measured with precision and, to overcome this limitation, the output feedback is used.

2.1 Optimal State Feedback

The aim of optimal control consists in finding an optimal control law $u(t) = g(x(t), t)$ for the system $\dot{x} = g(x(t), u(t), t)$ that drives any initial state $x(t_0)$ to a final state $x(t_1)$, which minimizes the performance index given by the following equation

$$J = \int_{t_0}^{t_1} h(x(t), u(t), t) dt. \tag{1}$$

The controller find in that way is called the deterministic optimal linear regulator.

Given a linear time invariant system

$$\dot{x}(t) = Ax(t) + Bu(t), \tag{2}$$

the performance index given by the expression

$$J = \int_{t_0}^{t_1} \left(x^T(t)Qx(t) + u^T(t)Ru(t) \right) dt, \tag{3}$$

where Q is a symmetric positive semi-definite matrix; this being a symmetric matrix whose eigenvalues as well as its pivots are non-negative.

The value $x^T(t)Qx(t)$ is a joint measure of the extension for which the state at time t is brought from the zero state. The elements of the matrix Q represent the weighs that are assigned to each component of the state, depicting in that way an cumulative deviation index for $x(t)$, with respect to the zero state and for the time interval $[t_0, t_1]$.

To avoid potential physical difficulties, the performance index also includes the input $u(t)$, where R is a symmetric positive semi-definite matrix. The incorporation of the second term in the performance index tries to induce a reduction in the amplitude of the inputs when the minimization of (3) is being done.

The Hamilton Jacobi [11] can be written as

$$\frac{\partial f}{\partial t} = -\min_u \left[x^T Q x + u^T R u + \left(\frac{\partial f}{\partial t} \right)^T (Ax + Bu) \right]. \tag{4}$$

Introducing the following relation

$$f(x,t) = x^T P x, \tag{5}$$

where P is a symmetric positive semi-definite square matrix, we have

$$\frac{\partial f}{\partial t} = x^T \frac{\partial}{\partial t} P x, \tag{6}$$

and

$$\frac{\partial f}{\partial x} = 2Px, \tag{7}$$

$$\left(\frac{\partial f}{\partial x} \right)^T = 2x^T P. \tag{8}$$

Substituting Eqs. (6) and (8) in (4) we get

$$x^T \frac{\partial}{\partial t} P x = -\min_u \left[x^T Q x + u^T R u + 2x^T P (Ax + Bu) \right], \tag{9}$$

in order to minimize u in Eq. (9)

$$\frac{\partial \left(\frac{\partial f}{\partial t} \right)}{\partial u} = 2u^T R + 2x^T P B = 0, \tag{10}$$

the previous Eq. (10) can be rewritten obtaining then

$$u_{opt} = -R^{-1}B^T Px \qquad (11)$$

or

$$u_{opt} = -Kx, \qquad (12)$$

where

$$K = R^{-1}B^T P. \qquad (13)$$

Substituting Eqs. (11) in (9) gives

$$x^T \dot{P}x = -x^T(Q + 2PA - PBR^{-1}B^T P)x, \qquad (14)$$

for which

$$\dot{P} = -PA - A^T P - Q + PBR^{-1}B^T P. \qquad (15)$$

Equation (15) is a nonlinear ordinary differential equation where the coefficients of $P(t)$ are found by inverse time integration. Kalman has shown that all $P(t)$ converge to a constant value as long as t_1 is infinite, that is very far from t_0, where Eq. (15) can be rewritten as

$$PA + A^T P + Q - PBR^{-1}B^T P = 0, \qquad (16)$$

which is known as Riccati equation.

Riccati equation is the key to obtain the optimal controller. Once the matrices Q and R are known, the matrix P can be obtained by solving the Riccati equation. From Eq. (11) one gets the optimal control vector u. However, the relationship between the weighting matrices and the closed-loop poles is not simple. The most common procedure to specify the matrix Q is search by trial and error. Different matrices Q_i result in different gain matrices K_i, which in turn result in different dynamic performances for the closed-loop system. There are many possibilities to test by trial and error, which makes this procedure burdensome.

The Optimal Control Theory here introduced, with the aim to determine the optimal controller, is well known for a long time. However, the task to design a optimal controller remains a problem hard to achieve even nowadays. This is due to the difficulty to select matrices R and Q. Different pairs of matrices (Q_i, R_i) will lead to different gain matrices K_i, resulting in different outputs for the same closed loop system. Methods for obtaining the pair of matrices (Q, R) will be analysed in the next section.

Fig. 1 Schematic representation of the non-controlled system
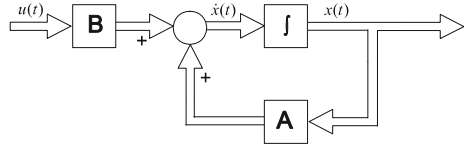
Fig. 2 System controlled by optimal state feedback
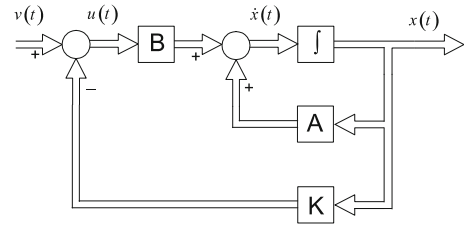
In a nutshell, given the LTI system depicted in Fig. 1,

$$\dot{x}(t) = Ax(t) + Bu(t), \tag{17}$$

and assuming that all state variables can be measured at any instant t, it is possible to implement a linear time invariant controller of the form

$$u(t) = -Kx(t) + v(t), \tag{18}$$

with

K being the constant feedback gain matrix, and
$v(t)$ being an additional input

If the controller (18) is applied to system (17), one will get a new closed loop system, as shown in Fig. 2, which will have the following state space model

$$\dot{x}(t) = (A - BK)x(t) + Bv(t). \tag{19}$$

The stability of the controlled system will not only be dependent on A and B, obviously, but also on the gain matrix K, and the eigenvalues of the controlled system will be a function of K. Hence, by choosing an appropriate K, we can improve the stability of the system. As a matter of fact, it is possible to choose K in order to place the eigenvalues anywhere in the complex plane, as we will see in the next section.

2.2   Optimal Output Feedback

The control of linear systems by optimal output feedback is known as a funda-mental problem in control theory that has attracted the attention in the last decades. This happens due to the fact that in a great deal of the practical applications only partial information of the state variable of the system are available from the output measurements, and also because it is where interesting results has been achieved [12–16].

Although the majority of the previously referred cases present a limitation with respect to the order of the system n, as well as in the number of its inputs and outputs, actually $m + r \geq n + 1$ where $m = rank(B)$ and $r = rank(C)$, there are also other cases which show that there is a solution to the optimal output control problem under a less restrictive condition $mr \geq n$ but nevertheless increase an additional restriction $rank(E) = n$, where E is a $n \times mr$ matrix for which its col-umns are given by $CA^k B$, with $k = 0, 1, \ldots, n - 1$.

So, this section presents some results from the optimal control theory for time invariant systems, which will allow us to determine a feedback gain matrix directly from the system output. Objectively that will allow us to solve this problem in the less restricted case $n \times mr$, and calculate the constants gain matrix, minimizing its performance index [17].

Thus, given a linear time invariant system

$$\begin{aligned} \dot{x}(t) &= Ax(t) + Bu(t) \\ y(t) &= Cx(t) \end{aligned}, \tag{20}$$

with $x \in \Re^n, u \in \Re^m, y \in \Re^r$, having all the state variables available, the optimal controller is given by

$$u(t) = -Kx(t) + v(t). \tag{21}$$

As seen in the previous section, the gain matrix K can be figured out by using the algebraic solution of the Riccati equation.

Now suppose that a restriction is introduced: the control variable $u(t)$ is acquired directly from the system output, i.e.,
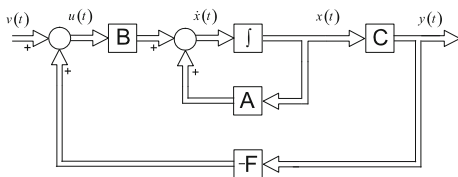
$$u(t) = -Fy(t) + v(t) \Leftrightarrow u(t) = -FCx(t) + v(t), \tag{22}$$

where F is the feedback gain matrix to be determined.

If the controller (22) is applied to system (20), one will get a new closed loop system, as shown in Fig. 3, which will have the following state space model

$$\dot{x}(t) = (A - BFC)x(t) + Bv(t). \tag{23}$$

Fig. 3 System controlled by optimal output feedback

3 Optimal Regulators Design

3.1 *Optimal State Feedback Design*

The proposed approach, based on optimal pole shift [18], assumes that the pair (A, B) in (2) is controllable, as was previously stated, and the coefficient matrix A has distinct eigenvalues.

Consider now a specific mode of the system, which can be obtained from an appropriate linear transformation. The above assumption guarantees that the selected mode is controllable so that it can be chosen a non-singular matrix M according to:

$$M^{-1}AM = \begin{bmatrix} A_{11} & \cdots & 0 \\ \vdots & \ddots & \vdots \\ 0 & \cdots & A_{nn} \end{bmatrix}, \tag{24}$$

and

$$M^{-1}BR^{-1}B^T\left(M^{-1}\right)^T = \begin{bmatrix} V_{11} & \cdots & V_{1n} \\ \vdots & \ddots & \vdots \\ V_{1n}^T & \cdots & V_{nn} \end{bmatrix}, \tag{25}$$

where $A_{11} = \begin{bmatrix} \alpha & \beta \\ -\beta & \alpha \end{bmatrix}$ and $V_{11} = \upsilon_o \begin{bmatrix} 1 & 0 \\ 0 & \upsilon \end{bmatrix}$, with $\upsilon_o > 0, 0 \le \upsilon \le 1$.

The first two columns of the transformation matrix A_{11} result from the real part and imaginary part of the eigenvectors of A, corresponding to the eigenvalues $\alpha \pm j\beta$. Let this transformation matrix be M_1, being the other columns of the transformation matrix irrelevant.

The matrix V_{11} is symmetric and positive semi-definite in general. Thus it can be diagonalized and the arbitrary ordering of the eigenvalues is possible with an orthogonal transformation matrix, append identity matrix to this orthogonal matrix to form a block diagonal matrix with the size of A. Let us denote this matrix as M_2, then the transformation matrix M is $M = M_1 M_2$.

The selection of weighting matrix R is arbitrary and is used as scaling factor for the input channels. Nevertheless, scaling R for the inputs of the system has no effect, since it will only result in a same amount of scaling on Q.

The weighting matrix Q is to be constructed according to the pole assignment; let Q_{11} be a positive semidefinite matrix with the same size as A_{11}, and set the weighting matrix Q that satisfies

$$Q = \left(M^{-1}\right)^T \begin{bmatrix} Q_{11}/v_o & 0 \\ 0 & 0 \end{bmatrix} M^{-1}. \tag{26}$$

Then the eigenvalues of A_{11} can be shifted while keeping all other eigenvalues of A unchanged.

3.1.1 Weighting Matrices Specification

When a real pole is to be shifted, the matrices A_{11}, V_{11}, Q_{11} are reduced to scalar. In this case the region of optimal closed-loop poles assigned is readily determined. It turns out that a real pole, either stable or unstable, can only be shifted along the real axis towards the left-half plane, and besides the absolute value of the closed-loop pole is larger than that of the open-loop pole. Moreover, Q can be expressed by (26), with $Q_{11} = \left(\alpha_d\right)^2 - \left(\alpha\right)^2$.

When a complex conjugate pole is to be shifted, the matrices A_{11}, V_{11}, Q_{11} are 2 by 2 matrices. In this case the Hamilton matrix assumes the form

$$H = \begin{bmatrix} A_{11} & V_{11} \\ -Q_{11} & -A_{11}^T \end{bmatrix}, \tag{27}$$

and is associated with the regulator problem of the second order system. Let the entries of Q_{11} be described as:

$$Q_{11} = \begin{bmatrix} q_1 & q_2 \\ q_3 & q_4 \end{bmatrix}. \tag{28}$$

Then, the characteristic equation of H has the form:

$$s^4 + C_2 s^2 + C_0 = 0. \tag{29}$$

The coefficients C_2 and C_0 turn out to be

$$C_2 = 2\left(\beta^2 - \alpha^2\right) - \bar{C}_2, \tag{30}$$

$$C_0 = \left(\beta^2 + \alpha^2\right)^2 - \bar{C}_0. \tag{31}$$

with

$$\overline{C}_2 = q_1 + v\, q_3 \tag{32}$$

$$\overline{C}_0 = \left(\alpha^2 + v\,\beta^2\right)q_1 + 2(1-v)\alpha\,\beta\,q_2 \\ + \left(v\alpha^2 + \beta^2\right)q_3 + v\left(q_1 q_3 - q_2^2\right) \tag{33}$$

where, $\bar{C}_2$ and $\bar{C}_0$ represent the terms that depend on the weighting matrix Q_{11}.

Let the weighting matrix Q_{11} correspond to the optimal closed-loop poles $\alpha_d \pm j\beta_d$, then the coefficients C_2 and C_0 are described by

$$C_2 = 2\left(\beta_c^2 - \alpha_c^2\right), \tag{34}$$

$$C_0 = \left(\beta_c^2 + \alpha_c^2\right)^2. \tag{35}$$

Assume that the 2 by 2 weighting matrix Q_{11} is restricted to be singular. In this case it can be described in dyadic form as

$$Q_{11} = \begin{bmatrix} \rho\cos^2(\theta) & \rho\sin(\theta)\cos(\theta) \\ \rho\cos(\theta)\sin(\theta) & \rho\sin^2(\theta) \end{bmatrix}, \tag{36}$$

where $\rho > 0$ and $0 \le \theta < \pi$.

Now the parameters $\bar{C}_2$ and $\bar{C}_0$ can be expressed in terms of ρ and θ as

$$\bar{C}_2 = \frac{\rho}{2}\left((1+v) + (1-v)\cos(2\theta)\right), \tag{37}$$

$$\bar{C}_0 = \frac{\rho}{2}\left(\alpha^2 + \beta^2\right)\left((1+v) + (1-v)\cos(2\theta + \phi)\right), \tag{38}$$

where ϕ satisfies

$$\sin(\phi) = \frac{-2\alpha\beta}{\alpha^2 + \beta^2}, \cos(\phi) = \frac{\alpha^2 - \beta^2}{\alpha^2 + \beta^2}. \tag{39}$$

Solving the system given by (37) and (38) one can obtain ρ and θ through (36). Then substituting in (26), the eigenvalues of A_{11} can be shifted, while keeping all other eigenvalues of A unchanged. In order to shift all poles together, the weighting matrix Q and the corresponding optimal feedback gain matrix K becomes, respectively,

$$Q = \sum_{i=0}^{n_x} Q_i \quad \text{and} \quad K = \sum_{i=0}^{n_x} K_i. \tag{40}$$

3.1.2 Algorithm to Specify the Weighting Matrices

The adopted method to perform the pole shifting is now summarized in the following steps:

Step1   Calculate the feedback closed-loop eigenvalues and eigenvectors corresponding to gain matrix K_i.

Step2   Choose a transformation matrix M such that the poles to be shifted of the partitioned matrices A_{11} and V_{11} are either real or complex conjugate.

Step3   Find a weighting matrix Q_{11} with which the desired pole positioning is accomplished.

Step4   Calculate the weighting matrix Q and the corresponding optimal feedback gain K for the whole system; then form a closed-loop system with K.

Step5   Go to Step1 unless there is no remaining pole to be shifted.

Step6   Calculate the sum of the matrices Q and K to obtain the weighting and optimal feedback gain matrices, which achieve the desired pole location.

An illustration of the proposed algorithm is shown in the flowchart of Fig. 4.

3.2 Optimal Output Feedback Design

Consider the system given by (20); the problem lies in finding a gain matrix F that guarantees

$$\sigma(A + BFC) = \Lambda, \tag{41}$$

with $\Lambda = \{\Lambda_1, \Lambda_2\}$ and $\Lambda_1 = \{\lambda_1, \ldots, \lambda_r\}$ and also $\Lambda_2 = \{\lambda_{r+1}, \ldots, \lambda_n\}$.

To achieve this we now present a method based on [16], in a synthesized form, leaving the proof of the stated lemmas to the author, in which the algorithm initially assigns Λ_1, and then Λ_2 without changing Λ_1.

Consider $i = 1, 2, \ldots, r$; the relationship between the eigenvectors u_i associated to the eigenvalues λ_i is given by
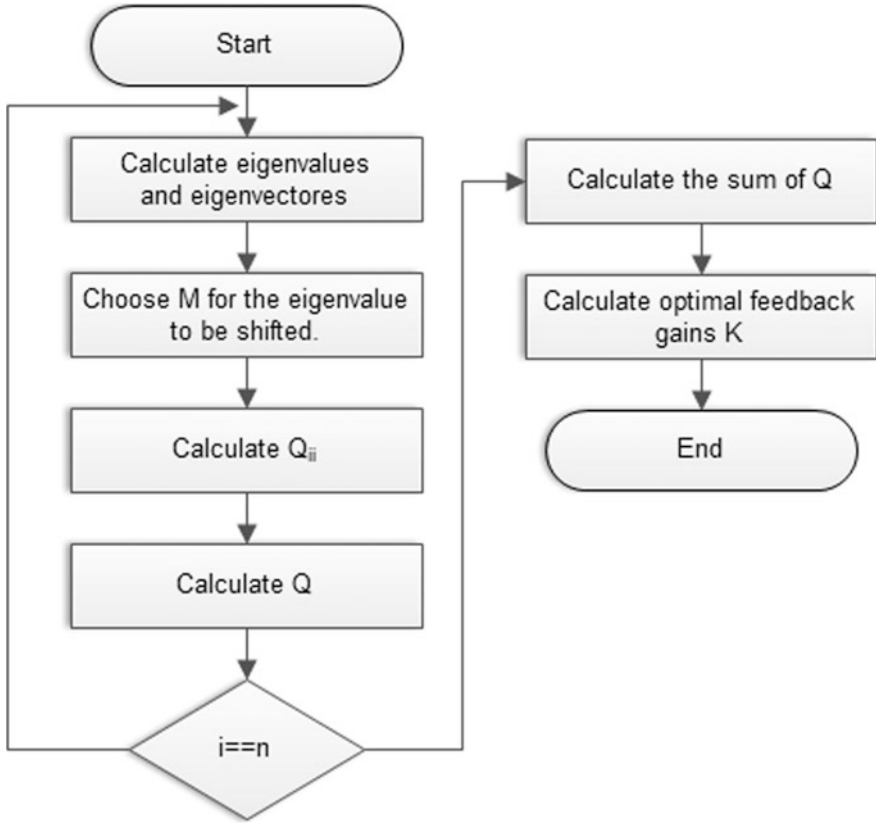
$$[A + BFC]u_i = \lambda_i u_i. \tag{42}$$

Now defining

$$\psi_i = FCu_i, \tag{43}$$

and writing (42) as

$$T(\lambda_i)\begin{bmatrix} u_i \\ \psi_i \end{bmatrix} = 0, \tag{44}$$

Fig. 4 Flowchart of the proposed algorithm to specify the weighting matrices

where $T(\lambda_i) = [A - \lambda_i I, B]$ and, if $\Psi_r = [\psi_1, \psi_2, \ldots, \psi_r]$, the Eq. (48) is given by the Sylvester matricidal equation namely

$$U_r \Lambda_r - A U_r = B \Psi_r, \tag{45}$$

with $U_r = [u_1, u_2, \ldots, u_r]$ and $\Lambda_r = diag[\Lambda_1]$.

So, using Eq. (43) to any index i the gain matrix F is given by

$$F = \Psi_r [C U_r]^{-1}, \tag{46}$$

where the matrix $C U_r$ must be invertible and this is possible as long as $rank(C) = n$ and if Λ_1 do not have any eigenvalue of A too.

Now consider $j = r+1, r+2, \ldots, n,$

$$V_i = (\lambda_i I - A)^{-1} B, \tag{47}$$

$$a_i = \left[a_{i1}\, a_{i2} \ldots a_{i(m-1)}\right]^T, \tag{48}$$

$$a_j = \left[a_{j1}\, a_{j2} \ldots a_{j(r-1)}\right]^T, \tag{49}$$

and

$$Y_j = \left[CAT_2\left(\lambda_j I - \bar{C}AT_2\right)^{-1}\right]^T, \tag{50}$$

where $\bar{C}$ can be any $(n-r) \times n$ matrix that satisfies

$$\begin{bmatrix} C \\ \bar{C} \end{bmatrix} = [T_1, T_2]^{-1} = T^{-1}, \tag{51}$$

with T a non singular matrix.

The Eqs. (47) and (50) conduct to the following expressions of Ψ_r and U_r

$$\Psi_r = [a_1, a_2, \ldots, a_r], \tag{52}$$

$$U_r = [V_1 a_1, V_2 a_2, \ldots, V_r a_r]. \tag{53}$$

The equation that relates Λ_1 with Λ_2 is given by

$$a_i^T M_{ij} a_j, \tag{54}$$

where M_{ij} is a matrix $m \times r$ given by

$$M_{ij} = V_i^T \left[\bar{C}^T Y_j + C^T\right], \tag{55}$$

or

$$M_{ij} = C\left[I + AT_2\left[\lambda_j I - \bar{C}AT_2\right]^{-1}\bar{C}\right][\lambda_i I - A]^{-1} B. \tag{56}$$

Solving the system of Eq. (54) with respect to a_i and a_j, consecutively we get (52) and (53) that enables us to obtain the gain matrix F given by Eq. (46).

3.2.1 Algorithm to Calculate the Optimal Output Feedback Gains

The adopted method to perform the pole shifting is now summarized in the following steps:

Step1 Select the size of the matrix I, which represents the state variables accessible, $y(t) = Cx(t) \Leftrightarrow y(t) = \begin{bmatrix} 0 & \vdots & I \end{bmatrix} x(t)$, guaranteeing $mr \geq n$.

Step2 Calculate $V_i = (\lambda_i I - A)^{-1} B$, for every $i = 1, 2, \ldots, r$.

Step3 Calculate $M_{ij} = C \begin{bmatrix} I + AT_2 [\lambda_j I - \bar{C} AT_2]^{-1} \bar{C} \end{bmatrix} [\lambda_i I - A]^{-1} B$, for every $j = r + 1, r + 2, \ldots, n$.

Step4 Solve the system $a_i^T M_{ij} a_j$, where $a_i = \begin{bmatrix} a_{i1} a_{i2} \ldots a_{i(m-1)} \end{bmatrix}^T$ and $a_j = \begin{bmatrix} a_{j1} a_{j2} \ldots a_{j(r-1)} \end{bmatrix}^T$

Step5 Calculate U_r, defined from (53). In the case of a conjugate pair of complex eigenvalues appears (λ_k and $\lambda_{k+1} = \bar{\lambda}_k$), U_r is define by $U_r = [V_1 a_1, V_2 a_2, \ldots, R_e\{u_k\}, I_m\{u_k\}, \ldots, V_n a_n]$ where $R_e\{u_k\} = R_e\{V_k\} a_k - I_m\{V_k\} a_{k+1}$ and $I_m\{u_k\} = R_e\{V_k\} a_{k+1} - I_m\{V_k\} a_k$

Step6 Then the output feedback gain-matrix, which assigns all the closed-loop eigenvalues, is readily calculated from (46).

An illustration of the proposed algorithm is shown in the flowchart of Fig. 5.
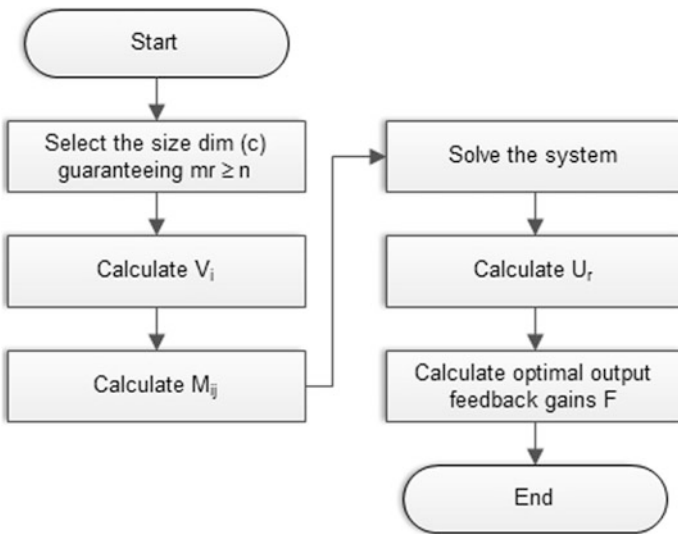

Fig. 5 Flowchart of the proposed algorithm to calculate the optimal output feedback gains

4 Description of the Test Power Sensitivity and PSS Models

The Power Sensitivity Model under study, which is used to illustrate how the proposed approach specifies the matrices Q and R, is shown in Fig. 6, and considers the system of one generator connected to an infinite bus.

The PSM is a linear analysis tool for the electric power systems. The fundamental concept is the application of active and reactive power balance, that can be represented by a set of differential and algebraic equations, as follows [9]

$$\dot{x} = f(x, y, u), \tag{57}$$

$$0 = g(x, y, u), \tag{58}$$

where x is a vector of dynamic state variables, y is a vector of algebraic variables and u is the vector of input variables. For small-signal stability analysis, we assume that the system parameter variation is small enough, so that the model can be linearized around some equilibrium point as

$$\begin{aligned} \Delta\dot{x} &= J_1\Delta x + J_2\Delta y + B\Delta u \\ 0 &= J_3\Delta x + J_4\Delta y \end{aligned}, \tag{59}$$

where J_1, J_2, J_3 and J_4 are Jacobian matrices of f and g, related to dynamic state and algebraic variables, respectively, and B is the perturbation matrix. For the system
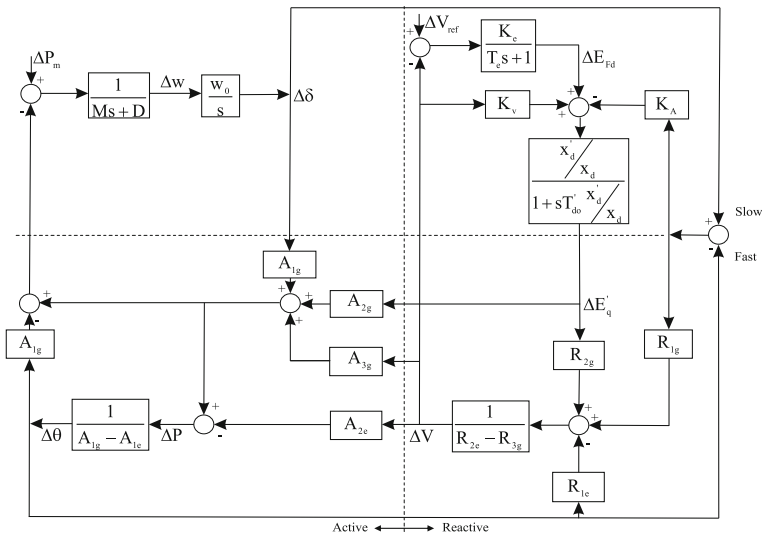

Fig. 6 Block diagram of a PSM

shown in [9], the following state equations can be formulated according to nodal power balance methodology:

$$
\begin{bmatrix} \Delta\dot{\delta} \\ \Delta\dot{w} \\ \Delta\dot{E}'_q \\ \Delta\dot{E}_{fd} \end{bmatrix} = \underbrace{\begin{bmatrix} 0 & w_0 & 0 & 0 \\ -\frac{A_{1g}}{M} & -\frac{D}{M} & -\frac{A_{2g}}{M} & 0 \\ -\frac{K_A}{Td'_o} & 0 & -\frac{x_d}{x'_d Td'_o} & \frac{1}{Td'_o} \\ 0 & 0 & 0 & -\frac{1}{T_e} \end{bmatrix}}_{J_1} \begin{bmatrix} \Delta\delta \\ \Delta w \\ \Delta E'_q \\ \Delta E_{fd} \end{bmatrix} + \underbrace{\begin{bmatrix} 0 & 0 \\ \frac{A_{1g}}{M} & -\frac{A_{3g}}{M} \\ \frac{K_A}{Td'_o} & \frac{K_v}{Td'_o} \\ 0 & -\frac{K_e}{T_e} \end{bmatrix}}_{J_2} \begin{bmatrix} \Delta\theta \\ \Delta v \end{bmatrix} + \underbrace{\begin{bmatrix} 0 & 0 \\ \frac{1}{M} & 0 \\ 0 & 0 \\ 0 & \frac{K_e}{T_e} \end{bmatrix}}_{B} \begin{bmatrix} \Delta T_m \\ \Delta V_{ref} \end{bmatrix},
$$

$$
\begin{bmatrix} 0 \\ 0 \end{bmatrix} = \underbrace{\begin{bmatrix} A_{1g} & 0 & A_{2g} & 0 \\ R_{1g} & 0 & R_{2g} & 0 \end{bmatrix}}_{J_3} \begin{bmatrix} \Delta\delta \\ \Delta w \\ \Delta E'_q \\ \Delta E_{fd} \end{bmatrix} + \underbrace{\begin{bmatrix} -A_{1g} - A_{1e} & A_{3g} - A_{2e} \\ -R_{1g} - R_{1e} & R_{3g} - R_{2e} \end{bmatrix}}_{J_4} \begin{bmatrix} \Delta\theta \\ \Delta v \end{bmatrix}.
$$

The coefficients A and R represent local sensitivity functions of active and reactive powers, respectively. Eliminating the vector of algebraic variables, provided that $|J_4| \neq 0$, the state-space system can be obtained as

$$
\Delta\dot{x} = \underbrace{\left[J_1 - J_2 J_4^{-1} J_3 \right]}_{A} \Delta x + B\Delta u. \tag{60}
$$

The most common way to suppress the generator electromechanical oscillations and enhance the overall stability of power system is done by means of a power system stabilizer PSS. The conventional PSS is, basically, composed by a static gain Kpss, which is adjusted to obtain the desired damping for unstable or poorly damped modes; a washout block works as a filter for low-frequencies; and two blocks lead-lag with time constants. A block diagram of a power system stabilizer is shown in Fig. 7.

A residue method is applied to design the controller, in order to calculate the time constants and the gain K_{pss}, introducing the necessary phase compensation to the displacement of the eigenvalue of interest. The Eqs. (61)–(63) show the relationship between the eigenvalue displacement and the correspondent residue [1]

$$
\phi_c = 180° - \arg(R_i), \quad \alpha = \frac{1 + \sin\left(\frac{\phi_c}{2}\right)}{1 - \sin\left(\frac{\phi_c}{2}\right)}, \tag{61}
$$

Fig. 7 Block diagram of a PSS
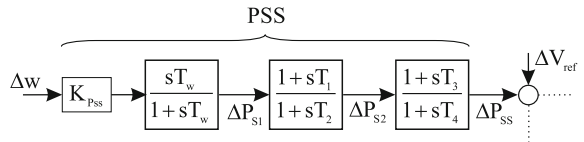
$$T \equiv T_2 = T_4 = \frac{1}{w_n\sqrt{\alpha}} \text{ and } T_1 = T_3 = \alpha T, \tag{62}$$

where $\arg(R_i)$ denotes phase angle of the residue R_i and w_n is the frequency of the mode of oscillation. The controller gain K_{pss} is computed as a function of the desired eigenvalue location $\lambda_{i,des}$ according to

$$K_{pss} = \left| \frac{\lambda_{i,des} - \lambda_i}{R_i H(\lambda_i)} \right|. \tag{63}$$

Thus, the inclusion of PSS in the PSM is formulated by the equations

$$\Delta\dot{V}_{Ps1} = K_{Pss}\Delta\dot{w} - \frac{1}{T_w}\Delta V_{Ps1}, \tag{64}$$

$$\Delta\dot{V}_{Ps2} = \frac{T_1}{T_2}\Delta\dot{V}_{Ps1} + \frac{1}{T_2}\Delta V_{Ps1} - \frac{1}{T_2}\Delta V_{Ps2}, \tag{65}$$

$$\Delta\dot{V}_{Pss} = \frac{T_3}{T_4}\Delta\dot{V}_{Ps2} + \frac{1}{T_4}\Delta V_{Ps2} - \frac{1}{T_4}\Delta V_{Pss}. \tag{66}$$

By analysing Eqs. (64)–(66), and observing (Fig. 7), the action of PSS, whose input signals are the variations of the angular speed, it is introduced three new state variables, namely ΔV_{Ps1}, ΔV_{Ps2} and ΔV_{Pss}.

Next section illustrates the computation of the optimal power sensitivity controllers, and makes a comparison between the results thus obtained with those obtained by optimal state feedback and classic control.

5   Illustration Results

The performance of the PSM depends on the values of the parameters. The parameters of the system change with the operating point. In particular, the system stability is sensitive to the parameter R_{1g}; this parameter changes sign and, for $R_{1g} < 0$, the system becomes unstable. Two operating points, Case 1 and Case 2, are here presented to illustrate the behaviour of the controllers, one case considering $R_{1g} < 0$ and another considering $R_{1g} > 0$. Case 1 was chosen to obtain the optimal controllers that have to be valid for all operating points. Case 2 was chosen to illustrate how effective the calculated controllers perform for a different operating point. Other operating points have been considered and the corresponding controllers remained valid for all of them. The parameters of these operating points are listed in Appendix.

Analysing the system eigenvalues without PSS, for the Case 1 operating point, the system is unstable due to the poles $\Lambda = 0.14 \pm j5.93$. The poles can be rewritten as: $-\zeta w_n \pm i w_n \sqrt{1 - \zeta^2}$, where ζ is the damping coefficient and w_n the

natural frequency. To lead the system to stability it is proposed the inclusion of PSS, whose parameters will be adjusted in accordance with the procedure previously described. The desired damping coefficient can be chosen as $\zeta = 0.20$ in order to damp the oscillation of speed and maintain the natural frequency constant, so that the closed loop poles specified for that $\zeta = 0.20$ lies in the imaginary and real parts, respectively, $w_n \sqrt{1 - \zeta^2} = 5.30$ and $-\zeta w_n = -1.19$.

With an optimal regulator, the closed-loop system eigenvalues can be arbitrarily placed anywhere in the left hand side of the complex plane. From an optimization point of view, the amount of improvement in system transients can be as large as we want.

5.1 State Feedback Optimal Regulator

The block diagram of the proposed state feedback optimal regulator is shown in Fig. 8 and is composed by a washout block with the optimal control signal u.

When compared with other methods, optimal control has especially effective results in damping fast and oscillatory responses of the state variables. However, the bigger the distance of the poles location to the imaginary axis is, the more demanding will be the physical control signal output. Thus, a careful study must be performed before selecting the pole assignment, in order to keep the control effort similar to that required by the classical controller PSS. Hence, the damping coefficient chosen for the optimal regulator was $\zeta = 0.6$.

By applying the proposed algorithm defined in Sect. 3.1.2, for the parameters given in the Appendix, we can specify the weighting matrix Q, while R is specified as the identity matrix since, as mentioned above, it is only used as scaling factor on the input channels to penalize for large control effort. The weighting matrix Q and the gain matrix K are respectively:

$$Q = \begin{bmatrix} 0.72 & 5.12 & 0.70 & 0.01 & 1.25 \\ 5.12 & 4193.55 & -53.05 & -0.64 & -92.97 \\ 0.70 & -53.05 & 1.52 & 0.02 & 2.61 \\ 0.01 & -0.64 & 0.02 & 0.01 & 2.61 \\ 1.25 & -92.97 & 2.61 & 2.61 & 4.73 \end{bmatrix},$$

$$K = \begin{bmatrix} 0.26 & -139.68 & 0.74 & -0.01 & -0.96 \end{bmatrix}.$$

Fig. 8 Block diagram of the optimal state feedback regulator
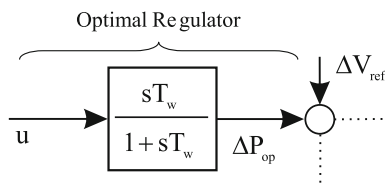
The obtained results are shown in Table 1. This table shows, for both Case 1 and Case 2, the poles for the open-loop system, for the system with classic controller—power system stabilizer added and for the system with optimal state feedback controllers added.

5.2 Output Feedback Regulator

The block diagram of the proposed output feedback optimal regulator is shown in Fig. 9 and it is constituted by a two washout blocks preceded by two optimal control signals u_1 and u_2. The addition of another input control allows to satisfy the condition related to the order of the system to be controlled, particularly condition $m + r \geq n + 1$, where $m = rank(B)$ and $r = rank(C)$, must be observed, as already mentioned earlier. Once this condition is assured, the procedure to be followed is similar to the one presented in the previous section for pole placement.

Now applying the algorithm described in Sect. 3.2.1, for the same parameters shown in the Appendix, we can determine the gain matrix for output feedback, having been considered the three following outputs: $\Delta\omega$, ΔE_{fd} and ΔP_{op2}.

$$F = \begin{bmatrix} 2.26 & -11.17 & 0.02 \\ -438.78 & 2949.90 & -2.60 \end{bmatrix}.$$

With the gain matrix F obtained such that the feedback system has the poles assigned in a similar way to the previous case, that is, by using only the system output feedback, we shall get a performance exactly alike for both controllers (state feedback and output feedback), having however an important difference with respect to the physical requirements of the control signals, as it will become clear ahead. The results obtained, for both Case 1 and Case 2, are shown on Table 2. This table presents the poles for the open-loop system, for the system with classic controller—power system stabilizer added and for the system with output feedback optimal regulator added. One should note that the difference with respect to the number of poles leads to the inclusion of the PSS for the system classic control and also to the inclusion of the two washout block, which allow maintaining the same output steady state value.

Next we are going to make a time analysis of the different regulators obtained, as well as of the input signals.

5.3 Controllers Time Response Analysis

A 10 % step increase in the mechanical torque ($\Delta P_m = 0.1\,pu$) is applied in order to illustrate the time evolution of the load angle deviation and the speed deviation, respectively shown in Figs. 10 and 11.

S.J.P.S. Mariano et al.

Table 1 Closed loop system poles for classic and state feedback optimal regulator

Power sensitivity model		Power sensitivity model with PSS		Optimal state feedback regulator	
Case 1	Case 2	Case 1	Case 2	Case 1	Case 2
−17.26	−18.07	−23.26	−23.50	−18.00	−16.56
+0.14 + j 5.93	−0.30 + j 6.03	−1.19 + j 5.30	−5.61 + j 7.13	−2.00 + j 5.3	−14.97
+0.14 − j 5.93	−0.30 − j 6.03	−1.19 − j 5.30	−5.61 − j 7.13	−2.00 − j 5.3	−2.74 + j 6.16
−3.41	−1.76	−5.95 + j 7.77	−2.21 + j 5.45	−7.00	−2.74 − j 6.16
		−5.95 − j 7.77	−2.21 − j 5.45	−10.00	−2.012
		−3.27	−1.05		
		−1.02	−1.72		

Fig. 9 Block diagram of the optimal output feedback regulator
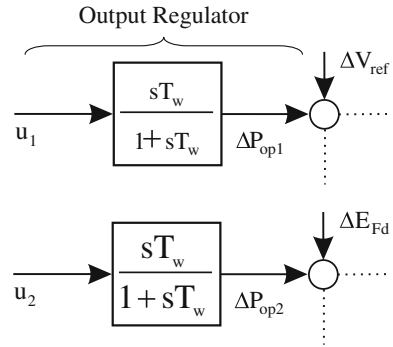
The step responses in Figs. 10 and 11 show that the power sensitivity model brings better damping effect on the state and output feedback variables, not only with respect to the open-loop system, but also with respect to the power sensitivity model with PSS. The response with optimal state feedback is very close to the response with output feedback and both optimal responses have better performances than the response with PSS.

The obtained output control signals u from the PSS and from the optimal state feedback controllers, as well as the obtained control signals u_1 and u_2 from the output feedback controller, are illustrated in Fig. 12, showing that the output control signals with optimal state feedback controller lead to results physically not more demanding than those from classical control. Concerning the output control signals with output feedback controller it is shown that these are more demanding than those from classical control. This is due to the fact that the number of the system outputs considered here is smaller than the number of the state variables.

As mentioned before, the performance of the power sensitivity model depends on the parameters of the system, which change with the operating point and therefore the performance of the system changes. The optimal controller previously obtained (for a specific operating point) and the conventional power system stabiliser controller have to be valid for all operating points. The results for Case 2 operating point are shown in Figs. 13, 14 and 15. Note that, the system performance is similar, since the poles have only been slightly displaced (with respect to Case 1).

As already mentioned above, to verify the validity of the controllers, numerous operating points have been considered and tested and the obtained controllers remained valid for all of them—the system remains stable and exhibits the desired performance.

Table 2 Closed loop system poles for classic and output feedback regulators

Power sensitivity model		Power sensitivity model with PSS		Output feedback regulator	
Case 1	Case 2	Case 1	Case 2	Case 1	Case 2
-17.26	-18.07	-23.26	-23.50	-18.00	$-18.80 + j\,8.40$
$+0.14 + j\,5.93$	$-0.30 + j\,6.03$	$-1.19 + j\,5.30$	$-5.61 + j\,7.13$	$-2.00 + j\,5.30$	$-18.80 - j\,8.40$
$+0.14 - j\,5.93$	$-0.30 - j\,6.03$	$-1.19 - j\,5.30$	$-5.61 - j\,7.13$	$-2.00 - j\,5.30$	$-2.93 + j\,6.80$
-3.41	-1.76	$-5.95 + j\,7.77$	$-2.21 + j\,5.45$	-7.00	$-2.93 - j\,6.80$
		$-5.95 - j\,7.77$	$-2.21 - j\,5.45$	-10.00	-2.95
		-3.27	-1.05	-11.00	-3.63
		-1.02	-1.72		

Fig. 10 Load angle deviation. Step responses for the different controllers
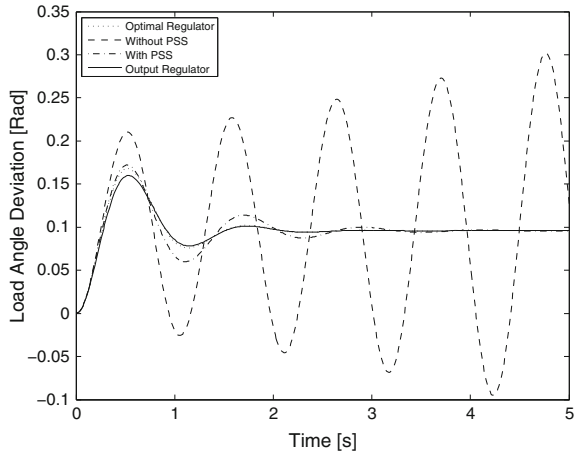
Fig. 11 Speed deviation. Step responses for the different controllers
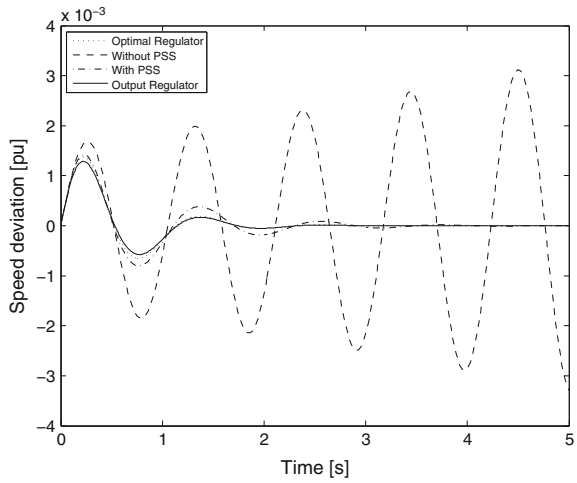
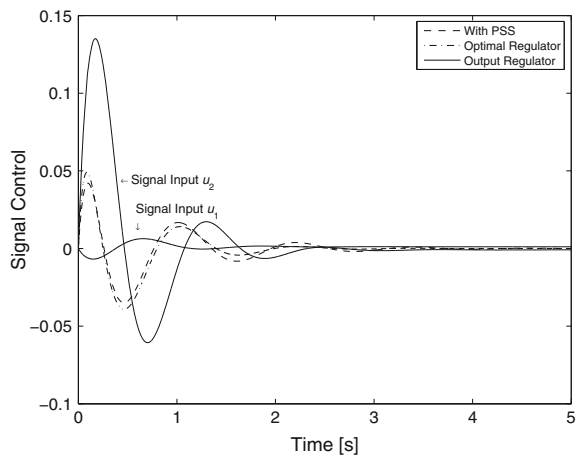**Fig. 12** Control signals from PSS, optimal state feedback and output feedback controllers

Fig. 13 Load angle deviation. Step responses for the different controllers
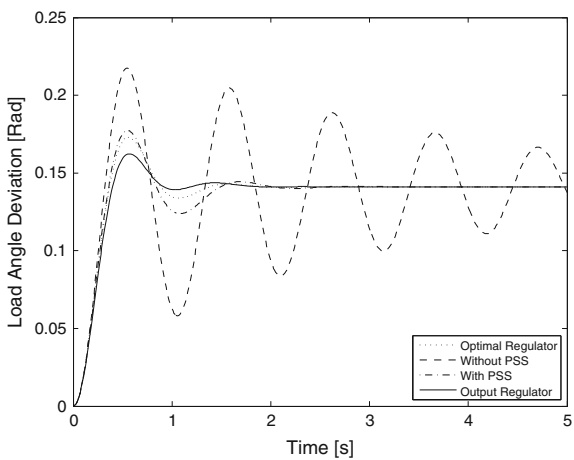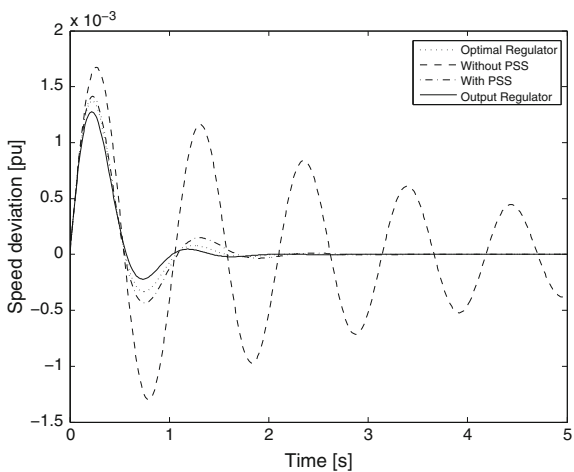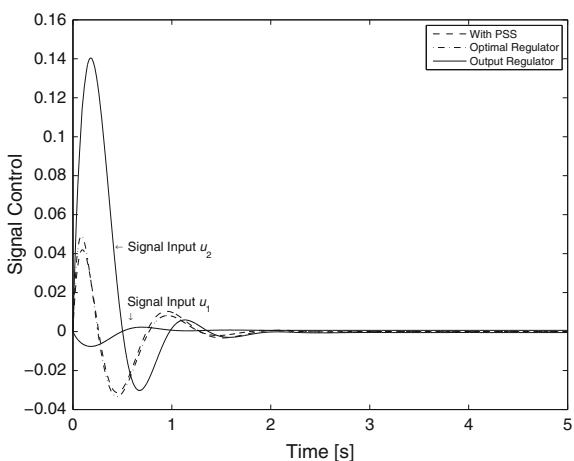

Fig. 14 Speed deviation. Step responses for the different controllers

Fig. 15 Control signals from PSS, optimal state feedback and output feedback controllers

6 Conclusion

This chapter presented studies on the performance of the PSS controllers for damping of low-frequency oscillations in an electric power system. The obtained results were compared with those obtained from the proposed optimal controllers. A new technique that allows the specification of the weighting matrices Q and R, avoiding the burdensome trial and error task, was applied. The proposed method builds Q and R in such a way that the system responses also obey conventional criteria for the system pole location, while satisfying the optimality, following the basic concept of shifting a single real pole or a pair of complex conjugate poles at a time. It was proposed an optimal output feedback approach, when the number of output variables is less than the order of the system, where a set of closed-loop system poles was allocated to an arbitrary position by means of a suitable output feedback. In this case the required physical effort revealed to be more demanding.

The algorithms for the proposed methodologies were clearly described. The optimal controllers are insensitive to the system parameter variation—ensuring stabilization with changes in operating point, and exhibiting the desired performance—better dynamic performance in terms of overshoot and settling time.

Appendix

System parameters:

$M = 10$, $D = 0$, $x_d = 1.6$, $x'_d = 0.32$, $T'_{do} = 6$, $K_e = 25$, $T_e = 0.05\,s$, $A_{1g} = 1.575$, $A_{2g} = 1.916$, $A_{3g} = -0.701$, $A_{1e} = 2.5$, $A_{2e} = 0.492$, $R_{1g} = -0.64$ (Case 1), $R_{1g} = 0.74$ (Case 2), $R_{2g} = 2.469$, $R_{3g} = -2.192$, $R_{1e} = 0.492$, $R_{2e} = 2.5$, $K_v = 3.16$, $K_A = 2.45$

Power system stabilizer parameters:

$T_w = 1$, $K_{pss} = 5.6$, $T = 4.66$, $\alpha = 0.09$.

References

1. Sadikovic R, Korba P, Andersson G (2005) Application of FACTS Devices for Damping of Power System Oscillations. In: Proc. of IEEE Power Tech St., Petersburg, Russia, 27-30 June 2005
2. Haque MH (2006) Damping improvement by FACTS devices: A comparison between STATCOM and SSSC. Electr Pow Syst Res 76:865–872
3. Dysko A, Leithead WE, O' Reilly J (2010) Enhanced. Power System Stability by Coordinated PSS Design. IEEE T Power Syst 25(1):413-422
4. Dudgeon GJW, Leithead WE, Dysko A, O'Reilly J, McDonald JR (2007) The effective role of AVR and PSS in power systems: Frequency response analysis. IEEE T Power Syst 22 (4):1986-1994

5. Elices A, Rouco L, Bourles H, Margotin T (2004) Design of robust controllers for damping interarea oscillations: Application to the European power system. IEEE T Power Syst 19 (2):1058-1067
6. Mariano SJPS, Ferreira LAFM (1999) A procedure to specify Q and R for an optimal voltage regulator. In: Proc. IASTED International Conference, Power and Energy Systems, Las Vegas, USA, November 1999
7. Chen GP, Malik OP, Qin YH, Xu Gy (1992) Optimization Technique for the Design of a Linear Optimal Power Systems Stabilizer. IEEE T Energy Conver 7(3):453-459
8. Mariano SJPS, Pombo JAN, Calado MRA, Ferreira LAFM (2010) Pole-shifting procedure to specify the weighting matrices for a load-frequency controller. In: MELECON 2010 - 2010 15th IEEE Mediterranean Electrotechnical Conference, La Valleta, Malta, 26-28 April 2010
9. Deckmann SM, da Costa VF (1994) A power sensitivity model for electromechanical oscillation studies. IEEE T Power Syst 9(2):965-971
10. IEEE Recommended Practice for Excitation System Models for Power System Studies (2006) IEEE Std. 421.5-2005:0_1-85
11. Burns RS (2001) Advanced Control Engineering. Butterworth-Heinemann
12. Kimura H (1975) Pole assignment by gain output feedback. IEEE T Automat Contr 20 (4):509-516
13. Davison EI, Wang SH (1975) On pole assignment in linear multivariable systems using output feedback. IEEE T Automat Contr 20(4):516-518
14. Chen CL, Yang TC, Munro N (1988) Output feedback pole assignment procedure. Int J Control 48:1503-1518
15. Kabamba PT, Longman RW (1982) Exact pole assignment using direct or dynamic output feedback. IEEE T Automat Contr 27(6):1244-1246
16. Alexandridis AT, Paraskevopoulos PN (1996) A New Approach to Eigenstructure Assignment by Output Feedback. IEEE T Automat Contr 41(7):1046-1050
17. Levine WS, Athans M (1970) On the Determination of the Optimal Constant Output Feedback Gains for Linear Multivariable Systems. IEEE T Automat Contr 15(1):44-48
18. Fujinaka T, Omatu S (2001) Pole Placement Using Optimal Regulators. T.IEE Japan 121-C (1):240-245

Design of Three-Phase LCL-Filter for Grid-Connected PWM Voltage Source Inverter Using Bacteria Foraging Optimization

Ehab H.E. Bayoumi

Abstract This paper presents an *LCL*-filters design and control for three-phase PWM voltage source grid inverter. The main objective is to achieve optimum damping with a desired system control bandwidth for the *LCL*-filter. This control algorithm is implemented by using Bacteria Foraging Optimization. Mathematical analysis has been presented to study the steady-state and dynamic performances of the overall system. Only one set of current sensors is required for the feedback control. The proposed system is simulated and results illustrated that bacterial foraging optimization is a skilful clarification for realizing the best parameters of *LCL*-filters and the PI current controller. Experimental results endorse the proposed technique and highlight its practicability.

1 Introduction

There is an ongoing increase in the number of embedded power sources connected to the power grid. These include variable speed wind turbines, gas turbine powered generators, fuel cell units, and photovoltaic arrays. The electrical output of many resources is incompatible with the fixed frequency electricity supply network; as a result power electronic interfacing is required. Power quality and transient performance of such distributed generation devices is dependent on inverter technology and control algorithms [1–4].

A filter is required as an interface between the PWM inverter and the power grid. For smoothing the currents injected into the grid, a single inductor (*L*) is usually used and connected in series with the output ports of the converter to perform filtering function. However, it is known that in high power applications where the switching frequency of the converter is always limited by the associated switching losses, such a simple configuration may lead to bulky and costly passive filters, and

E.H.E. Bayoumi (✉)
Electrical and Electronics Engineering Technology Department, Abu Dhabi Men's College,
Abu Dhabi P.O.Box: 25035, United Arab Emirates
e-mail: ehab.bayoumi@hct.ac.ae

may also slow down the system dynamic response if the designed converter needs to comply with stringent grid codes specified by IEEE 519-1992 and IEC 61000-3-12. However, *LCL*-filter is considered to be a perfect choice compared with L-filter [1]. But, due to the resonance hazard of the *LCL*-filter [5], damping solutions are needed for the grid connected inverters to stabilize the system. In addition to the resonance hazard, the grid-connected inverter with an *LCL*-filter is more sensitive to the grid voltage. Therefore, the control scheme dominates the injected grid current harmonics caused by the grid voltage distortion, which is significant for the grid-connected inverter with an *LCL*-filter. IEEE Standard (1547-2003) [6] gives the limitation of the injected grid current harmonics.

Mainly, there are three solutions to suppress the injected grid current harmonics caused by the grid voltage distortion. First solution is realizing infinite loop gain at the harmonic frequencies. In [7] the proportional-integral (PI) regulators together with multiple proportional-resonant (PR) regulators in the synchronous *dq* frame are implemented. Multiple PR regulators in the stationary frame are given in [8]. PI regulators in multiple synchronous *dq* frames are employed in [9]. With these control schemes, the steady-state error of the injected grid current is eliminated and the low order injected grid currents harmonics are effectively concealed. However, these schemes reduce the phase margin of the system if the current harmonics to be suppressed are close to or above the cross-over frequency of the loop gain, which might lead to the instability of the system [8].

The second solution is using feedforward scheme. The feedforward scheme is not affect the loop gain of the system, and the stability of the system is guaranteed. In [10], the feedforward of the filter capacitor current, which can be seen as the derivative of the filter capacitor voltage was proposed, and the injected grid current harmonics at low frequencies caused by the grid voltage distortion were greatly reduced. In [11], the proportional feedforward of the filter capacitor voltage was introduced to eliminate the steady-state error of the inverter-side inductor current. The full-feedforward scheme of the grid voltage for a single-phase grid-connected inverter with an *LCL*-filter was derived [12]. This full-feedforward function of the grid voltage consists of three parts, which were the proportional, derivative and second derivative parts. With this full-feedforward scheme, the injected grid current harmonics caused by the grid voltage distortion were effectively reduced.

The third solution is passive and active damping for *LCL*-filter, which have been comprehensively discussed in literature [5, 13, 14]. Due to their high efficiency and flexibility, active damping solutions have attracted much consideration [15]. An analytical design approach for passively damping *LCL*-filters was discussed in [13]. Moreover, the passively damped filter may downgrade the *LCL*-filter to a second-order system, which is definitely affect its attenuation factor at higher frequencies, and hence neutralizing those benefits originally introduced by the undamped filters. The main reason for that is related to the theoretical fact: at certain frequencies, the resulting network may appear to have zero or very low impedance, inferring resonances and hence closed-loop instability. A straightforward method to dampen this resonance is to add real passive damping resistors in series with the filter capacitors

On the other hand, active damping technique with no additional power losses can be considered. The basic idea is to introduce other control variables to the feedback current control loop so that they can perform a damping terms. Implementation of this scheme requires more sensors for sensing the filter capacitor currents [5, 15, 16], voltages [14, 17] or both [19]. In [14] it explored various active damping approaches for *LCL*-filters and compared their performances at resonance damping. Certainly, the overall system costs and realization complexity is increased, which is commonly unattractive. That leads to the development of a number of sensorless active damping methods [18–22], where the required control variables were obtained either through estimation from dc-link voltage and switching duty ratios, or using complex state observers. Unfortunately, the performance of such methods may largely depend on the accuracy of plant parameters, which are usually unknown or vary over a wide range of operation for complex power systems.

In [23, 24] two current feedbacks for *LCL*-filter are used to increase the flexibility of the overall system. Measuring the grid current or converter current, or even their weighted value for the re-organized *LCCL* filter is studied. In [25] grid current feedback is selected, it is shown from the root locus analysis that it is slightly more stable than converter current feedback. A design algorithm for optimizing *LCL*-filters is given in [26]; the system is stable at particular switching frequencies even without any kind of damping. Low-order harmonic distortions in the line currents are quite observable. However, converter current feedback had verified that excellent steady-state and transient performances can be achieved, as long as proper damping techniques are presented [13].

In this paper comprehensively investigates the intrinsic damping characteristic of a *LCL*-filter. It shows that the current control loop has an inherent damping term embedded, when the converter current is sensed for feedback. This inherent damping term can be used for optimal damping of the *LCL* resonance without demanding for additional passive or active damping, as long as the filter component values are designed properly. Although, inherent damping is not exist when the grid current is measured for feedback control. This is leading to a conclusion that converter current feedback is more stable than grid current feedback. A simple approach for tuning the damping factor is proposed, which would preserve the advantage of using only one set of current sensors, but at the expense of a more compromised transient response. The controller algorithm and the proposed damping tuning technique used are implemented by using Bacteria Foraging Optimization (BFO). Simulation and experimental results for endorsing those findings are given and ultimately showing mutual agreement.

2 System Modelling and Description

Figure 1 shows the grid-connected three-phase PWM voltage source inverter diagram through an *LCL*-filter. The following assumptions are considered:
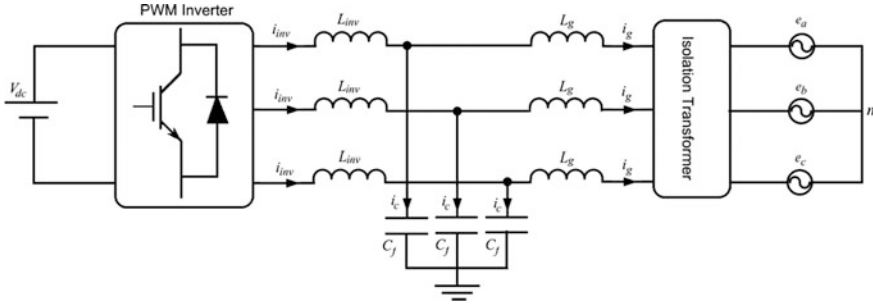
Fig. 1 Three-phase grid-connected PWM inverter with LCL-filter

1. All the equivalent series resistance for grid-side filter inductor, inverter-side filter inductor, filter capacitor and transformer inductor are neglected.
2. The ac supply voltages contain only positive-sequence fundamental component.

By applying both assumptions, Fig. 1 is simplified to the per-phase equivalent circuit shown in Fig. 2, whose s-domain transfer functions, representing the plant model $Gp(s)$ at non- fundamental frequencies. The circuit can be modelled as:
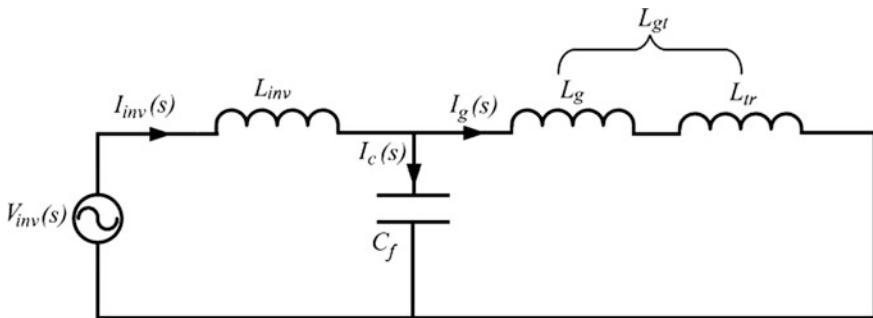
$$L_{gt} = L_g + L_{tr}. \tag{1}$$

$$V_{inv}(s) = \left(L_{inv}s + \frac{1}{C_f s}\right)I_{inv}(s) - \left(\frac{1}{C_f s}\right)I_g(s) \tag{2}$$

$$I_{inv}(s) = (L_g C_f s^2 + 1)I_g(s) \tag{3}$$

By substituting Eq. (2) in (1), the $Gp(s)$ can be expressed as:

$$G_p(s) = \frac{I_g(s)}{V_{inv}(s)} = \frac{1}{L_{inv}L_{gt}C_f s^3 + (L_{inv} + L_{gt})s} \tag{4}$$

Fig. 2 Per phase equivalent circuit for a grid-connected PWM inverter with LCL-filter

$$\frac{I_c(s)}{I_g(s)} = L_{gt}C_f s^2 \tag{5}$$

where v_{inv}, i_{inv}, i_g, and i_c represent the inverter voltage, inverter current, grid current and filter capacitor current in the time domain, respectively, while their capitalized notations are for representing them in the s-domain. L_{inv}, L_g, and L_{tr} stand for inverter-side filter inductor, grid-side filter inductor and transformer inductor, respectively.

The PWM inverter can be modelled as a linear amplifier with a delay. The delay can combined with the current PI controller. The transfer-function of the PI current controllers in dq reference frame is:

$$G_c(s) = K_p V_{dc}(1 + \frac{1}{\tau_c s}) \tag{6}$$

where K_p, τ_c, and V_{dc} represent the proportional gain, integral time-constant of PI controller and dc-link voltage, respectively.

2.1   Grid-Current Feedback

Figure 3a illustrates the control block diagram of *LCL*-filter-based three-phase PWM inverter with grid current feedback. From Eqs. (4) and (6), the system open-loop transfer function is:

$$\frac{I_g(s)}{I_g^*(s) - I_g(s)} = G_C(s)\,G_p(s) = \frac{K_p V_{dc}(s + \frac{1}{\tau_c})}{L_{inv}L_{gt}C_f s^4 + (L_{inv} + L_{gt})s^2} \tag{7}$$

Equation (7) shows the absent of third order term in the characteristic equation, which implies that:

1. The overall closed-loop system is challenging to be stable,
2. Even if a passive element (R) is included, it is generally inadequate to assure a well-damped plant.
3. The plant response is dynamically slow with a small control bandwidth.

Improvement of this technique can be done by adding either external passive or active damping to limit the infinite gain at the *LCL* response frequency [25].

2.2   Converter-Current Feedback

The converter current can be sensed for feedback control as shown in Fig. 3b. Since the grid current is not directly controlled, the *q*-axis current reference should be set
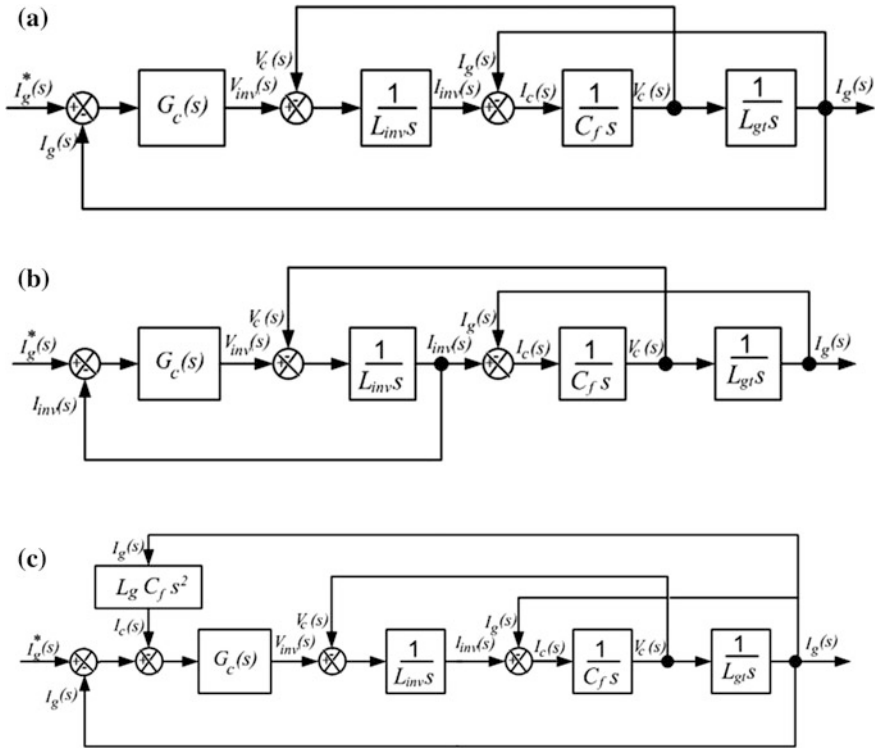
Fig. 3 Block diagram of **a** grid current feedback control, **b** converter current feedback control, and **c** equivalent converter current feedback control

to $\omega_o C_f v_g$ (v_g is the phase-grid voltage) instead of zero, where ω_o is the fundamental angular frequency. This is to guarantee unity power factor operation. Figure 3b is modified to Fig. 3c to be more convenient in performing the open loop analysis. The converter current can be expressed as the summation of the grid current and filter capacitor current as shown in Fig. 3c.

Contrasting Fig. 3c with 3a shows that converter current feedback is equivalent to grid current feedback, with an additional i_c term added to the forward path. The open loop transfer function from Fig. 3c can be expressed as follows:

$$\frac{I_g(s)}{I_g^*(s) - I_q(s) - I_c(s)} = G_c(s)\,G_p(s) = \frac{K_p V_{dc}\left(s + \frac{1}{\tau_c}\right)}{L_{inv}L_{gt}C_f s^4 + (L_{inv} + L_{gt})s^2} \qquad (8)$$

Substituting Eq. (5) into Eq. (8) yields:

$$\frac{I_g(s)}{I_g^*(s) - I_g(s)} = \frac{K_p V_{dc}\left(s + \frac{1}{\tau_c}\right)}{L_{inv}L_{gt}C_f s^4 + K_p V_{dc}L_{gt}C_f s^3 + \left(\frac{K_p V_{dc}L_{gt}C_f}{\tau_c} + L_{inv}L_{gt}\right)s^2} \qquad (9)$$

Compare the denominators in Eq. (7) by Eq. (9), it is clear that the latter has an additional s^3-term, which would provide damping by shifting two of its poles further into the left half plane, while the remaining two poles remain at the origin. The damping initiated can be adjusted by tuning the controller gains and the passive parameters to the coefficient of s^3-term.

Equation (9) can be rewritten as:

$$\frac{I_g(s)}{I_g^*(s) - I_g(s)} = \frac{K_p V_{dc}\left(s + \frac{1}{\tau_c}\right)}{\left[L_{inv}L_{gt}C_f s^2 + K_p V_{dc}L_{gt}C_f s + \left(\frac{K_p V_{dc}L_{gt}C_f}{\tau_c} + L_{inv}L_{gt}\right)\right]s^2} \tag{10}$$

For a second order characteristic equation in the brackets given in Eq. (10), tuning should be done until the following condition is met:

$$\frac{K_p V_{dc}}{L_{inv}} = 2\xi\omega_{res} = 2\xi\sqrt{\frac{\frac{K_p V_{dc}L_{gt}C_f}{\tau_c} + L_{inv} + L_{gt}}{L_{inv}L_{gt}C_f}} \tag{11}$$

where,

$$\omega_{res} = \text{undamped resonance frequency} = \sqrt{\frac{\frac{K_p V_{dc}L_{gt}C_f}{\tau_c} + L_{inv} + L_{gt}}{L_{inv}L_{gt}C_f}} \tag{12}$$

As the integral term of the PI controller typically does not affect the resonance frequency extensively [10], therefore $\frac{K_p V_{dc}L_{gt}C_f}{\tau_c} \approx 0$ and the ω_{res} expression can be simplified to:

$$\omega_{res} \approx \sqrt{\frac{L_{inv} + L}{L_{inv}L_{gt}C_f}} \tag{13}$$

To assess an *LCL*-filter, two aspects should be considered [27]:

1. The selected inductors and capacitor should be as small as possible if the *LCL*-filter can fulfil the design requirement. As a small filter parameters can not only save money but also improve the dynamic response and stability.
2. To achieve good filter performance, the harmonic attenuation rate f_s can be used to evaluate the harmonic components, in theory, the harmonics is less when f_s is less. In practical, other aspects should be considered, so f_s should be less than 0.2.

3 Optimum Damping Control of LCL-Filter

The Bode plots in Fig. 4 show the frequency response of the *LCL*-filter. It is clear that the *LCL*-filter has approximately the same magnitude response as an *L*-filter over the low frequency range and under various damping factors. The phase
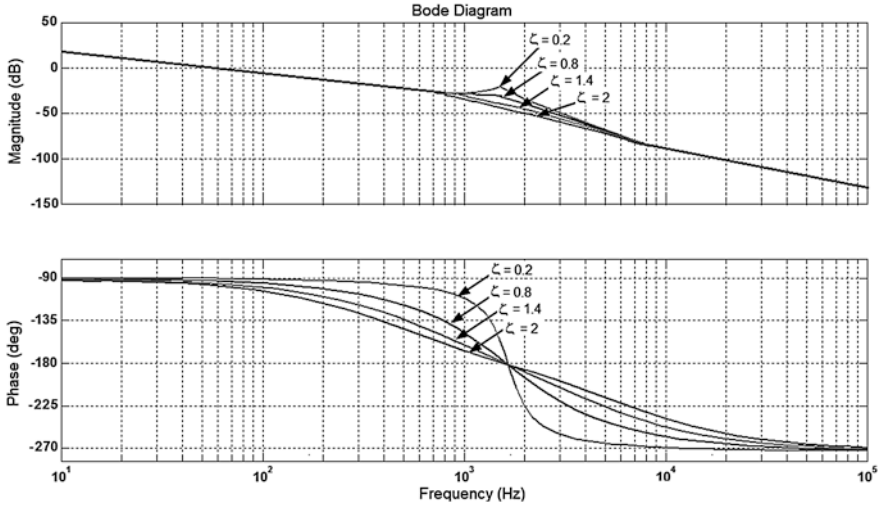
Fig. 4 Bode plots of LCL filter for different damping factors

response is quite different in *LCL*-filter. The maximum phase lag of an *L*-filter is $\pi/2$ radius, while that of an *LCL*-filter always exceeding this value. The phase different in the *LCL*-filter would grow larger as the damping factor and operating frequency increase. Therefore, two design cases are suggested:

1. Since, an under damped system lead to serious transient oscillations when a step change is applied, while an over-damped system is severely decrease the system phase margin, and the dynamic response. Therefore, the damping factor of *LCL* resonance has to be optimally adjusted.
2. Due to, the dependence of the system crossover frequency (ω_c) with reference to its damping factor (ζ) and resonance frequency (ω_{res}) Fig. 4 shows that ω_c is mainly limited by the phase lag of the *LCL*-filter. Therefore, the better guideline is to select ω_c as a fraction of the undamped resonance frequency (ω_{res}) [14], consequently:

$$\alpha = \frac{\omega_c}{\omega_{res}} \tag{14}$$

The phase lag ϕ_{LCL} is function of its damping factor ζ and the ratio of crossover frequency to resonance frequency α. Then, the system phase margin can be estimated by taking the time delay (T_d) of the PWM inverter into consideration as follows:

$$\varphi_{LCL} = \frac{\pi}{2} - \omega_c T_d - \arctan\left(\frac{2\xi\alpha}{1-\alpha^2}\right) \tag{15}$$

Upon determining ω_c, it is now possible to design the optimum damping control for *LCL*-filter. Assuming LCL-filter is approximated as an L, the proportional gain of the PI controller and the system crossover frequency are simply related by [17]:

$$\varphi_{LCL} = \frac{\pi}{2} - \omega_c T_d - \arctan\left(\frac{2\xi\alpha}{1-\alpha^2}\right) \tag{16}$$

Combining Eqs. (11), (14) and (16) gives the following relationship between L_{inv} and L_g,

$$2\xi L_{inv} = \alpha(L_{inv} + L_g), \quad \frac{L_{inv}}{L_g} = \frac{\alpha}{2\xi - \alpha} \tag{17}$$

4 Design Tools

4.1 Bacteria Foraging Optimization (Bfo)

Nowadays, bacterial foraging behaviors (i.e. bacterial chemotaxis) as a rich source of potential engineering applications and computational model have attracted more and more attentions. Few models have been developed to mimic bacterial foraging behaviors and have been applied for solving practical problems. Among them, Bacterial Foraging Optimization (BFO) is a population-based numerical optimization algorithm. Bacteria search for nutrients in a manner to maximize energy obtained per unit time. Individual bacterium also communicates with others by sending signals. A bacterium takes foraging decisions after considering two previous factors. The process, in which a bacterium moves by taking small steps while searching for nutrients, is called chemotaxis and key idea of BFO is mimicking chemotactic movement of virtual bacteria in the problem search space. The original Bacterial Foraging Optimization system consists of three principal mechanisms, namely chemotaxis, reproduction, and elimination-dispersal. The details description of these processes is given in [28, 29] and a flowchart for BFO routine is presented in Appendix 1.

4.1.1 Chemotaxis

In the original BFO, a unit walk with random direction represents a "tumble" and a unit walk with the same direction in the last step indicates a "run". Suppose θ^i (j, k, l) represents the bacterium at jth chemotactic, kth reproductive, and lth elimination-dispersal step. $C(i)$ is the chemotactic step size during each run or tumble (i.e., run-length unit). Then in each computational chemotactic step, the movement of the ith bacterium can be represented as

$$\theta^i(j+1,k,l) = \theta^i(j,k,l) + C(i)\frac{\Delta(i)}{\sqrt{\Delta^T(i)\Delta(i)}} \tag{18}$$

where $\Delta(i)$ is the direction vector of the jth chemotactic step. When the bacterial movement is *run*, $\Delta(i)$ is the same with the last chemotactic step; otherwise, $\Delta(i)$ is a random vector whose elements lie in $[-1, 1]$. With the activity of run or tumble taken at each step of the chemotaxis process, a step fitness, denoted as $J(i,j,k,l)$, will be evaluated.

4.1.2   Reproduction

The health status of each bacterium is calculated as the sum of the step fitness during its life, i.e. $\sum_{j=1}^{N_c} J(i,j,k,l)$, where N_c is the maximum step in a chemotaxis process. All bacteria are sorted in reverse order according to health status. In the reproduction step, only the first half of population survives and a surviving bacterium splits into two identical ones, which are then placed in the same locations. Thus, the population of bacteria keeps constant.

4.1.3   Elimination and Dispersal

The chemotaxis provides a basis for local search, and the reproduction process speeds up the convergence which has been simulated by the classical BFO. While to a large extent, only chemotaxis and reproduction are not enough for global optima searching. Since bacteria may get stuck around the initial positions or local optima, it is possible for the diversity of BFO to change either gradually or suddenly to eliminate the accidents of being trapped into the local optima. In BFO, the dispersion event happens after a certain number of reproduction processes. Then some bacteria are chosen, according to a preset probability P_{ed}, to be killed and moved to another position within the environment.

4.2   LCL-Filter Design Algorithm

The *LCL*-filter purpose is to reduce high-order harmonics on the grid side (a poor filter design can cause lower attenuation, or increase the grid current distortion due to oscillation effects). In fact, the current harmonics generated by the PWM inverter can cause saturation of the inductors or filter resonance. Therefore, the inductors should be well designed, to avoid resonances and minimize the current ripples. However, the damping level is limited by the cost, value of inductors, losses, and degradation of the filter performance.

The *LCL*-filter parameters are designed by using Bacteria Foraging Optimization (BFO). The BFO algorithm is employed based on optimal damping control of the *LCL*-filter. The step by step design algorithm is:

1. The bacteria in colony of BFO algorithm can be denoted by a set of 4-dimentional vector:

$$N = \begin{bmatrix} L_g & L_{inv} & C_f & \omega_{sw} \end{bmatrix}.$$

2. Select C_f: to avoid a low power factor. The reactive power that caused by the filter capacitor C_f should be less than 5 % of the rated active power. Therefore,

$$C_f < \left(\frac{5}{100} \cdot \frac{P}{3.2\pi.50.E^2} \right) \tag{19}$$

   where, P is the rated active power of the system and E is the RMS value of the grid voltage.

3. Select α and ς for optimal damping control of the *LCL*-filter. The recommended values for optimal control are ζ = 0.707 at α = 0.3 [27]. When the damping factor ζ decreased to 0.5, a higher crossover frequency ω_c can be obtained as shown in Fig. 4 and hence it yield to faster current control loop response. Therefore α and ζ can selected from the following inequalities:

$$\begin{aligned} 0.2 \le \alpha \le 0.4 \\ 0.4 \le \xi \le 0.9 \end{aligned} \tag{20}$$

4. Select Lg and Linv by using Eq. (17) and

$$\frac{L_{inv}}{L_g} < 2.5$$

5. Fitness function (J): uses the harmonic attenuation rate given in Eq. (21). To achieve good filter effort, the harmonic attenuation rate should be minimized. The LCL-filter parameter selected grantee the minimum harmonic attenuation rate is selected. If not, go to step 3.

$$f = Minimize \; J = \frac{i_g(h_{sw})}{i_{inv}(h_{sw})} = \frac{\frac{1}{C_f L_g}}{\left| \omega_{res}^2 - \omega_{sw}^2 \right|} \tag{21}$$

6. Calculate if the designed parameters can fulfill the requirement of the resonance frequency. If not, go to step 3. To avoid resonance at lower order or high order frequency, the resonance frequency should be:

$$1000\pi < \omega_{res} < \omega_{sw} \tag{22}$$

   where, ω_{res} is given in Eq. (13).

The BFO needs only a few information of the overall system such as, rated active power of the system and the RMS value of the grid voltage. The main purpose of BFO is to find the best individual (i.e. the best set of parameters for the *LCL*- filter and the best proportional constant of the PI current controller) in order to have the desired minimum damping control and the bandwidth of the current loop.

The BFO algorithm was written in MATLAB. The designed parameters for the BFO algorithm are given in Appendix 1.

5 Results

5.1 Simulation Results

In order to confirm the effectiveness of the proposed system, a MATLAB/Simulink model has been implemented. The schematic diagram of grid-connected PWM voltage source inverter with the proposed control system is given in Fig. 5. The BFO algorithm written by MATLAB is used to determine the best set of parameters for the *LCL*- filter and the best proportional parameters of the PI current controller in order to have the desired minimum damping control and bandwidth of the current loop. *LCL*-filter parameters are: $L_{gt} = 1.7$ mH, $L_{inv} = 1.2$ mH, $C_f = 27$ μF, $\omega_c = 314$ rad/sec and $V_{dc} = 300$ V. The switching frequency is 5 kHz and the deadtime is 2 μs. The specification and parameters of the designed proposed system are given in Appendix 2. The BFO algorithm takes 87 iterations to generate the
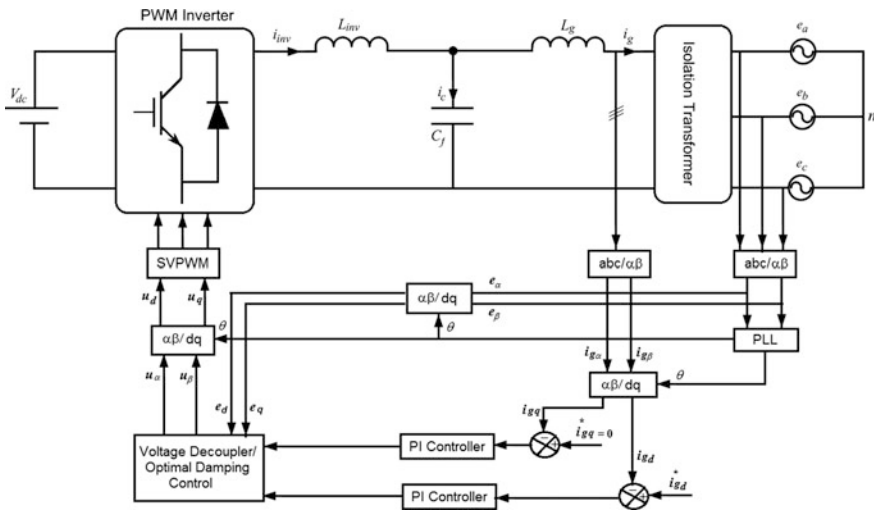
Fig. 5 Schematic diagram of grid-connected PWM voltage source inverter with the proposed control technique

Fig. 6 Fitness function versus iterations
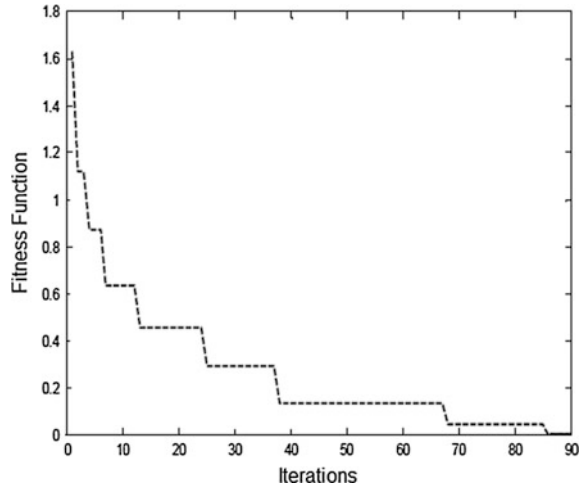
designed parameters for the *LCL*-filter and the PI current controllers as shown in Fig. 6.

The recommended values for optimal control are $\zeta = 0.707$ at $\alpha = 0.3$. When the damping factor ζ decreased to 0.5, a higher crossover frequency ω_c can be obtained as shown in Fig. 4 and hence it yield to faster current control loop response. Therefore α and ζ can be selected from the inequalities in (19). To test the optimal damping control capability and to show how it affect inverter and grid currents, the BFO algorithm was run at $\alpha = 0.3$ and three damping gain values $\zeta = 0.4$, 0.9 and 0.7 respectively. Figure 7a, c, e show the grid voltage and current and the inverter current at $\alpha = 0.3$ and $\zeta = 0.4$, 0.9 and 0.7 respectively. Figure 7b, d, f show the harmonics contents of grid current for the three-grid currents in Fig. 7a, c, e. The total harmonic distortion (THD) for the grid current in the three figures are: 9.35, 5.98 and 2.14 % respectively. Consequently, the dynamic performances of the simulated system are presented in Figs. 8 and 9. The current reference is stepped up from 7 to 22 A in Fig. 8, and stepped down from 22 to 7 A in Fig. 9. Both figures, show that the grid current is well regulated under both steady-state and transient operations. There is no overshoot in the current response observed during the two dynamic responses. This confirms that, the good damping performance of the proposed control scheme is successfully engaged.

5.2 Experimental Results

A prototype of three-phase *LCL*-filter for grid-connected PWM voltage source inverter was developed. It is operating at 15 kW, 5 kHz. The specifications and design values of the major components of the converter are summarized in Appendix 2. The three-phase inverter contain of three insulated gate polar transistor
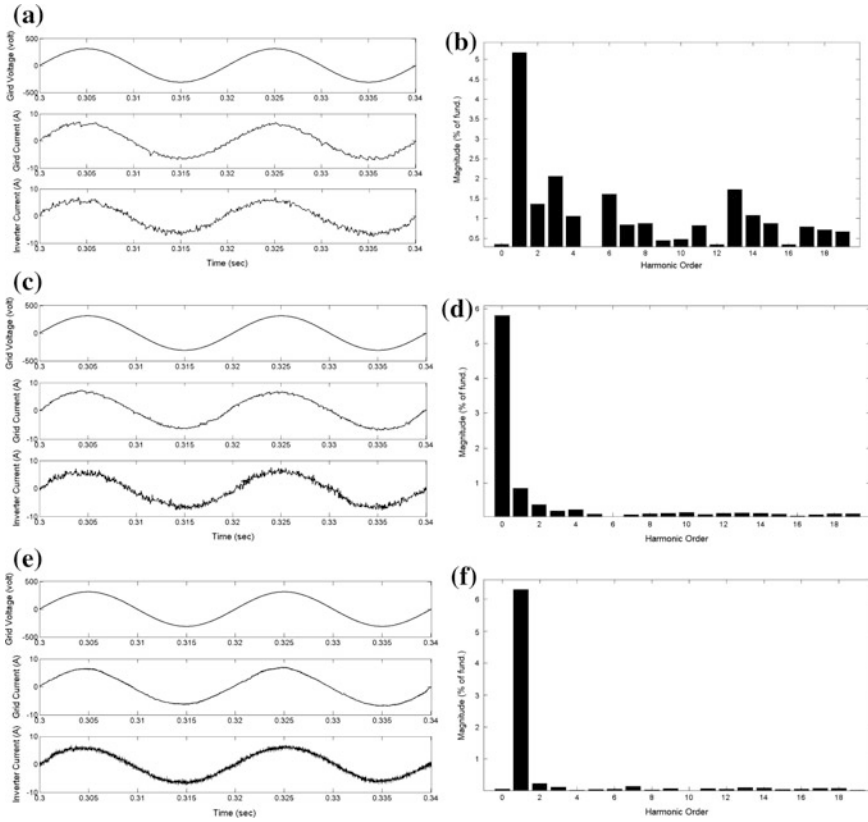
Fig. 7 **a**, **c**, and **e** Grid voltage and current and inverter current waveforms at $\zeta = 0.4$, 0.9, and 0.7 respectively, **b**, **d** and **f** harmonic contents of grid current at $\zeta = 0.4$, 0.9, and 0.7 respectively

(IGBT) modules from *Semikron* (SKM50GB063D), having two switches per module for forming a phase-leg. The inverter was interfaced to the utility grid (415 V line-line rms) through three single-phase 70 V/240 V step-up transformer connected in star-cofiguration. The leakage inductance of the transformer together with the grid impedance was estimated to be 1.7 mH A SHARC DSP (ADSP-21262) 32-Bit Floating-Point is used to generate driving pulses. These pulses are amplified using the driver IC IR2110. The two identical PI current controllers programs are implemented by the DSP. The controller's gains and *LCL*-filter parameters are evaluated off line by the BFO algorithm by using MATLAB.

Figure 10 shows the experimental sinusoidal grid voltage, sinusoidal grid current and input filter capacitor current. The harmonic content of the sinusoidal grid current is given in Fig. 11. The THD of the grid current is 3.12 %. These results agree with the simulation results presented in Fig. 7e, f. This confirms the superior filtering performance of the *LCL*-filter.
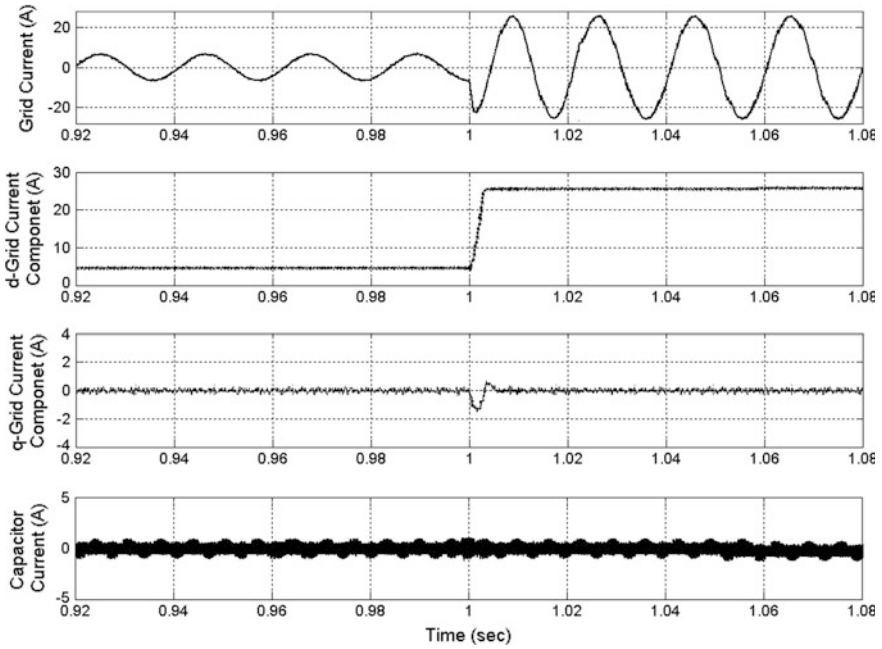
Fig. 8 The LCL- filter based inverter subjected to a step-up current reference from 7A to 22A
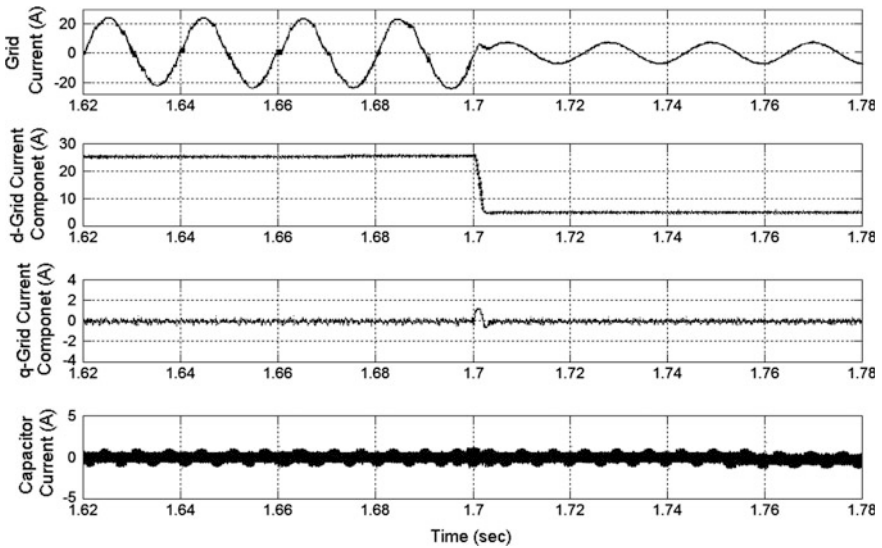
Fig. 9 The LCL- filter based inverter subjected to a step-down current reference from 22A to 7A
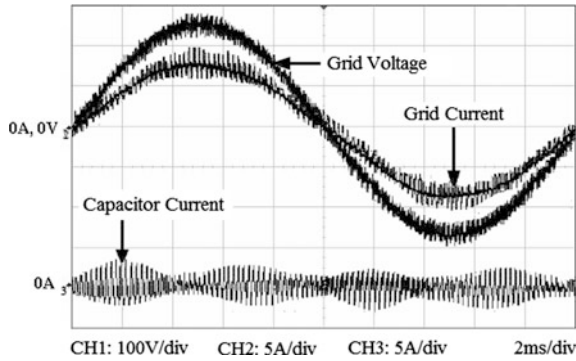
Fig. 10 Experimental grid voltage (50 V/div), grid current and input filter capacitor current waveforms (5A/div)
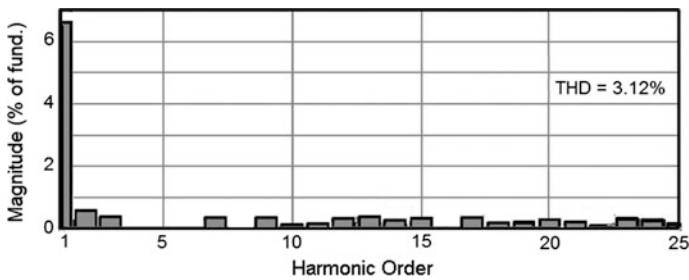
Fig. 11 Harmonic content of the grid current

The steady-state and transient experimental results under PWM inverter current control are captured and shown in Figs. 12 and 13. The reference current is changed from 7 to 22 A step-up transient, and the captured result is shown in Fig. 12, and reference current is changed from 22 to 7 A step-down transient, and the captured

Fig. 12 Step-up in the current reference from 7A to 22A
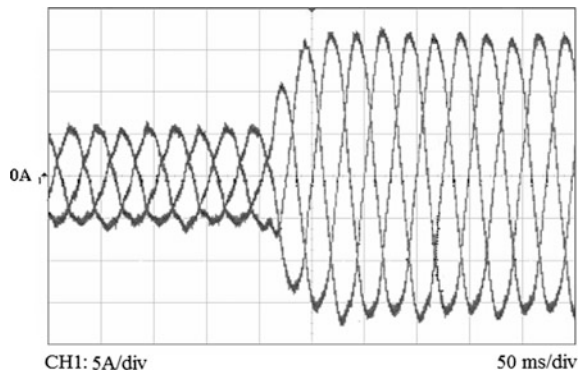
Fig. 13 Step-down in the
current reference from 22A to
7A
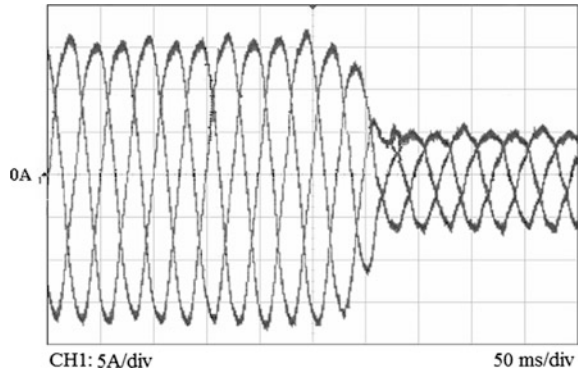
result is shown in Fig. 13. It is observed that the grid current is well regulated and
the *LCL* resonance has been successfully suppressed, which is in good agreement
with the simulation result.

6   Conclusions

This paper is focused on designing a Bacteria Foraging Optimization
(BFO) algorithm of optimal damping LCL filter for three-phase PWM grid inverter.
The main objective is to provide the design procedure for the *LCL*-filter that allows
the optimum damping attained with a desired system control bandwidth.
Mathematical analysis has been presented to study the steady-state and dynamic
performances of the overall system. The fascination of the proposed control tech-
niques is that they only desire one set of current sensors for implementing the
feedback control and momentarily performing the necessary damping of *LCL*
resonance. Simulation and experimental results have been presented to validate the
theoretical inference developed in this paper. It is concluded that the proposed
system based on bacterial foraging optimization are a perfect solution to find the
best parameters for the *LCL*-filters and the proportional gain of the PI current
controller.

Appendix 1

The flowchart of the proposed BFO algorithm.
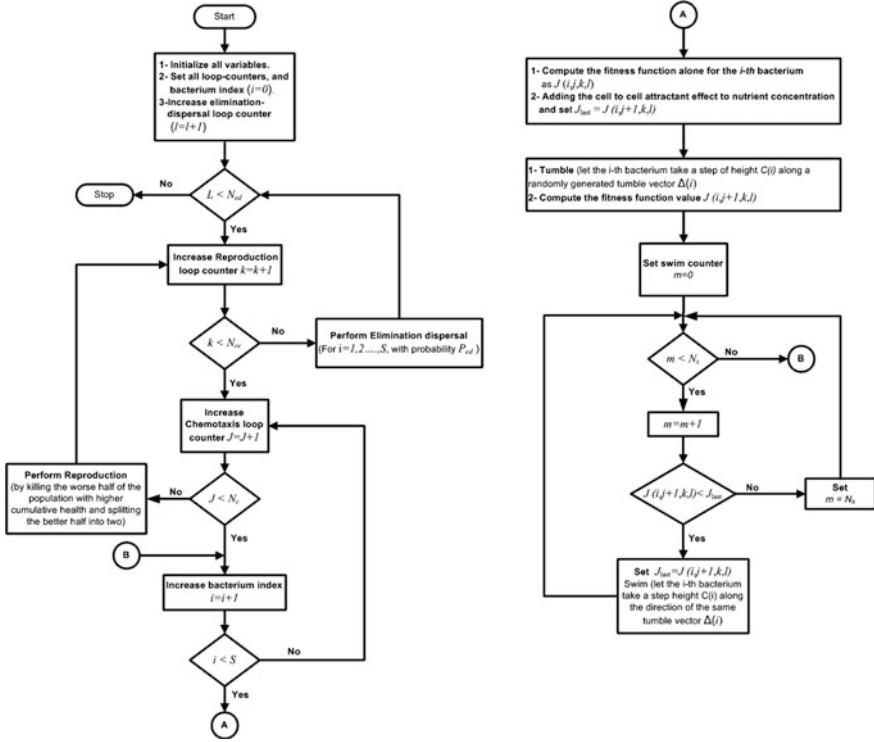
BFO parameters.

Type	BFO
S	100
N_c	4
N_s	100
N_{re}	5
N_{ed}	2
$d_{attract}$	0.1
$\omega_{attract}$	0.2
$h_{repellent}$	0.1
$\omega_{repellent}$	10
P_{ed}	0.1
C	10^{-3}x [−5.12, 5.12]

Appendix 2

Specifications and parameters of the proposed system

Part	Parameters	Values
PWM inverter	Power	7.5 kW
	Switching frequency	5 kHz
	Deadtime	2 μs
	DC-link voltage	300 V
Grid	Grid voltage	140 V
	Line frequency	50 Hz
	Grid inductance ($L_{gt} = L_g + L_{tr}$)	1.7 mH
LCL-Filter	Grid-side inductor (L_g)	0.9 mH
	Inverter-side inductor (L_{inv})	1.2 mH
	Filter capacitor (C_f)	20 μF
Controller	Proportional gain	1.324
	Integral time constant	0.356
	Damping gain	0.7

References

1. S.R. Bull, "Renewable energy today and tomorrow," Proceedings of IEEE, Vol. 89, No. 0018-9219, pp. 1216-1226, 2001.
2. E.H.E.Bayoumi, "Analysis and Design of Linear and Variable Structure Control Techniques for PWM Rectifier," Electromotion Scientific Journal, Vol. 11, No. 4, pp. 205–212, Oct.-Dec., 2004.
3. E.H.E.Bayoumi, A.Maamoun, O.Pyrhönen, M.O.Khalil, and A.Mhfouz, "Enhanced Method for Controlling PWM Converter-Inverter System," in Proc.of the IASTED International Conf. of POWER AND ENERGY SYSTEMS, PES'02, California, USA, May2002, pp. 425–430.
4. E.H.E.Bayoumi, O.Pyrhönen, M.O.Khalil, A.Mhfouz and A.Maamoun, "Control Method for Minimising The dc Link Capacitance of Integrated PWM Converter/Inverter Systems," in Proc. of the 8th international Middle East Power Systems Conference, MPECON'01, Cairo, Egypt, 2001, pp.139–145.
5. E. Twining and D. G. Holmes, "Grid current regulation of a three phase voltage source inverter with an LCL input filter," IEEE Transactions on Power Electronics, vol. 18, no. 3, pp. 888–895, May 2003.
6. IEEE Standard for Interconnecting Distributed Resources with Electric Power Systems, IEEE Std. 1547-2003, July 28, 2003.
7. M. Liserre, R. Teodorescu, and F. Blaabjerg, "Multiple harmonics control for three-phase grid converter systems with the use of PI-RES current controller in a rotating frame," IEEE Transactions on Power Electronics, vol. 21, no. 3, pp. 836–841, May 2006.

8. M. Liserre, R. Teodorescu, and F. Blaabjerg, "Stability of photovoltaic and wind turbine grid-connected inverters for a large set of grid impedance values," IEEE Transactions on Power Electronics, vol. 21, no. 1, pp. 263–272, Jan. 2006.

9. P. Xiao, K. A. Corzine, and G. K. Venayagamoorthy, "Multiple reference frame-based control of three-phase pwm boost rectifiers under unbalanced and distorted input conditions," IEEE Transactions on Power Electronics, vol. 23, no. 4, pp. 2006–2017, Jul. 2008.

10. T. Abeyasekera, C. M. Johnson, D. J. Atkinson, and M. Armstrong, "Suppression of line voltage related distortion in current controlled grid connected inverters," IEEE Transactions on Power Electronics, vol. 20, no. 6, pp. 1393–1401, Nov. 2005.

11. S. Y. Park, C. L. Chen, J. S. Lai, and S. R. Moon, "Admittance compensation in current loop control for a grid-tie LCL fuel cell inverter," IEEE Transactions on Power Electronics, vol. 23, no. 4, pp. 1716–1723, Jul. 2008.

12. X. Wang, X. Ruan, S. Liu and C. K. Tse, "Full feedforward of grid voltage for grid-connected inverter with LCL filter to suppress current distortion due to grid voltage harmonics," IEEE Transactions on Power Electronics, vol. 25, no. 12, pp. 3119–3127, Dec. 2010.

13. M. Liserre, F. Blaabjerg, and S. Hansen, "Design and control of an LCL-filter-based three-phase active rectifier," IEEE Transactions on Industry Applications, vol. 41, no. 5, pp. 1281–1291, Sep./Oct. 2005.

14. J. Dannehl, F. W. Fuchs, S. Hansen, and P. B. Thøgersen, "Investigation of active damping approaches for PI-based current control of grid-connected pulse width modulation converters with LCL filters," IEEE Transactions on Industry Applications, vol. 46, no. 4, pp. 1509–1517, Jul./Aug. 2010.

15. F. Liu, Y. Zhou, S. X. Duan, J. J. Yin, B. Y. Liu, and F. R. Liu, "Parameter design of a two-current-loop controller used in a grid-connected inverter system with LCL-filter," IEEE Trans. Ind. Electron., vol. 56, no. 11, pp. 4483–4491, Nov. 2009.

16. Y. Chen and F. Liu, "Design and control for three-phase grid-connected photovoltaic inverter with LCL-filter," in Proc. 2009 IEEE Circuits and Systems International Conf., pp. 1–4.

17. V. Blasko and V. Kaura, "A novel control to actively damp resonance in input LC filter of a three-phase voltage source converter," IEEE Trans. Ind. Appl., vol. 33, no. 2, pp. 542–550, Mar./Apr. 1997.

18. E. Wu and P. W. Lehn, "Digital current control of a voltage source converter with active damping of LCL resonance," IEEE Trans. Power Electron., vol. 21, no. 5, pp. 1364–1373, May 2006.

19. J. Dannehl, F. W. Fuchs, S. Hansen, and P. B. Thogersen, "Investigation of active damping approaches for PI-based current control of grid-connected pulse width modulation converters with LCL-filters," IEEE Trans Ind. Appl., vol. 46, no. 4, pp. 1509–1517, Jul./Aug. 2010.

20. H.G. Jeong, K. B. Lee, S. Choi, and W. Choi, "Performance improvement of LCL-filter-based grid-connected inverters using PQR power transformation," IEEE Trans. Power Electron., vol. 25, no. 5, pp. 1320–1330, May 2010.

21. S. Mariethoz and M. Morari, "Explicit model-predictive control of a PWM inverter with an LCL-filter," IEEE Trans. Ind. Electron., vol. 56, no. 2, pp. 389–399, Feb. 2009.

22. L. A. Serpa, S. Ponnaluri, P. M. Barbosa and J. W. Kolar, "A modified direct power control strategy allowing the connection of three-phase inverters to the grid through LCL-filters," IEEE Trans. Ind. Appl., vol. 43, no. 5, pp. 1388–1400, Sep./Oct. 2007.

23. G. Shen, D. Xu, L. Cao, and X. Zhu, "An improved control strategy for grid-connected voltage source inverters with an LCL-filter," IEEE Trans. Power Electron., vol. 23, no. 4, pp. 1899–1906, Jul. 2008.

24. Ehab H.E. Bayoumi," Design and Control of an LCL Series Parallel Resonant Converters Using Bacterial Foraging Optimization," International Journal of Power Electronics (IJPELEC), Vol.4, No.5, pp. 497–504, 2012.

25. J. Dannehl, C. Wessels, and F. W. Fuchs, "Limitations of voltage-oriented PI current control of grid-connected PWM rectifiers with LCL-filters," IEEE Ind. Electron., vol. 56, no. 2, pp. 380–388, Feb. 2009.

26. R. Teodorescu, F. Blaabjerg, M. Liserre, and A. Dell'Aquila, "A stable three-phase LCL-filter based active rectifier without damping," in Proc. 2003 IEEE Industry Applications Society Annual Meeting, pp. 1552–1557.
27. Y. Tang, P. C. Loh, P. Wang, F. H. Choo, and K. K. Tan, "Improved one cycle- control scheme for three-phase active rectifiers with input inductor capacitor- inductor filters," IET Power Electron, vol. 4, no. 5, pp. 603–614, 2011.
28. E.H.E. Bayoumi and F.Salem, "PID controller for series-parallel resonant converters using bacterial foraging optimization," Electromotion Journal, vol. 19, no. 1–2, pp. 64-79, 2012.
29. E.H.E. Bayoumi, "Parameter Estimation of Cage Induction Motors Using Cooperative Bacteria Foraging Optimization," Electromotion Scientific Journal,Vol.17, No.4, pp.247–260, Oct.-Dec.2010.

Real Time Monitoring of Incipient Faults in Power Transformer

Nikolina Petkova, Petar Nakov and Valeri Mladenov

Abstract Power transformers in the power electric system are of particular significance for the reliability of electric power consumers. Up-to-date monitoring systems for power transformers support taking measurements and analysis of: temperature of the hot spots in the winding (calculated automatically by the system); gas and moisture contents in the oil inside transformer's tank; partial discharge activity; winding insulation humidity and other important parameters, but do not render an account of the small amplitude of partial discharges availability under 300 pC. In this article a method for locating the place of origin of the partial discharges in the three-dimensional space is described. Future efforts are to be dedicated on finding an algorithm for on-line measurement and locating of the partial discharge from incipient fault.

1 Introduction

The electrical partial discharge measurement is the most suitable method for assessing the condition of insulation systems in high voltage equipment. Conventional partial discharge measurement systems have proven to have some difficulties in the measurements, particularly in online conditions and noisy environments [4].

N. Petkova (✉) · V. Mladenov
Department of Theoretical Electrical Engineering, Technical University of Sofia,
8, Kliment Ohridski St., 1000 Sofia, Bulgaria
e-mail: npetkova@tu-sofia.bg

V. Mladenov
e-mail: valerim@tu-sofia.bg

P. Nakov
Department of Electrical Engineering, Technical University of Sofia,
Faculty of Electrical Engineering, 8, Kliment Ohridski St., 1000 Sofia, Bulgaria
e-mail: pnakov@tu-sofia.bg

The measurement of the partial discharge begins with the sensors placement around the transformer, where their outputs are linked to the monitoring system. During the process of sensors positioning, the power transformer should be switch off from the network.

Partial discharges (PDs) are in general a consequence of local electrical stress concentrations in the insulation or on the surface of the insulation [1].

Power transformers are used to transform voltage from one to another voltage level and are an integral component of power system. A typical transformer incorporates coils of conducting wire wrapped around a core and covered with a paper-based insulator. Essential to the operation of these units are transformer oils that have two functions: electrical insulation and heat dissipation. Regrettably, there are instances of transformers failing whilst in service, creating significant cost implications for the power supplier and, in extreme cases, explosion with a consequent threat for workers for severe injury or death and significant environmental impacts [5].

Aging depends not just on loading, but is also influenced significantly by the type of paper, pulp composition, humidity and oxygen contents, as well as the acidity level of the insulating liquid. Insulation is a major component, which plays an important role in the life expectancy of the transformer. Oil suffers continuous deterioration and degradation due to the sustained effect of the electric and cyclic thermal stresses because of loading and climatic conditions. This may be hazardous to the electric equipment and installation. Continuous monitoring of oil insulation characteristics has become an important task to avoid deterioration of oil characteristics under working conditions. Several efforts have been made over the past years to study the electrical, physical and chemical properties of the insulating oils [3]. Preventive maintenance for transformers includes daily recordings of oil level readings and temperature readings. Twice a year, oil samples should be taken to test chemical, physical and electrical properties. Oil testing includes specific gravity, kinematics viscosity, flash point, total acidity, humidity, breakdown voltage and dissolved gases evaluation. These kinds of tests are made by substation staff and the results are known. That is the monitoring of the condition of the transformer oil and the collected information are integrated together and classified as "GOOD" or "BAD".

The PD phenomenon is manifested in a variety of physically observable signals, including electric pulses and is currently detected using a host of external measurement techniques. This technique of electrical detection is a widely accepted technology, because it allows for the source to be located, when several sensors are mounted to the exterior of the tank.

Briefly, in order for a PD to occur, a free electron must be present within a voltage dependent volume, while the electric field strength should be sufficiently high to cause a cascading flow of electrons from the movement of a single free accelerated electron. The electron occurrence has a stochastic nature, which makes the PD phenomenon very unpredictable. Therefore, a PD can occur within minutes or within hours of reaching the breakdown field strength within the void. The test of

PDs available in transformer should be done before the experts take a decision about the future work of the transformer.

In order to improve the existing monitoring systems, an algorithm for partial discharges in the volume of the transformer was established. Time delays of the electromagnetic waves travelling in the volume of the power transformer, from the assumed location of the partial discharges to the location of each of the measuring sensors, turned out to be of paramount importance.

The analysis is based on the monitoring method consisting of some modules, which process the data step by step, as shown in Fig. 1.

The measurement of the partial discharge begins with determining of the calibration matrix. It is done by measuring the characteristics of the partial discharges with the equipment being switched off. To each measurement input consequently a signal from a calibrating generator is let out, as the characteristics of the signals, emitted to the remaining measuring impedances are being measured.

The calibration matrix includes the factors of signal transmission, from the calibrating generator connection point to the partial discharges measurement points and the time delay.

The input data is acquired from real measurements and are applied during the procedure. When the measurement system is connected, the signals are registered. Next, the PD impulses are separated and through the data transfer module, the data is transferred to the comparison module. There are obtained the time delays between the registered PDs from each measuring channel as well as the time of their occurrence. This information is then transferred into the calculation module, where the approximate position of PD is established. This position of the PD is visualized through the visualization module and an expert determines the part of the
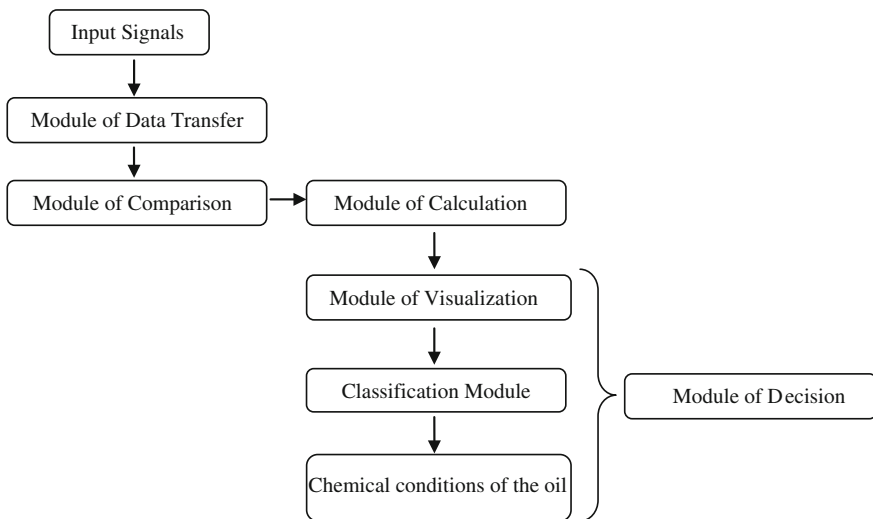

Fig. 1 Block diagram of the software system

transformer that the partial discharge occurs, based on the technical design of the transformer. Using the partial discharge signal structure, the Module of Classification determines the type of the partial discharge. Together with the chemical condition of the oil in the power transformer, the final decision is taken in the Module of Decision.

2 Module of Data Transfer

The main features are as follows:

- It consists of some sensors, placed on the tank of power transformer and connected with the oscilloscope through coaxial cables.
- The signals measured from the oscilloscope have different shapes and delays due to the different sensors. Measured data from the oscilloscope can be both visualized directly on the screen or sent to the Measurement Unit, Registration Unit and Software.
- It is recommended the measurement signals will be storage at "Low level" Measurement Unit and then send through a Wi-Fi connection to the "High level" Registration unit.
- The acquired data is sent to the central server for processing. The software will give information about the current status of the power transformer, under the labels "work", "danger" or "attention". Thus, the expert engineer will be informed about the level of emergency and take the necessary measures as appropriate.

2.1 *Measurement Unit*

The block diagram in Fig. 2 shows the input and output data for the Measurement Unit.

To track the data processing algorithms for results and processing, it is assembled a new devices—Measurement Unit and Registration Unit. The device uses a method that acquires and stores the values through the developed controller that tracks the signals from the measurement channels. To diminish the occurrence of errors and maintain the accuracy of the data signals and the time delay, it is used the
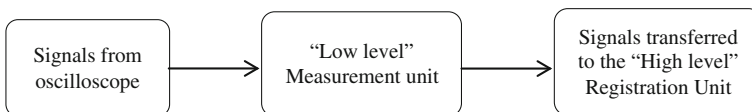
Fig. 2 Block diagram with input and output data for the Measurement Unit

return channel. One of the traditional approaches, that is to process data with a validated software, has been adapted to our case. For this purpose, a system is used for managing the transformer with validated software that has no relation to the study processes and the development task. The aim is to obtain an adequate assessment of the data transmitted on the new channel.

2.2 "High Level"—Registration Unit

Its purpose is to register in real time and store all information for selected values of the controlled objects in both normal and emergency modes. The length of the record is programmable and depends on the introduction settings.

The Registration Unit works, depending on the conditions, in a cyclical scan of data regime or it is in a passive state of waiting for data exchange, after having registered selectable emergency events or processes.

A data exchange is possible in transparent mode, where each processed logical signal is transmitted through the communication link. This exchange does not change the selected mode for recording data in the memory. Access to the data is possible through a specialised protocol.

The block diagram shown in Fig. 3 presents the input and output data for the "High level" Registration Unit. Data is transferred from the "Low level" Measurement Unit to the "High level" Registration Unit through a wireless connection.

The collected measured data is stored in a memory device after the appropriate digital processing has been done, which enables us to obtain values of the variables. Processed data is now ready to be transmitted to the "High level". In order to seal the information flow, to reduce the size of the array programs and increase the reliability, the data is transmitted to the "High level" in binary code with additional noise resistant coding. Subsequent processing, which converts the data into a format suitable for software processing, is performed by the device—"Registration Unit." The period of refreshment of the data is an adjustable parameter. The interval between two registered emissions is adjusted depending on the dynamics of the process. This can be set when the system is installed. A sporadic (random) phenomenon such as partial discharge is recorded by the oscilloscope and/or the suitable equipment. The tools for processing the signals are the same as above, i.e., when PD appears, the oscilloscope stops the recording and through serial interfacing for the connection, the controller reads the data files from the oscilloscope.

Fig. 3 Block diagram with input and output data for the Registration Unit

When a new message is initiated, the package is changed and the recorded data file is transmitted in binary code and with noise resistant coding to "High level". Once the signals are received, filtered and cleaned, they are dispatched to the decoder program.

The power supply should have galvanic separation from the oscilloscope, in order to reduce noise. When the oscilloscope is switched on the power supply mode, the "Measurement Unit" reads the data and sends them to the "Registration Unit". Each data package is added to the actual real-time data acquisition. The information is used as a marker for the software part. The "Registration Unit" codes data packets in binary code—ASCII code table, which are then transmitted by the register to the computer unit.

In the computer, a standard program that controls the communication port is activated. The USB interface is interpreted as a virtual com port.
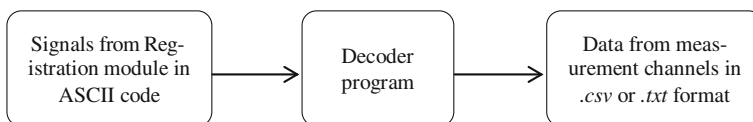
2.3   Decoder Program

This program decodes the data from the Registration Unit, which is received in ASCII code, to suitable file formats.

The block diagram of Fig. 4 shows the input and output data for the Decoder program.

The values of the actual parameters are converted into additional BCD (binary—coded decimal) code. The COM port records a file for each message received on the hard disk. The software for the final conversion is not taken into consideration because the control of analogue values is an additional option.

ASCII format affects the visualization of data, which are in hexadecimal code.

Arrays with data from the oscilloscope are coded as follows:

- The accepted data is preformatted in four arrays with two columns and a corresponding number of rows (2n)
- This reformatting is improved during the transmission of data from the COM port to the register of the computer.
- To maintain the analogy when processing the received messages, i.e., the program should record input data as separate files, proceeding as follows—The register transmits a first array containing information from the first channel. In the process of transmission, the recoding of a binary format in the BCDS format with a sign is mandatory. In addition, the transmitted symbols are transferred.

Fig. 4 Block diagram of Decoder program
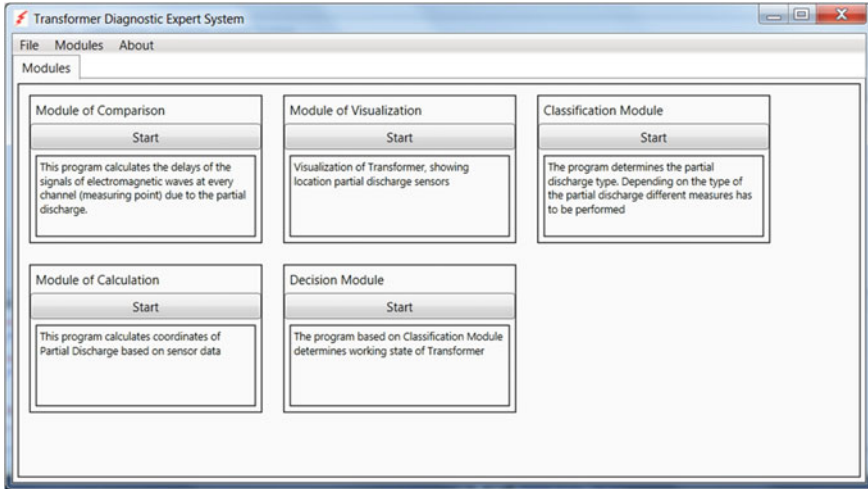
Fig. 5 Transformer Diagnostic Expert System

This ensures that the file is saved and can be directly read by the software program as input data. The same procedure is repeated three or more times for the other measurement channels.

The number of decoded files depends on the number of measurement channels or the number of measurement sensors.

The software of Transformer Diagnostic Expert System is included all modules and starts with a window which is shown in Fig. 5.

3 Module of Comparison

After the PD signals are acquired from the different channels, they are transferred to the local control centre, where they are processed.

In case there is still noise in the signals, noise removal techniques are applied to minimise noise and to extract PDs from the interferences. For this reason, the Fast Fourier Transform (FFT) is applied to each signal and harmonics with amplitude less than a given threshold are removed.

The method that is applied for determining the position of the partial discharge uses the relative delay of the signals from different channels. When the signals are filtered, the delays are calculated easily based on their first appearance. The procedure can be carried out in various ways.

The block diagram shown in Fig. 6 presents the input and output data for the Module of Comparison.

Fig. 6 Block diagram with input and output data for the Comparison module

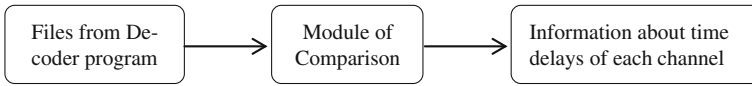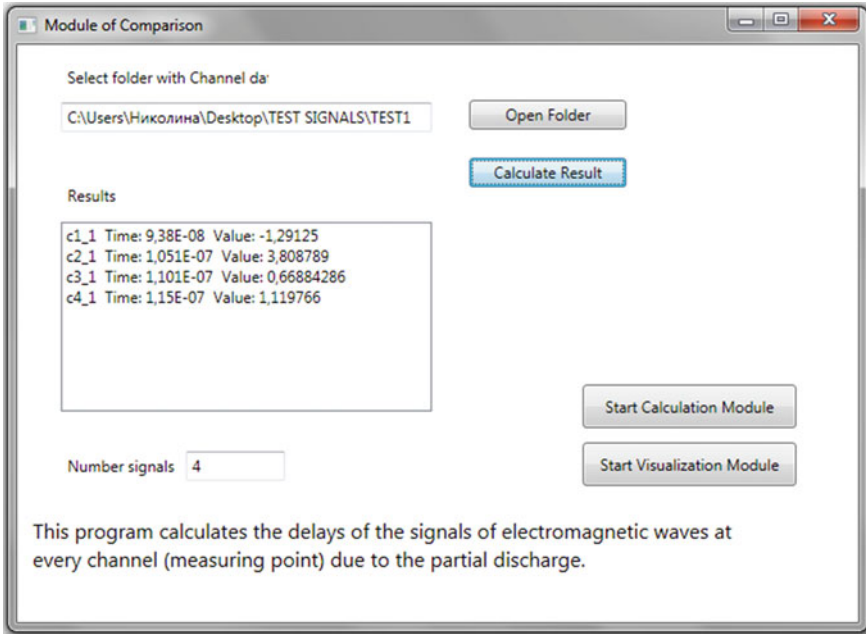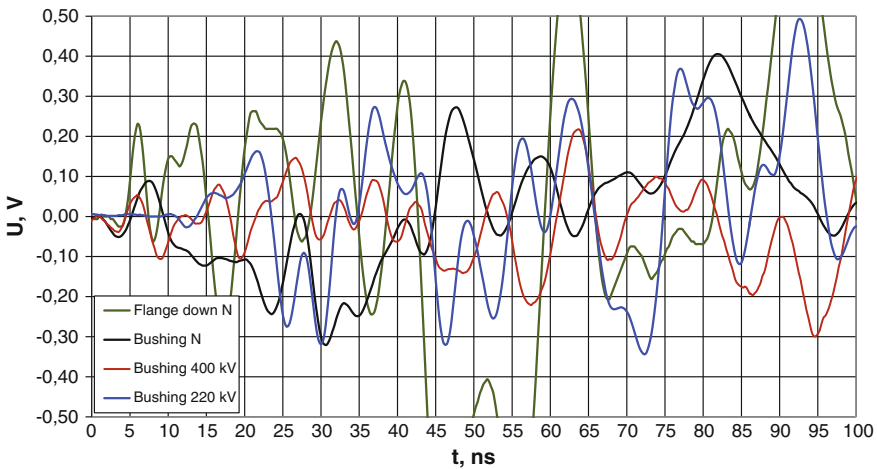**Fig. 7** Module of Comparison screenshot

Fig. 8 Obtained signals for Test 1

When the button "Start" of Module of Comparison is pushed, first window from Module of Comparison is appeared the falter with data (measured signals) has to be chosen, for example falter with name "TEST1". Then OK should be pushed.

The software start when the Press "Calculate Result" and then another window appears, where the user selects TEST1. Press "OK" and the software will generate the time delays of each of the four measurement channels and the values of the measurement signals from TEST1, as shown in Fig. 7.

Signals from TEST1 with their delays are shown in Fig. 8.

4 Module of Calculation

In order to localize the flaw in the power transformer, every source of partial discharge has to be connected to a flaw, which does not change its place in the volume of the transformer. The aroused electromagnetic wave is distributed in the winding of the transformer and in the volume of the insulation construction and reaches the place, where the measurement is taken with a delay, corresponding to the speed of propagation. During propagation, the electromagnetic wave is being refracted, cut and deformed depending on the path taken. Consequently, the shape of the voltage or current wave, measured by the instruments is unique for every source of partial discharge and every place of conducting the measurement. The block diagram shown in Fig.9 presents the input and output data for the Module of Calculation.

The input data is: the number of measurement sensors, the speed of electromagnetic wave from PD, the coordinates of the sensors and the time delay.

n   number of measurement sensors (in this example the sensors are six);
V   speed of the electromagnetic wave calculate from calibration data;
X_i, Y_i, Z_i coordinates of the sensors;
Delta T_i time delay for each sensor.

In the Module of Calculation all parameters have to be given in International System (SI). The results are the coordinates of partial discharges in the power transformer volume, i.e., there is information for the estimated position of the fault with the exact coordinates x, y and z.

After all the sensors coordinates are provided, the "CALCULATE" button is selected and then the program calculates the coordinates of the partial discharge in the transformer volume, as in Fig. 10:
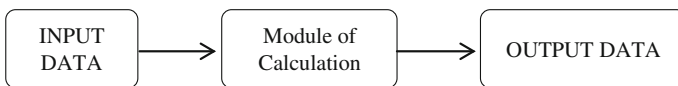
Fig. 9 Block diagram of Module of Calculation

n= 6		Xi [m]	Yi [m]	Zi [m]	delta Ti [s]
V= 1220000 m/s	1	0.600	6.375	5.000	0.00000000625
	2	0.325	3.550	4.200	0.00000001663
Сметни	3	0.750	0	3.825	0.00000005462
	4	2.125	0	3.825	0.00000005062
X=1.595 m. Y=7.362	5	2.375	9.875	3.875	0.00000000500
Z=3.303 m.	6	2.425	9.575	1.000	0.00000001000
t=17.300 ns					
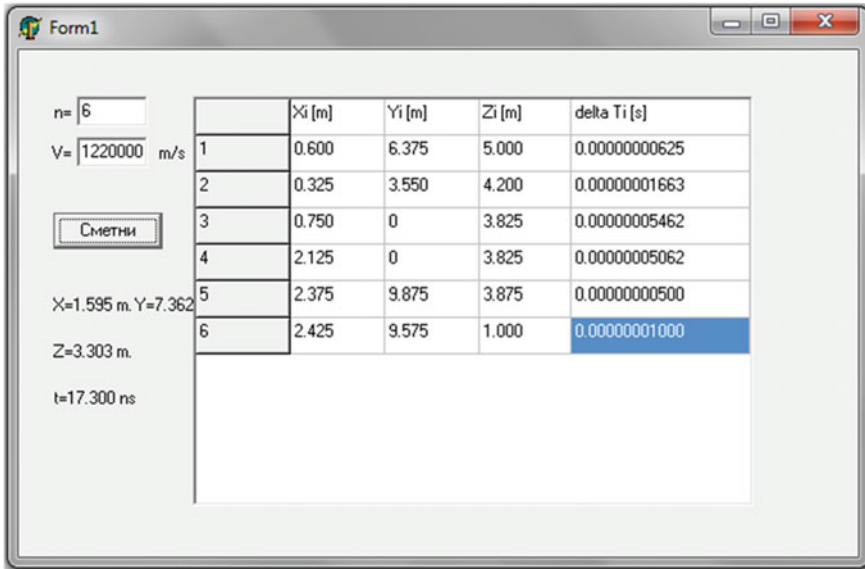
Fig. 10 Module of Calculation screenshot

The output is the coordinates of the partial discharge in the transformer volume and the time which with consequent degree of t are made different spheres till they crossed (X = 1,595 m, Y = 7,362 m, Z = 3,303 m, t = 17,300 ns).

5 Module of Visualization

When the position of the partial discharge is determined in the corresponding coordinate system, the exact location has to be verified. The aim of this module is to visualize the main framework of the transformer under investigation, the positions of the measuring sensors and the position of the partial discharge. Based on the image, the operator has to decide where the exact place of the partial discharge is.

The most important places where partial discharges appear can be summarized as follows:

- TAPCHANGER: includes tap changer, tap board terminals, in-tank tap changer components and surrounding areas. Conventionally, the tap changer inside the tank is one of the most troublesome components of power transformers. Its mechanical parts become loose due to frequent operation. Its contacts experience overheating and/or arcing when changing taps under load conditions. All these factors contribute to the fault occurrence. Although modern transformers usually have a separate tab changer compartment, the tap board is still inside the

tank and causes problems because the mechanical and thermal stress can transfer from the separate compartment to it.

- TANK: includes the oil tank case, core laminations, assembly bolts, etc. The major problem is overheating caused by close loop current. Careless assemblage of core or tank parts may leave conducting loops in the magnetic circuit. Vibration of the core may damage the core bolt insulation and generate conducting loops as well. These loops may allow large currents to flow and the core/tank could be seriously overheated.
- LEADS: including leads between winding coils, between windings and bushings, between windings and tap changer tap board, between neutral point and ground, etc. The high voltage leads are more likely to have problems than the low voltage ones. These leads are often related to high-energy discharges because they are usually close to ground potential. They can also experience electrical overheating because they usually have joints, whose resistance may generate a large amount of heat under normal and particularly overload conditions.
- WNDG: this category refers to windings. Problems with windings are mostly insulation degradation or breakdown. The degradation is caused by the high temperature of the core or the conductor, and the electric field applied to the insulation. Symptoms include the development of partial discharges and arcing. Overloading and through fault cause excessive electrical overheating. Abnormal eddy currents in the core cause excessive magnetic overheating. Overheating accelerates the degradation process.
- OTHER: this category includes areas other than the aforementioned ones, such as forgotten tools in the tank, static shielding, cooling systems (fans, oil pumps), etc. The block diagram shown in Fig.11 presents the input and output data for the Module of Visualization. .

The input data of this module is the number of coils, their radius, their coordinates and sensor parameters. The actual parameters of the transformer, coils and sensor positions remain the same for all tests.

The output of this module is the graphical representation of the partial discharge.

After all data has been entered, the button "Visualize" is pressed and the software generates the graphical representation of the partial discharge (red point), as in Fig. 12:

The operator decides where the partial discharge occurs (tap changer, tank, leads, winds or other).

Fig. 11 Block diagram for Module of Visualization
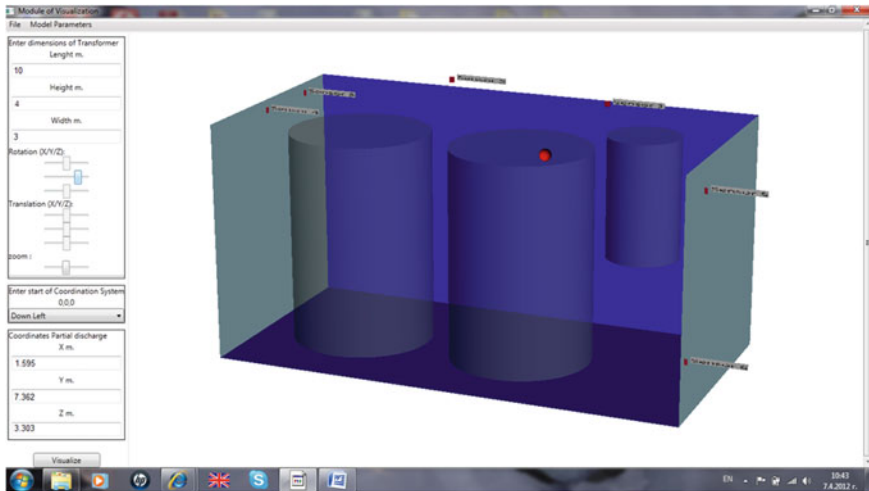
Fig. 12 Module of Visualization screenshot

6 Module of Classification

After the data is acquired from the Module of Visualization, the analysis is continued in the Module of Classification.

The most popular cases for partial discharges appearance are given in IEC 60076-3:2000-03. These depend on parameters such as location of discharges on test voltage, variability of response, relative magnitude of discharges on positive/negative half cycle and variation of discharge magnitude depending on test voltage and time of application. The block diagram shown in Fig.13 presents the input and output data for the Module of Classification. .

The input data is shown in Fig. 14.

The measurement signals and the type of oscillations can be classified depending on the following parameters:

- Location of discharge: most pulses in advance of the voltage peaks;
- Variability of Response: random movement;
- Relative Magnitude of discharge: different magnitude on two half cycles;
- Test voltage: rises with test voltage;
- Time of application: constant with time.

Fig. 13 Block diagram for Module of Classification
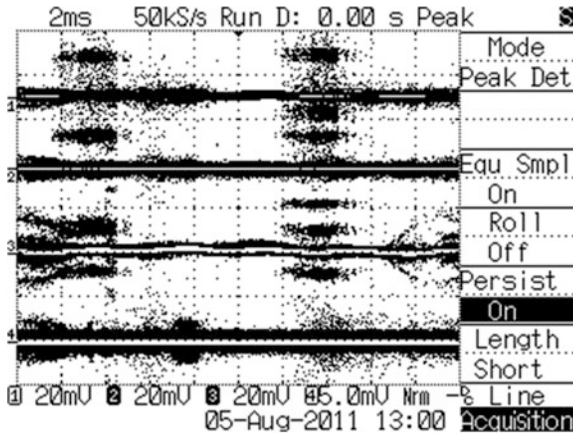
Fig. 14 Input Data
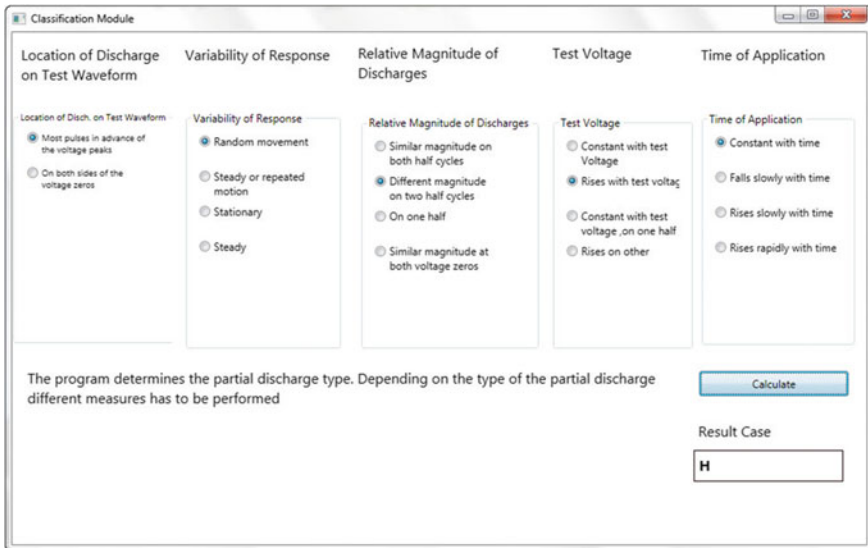
Fig. 15 Module of Classification screenshot

The input and output data of this case of PD occurrence can be seen in Fig.15. The output data is the result case H:

In case H, discharges that occur in advance of the test voltage peaks are described and these discharges on one half cycle of the test waveform are greater in number and smaller in magnitude than on the other half cycle. The amplitude difference on the two half cycles may be as low as 3:1, however a difference of 10:1 is possible if the applied voltage is raised. There is a degree of random variation in both amplitude and location [2].

Indication

Internal discharges between metal or carbon and dielectric in a number of cavities of various sizes are possible. It is often difficult to ensure that a response of this type indicates cavities between metal or carbon and dielectric, as cavities within the dielectric may have metallic or carbonaceous inclusions or non-uniform surface conductivity [2].

There are surface discharges taking place between external metal or carbon and dielectric surfaces and internal discharges in a dielectric-bounded cavity. If a response with greater discharge magnitude occurs at a higher voltage, this will indicate discharges in a second cavity [2].

7   Module of Decision

This module determines the state of the power transformer.

The most important parameters regarding the final decision about the actual transformer state are the location of the partial discharge, the partial discharge case and the transformer oil conditions.

The possible cases of partial discharge occurrence are A, B, C, D, E, F, G, H, J, K, L, M and N. The possible locations of partial discharges are in the tank, windings, leads, tap changer and the other. Only two cases of oil conditions are considered- good and bad oil.

In a substation, the condition of the oil can be examined using Dissolved Gas Analysis (DGA).

The gasses that are dissolved in the insulating oil are energy generated due to a fault, thus resulting in the partial or complete destruction of the Hydrocarbon molecular chains of the insulating oil. The fractions consist of: Ethane C_2H_6, Ethylene C_2H_4, Ethane C_2H_2, Hydrogen H_2, Methane CH_4, Propane C_3H_8 and Propene C_3H_6.

Due to the de-polymerization of the solid paper insulation additionally Carbon Dioxide CO_2 and Carbon Monoxide CO are generated.

The atmospheric gases Oxygen O_2 and Nitrogen N_2 are dissolved in the insulating liquid as well if the transformer is of breathing type and is exposed to the environment.

This relation is dominated by the form and amount of energy that has been applied in the transformer failure, thus thermal faults and electrical faults can be distinguished. A more precise distinction between the sizes of the failures and the level of concentration of gases is also specified in the standard IEC 60599.

In our paper, the results from the chemical conditions of the oil could be summarized as GOOD OIL (if the concentrations of the gases are in compliance to standard IEC 60599) or BAD OIL (if the concentrations of the gases are not in compliance to standard IEC 60599). These results are used in the decision module where the operator takes the final decision regarding the emergency of the partial

Table 1 The emergency regarding to PD case, PD location and oil condition

Case of PD occurence		PD location categories	Oil condition	Emergency
Case	Indication			
A	Internal discharges in a dielectric-bounded cavity; indicates discharges in a second cavity	TANK	GOOD	WORK
		TANK	BAD	ATTENTION
		WNDG	GOOD	WORK
		WNDG	BAD	ATTENTION
B	The behaviour described has been detected in elastomeric insulation containing a cavity in the form of a fissure in the direction of the electric field; It has also been detected with rounded cavities in thermoplastic insulation containing certain inhibitors and/or plasticizers and in certain elastomers such as ethylene, propylene rubber	TANK	GOOD	WORK
			BAD	ATTENTION
C	Internal discharges in a number of dielectric-bounded cavities of various sizes; Discharges on external dielectric surfaces between two touching insulated conductors; Discharges on external dielectric surfaces at areas of high tangential stress	LEADS	GOOD	ATTENTION
		LEADS	BAD	DANGER
		WNDG	GOOD	ATTENTION
		WNDG	BAD	DANGER
D	Internal discharges in a number of dielectric-bounded cavities of various sizes. This behaviour is found mainly in cast-resin insulation, and is caused by the production of electrically-conducting products (e.g. water) by the action of the discharges on the resin	LEADS	GOOD	ATTENTION
		LEADS	BAD	DANGER
		WNDG	GOOD	ATTENTION
		WNDG	BAD	DANGER
E	I Internal discharges in laminar cavities. The behaviour described is found in machine insulation containing mica	LEADS	GOOD	ATTENTION
		LEADS	BAD	DANGER
		WNDG	GOOD	ATTENTION
		WNDG	BAD	DANGER
F	Internal discharges in gas bubbles in an insulating liquid in contact with moist cellulose (ejj. oil-impregnated paper) mainly in capacitors. The bubbles are generated by the action of electric stress on the moist cellulose. The bubbles increase in size and number under the action of discharges, but dissolve in the liquid and so disappear upon removing the stress for a sufficient period of time	TANK	GOOD	ATTENTION
			BAD	DANGER

Table 1 (continued)

Case of PD occurence		PD location categories	Oil condition	Emergency
Case	Indication			
G	Internal discharges between metal or carbon and dielectric in a cavity. If a response having greater discharge magnitude occurs at a higher voltage, this indicates discharges in a second cavity. It is often difficult to be sure that a response of this type indicates a cavity between metal or carbon and dielectric, as cavities within the dielectric may have metallic or carbonaceous inclusions or a non-uniform surface conductivity	TAP CHANGER	GOOD	ATTENTION
			BAD	DANGER
H	Internal discharges between metal or carbon and dielectric in a number of cavities of various sizes. It is often difficult to be sure that a response of this type indicates cavities between metal or carbon and dielectric, as cavities within the dielectric may have metallic or carbonaceous inclusions or non-uniform surface conductivities; Surface discharges taking place between external metal or carbon and dielectric surfaces	TAP CHANGER	GOOD	ATTENTION
			BAD	DANGER
		TANK	GOOD	ATTENTION
			BAD	DANGER
J	"Floating objects": discharge or unwanted disturbance caused by an air gap between metallic or carbonaceous conductors. The gap may be actually inside the specimen itself, e.g. a loose connection to a screen, or it may be located at various points in the test circuit. More usually it is a gap between two quite independent metallic objects (or a single metallic object and earth) across which a voltage is produced by electrostatic induction from the test circuit. The disturbance may, for example, be caused by metallic objects lying on the ground. In consequence, a clean laboratory floor is required for tests at voltages above 30 kV. It should be noted that similar but very large discharges may be produced by gas discharge tubes built into the input circuit of the discharge detector for overvoltage	LEADS	GOOD	DANGER
			BAD	DANGER

Table 1 (continued)

Case of PD occurence		PD location categories	Oil condition	Emergency
Case	Indication			
K	Electrical transient produced by mechanical movement of part of an electrode under the influence of the electric field. This effect is usually observed in defective capacitors in which a small section of an electrode in the form of a metallic foil or metalizing is free to move	OTHER	GOOD	DANGER
			BAD	DANGER
L	External corona discharge from a sharp metal point or edge. If the discharges are on the negative half cycle of the test waveform, the point is at high voltage. If the discharges are on the positive half cycle the point is at earth potential. In consequence a test installation, in which both the high-voltage and earthed conductors are free from sharp edges and points, is needed for tests at voltages above 30 kV	TAP CHANGER	GOOD	ATTENTION
			BAD	DANGER
M	Corona discharge from a sharp metal point or edge in an insulating liquid. If the larger discharges are on the positive half cycle of the test waveform, the point is at high voltage. If the larger discharges are on the negative half cycle, the point is at earth potential. A multiple pattern may be obtained if an edge having more than one radius of curvature is involved	TAP CHANGER	GOOD	ATTENTION
			BAD	DANGER
		TANK	GOOD	ATTENTION
			BAD	DANGER
N	Contact noise due to imperfect metal-to-metal joints, or due to contact between graphite particles in semi-conducting screens (particularly carbon-black paper and semi-conducting screens in plastics-insulated cables). The contacts producing the noise may be actually inside the specimen itself or they may be located at various points in the test circuit. If the resolution of the discharge detector can be improved (e.g. by reducing the time constant of the detection circuit), this may reduce superposition of discharge pulses and so reduce the magnitude of the response. Contact noise frequently occurs in capacitors in which connection to the foils is made via metallic inserts. Such noise can often be eliminated by charging the capacitor then short-circuiting it	OTHER	GOOD	WORK
			BAD	ATTENTION

discharge that is detected. In substations, information for the condition of the oil is provided by technical labs in six month intervals.

In Table 1 a number of possible classifications of power transformer states are presented according to emergency (Fig. 16).

The block diagram shown in Fig.16 presents the input and output data for the Module of Decision.

The input data is:

- Case of PD occurrence—case H and M;
- Partial discharge location—TANK;
- Oil condition—GOOD.

The output data is related to the state of the transformer -Attention.

When the data from the Module of Classification is acquired, as in Fig. 17 the procedure is continued with the Module of Decision following the software implementation.
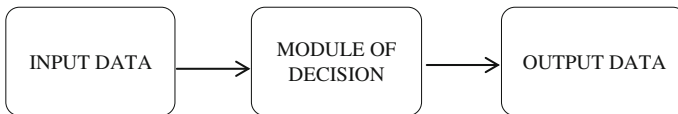

Fig. 16 Block diagram for Module of Decision
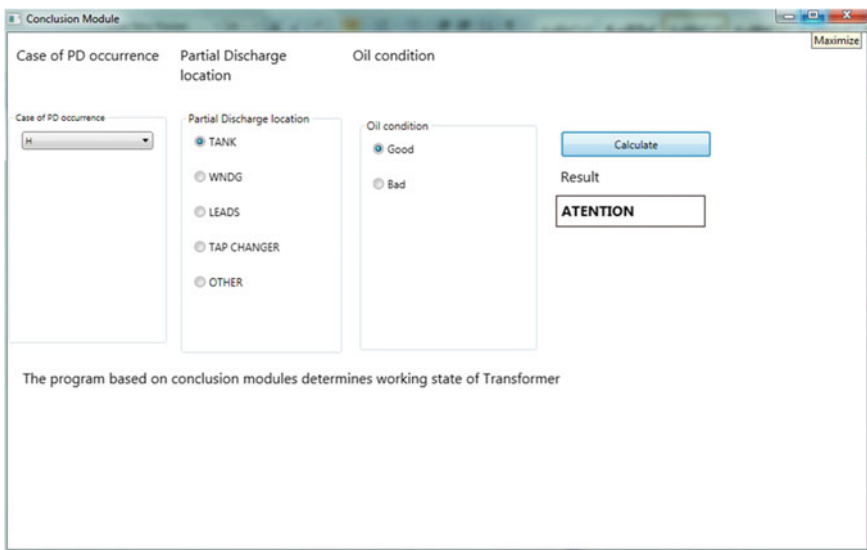
Fig. 17 Module of Conclusion screenshot

Case H

Case M
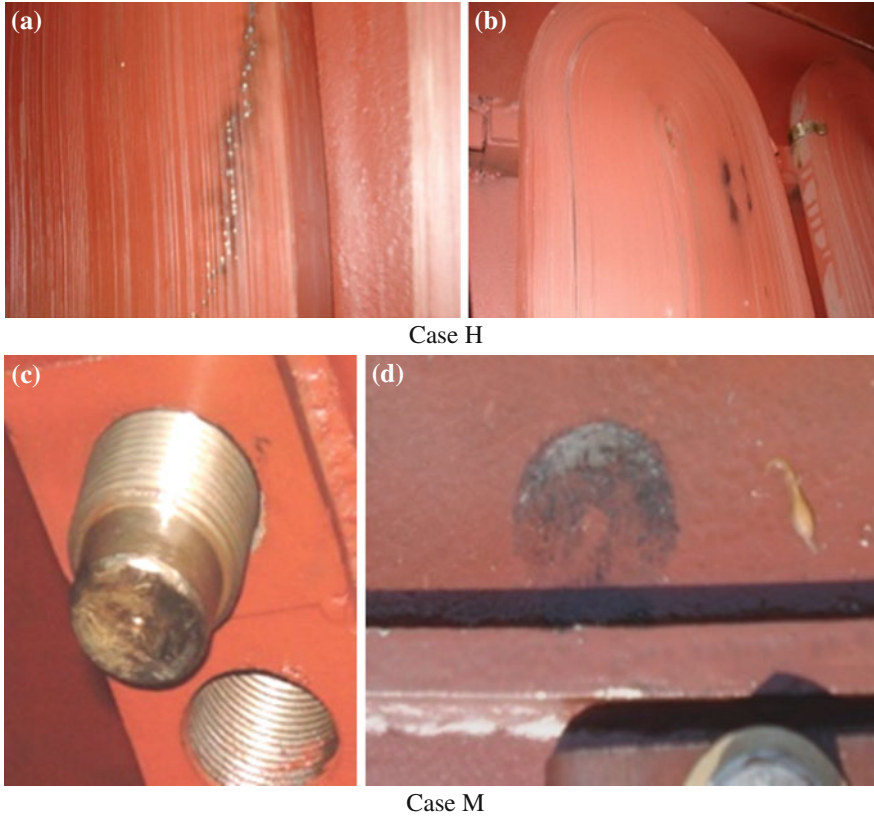
Fig. 18 Trace of partial discharges track and corona in oil

The software determines the level of criticality of the power transformer state. The software result was: ATTENTION. This means attention should be paid till the transformer should be open for repaired.

The trace of track at the tank of transformer was obtained after inspection. Pictures with marks from partial discharges are shown in Fig. 18.

There are many methods to diagnose the state of the power transformers. The electrical method of measurement of the electromagnetic waves caused by the partial discharges in the volume of the power transformer provides the maximum information, it can be analyzed.

The new software system was described. This kind of software analysis is considerably new and it is still in progress. The possibility to make calculations of the pulse shape features offers a powerful tool for pulse classification. The proposed new features provide meaningful and additional information for PD analysis.

The chosen approach provides accurate method for determining the incipient faults accompanied with partial discharges and also the final assessment of condition of the power transformer.

References

1. IEC 60270:2000—High-voltage test techniques—Partial discharge measurements
2. IEC 60076-3:2000-03—Power transformers—Insulation levels, dielectric tests and external clearances in air
3. IEC 60559, Mineral oil-impregnated electrical equipment in service - Guide to the interpretation of dissolved and free gases analysis
4. Nikolina Petkova, Petar Nakov, Valeri Mladenov, Power transformer's state analysis at partial discharges availability, published in The 4th International Scientific Symposium, September 2007, Kosice, Slovakia
5. P. Nakov, N. Petkova, V. Mladenov, "A method for determination of partial discharges in power transformers", Energetika" BG, № 4, pp. 26–30, 2007

Advanced Short-Circuit Analysis for the Assessment of Voltage Sag Characteristics

Marios N. Moschakis

Abstract An advanced assessment of voltage sag characteristics requires analytical mathematical expressions extracted from proper short-circuit analysis. In this document, the procedure for the extraction of those expressions is analytically described. All parameters affecting the response of a power network to a fault are taken into account. The expressions extracted enable the calculation of the during-fault voltage vector for a fault not only at the network's buses but also at every position within the network. They also enable the drawing of the voltage magnitude or the phase-angle jump in relation with the distance to the fault from the one power line end. Moreover, a simple and effective way to incorporate the phase shift introduced by devices or transformers is proposed. A test network is used for the demonstration of the effectiveness of those expressions and the understanding of voltage sag characteristics.

Keywords Power systems · Short-circuit · Voltage sags (dips) · Fault distance · Phase shift (angular displacement) · Transformer's vector group

1 Introduction

Voltage sags are rapid drops in the rms voltage and are mainly caused by short-circuits in the electric power transmission or distribution system. They are characterized by the remaining (retained or during-fault) voltage magnitude. Short-circuits give the most severe sags and their consequences on sensitive equipment, such as computers, adjustable speed drives or control devices, can be significant. Voltage sags are as critical as voltage interruptions for common

M.N. Moschakis (✉)
Technological Educational Institute of Thessaly, GR 41-110 Larissa, Greece
e-mail: mmoschakis@teilar.gr

industrial sites, which are more severe but less frequent. The sensitivity of equipment and sag frequency (annual number of sags) causes financial losses that may be enormous for some industrial customers. The current short-circuit analysis aims at the calculation of voltage sag characteristics during short-circuits at electricity transmission and distribution networks.

A short-circuit is accompanied with large currents flowing throughout a power network. As voltage sags is a major concern of industrial customers in the recent years, the short-circuit analysis became more orientated on the assessment of voltage sag characteristics rather than the assessment of overcurrents. However, the basic principles on which the short-circuit analysis is based on both cases, are the same. The response of an electric power network can be assessed if a number of affecting factors are known. These factors include the fault characteristics, the structure and topology of a power network and the pre-fault voltages of the network's buses or nodes.

For a high accuracy on the assessment of voltage sag characteristics due to faults on a power network, analytical mathematical expressions should be used, which will incorporate all those factors. In the next Sections, mathematical expressions will be analytically extracted and presented, which will calculate the sag magnitude or during-fault voltage vector due to faults not only on the network's buses but also on every position of the power network. Those expressions will allow the drawing of the during-fault voltage magnitude versus the distance to the fault from the one power line end. For the verification and further understanding of those analytical expressions that give the during-fault voltage for each phase, a properly designed test network is used. Using this network, the sag characteristics are studied. The studied power network includes a phase-shifting power transformer in order to show how its phase shift can be incorporated in a simple and effective way into the mathematical expressions.

2 Advanced Short-Circuit Analysis

Short circuits (or faults) at power networks are distinguished in symmetrical (or three-phase) and asymmetrical (one-phase-to-ground, the two-phase and the two-phase-to-ground) faults. Voltage sags are distinguished in a similar way to symmetrical (or balanced) and asymmetrical (or unbalanced) sags.

For the calculation of voltages and currents during faults at large and meshed power networks, digital methods have been developed in order to provide results in a short time with high accuracy. The main digital short-circuit analysis method is the method of current injection. According to this method, a short-circuit in a random position can be represented by a current injection (or absorption) at this position. The during-fault voltage is then given by the pre-fault voltage plus (minus) the voltage change due to this current injection (absorption).

By representing the power network by the bus impedance matrix $[Z_z]$, it can be proved that the voltage of a network bus k during a fault at another network bus f (fault) is given by the following equation:

$$\tilde{V}_{kf} = \tilde{V}_k^{pref} - Z_{kf} \cdot \tilde{I}_f, \tag{1}$$

where k is the bus where the voltage is calculated, f the faulted bus, $\tilde{V}_k^{pref}$ is the pre-fault voltage of bus k, Z_{kf} the non-diagonal element of the bus impedance matrix $[Z_z]$ and $\tilde{I}_f$ the fault current of bus f.

The fault current $\tilde{I}_f$ is proved to be given by the following equation:

$$\tilde{I}_f = \frac{\tilde{V}_f^{pref}}{Z_{ff} + Z_f}, \tag{2}$$

where Z_{ff} the diagonal element of bus impedance matrix $[Z_z]$ and Z_f the fault impedance. Thus, the voltage of bus k due to a fault on bus f is given by:

$$\tilde{V}_{kf} = \tilde{V}_k^{pref} - \frac{Z_{kf}}{Z_{ff} + Z_f} \cdot \tilde{V}_f^{pref}, \tag{3}$$

In case of symmetrical (three-phase) faults, the positive-sequence components are used for Z_{kf} and Z_{ff}. For the calculation of voltages and currents in case of an asymmetrical fault, the method of sequence components is used where the three-phase vector system is transformed to three other systems: the positive-, the negative- and the zero-sequence system. The three-phase circuit is also represented by three sequence circuits. The basic principles of the method of current injection can be applied to each sequence circuit. Assuming pre-fault three-phase voltage symmetry, which means that only positive-sequence voltage is non-zero, the sequence voltages of a bus k during an asymmetrical fault on bus f are given by the following equations:

$$\tilde{V}_{kf}^{(0)} = 0 - Z_{kf}^{(0)} \cdot \tilde{I}_f^{(0)} = -Z_{kf}^{(0)} \cdot \tilde{I}_f^{(0)}, \tag{4a}$$

$$\tilde{V}_{kf}^{(1)} = \tilde{V}_k^{pref} - Z_{kf}^{(1)} \cdot \tilde{I}_f^{(1)}, \tag{4b}$$

$$\tilde{V}_{kf}^{(2)} = 0 - Z_{kf}^{(2)} \cdot \tilde{I}_f^{(2)} = -Z_{kf}^{(2)} \cdot \tilde{I}_f^{(2)}, \tag{4c}$$

where $\tilde{V}_{kf}^{(0)}, \tilde{V}_{kf}^{(1)}, \tilde{V}_{kf}^{(2)}, \tilde{I}_f^{(0)}, \tilde{I}_f^{(1)}, \tilde{I}_f^{(2)}$ and $Z_{kf}^{(0)}, Z_{kf}^{(1)}, Z_{kf}^{(2)}$ are the zero (0), positive (1) and negative (2) voltages of bus k due to fault on bus f, the fault currents flowing in the sequence circuits and the non-diagonal elements of the bus impedance matrices $[Z_z^{(0)}], [Z_z^{(1)}], [Z_z^{(2)}]$, respectively.

The fault currents of each sequence have different value for every fault type due to the different way the three sequence circuits are connected at the fault position. Consequently, the sequence voltages are different for each fault type. For the calculation of phase voltages $\tilde{V}_{kf}^A$, $\tilde{V}_{kf}^B$, $\tilde{V}_{kf}^C$ of bus k due to asymmetrical faults on bus f, the following transformation is used:

$$
\begin{bmatrix} \tilde{V}_{kf}^A \\ \tilde{V}_{kf}^B \\ \tilde{V}_{kf}^C \end{bmatrix} = \begin{bmatrix} 1 & 1 & 1 \\ 1 & a^2 & a \\ 1 & a & a^2 \end{bmatrix} \cdot \begin{bmatrix} \tilde{V}_{kf}^{(0)} \\ \tilde{V}_{kf}^{(1)} \\ \tilde{V}_{kf}^{(2)} \end{bmatrix},
\tag{5}
$$

where $a = e^{j2\pi/3}$ is the Fortesque operator.

2.1 Fault Position f as a New Bus

For a more precise assessment of voltages and currents, it is important to use analytical expressions that calculate those quantities due to all fault types on every bus or fault position within a power line. These expressions should be applicable on meshed and radial power networks.

In order to express the during-fault voltage and currents in relation with the fault position on a power line, we assume a new bus added on this line. Specifically, we assume short-circuit on line p-q at position f between the buses p and q and in fault distance equal to $\ell \cdot L_{pq}$ from bus p, where $0 \leq \ell \leq 1$ and L_{pq} is the line length as shown in Fig. 1.

2.2 Pre-fault Voltage $V_f^{pref}(\ell)$ as a Function of Fault Distance

When a bus f is inserted on an already existing line p-q of a power network, the bus impedance matrix $[Z_z]$ is altered. The diagonal and the non-diagonal elements of the new matrix $[Z_z']$ can be expressed as a function of the distance ℓ of this new bus from the one point of the power line (sliding-bus technique). However, the calculation of the new matrix $[Z_z']$ is not required. Only the general expression of the new matrix elements is required for the expression of the during-fault voltage versus distance of the fault position from the one power line end.

Fig. 1 Fault position f on line p-q
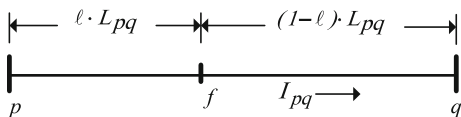
Let us assume that a current $\tilde{I}_{pq}$ flows on power line p-q as shown in Fig. 1. For the part p-f of the line p-q, it can be written:

$$\tilde{V}_f - \tilde{V}_p = z_{pf} \cdot \tilde{I}_{pq} = \ell \cdot z_{pq} \cdot \tilde{I}_{pq} \Rightarrow \frac{\tilde{V}_f - \tilde{V}_p}{\ell} = z_{pq} \cdot \tilde{I}_{pq}$$

Similarly for the part f-q:

$$\frac{\tilde{V}_q - \tilde{V}_f}{1 - \ell} = z_{pq} \cdot \tilde{I}_{pq}$$

where z_{pq}, z_{pf}, z_{fq} are the physical impedances of each part of the power line. Combining those two equations:

$$\frac{\tilde{V}_f - \tilde{V}_p}{\ell} = \frac{\tilde{V}_q - \tilde{V}_f}{1 - \ell} \Rightarrow \tilde{V}_f = (1 - \ell) \cdot \tilde{V}_p + \ell \cdot \tilde{V}_q$$

This expression applies also for the pre- and during-fault voltages and for all sequence components. Thus, the following expression is derived:

$$\tilde{V}_f^{pref}(\ell) = (1 - \ell) \cdot \tilde{V}_p^{pref} + \ell \cdot \tilde{V}_q^{pref}, \tag{6}$$

where the voltages $\tilde{V}_p^{pref}$ and $\tilde{V}_q^{pref}$ are usually assumed equal to 1 pu.

2.3 Non-diagonal Element $Z_{kf}(\ell)$ Versus Fault Distance

The diagonal elements of the bus impedance matrices are the impedance of each bus (or node) with respect to a reference bus. In other words, each diagonal element is the equivalent Thevenin impedance as it is seen from this bus. Thus, the diagonal elements can give the fault current for every fault on power network buses.

The diagonal element Z_{kk} is defined as the change in voltage of a bus k due to a current injection on position k divided by this current when the currents on the other network buses are zero. Thus, it can be expressed by the following equation in case of a short-circuit (sc) on bus k:

$$Z_{kk} = \frac{\Delta \tilde{V}_k}{\tilde{I}_{k,sc}}\bigg|_{\tilde{I}_{\mu,sc}=0} \quad \forall \mu \neq k$$

Similarly, a non-diagonal element Z_{kv} is defined as the change in voltage of bus k due to a current injection on position v divided by this current when the currents on the other network buses are zero. These elements allow the calculation of

during-fault voltages and their general expression in case of a short-circuit (sc) on bus v is given by:

$$Z_{kv} = \frac{\Delta \tilde{V}_k}{\tilde{I}_{v,sc}} |_{\tilde{I}_{\mu,sc}=0} \quad \forall \mu \neq v$$

Consequently, the non-diagonal elements Z_{kf} and Z_{fk} are equal and are defined by the following expressions:

$$Z_{kf} = \frac{\Delta \tilde{V}_k}{\tilde{I}_f} |_{\tilde{I}_{\mu,sc}=0} \quad \forall \mu \neq f, Z_{fk} = \frac{\Delta \tilde{V}_f}{\tilde{I}_{k,sc}} |_{\tilde{I}_{\mu,sc}=0} \quad \forall \mu \neq k$$

Equation (6) can be written for the change in voltage of bus f during a fault on bus k. By dividing this relationship with the fault current $\tilde{I}_{k,sc}$ of bus k, we obtain:

$$\frac{\Delta \tilde{V}_f}{\tilde{I}_{k,sc}} = (1 - \ell) \cdot \frac{\Delta \tilde{V}_p}{\tilde{I}_{k,sc}} + \ell \cdot \frac{\Delta \tilde{V}_q}{\tilde{I}_{k,sc}}$$

Thus, we finally obtain the expression for the non-diagonal element $Z_{kf}(\ell)$:

$$Z_{kf}(\ell) = Z_{fk}(\ell) = (1 - \ell) \cdot Z_{pk} + \ell \cdot Z_{qk}, \tag{7}$$

2.4 Diagonal Element $Z_{ff}(\ell)$ Versus Fault Distance

We assume a fault on position f of line p-q, which means a current injection $\tilde{I}_f$ on position f as shown in Fig. 2.

For the parts p-f and f-q of line p-q, the following expression can be written:

$$\tilde{V}_f - \tilde{V}_p = \ell \cdot z_{pq} \cdot \tilde{I}_2, \tilde{V}_f - \tilde{V}_q = (1 - \ell) \cdot z_{pq} \cdot \tilde{I}_1$$

Multiplying the first expression with the quantity $(1 - \ell)$ and the second one with ℓ, adding left and right parts of the equal sign and taking into account equation $\tilde{I}_f = \tilde{I}_1 + \tilde{I}_2$, we finally obtain:

Fig. 2 Current injection $\tilde{I}_f$ on position f of line p-q
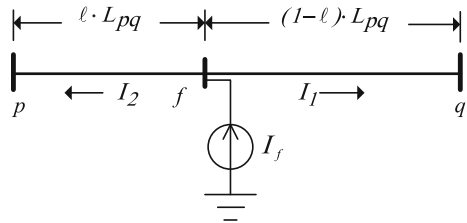
$$\tilde{V}_f - (1 - \ell) \cdot \tilde{V}_p - \ell \cdot \tilde{V}_q = \ell \cdot (1 - \ell) \cdot z_{pq} \cdot \tilde{I}_f$$

By dividing this expression by the quantity $\tilde{I}_f$ we obtain:

$$\frac{\tilde{V}_f}{\tilde{I}_f} - (1 - \ell) \cdot \frac{\tilde{V}_p}{\tilde{I}_f} - \ell \cdot \frac{\tilde{V}_q}{\tilde{I}_f} = \ell \cdot (1 - \ell) \cdot z_{pq} \Rightarrow Z_{ff}$$
$$= (1 - \ell) \cdot Z_{pf} + \ell \cdot Z_{qf} + \ell \cdot (1 - \ell) \cdot z_{pq}$$

By replacing the elements Z_{pf} and Z_{qf} from the following relationships based on Eq. (7):

$$Z_{pf} = (1 - \ell) \cdot Z_{pp} + \ell \cdot Z_{pq}, Z_{qf} = (1 - \ell) \cdot Z_{pq} + \ell \cdot Z_{qq}$$

we finally obtain the diagonal element $Z_{ff}(\ell)$:

$$Z_{ff}(\ell) = (1 - \ell)^2 \cdot Z_{pp} + \ell^2 \cdot Z_{qq} + 2 \cdot \ell \cdot (1 - \ell) \cdot Z_{pq} + \ell \cdot (1 - \ell) \cdot z_{pq}, \quad (8)$$

where the elements Z_{pp}, Z_{qq} and Z_{pq} are defined in the bus impedance matrix, and Z_{pq} is the physical impedance of line p-q. As for the Eqs. (6) and (7), Eq. (8) applies for all sequence components.

3 Analytical Expressions Per Fault Type Versus Fault Distance

Based on the above analysis, analytical expressions can be obtain for every fault type anywhere on a power network as a function of the fault distance from the one power line end.

3.1 Three-Phase Faults

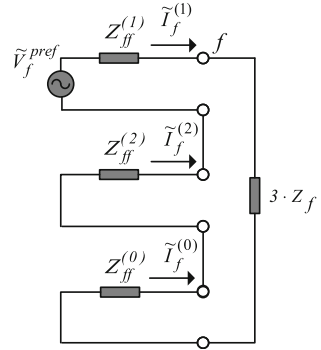Equation (3) can be written as a function of the distance to the fault ℓ in the following way:

$$\tilde{V}_{kf}(\ell) = \tilde{V}_k^{pref} - \frac{Z_{kf}^{(1)}(\ell)}{Z_{ff}^{(1)}(\ell) + Z_f} \cdot \tilde{V}_f^{\pi\rho o}(\ell), \quad (9)$$

This equation gives the during-fault voltage vector and also the voltage sag magnitude $|\tilde{V}_{kf}(\ell)|$ and the subsequent phase-angle jump.

Fig. 3 Sequence circuits as
connected in case of a
one-phase-to-ground fault on
bus f

3.2 One-Phase-to-Ground Faults

In case of a one-phase-to-ground fault on a random bus (or position) f, the positive-,
negative- and zero-sequence circuits are connected is series, as shown in Fig. 3.

The sequence currents are given by the following expressions:

$$\tilde{I}_f^{(1)} = \frac{\tilde{V}_f^{pref}}{Z_{ff}^{(1)} + Z_{ff}^{(2)} + Z_{ff}^{(0)} + 3 \cdot Z_f}, \tag{10a}$$

$$\tilde{I}_f^{(2)} = \tilde{I}_f^{(1)}, \tag{10b}$$

$$\tilde{I}_f^{(0)} = \tilde{I}_f^{(1)}, \tag{10c}$$

By combining Eqs. (4a, 4b, 4c) and (10a, 10b, 10c), expressions for the sequence
voltage are derived:

$$\tilde{V}_{kf}^{(1)} = \tilde{V}_k^{pref} - \frac{Z_{kf}^{(1)}}{Z_{ff}^{(1)} + Z_{ff}^{(2)} + Z_{ff}^{(0)} + 3 \cdot Z_f} \cdot \tilde{V}_f^{pref}, \tag{11a}$$

$$\tilde{V}_{kf}^{(2)} = -\frac{Z_{kf}^{(2)}}{Z_{ff}^{(1)} + Z_{ff}^{(2)} + Z_{ff}^{(0)} + 3 \cdot Z_f} \cdot \tilde{V}_f^{pref}, \tag{11b}$$

$$\tilde{V}_{kf}^{(0)} = -\frac{Z_{kf}^{(0)}}{Z_{ff}^{(1)} + Z_{ff}^{(2)} + Z_{ff}^{(0)} + 3 \cdot Z_f} \cdot \tilde{V}_f^{pref}, \tag{11c}$$

Applying the transformation to the phase components, the following expressions
are derived for the during-fault phase voltages of bus k due to a
one-phase-to-ground fault on bus f. If no phase-shifting component exists between

buses *k* and *f*, e.g. a power transformer of a certain vector group, the sag magnitude is the during-fault voltage of phase A.

$$\tilde{V}_{kf}^{A}(\ell) = \tilde{V}_{k}^{pref} - \frac{Z_{kf}^{(1)}(\ell) + Z_{kf}^{(2)}(\ell) + Z_{kf}^{(0)}(\ell)}{Z_{ff}^{(1)}(\ell) + Z_{ff}^{(2)}(\ell) + Z_{ff}^{(0)}(\ell) + 3 \cdot Z_f} \cdot \tilde{V}_{f}^{pref}(\ell), \tag{12a}$$

$$\tilde{V}_{kf}^{B}(\ell) = a^2 \cdot \tilde{V}_{k}^{pref} - \frac{a^2 \cdot Z_{kf}^{(1)}(\ell) + a \cdot Z_{kf}^{(2)}(\ell) + Z_{kf}^{(0)}(\ell)}{Z_{ff}^{(1)}(\ell) + Z_{ff}^{(2)}(\ell) + Z_{ff}^{(0)}(\ell) + 3 \cdot Z_f} \cdot \tilde{V}_{f}^{pref}(\ell), \tag{12b}$$

$$\tilde{V}_{kf}^{C}(\ell) = a \cdot \tilde{V}_{k}^{pref} - \frac{a \cdot Z_{kf}^{(1)}(\ell) + a^2 \cdot Z_{kf}^{(2)}(\ell) + Z_{kf}^{(0)}(\ell)}{Z_{ff}^{(1)}(\ell) + Z_{ff}^{(2)}(\ell) + Z_{ff}^{(0)}(\ell) + 3 \cdot Z_f} \cdot \tilde{V}_{f}^{pref}(\ell), \tag{12c}$$

3.3 Two-Phase Faults

In this case, the sequence circuits are connected in parallel as shown in Fig. 4. The sequence currents are given by the following expressions:
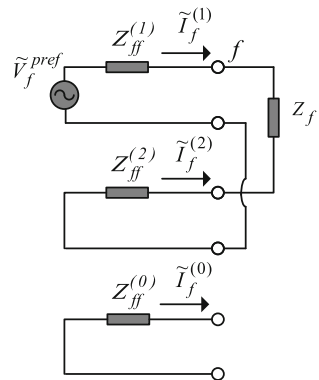
$$\tilde{I}_{f}^{(1)} = \frac{\tilde{V}_{f}^{pref}}{Z_{ff}^{(1)} + Z_{ff}^{(2)} + Z_f}, \tag{13a}$$

$$\tilde{I}_{f}^{(2)} = \tilde{I}_{f}^{(1)}, \tag{13b}$$

$$\tilde{I}_{f}^{(0)} = 0, \tag{13c}$$

By combining Eqs. (4b, 4b, 4c) and (13a, 13b, 13c), expressions for the sequence voltage are derived:

Fig. 4 Sequence circuits and their connection in case of a two-phase fault on bus *f*

$$\tilde{V}_{kf}^{(1)} = \tilde{V}_k^{pref} - \frac{Z_{kf}^{(1)}}{Z_{ff}^{(1)} + Z_{ff}^{(2)} + Z_{ff}^{(0)} + 3 \cdot Z_f} \cdot \tilde{V}_f^{pref}, \tag{14a}$$

$$\tilde{V}_{kf}^{(2)} = -\frac{Z_{kf}^{(2)}}{Z_{ff}^{(1)} + Z_{ff}^{(2)} + Z_{ff}^{(0)} + 3 \cdot Z_f} \cdot \tilde{V}_f^{pref}, \tag{14b}$$

$$\tilde{V}_{kf}^{(0)} = -\frac{Z_{kf}^{(0)}}{Z_{ff}^{(1)} + Z_{ff}^{(2)} + Z_{ff}^{(0)} + 3 \cdot Z_f} \cdot \tilde{V}_f^{pref}, \tag{14c}$$

Transforming back to the phase components, the expressions below are derived for the during-fault phase voltages of bus k due to a two-phase fault on bus f. Voltage sag magnitude is derived by the minimum among them. If no phase-shifting component exists between buses k and f, e.g. a power transformer of a certain vector group, the sag magnitude is calculated by the minimum during-fault voltage of phases B and C.

$$\tilde{V}_{kf}^A(\ell) = \tilde{V}_k^{pref} - \frac{Z_{kf}^{(1)}(\ell) - Z_{kf}^{(2)}(\ell)}{Z_{ff}^{(1)}(\ell) + Z_{ff}^{(2)}(\ell) + Z_f} \cdot \tilde{V}_f^{pref}(\ell), \tag{15a}$$

$$\tilde{V}_{kf}^B(\ell) = a^2 \cdot \tilde{V}_k^{pref} - \frac{a^2 \cdot Z_{kf}^{(1)}(\ell) - a \cdot Z_{kf}^{(2)}(\ell)}{Z_{ff}^{(1)}(\ell) + Z_{ff}^{(2)}(\ell) + Z_f} \cdot \tilde{V}_f^{pref}(\ell), \tag{15b}$$

$$\tilde{V}_{kf}^C(\ell) = a \cdot \tilde{V}_k^{pref} - \frac{a \cdot Z_{kf}^{(1)}(\ell) - a^2 \cdot Z_{kf}^{(2)}(\ell)}{Z_{ff}^{(1)}(\ell) + Z_{ff}^{(2)}(\ell) + Z_f} \cdot \tilde{V}_f^{pref}(\ell), \tag{15c}$$
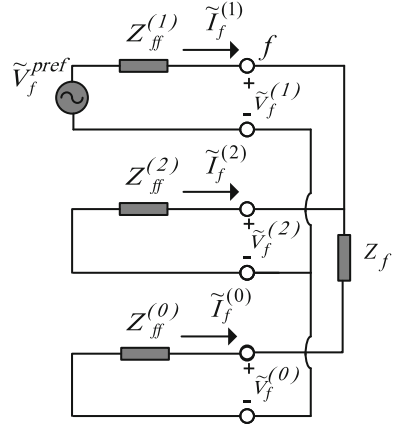
3.4 Two-Phase-to-Ground Faults

In this case, the sequence circuits are connected in parallel as shown in Fig. 5.

The total circuit impedance and the sequence currents are given by the following expressions:

Fig. 5 Sequence circuits as
connected in case of a
two-phase-to-ground fault on
bus f

$$Z_{tot} = Z_{ff}^{(1)} + [Z_{ff}^{(2)} // (Z_{ff}^{(0)} + 3 \cdot Z_f)] = Z_{ff}^{(1)} + \frac{Z_{ff}^{(2)} \cdot (Z_{ff}^{(0)} + 3 \cdot Z_f)}{Z_{ff}^{(2)} + Z_{ff}^{(0)} + 3 \cdot Z_f}$$

$$\tilde{I}_f^{(1)} = \frac{\tilde{V}_f^{pref}}{Z_{tot}},$$

$$\tilde{I}_f^{(2)} = -\tilde{I}_f^{(1)} \cdot \frac{Z_{ff}^{(0)} + 3 \cdot Z_f}{Z_{ff}^{(2)} + Z_{ff}^{(0)} + 3 \cdot Z_f},$$

$$\tilde{I}_f^{(0)} = -\tilde{I}_f^{(1)} \cdot \frac{Z_{ff}^{(2)}}{Z_{ff}^{(2)} + Z_{ff}^{(0)} + 3 \cdot Z_f},$$

Thus, the final expressions for the sequence currents are as follows:

$$\tilde{I}_f^{(1)} = \frac{Z_{ff}^{(2)} + Z_{ff}^{(0)} + 3 \cdot Z_f}{Z_{ff}^{(1)} \cdot Z_{ff}^{(0)} + Z_{ff}^{(2)} \cdot Z_{ff}^{(1)} + Z_{ff}^{(0)} \cdot Z_{ff}^{(2)} + 3 \cdot Z_f \cdot (Z_{ff}^{(1)} + Z_{ff}^{(2)})} \cdot \tilde{V}_f^{pref}, \quad (16a)$$

$$\tilde{I}_f^{(2)} = -\frac{Z_{ff}^{(0)} + 3 \cdot Z_f}{Z_{ff}^{(1)} \cdot Z_{ff}^{(0)} + Z_{ff}^{(2)} \cdot Z_{ff}^{(1)} + Z_{ff}^{(0)} \cdot Z_{ff}^{(2)} + 3 \cdot Z_f \cdot (Z_{ff}^{(1)} + Z_{ff}^{(2)})} \cdot \tilde{V}_f^{pref}, \quad (16b)$$

$$\tilde{I}_f^{(0)} = -\frac{Z_{ff}^{(2)}}{Z_{ff}^{(1)} \cdot Z_{ff}^{(0)} + Z_{ff}^{(2)} \cdot Z_{ff}^{(1)} + Z_{ff}^{(0)} \cdot Z_{ff}^{(2)} + 3 \cdot Z_f \cdot (Z_{ff}^{(1)} + Z_{ff}^{(2)})} \cdot \tilde{V}_f^{pref}, \quad (16c)$$

By combining Eqs. (4b, 4b, 4c) and (16a, 16b, 16c), expressions for the sequence voltage are derived:

$$\tilde{V}_{kf}^{(1)} = \tilde{V}_k^{pref} - \frac{Z_{kf}^{(1)} \cdot (Z_{ff}^{(0)} + Z_{ff}^{(2)} + 3 \cdot Z_f)}{Z_{ff}^{(1)} \cdot Z_{ff}^{(0)} + Z_{ff}^{(2)} \cdot Z_{ff}^{(1)} + Z_{ff}^{(0)} \cdot Z_{ff}^{(2)} + 3 \cdot Z_f \cdot (Z_{ff}^{(1)} + Z_{ff}^{(2)})} \cdot \tilde{V}_f^{pref},$$

$$(17a)$$

$$\tilde{V}_{kf}^{(2)} = \frac{Z_{kf}^{(2)} \cdot (Z_{ff}^{(0)} + 3 \cdot Z_f)}{Z_{ff}^{(1)} \cdot Z_{ff}^{(0)} + Z_{ff}^{(2)} \cdot Z_{ff}^{(1)} + Z_{ff}^{(0)} \cdot Z_{ff}^{(2)} + 3 \cdot Z_f \cdot (Z_{ff}^{(1)} + Z_{ff}^{(2)})} \cdot \tilde{V}_f^{pref}, \quad (17b)$$

$$\tilde{V}_{kf}^{(0)} = \frac{Z_{kf}^{(0)} \cdot Z_{ff}^{(2)}}{Z_{ff}^{(1)} \cdot Z_{ff}^{(0)} + Z_{ff}^{(2)} \cdot Z_{ff}^{(1)} + Z_{ff}^{(0)} \cdot Z_{ff}^{(2)} + 3 \cdot Z_f \cdot (Z_{ff}^{(1)} + Z_{ff}^{(2)})} \cdot \tilde{V}_f^{pref}, \quad (17c)$$

Transforming back to the phase components, the expressions below are derived for the during-fault phase voltages of bus k due to a two-phase-to-ground fault on bus f. Voltage sag magnitude is derived by the minimum among them. If no phase-shifting component exists between buses k and f, e.g. a power transformer of a certain vector group, the sag magnitude is calculated by the minimum during-fault voltage of phases B and C.

$$\tilde{V}_{kf}^A(\ell) = \tilde{V}_k^{pref} - \frac{[Z_{kf}^{(1)}(\ell) \cdot (Z_{ff}^{(2)}(\ell) + Z_{ff}^{(0)}(\ell) + 3Z_{\sigma\varphi}) - \cdots}{Z_{ff}^{(1)}(\ell) \cdot Z_{ff}^{(2)}(\ell) + Z_{ff}^{(1)}(\ell) \cdot Z_{ff}^{(0)}(\ell) + Z_{ff}^{(2)}(\ell) \cdot Z_{ff}^{(0)}(\ell) + \cdots}$$
$$\frac{\cdots - Z_{kf}^{(2)}(\ell) \cdot (Z_{ff}^{(0)}(\ell) + 3Z_f) - Z_{kf}^{(0)}(\ell) \cdot Z_{ff}^{(2)}(\ell)] \cdot \tilde{V}_f^{pref}(\ell)}{\cdots + [Z_{ff}^{(1)}(\ell) + Z_{ff}^{(2)}(\ell)] \cdot 3 \cdot Z_f},$$

$$(18a)$$

$$\tilde{V}_{kf}^B(\ell) = a^2 \cdot \tilde{V}_k^{pref} - \frac{[a^2 \cdot Z_{kf}^{(1)}(\ell) \cdot (Z_{ff}^{(2)}(\ell) + Z_{ff}^{(0)}(\ell) + 3Z_{\sigma\varphi}) - \cdots}{Z_{ff}^{(1)}(\ell) \cdot Z_{ff}^{(2)}(\ell) + Z_{ff}^{(1)}(\ell) \cdot Z_{ff}^{(0)}(\ell) + \cdots}$$
$$\frac{\cdots - a \cdot Z_{kf}^{(2)}(\ell) \cdot (Z_{ff}^{(0)}(\ell) + 3Z_f) - Z_{kf}^{(0)}(\ell) \cdot Z_{ff}^{(2)}(\ell)] \cdot \tilde{V}_f^{pref}(\ell)}{cdots + Z_{ff}^{(2)}(\ell) \cdot Z_{ff}^{(0)}(\ell) + [Z_{ff}^{(1)}(\ell) + Z_{ff}^{(2)}(\ell)] \cdot 3 \cdot Z_f}, \quad (18b)$$

$$\tilde{V}_{kf}^C(\ell) = a \cdot \tilde{V}_k^{pref} - \frac{[a \cdot Z_{kf}^{(1)}(\ell) \cdot (Z_{ff}^{(2)}(\ell) + Z_{ff}^{(0)}(\ell) + 3Z_f) - \cdots}{Z_{ff}^{(1)}(\ell) \cdot Z_{ff}^{(2)}(\ell) + Z_{ff}^{(1)}(\ell) \cdot Z_{ff}^{(0)}(\ell) + \cdots}$$
$$\frac{\cdots - a^2 \cdot Z_{kf}^{(2)}(\ell) \cdot (Z_{ff}^{(0)}(\ell) + 3Z_f) - Z_{kf}^{(0)}(\ell) \cdot Z_{ff}^{(2)}(\ell)] \cdot \tilde{V}_f^{pref}(\ell)}{\cdots + Z_{ff}^{(2)}(\ell) \cdot Z_{ff}^{(0)}(\ell) + [Z_{ff}^{(1)}(\ell) + Z_{ff}^{(2)}(\ell)] \cdot 3 \cdot Z_f}, \quad (18c)$$

4 Effects of Phase-Shifting Transformers or Devices

A phase-shifting transformer or device connected at transmission or distribution level will alter the power network's response to short-circuits. The bus impedance matrices will be different but also the analytical expressions extracted in the previous must be modified. As power transformers with a phase shift (angular displacement) are commonly used in power networks, we focus on their effect on during-fault voltages. Common vector groups of transformers related with their winding connectivity and angular displacement can be found in IEC 60076-1 Standard [1]. In this document, the related terminology is defined. It consists of:

- Letters identifying the configuration of the phase windings. In three-phase ac systems, winding connections are categorized as Delta (D, d), Star or Wye (Y, y), Interconnected star or zigzag (Z, z) and Open or Independent (III, iii) windings [1]. Capital letters relate to the High-Voltage (HV) windings, lower-case letters to the Medium-Voltage (MV) and Low-Voltage (LV) windings. The vector group begins with the capital letter.
- A letter (N, n), which indicates that the neutral of a winding in star or interconnected star is brought out.
- A number indicating the phase displacement between the voltages of the windings taking as a reference the HV winding. This number, multiplied by 30°, denotes the angle by which the vector of the LV winding (phase voltages) *lags* that of the HV winding. The angle of any LV winding is conventionally expressed by the 'clock notation', that is, the hour indicated by the winding phasor when the HV winding phasor is at 12 o' clock (rising numbers indicate increasing phase lag). Common three-phase transformer connections (with no reference to the neutral point of the star-connected windings) according to IEC 60076-1 are presented in Table 1.

For example, a transformer with a vector group of Dyn1 has a delta-connected HV winding and a wye-connected LV winding with its neutral point brought out. The angle of the LV winding phase voltages lags the HV by 30°. Moreover, a transformer with a star-connected HV winding having its neutral ungrounded, and a delta-connected LV winding with 330° lagging (or 30° leading) angular displacement, is denoted as Yd11.

Table 1 Three-phase faults (Coefficients d and n)

Coefficients $\mathbf{d}$	Coefficients $\mathbf{n}$
$\mathbf{d_2} = Z_{pp}^{(1)} + Z_{qq}^{(1)} - 2 \cdot Z_{pq}^{(1)} - z_{pq}^{(1)}$	$\mathbf{d_2} = \mathbf{n_2}$
$\mathbf{d_1} = 2 \cdot Z_{pq}^{(1)} - 2 \cdot Z_{pp}^{(1)} + z_{pq}^{(1)}$	$\mathbf{n_1} = \mathbf{d_1} + Z_{pk}^{(1)} - Z_{qk}^{(1)}$
$\mathbf{d_0} = Z_{pp}^{(1)}$	$\mathbf{n_0} = \mathbf{d_0} - Z_{pk}^{(1)}$

## 4.1 Incorporation of Phase Shift on Analytical Expressions

In case of three-phase faults, the power transformer's phase shift will not affect the analytical expressions which give the during-fault voltage. In case of asymmetrical (unbalanced) faults, the transformer's vector group should be taken into account and proper modifications in the analytical equations giving during-fault rms phase voltages should be done. These modifications include the adjustment of zero-sequence bus impedance matrix which is related with the winding connections. Moreover, the phase displacement (if any) introduced by the transformer should be incorporated into the analytical equations.

For example, a Dy1 (or Yd1) transformer introduces a phase displacement of $-1 \times 30°$ in the positive-sequence voltage and a $+30°$ in the negative-sequence voltage when passing through this transformer from the HV to the LV winding, which is also applies for the fault currents [2]. Thus, a phase shift of $+60°$ (or $-a^2$ in terms of Fortesque operator) in the negative-sequence voltage can be applied, which is finally applied at the negative-sequence transfer impedance Z_{kf} of buses at HV (bus k) and LV (bus f) winding [3, 4]. Similarly, a phase shift of $-60°$ (or $-a$) in the negative-sequence voltage should be applied when a fault occurs on the LV side and observed by a node on the HV side as shown in Fig. 6.

4.2 Transformer's Phase-Shift and Sag Magnitude

The phase displacement introduced by transformers of certain vector groups will also affect the characteristics of the during-fault voltages and the sag magnitude. This happens when faults occur at the other side of a transformer from which the during-fault voltages are calculated. Specifically, two-phase- and two-phase-to-ground faults result in only one sagged phase and one-phase-to-ground faults result in two sagged phase voltages.

Fig. 6 Effect on positive- and negative-sequence voltage vectors
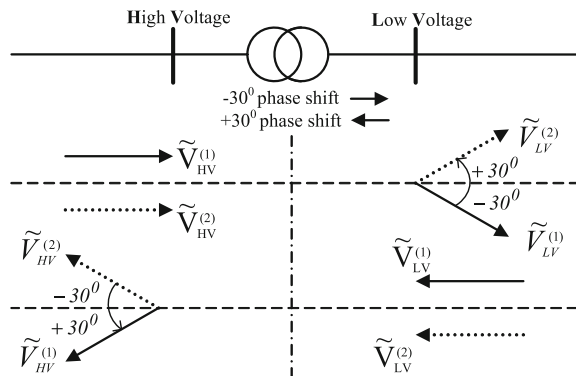
The most interesting effect of transformers of certain vector groups (1, 5, 7 or 11) is related with the sag magnitude, which is the minimum among the three during-fault phase voltages. The sag magnitude at one side of the transformer is equal for either three-phase, two-phase or two-phase-to-ground faults on the other side of the transformer. Only one-phase-to-ground faults give different sag magnitude. This was proved in [4] using the mathematical equations derived for the during-fault calculation and by incorporating the effect of transformer's vector group on zero- and negative-sequence bus impedance matrices. It should be noted that this applies for zero fault impedance and equal positive and negative bus impedance matrices, which are common assumptions used in short-circuit analysis, and described by the following equations:

$$Z_{bus}^{(1)} = Z_{bus}^{(2)}, \tilde{V}_f^{pref} = 1, Z_f = 0. \tag{19}$$

5 Further Processing of Analytical Expressions

The analytical expressions presented in Sect. 3 can be further processed in order to be easily implemented by software for mathematical applications. This is done by replacing the expressions (6)–(8) of $\tilde{V}_f^{pref}(\ell), Z_{kf}(\ell), Z_{ff}(\ell)$ respectively into Eqs. (9), (12a, 12b, 12c), (15a, 15b, 15c) and (18a, 18b, 18c) that give the during-fault phase voltages in case of each of the four fault types. In case of three-phase, one-phase-to-ground and two-phase faults, the general expression taken for each phase voltage is:

$$\tilde{V}_{kf}(\ell) = \frac{n_2 \cdot \ell^2 + n_1 \cdot \ell + n_0}{d_2 \cdot \ell^2 + d_1 \cdot \ell + d_0}, \tag{20}$$

In case of two-phase-to-ground faults, the expression is:

$$\tilde{V}_{kf}(\ell) = \frac{n_4 \cdot \ell^4 + n_3 \cdot \ell^3 + n_2 \cdot \ell^2 + n_1 \cdot \ell + n_0}{d_4 \cdot \ell^4 + d_3 \cdot \ell^3 + d_2 \cdot \ell^2 + d_1 \cdot \ell + d_0}, \tag{21}$$

The coefficients n and d are complex numbers. In case of three-phase faults on a line p-q, the coefficients d, n for the calculation of during-fault voltage of bus k when common assumptions described by Eq. (19) are applied, are given by the expressions shown in Table 1.

Furthermore, the effect of the transformer's phase shift should also be incorporated in an easier way. In Sect. 4.1, it is mentioned that a phase shift on the negative-sequence voltage $V_{kf}^{(2)}$ can be suitably applied. By a closer examination of expressions (11b), (14b) and (17b), it can be easily observed that this phase shift can be equivalently applied on the element $Z_{kf}^{(2)}$.

Table 2 One-phase-to-ground faults (Coefficients d and n)

$\mathbf{d_2} = 2 \cdot Z_{pp}^{(1)} + 2 \cdot Z_{qq}^{(1)} + Z_{pp}^{(0)} + Z_{qq}^{(0)} - 4 \cdot Z_{pq}^{(1)} - 2 \cdot Z_{pq}^{(0)} - 2 \cdot z_{pq}^{(1)} - z_{pq}^{(0)}$
$\mathbf{d_1} = 4 \cdot Z_{pq}^{(1)} + 2 \cdot Z_{pq}^{(0)} - 4 \cdot Z_{pp}^{(1)} - 2 \cdot Z_{pp}^{(0)} + 2 \cdot z_{pq}^{(1)} + z_{pq}^{(0)}$
$\mathbf{d_0} = 2 \cdot Z_{pp}^{(1)} + Z_{pp}^{(0)}$
$\mathbf{n_2^A} = \mathbf{d_2} - (Z_{pk}^{(0)} + Z_{pk}^{(1)} + Z_{pk}^{(2)^*})$
$\mathbf{n_2^B} = a^2 \cdot \mathbf{d_2} - (Z_{pk}^{(0)} + a^2 \cdot Z_{pk}^{(1)} + a \cdot Z_{pk}^{(2)^*})$
$\mathbf{n_1^A} = \mathbf{d_1} + (Z_{pk}^{(0)} + Z_{pk}^{(1)} + Z_{pk}^{(2)^*}) - (Z_{qk}^{(0)} + Z_{qk}^{(1)} + Z_{qk}^{(2)^*})$
$\mathbf{n_1^B} = a^2 \cdot \mathbf{d_1} + (Z_{pk}^{(0)} + a^2 \cdot Z_{pk}^{(1)} + a \cdot Z_{pk}^{(2)^*}) - (Z_{qk}^{(0)} + a^2 \cdot Z_{qk}^{(1)} + a \cdot Z_{qk}^{(2)^*})$
$\mathbf{n_0^A} = \mathbf{d_0} - (Z_{pk}^{(0)} + Z_{pk}^{(1)} + Z_{pk}^{(2)^*})$
$\mathbf{n_0^B} = a^2 \cdot \mathbf{d_0} - (Z_{pk}^{(0)} + a^2 \cdot Z_{pk}^{(1)} + a \cdot Z_{pk}^{(2)^*})$

*Multiplied by a proper phase shift in case of phase-shifting components

Table 3 Two-phase faults (Coefficients d and n)

$\mathbf{d_2} = 2 \cdot Z_{pp}^{(1)} + 2 \cdot Z_{qq}^{(1)} - 4 \cdot Z_{pq}^{(1)} - 2 \cdot z_{pq}^{(1)}$
$\mathbf{d_1} = 4 \cdot Z_{pq}^{(1)} - 2 \cdot Z_{pp}^{(1)} + 2 \cdot z_{pq}^{(1)}$
$\mathbf{d_0} = 2 \cdot Z_{pp}^{(1)}$
$\mathbf{n_2^B} = a^2 \cdot \mathbf{d_2} - a^2 \cdot Z_{pk}^{(1)} + a \cdot Z_{pk}^{(2)^*}$
$\mathbf{n_2^C} = a \cdot \mathbf{d_2} - a \cdot Z_{pk}^{(1)} + a^2 \cdot Z_{pk}^{(2)^*}$
$\mathbf{n_1^B} = a^2 \cdot \mathbf{d_1} + a^2 \cdot Z_{pk}^{(1)} - a \cdot Z_{pk}^{(2)^*} - a^2 \cdot Z_{qk}^{(1)} + a \cdot Z_{qk}^{(2)^*}$
$\mathbf{n_1^C} = a \cdot \mathbf{d_1} + a \cdot Z_{pk}^{(1)} - a^2 \cdot Z_{pk}^{(2)^*} - a \cdot Z_{qk}^{(1)} + a^2 \cdot Z_{qk}^{(2)^*}$
$\mathbf{n_0^B} = a^2 \cdot \mathbf{d_0} - a^2 \cdot Z_{pk}^{(1)} + a \cdot Z_{pk}^{(2)^*}$
$\mathbf{n_0^C} = a \cdot \mathbf{d_0} - a \cdot Z_{pk}^{(1)} + a^2 \cdot Z_{pk}^{(2)^*}$

*Multiplied by a proper phase shift in case of phase-shifting components

Table 4 Two-phase-to-ground faults (Coefficients d only)

$\mathbf{d_4} = (Z_{pp}^{(1)} + Z_{qq}^{(1)} - Z_{pq}^{(1)} - z_{pq}^{(1)})^2$ $\quad + 2 \cdot (Z_{pp}^{(1)} + Z_{qq}^{(1)} - Z_{pq}^{(1)} - z_{pq}^{(1)}) \cdot (Z_{pp}^{(0)} + Z_{qq}^{(0)} - Z_{pq}^{(0)} - z_{pq}^{(0)})$
$\mathbf{d_3} = [2 \cdot (Z_{pp}^{(1)} + Z_{qq}^{(1)} - 2 \cdot Z_{pq}^{(1)} - z_{pq}^{(1)}) + Z_{pp}^{(0)} + Z_{pp}^{(0)} - 2 \cdot Z_{pq}^{(0)}$ $\quad - z_{pq}^{(0)}] \cdot (2 \cdot Z_{pq}^{(1)} - 2 \cdot Z_{pp}^{(1)} + z_{pq}^{(1)} + 2 \cdot Z_{pq}^{(0)} - 2 \cdot Z_{pp}^{(0)} + z_{pq}^{(0)})$
$\mathbf{d_2} = 2 \cdot (Z_{pp}^{(1)} + Z_{qq}^{(1)} - 2 \cdot Z_{pq}^{(1)} - z_{pq}^{(1)}) \cdot (Z_{pp}^{(1)} + Z_{pp}^{(0)}) + 2 \cdot Z_{pp}^{(1)} \cdot (Z_{pp}^{(0)} + Z_{qq}^{(0)} - 2 \cdot Z_{pq}^{(0)} - z_{pq}^{(0)})$ $\quad + (2 \cdot Z_{p1}^{(1)} - 2 \cdot Z_{pp}^{(1)} + z_{pq}^{(1)}) \cdot (2 \cdot Z_{pq}^{(1)} - 2 \cdot Z_{pp}^{(1)} - 4 \cdot Z_{pp}^{(0)} + 4 \cdot Z_{pq}^{(0)} + z_{pq}^{(1)} + 2 \cdot z_{pq}^{(0)})$
$\mathbf{d_1} = 2 \cdot (2 \cdot Z_{pq}^{(1)} - 2 \cdot Z_{pp}^{(1)} + z_{pq}^{(1)}) \cdot (Z_{pp}^{(1)} + Z_{pp}^{(0)}) + 2 \cdot Z_{pp}^{(1)} \cdot (2 \cdot Z_{pq}^{(0)} - 2 \cdot Z_{pp}^{(0)} + z_{pq}^{(0)})$
$\mathbf{d_0} = Z_{pp}^{(1)} \cdot (Z_{pp}^{(1)} + 2 \cdot Z_{pp}^{(0)})$

Table 5 Two-phase-to-ground faults (Coefficients n only)

$$\mathbf{n_4^B} = a^2 \cdot \mathbf{d_4}, \mathbf{n_4^C} = a \cdot \mathbf{d_4}$$

$$\mathbf{n_3^B} = a^2 \cdot [\mathbf{d_3} - (Z_{qk}^{(1)} - Z_{pk}^{(1)}) \cdot (Z_{pp}^{(1)} + Z_{qq}^{(1)} - 2 \cdot Z_{pq}^{(1)} - 2 \cdot z_{pq}^{(1)} + Z_{pp}^{(0)} + Z_{qq}^{(0)} - 2 \cdot Z_{pq}^{(0)} - z_{pq}^{(0)})$$
$$+ (Z_{pp}^{(1)} + Z_{qq}^{(1)} - 2 \cdot Z_{pk}^{(1)} - z_{pq}^{(1)}) \cdot (Z_{qk}^{(0)} - Z_{pk}^{(0)}) + a \cdot (Z_{pp}^{(0)} + Z_{qq}^{(0)} - 2 \cdot Z_{pq}^{(0)} - z_{pq}^{(0)}) \cdot (Z_{qk}^{(2)^*} - Z_{pk}^{(2)^*})$$
$$+ (Z_{pp}^{(1)} + Z_{qq}^{(1)} - 2 \cdot Z_{pk}^{(1)} - z_{pq}^{(1)}) \cdot (Z_{qk}^{(0)} - Z_{pk}^{(0)}) + a^2 \cdot (Z_{pp}^{(0)} + Z_{qq}^{(0)} - 2 \cdot Z_{pq}^{(0)} - z_{pq}^{(0)}) \cdot (Z_{qk}^{(2)^*} - Z_{pk}^{(2)^*})$$

$$\mathbf{n_3^C} = a \cdot [\mathbf{d_3} - (Z_{qk}^{(1)} - Z_{pk}^{(1)}) \cdot (Z_{pp}^{(1)} + Z_{qq}^{(1)} - 2 \cdot Z_{pq}^{(1)} - z_{pq}^{(1)}) \cdot (Z_{pp}^{(0)} + Z_{qq}^{(0)} - 2 \cdot z_{pq}^{(0)})$$

$$\mathbf{n_2^B} = a^2 \cdot \{\mathbf{d_2} - [Z_{pk}^{(1)} \cdot (Z_{pp}^{(1)} + Z_{qq}^{(1)} - 2 \cdot Z_{pq}^{(1)} - z_{pq}^{(1)} + Z_{pp}^{(0)} + Z_{qq}^{(0)} - 2 \cdot Z_{pq}^{(0)} - z_{pq}^{(0)}) + (Z_{qk}^{(1)} - Z_{pk}^{(1)}) \cdot (2 \cdot Z_{pq}^{(1)}$$
$$- 2 \cdot Z_{pp}^{(1)} + z_{pq}^{(1)} + 2 \cdot Z_{pq}^{(0)} - 2 \cdot Z_{pp}^{(0)} + z_{pq}^{(0)}) + Z_{pk}^{(0)} \cdot (Z_{pp}^{(1)} + Z_{qq}^{(1)} - 2 \cdot Z_{pq}^{(1)} - z_{pq}^{(1)}) + (Z_{qk}^{(0)} - Z_{pk}^{(0)}) \cdot (2 \cdot Z_{pq}^{(1)}$$
$$- 2 \cdot Z_{pp}^{(1)} + z_{pq}^{(1)}) + a[Z_{pk}^{(2)^*} \cdot (Z_{pp}^{(0)} + Z_{qq}^{(0)} - 2 \cdot Z_{pq}^{(0)} - z_{pq}^{(0)}) + (Z_{qk}^{(2)^*} - Z_{pk}^{(2)^*}) \cdot (2 \cdot Z_{pq}^{(0)} - 2 \cdot Z_{pp}^{(0)} + z_{pq}^{(0)})]$$

$$\mathbf{n_2^C} = a \cdot \{\mathbf{d_2} - [Z_{pk}^{(1)} \cdot (Z_{pp}^{(1)} + Z_{qq}^{(1)} - 2 \cdot Z_{pq}^{(1)} - z_{pq}^{(1)} + Z_{pp}^{(0)} + Z_{qq}^{(0)} - 2 \cdot Z_{pq}^{(0)} - z_{pq}^{(0)}) + (Z_{qk}^{(1)} - Z_{pk}^{(1)}) \cdot (2 \cdot Z_{pq}^{(1)}$$
$$- 2 \cdot Z_{pp}^{(1)} + z_{pq}^{(1)} + 2 \cdot Z_{pq}^{(0)} - 2 \cdot Z_{pp}^{(0)} + z_{pq}^{(0)}) + Z_{pk}^{(0)} \cdot (Z_{pp}^{(1)} + Z_{qq}^{(1)} - 2 \cdot Z_{pq}^{(1)} - z_{pq}^{(1)}) + (Z_{qk}^{(0)} - Z_{pk}^{(0)}) \cdot (2 \cdot Z_{pq}^{(1)}$$
$$- 2 \cdot Z_{pp}^{(1)} + z_{pq}^{(1)}) + a^2[Z_{pk}^{(2)^*} \cdot (Z_{pp}^{(0)} + Z_{qq}^{(0)} - 2 \cdot Z_{pq}^{(0)} - z_{pq}^{(0)}) + (Z_{qk}^{(2)^*} - Z_{pk}^{(2)^*}) \cdot (2 \cdot Z_{pq}^{(0)} - 2 \cdot Z_{pp}^{(0)} + z_{pq}^{(0)})]$$

$$\mathbf{n_1^B} = a^2 \cdot \{\mathbf{d_1} - [(Z_{qk}^{(1)} - Z_{pk}^{(1)}) \cdot (Z_{pp}^{(1)} + Z_{pp}^{(0)}) + Z_{pk}^{(1)} \cdot (2 \cdot Z_{pq}^{(1)} - 2 \cdot Z_{pp}^{(1)} + z_{pq}^{(1)} + 2 \cdot Z_{pp}^{(0)} - 2 \cdot Z_{pp}^{(0)} + z_{pq}^{(0)})]\}$$
$$+ \{Z_{pp}^{(1)} \cdot (Z_{qk}^{(0)} - Z_{pk}^{(0)}) + Z_{pk}^{(0)} \cdot (2 \cdot Z_{pq}^{(0)} - 2 \cdot Z_{pp}^{(0)} + z_{pq}^{(0)}) + a \cdot [Z_{pp}^{(0)} \cdot (Z_{qk}^{(2)^*} - Z_{pk}^{(2)^*}) + Z_{pk}^{(2)^*} \cdot (2 \cdot Z_{pq}^{(0)} - 2 \cdot Z_{pp}^{(0)} + z_{pq}^{(0)})]\}$$

$$\mathbf{n_1^C} = a \cdot \{\mathbf{d_1} - [(Z_{qk}^{(1)} - Z_{pk}^{(1)}) \cdot (Z_{pp}^{(1)} + Z_{pp}^{(0)}) + Z_{pk}^{(1)} \cdot (2 \cdot Z_{pq}^{(1)} - 2 \cdot Z_{pp}^{(1)} + z_{pq}^{(1)} + 2 \cdot Z_{pp}^{(0)} - 2 \cdot Z_{pp}^{(0)} + z_{pq}^{(0)})]\}$$
$$+ \{Z_{pp}^{(1)} \cdot (Z_{qk}^{(0)} - Z_{pk}^{(0)}) + Z_{pk}^{(0)} \cdot (2 \cdot Z_{pq}^{(0)} - 2 \cdot Z_{pp}^{(0)} + z_{pq}^{(0)}) + a^2 \cdot [Z_{pp}^{(0)} \cdot (Z_{qk}^{(2)^*} - Z_{pk}^{(2)^*}) + Z_{pk}^{(2)^*} \cdot (2 \cdot Z_{pq}^{(0)} - 2 \cdot Z_{pp}^{(0)} + z_{pq}^{(0)})]\}$$

$$\mathbf{n_0^B} = a^2 \cdot [\mathbf{d_1} - (Z_{pp}^{(1)} + Z_{pp}^{(0)}) \cdot Z_{pk}^{(1)}] + Z_{pp}^{(1)} \cdot Z_{pk}^{(0)} + a \cdot Z_{pk}^{(2)^*} \cdot Z_{pp}^{(0)}$$

$$\mathbf{n_0^C} = a \cdot [\mathbf{d_1} - (Z_{pp}^{(1)} + Z_{pp}^{(0)}) \cdot Z_{pk}^{(1)}] + Z_{pp}^{(1)} \cdot Z_{pk}^{(0)} + a^2 \cdot Z_{pk}^{(2)^*} \cdot Z_{pp}^{(0)}$$

*Multiplied by a proper phase shift in case of phase-shifting components

One-phase-to-ground faults on phase A will lead to voltage sag only on phase A if no phase-shifting components exist between the fault and the observation position. When a phase-shifting component exists e.g. a power transformer of certain vector group, two phases will be sagged. In Table 2, the coefficients d, n in case of one-phase-to-ground faults are given for phases A and B. For phase C, the coefficients a^2 and a change position in relation with the expressions for phase B. The negative-sequence bus impedance matrix elements that should be multiplied by phase shift in case of phase-shifting devices are marked with a (*).

In case of two-phase or two-phase-to-ground faults between phases B and C, the coefficients d, n for phases B and C only are presented in Tables 3, 4 and 5. The coefficients d, n for phase A can be easily extracted. The negative-sequence bus impedance matrix elements that should be multiplied by phase shift in case of phase-shifting component intervenes are marked with a (*).

6   Study Case

Voltage sag assessment is mainly important for industrial customers and usually is performed in distribution networks. For a more accurate assessment, the contribution of faults at the transmission network feeding the distribution network should not be ignored. Therefore, a suitable power network for the application of a voltage stochastic assessment method is as the one shown in Fig. 7. Six industrial customers are connected at six nodes of the same 20 kV distribution line through a solidly grounded Dyn1 transformer, widely used in Greece. The equivalent transmission system consists of three 150 kV lines and is relatively of large size to take into account the fact that faults even at hundred kilometers away from the critical customers will cause them severe sags [5].

Assuming a base power of 100 MVA, the positive- and negative-sequence impedances of the power transformer and the equivalent sources of buses 8 and 9 are j0.4 pu, j0.02 pu and j0.005 pu, respectively. The impedances of the power lines in ohm/km and in pu are presented in Table 6.
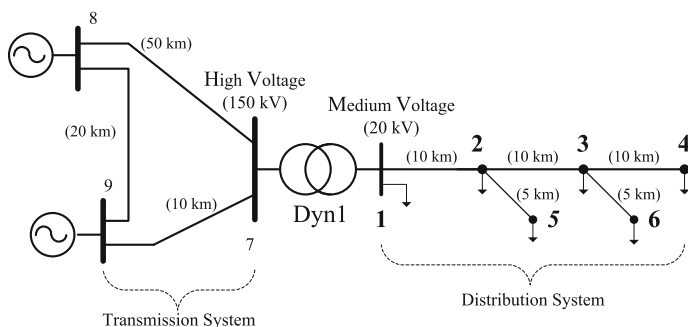

Fig. 7 Single-line diagram of the studied power network

Table 6 Data of the electric power lines

Power Line (s)	Positive- and negative-sequence impedances $z^{(1)}$, $z^{(2)}$	Zero-sequence impedances $z^{(0)}$
1–2, 2–3, 3–4	0.22 + j·0.37 ohm/km *0.55 + j·0.925 pu*	0.37 + j·1.56 ohm/km *0.925 + j·3.9 pu*
2–5, 3–6	1.26 + j·0.42 ohm/km *1.575 + j·0.525 pu*	1.37 + j·1.67 ohm/km *1.7125 + j·2.0875 pu*
7–8	0.097 + j·0.391 ohm/km *0.215 + j·0.868 pu*	0.497 + j·2.349 ohm/km *1.104 + j·5.22 pu*
7–9	0.097 + j·0.391 ohm/km *0.0431 + j·0.17375 pu*	0.497 + j·2.349 ohm/km *0.22085 + j·1.044 pu*
8–9	0.097 + j·0.391 ohm/km *0.0862 + j·0.3475 pu*	0.497 + j·2.349 ohm/km *0.4417 + j·2.088 pu*

In order to study symmetrical and asymmetrical short-circuits, the formation of the positive- and zero-sequence bus impedance matrices $[Z_{\tilde{z}}^{(1)}](= [Z_{\tilde{z}}^{(2)}]$ and $[Z_{\tilde{z}}^{(0)}])$ is required. Assuming the node behind the sources as the reference node, the equivalent networks for the calculation of the bus impedance matrices are as shown in Figs. 8 and 9.
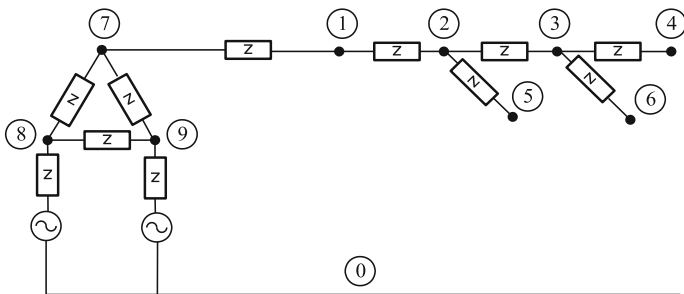
Fig. 8 Positive-sequence circuit of the studied network
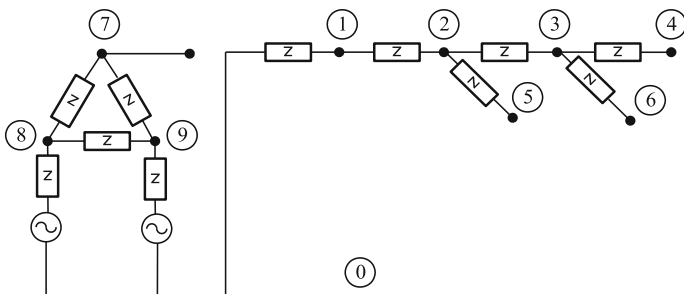
Fig. 9 Zero-sequence circuit of the studied network

The bus impedance matrices $[Z_z^{(1)}]$ and $[Z_z^{(0)}]$) are calculated in pu values by the inversion of the bus conductance matrices and are as follows:

$[Z_z^{(1)}] =$

	1	2	3	4	5	6	7	8	9
1	0.036+ j·0.559	0.036+ j·0.559	0.036 + j·0.559	0.036+ j·0.559	0.036+ j·0.559	0.036+ j·0.559	0.036+ j·0.159	j·0.0042	0.0002+ j·0.016
2	0.036+ j·0.559	0.586+ j·1.484	0.586+ j·1.484	0.586+ j·1.484	0.586+ j·1.484	0.586+ j·1.484	0.036+ j·0.159	j·0.0042	0.0002+ j·0.016
3	0.036+ j·0.559	0.586+ j·1.484	1.136+ j·2.409	1.136+ j·2.409	0.586+ j·1.484	1.136+ j·2.409	0.036+ j·0.159	j·0.0042	0.0002+ j·0.016
4	0.036+ j·0.559	0.586+ j·1.484	1.136+ j·2.409	1.686+ j·3.334	0.586+ j·1.484	1.136+ j·2.409	0.036+ j·0.159	j·0.0042	0.0002+ j·0.016
5	0.036+ j·0.559	0.586+ j·1.484	0.586+ j·1.484	0.586 + j·1.484	2.161+ j·2.009	0.586+ j·1.484	0.036+ j·0.159	j·0.0042	0.0002+ j·0.016
6	0.036+ j·0.559	0.586+ j·1.484	1.136+ j·2.409	1.136 + j·2.409	0.586+ j·1.484	2.711+ j·2.934	0.036+ j·0.159	j·0.0042	0.0002+ j·0.016
7	0.036+ j·0.159	0.036+ j·0.159	0.036+ j·0.159	0.036+ j·0.159	0.036+ j·0.159	0.036+ j·0.159	0.036+ j·0.159	j·0.0042	0.0002+ j·0.016
8	j·0.0042	j·0.0042	j·0.0042	j·0.0042	j·0.0042	j·0.0042	j·0.0042	0.0003+ j·0.019	j·0.0013
9	0.0002+ j·0.016	0.0002+ j·0.016	0.0002+ j·0.016	0.0002+ j·0.016	0.0002+ j·0.016	0.0002+ j·0.016	0.0002+ j·0.016	j·0.0013	0.0003+ j·0.019

$[Z_z^{(0)}] =$

	1	2	3	4	5	6	7	8	9
1	j·0.4	j·0.4	j·0.4	j·0.4	j·0.4	j·0.4	0	0	0
2	j·0.4	0.925+ j·4.3	0.925+ j·4.3	0.925+ j·4.3	0.925+ j·4.3	0.925+ j·4.3	0	0	0
3	j·0.4	0.925+ j·4.3	1.85+ j·8.2	1.85+ j·8.2	0.925+ j·4.3	1.85+ j·8.2	0	0	0
4	j·0.4	0.925+ j·4.3	1.85+ j·8.2	2.775+ j·12.1	0.925+ j·4.3	1.85+ j·8.2	0	0	0
5	j·0.4	0.925+ j·4.3	0.925+ j·4.3	0.925+ j·4.3	2.638+ j·6.388	0.925+ j·4.3	0	0	0
6	j·0.4	0.925+ j·4.3	1.85+ j·8.2	1.85+ j·8.2	0.925+ j·4.3	3.563+ j·10.287	0	0	0
7	0	0	0	0	0	0	0.184+ j·0.874	j·0.0008	j·0.005
8	0	0	0	0	0	0	j·0.0008	j·0.005	0
9	0	0	0	0	0	0	j·0.005	0	j·0.005

7 Results and Discussion

From the analytical expressions given in the previous Sections, the during-fault voltage vector per phase can be calculated for every fault position within a power network. That, is the voltage magnitude as well as the phase-angle jump during every fault type can be drawn as a function of the distance to the fault from the one

line end. In the current document, we focus only on the voltage magnitude $|\tilde{V}_{kf}(\ell)|$ and especially on the sag magnitude, which is the minimum remaining (or during-fault) voltage among the three phase voltages.

As it is mentioned in Sect. 4, the existence of a phase-shifting device such as a power transformer of certain vector group between the fault and the calculation positions affects the results. For our study case where a Dyn1 transformer separates the two voltage levels, there two different cases that should be examined separately: without and with the effects of a phase-shifting transformer.

7.1 No Phase-Shifting Devices

In this case, the fault positions and the calculations are applied at the same voltage level. Equations (20) for three-phase (3ph), one-phase-to-ground (1ph) and two-phase (2ph) faults as well as Eq. (21) for the two-phase-to-ground (2ph-g) faults will give the results by using the coefficients from Tables 1, 2, 3, 4 and 5.

In case of 3ph faults, the during-fault voltage magnitude, which is also the sag magnitude, is calculated for faults applied to Lines 1–2 and 2–5. For Line 1–2, the
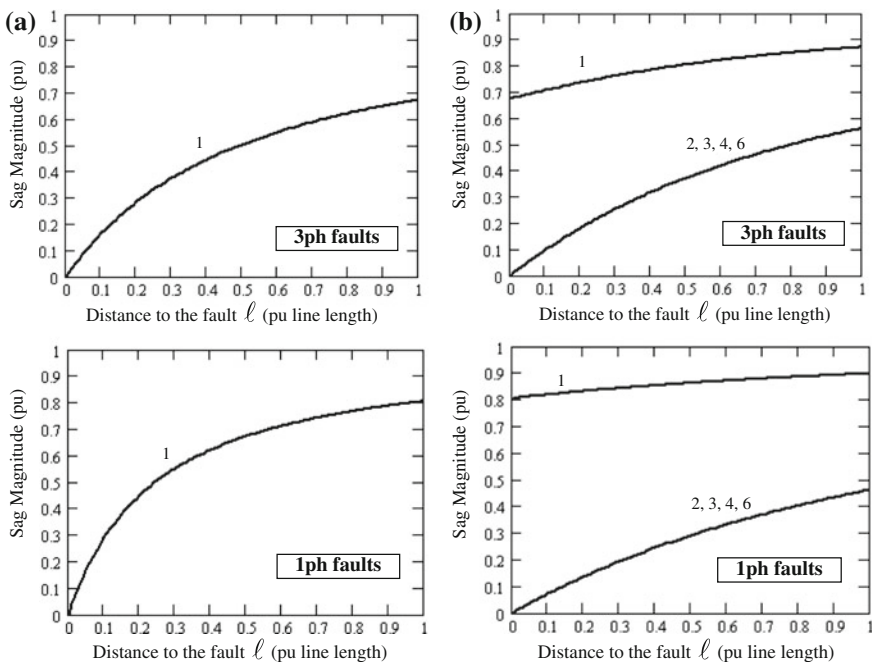
Fig. 10 Sag magnitude of Nodes 1–6 for three-phase and one-phase-to-ground faults on: **a** Line 1–2, **b** Line 2–5. In brackets are the sagged phases
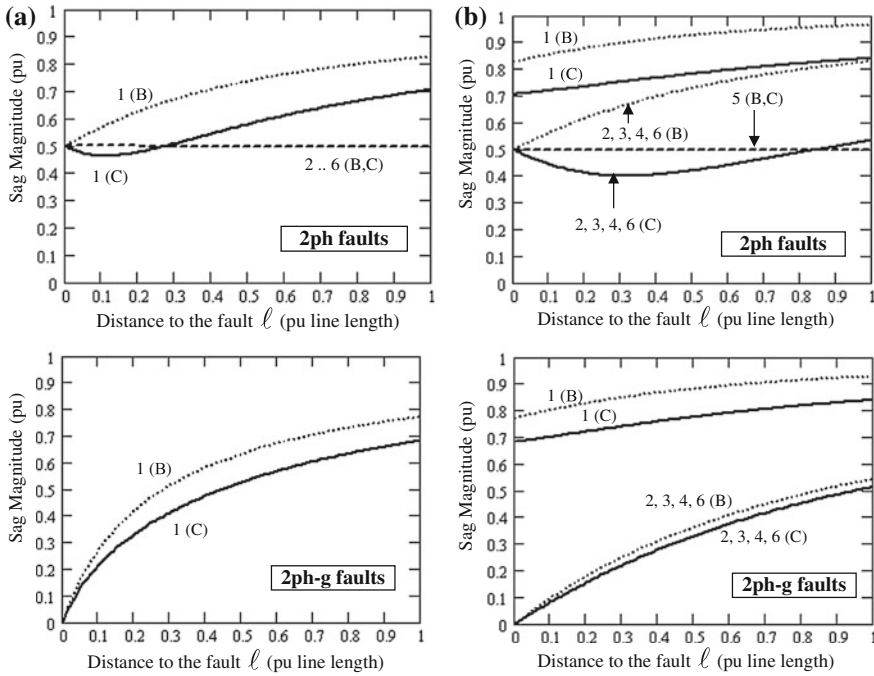
Fig. 11 Sag magnitude of Nodes 1–6 for two-phase and two-phase-to-ground faults on: **a** Line 1–2, **b** Line 2–5. In brackets are the sagged phases

results concern the voltage magnitude of Node 1 and for Line 2–5 the voltage magnitude of all six nodes. The sag magnitude is drawn as a function of the distance to the fault in case of 3ph and 1ph faults, and presented in Fig. 10.

In Fig. 11, the results for 2ph and 2ph-g faults between phases B and C are given. It can be observed that the sag magnitude is given by the during-fault voltage of phase C. This is further analyzed and proved in [6]. The during-fault voltage of phase B is also shown for comparisons.

7.2 Effect of Transformer's Phase Shift

When fault positions and calculations are performed at a different voltage level of the studied power network shown in Fig. 7, the effect of transformer's phase shift should be taken into account. The negative-sequence bus impedance elements should be multiplied with a certain phase shift angle as described in Sect. 4.

In case that faults occur at the HV transmission lines of the studied network, the sag magnitude of MV nodes 1–6 is the same for all nodes. In Fig. 12, the sag magnitude versus fault distance on lines 7–8 and 7–9 for each fault type is depicted.
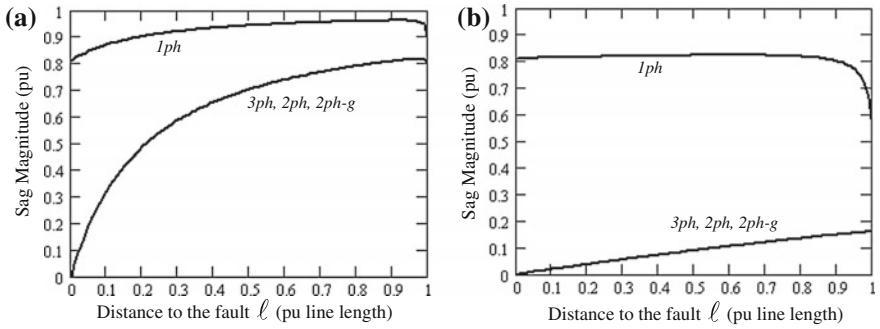
Fig. 12 Sag magnitude of Nodes 1–6 for all fault types on: **a** Line 7–8, **b** Line 7–9
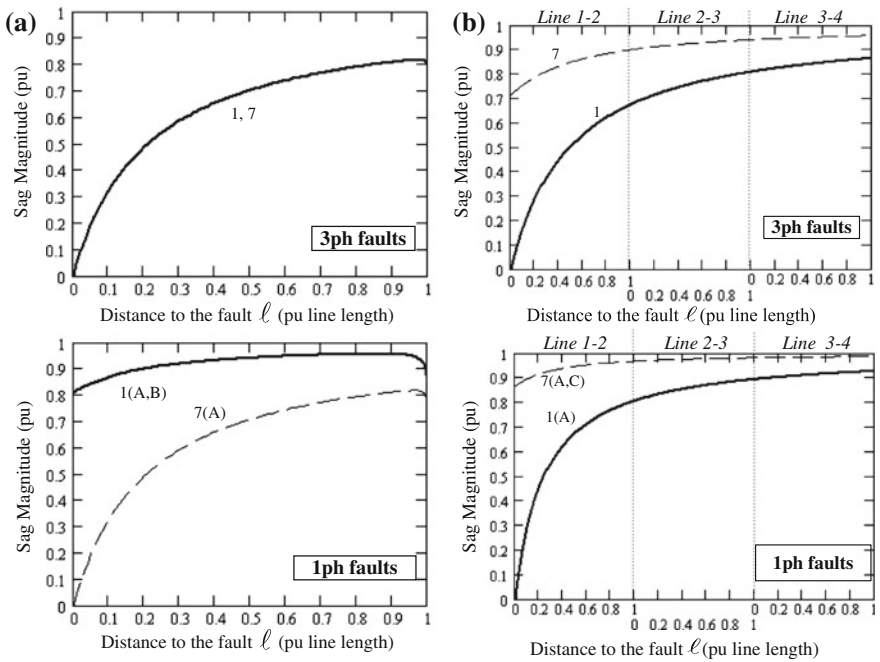
Fig. 13 Sag magnitude (*solid line*) of nodes 7 and 1 for three-phase and one-phase-to-ground faults on: **a** Line 7–8, **b** Line 1–4. In brackets are the sagged phases

Three-phase (3ph), two-phase (2ph) and two-phase-to-ground (2ph-g) faults on HV side give the same sag magnitude at MV side and one-phase-to-ground (1ph) faults give shallow sags, which is due to transformer's vector group [4].

The effect of transformer's phase shift is further analyzed by comparing the sag magnitude of nodes 1 and 7 (Fig. 7) for faults at the MV and HV power lines. In Fig. 13, the sag magnitude of those nodes due to 3ph and 1ph faults on Line 7–8
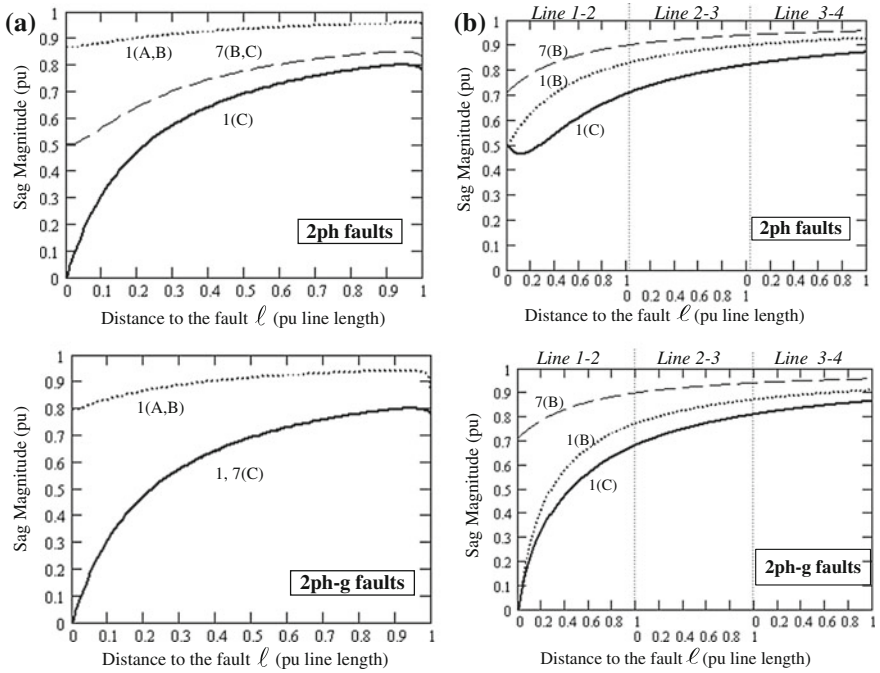
Fig. 14 Sag magnitude (*solid line*) of nodes 7 and 1 for two-phase and two-phase-to-ground faults on: **a** Line 7–8, **b** Line 1–4. In brackets are the sagged phases

(HV area) and Line 1-4 is drawn in relation with the fault distance. It can be easily observed the positive effect of the transformer's on the sag magnitude.

In Fig. 14, 2ph and 2ph-g faults between phases B and C on Lines 7–8 and 1–4 are considered. It can be seen in Fig. 14a that for 2ph faults on Line 7–8, the transformer results in deterioration as regards the sag magnitude of node 1 with respect to node 7, which is also higher for faults close to node 7. In Fig. 14b, the difference on during-fault voltage of phases B and C can be observed.

8 Conclusions

This document presents advanced methods in short-circuit analysis. A procedure is proposed in order to the extraction of analytical mathematical expressions. These expressions allow the assessment of voltage sag basic characteristics, that is magnitude and phase-angle jump. They are applicable in any network topology and the give the during-fault voltage vector for all fault types in any position of network. They allow the drawing of the voltage magnitude or the phase-angle jump in relation with the distance to the fault from the one power line end.

Moreover, a procedure to incorporate the phase shift introduced by devices or transformers is proposed. Thus, the set of mathematical expressions presented in this document will allow a fast and accurate assessment of phase shift introduced by any device or transformer vector group.

Furthermore, a relatively small test network is used for the demonstration of the effectiveness of those expressions and the understanding of voltage sag characteristics. However, those expressions allow a fast and accurate short-circuit and voltage sag analysis of much larger power networks of many different voltage levels and more than one phase-shifting device or transformer.

References

1. IEC 60076-1 Standard, Power Transformers – Part 1: General, 1999.
2. J. Grainger, and W. Stevenson, Power System Analysis, McGraw-Hill, 1994, pp. 449-459.
3. M. Moschakis, and N. Hatziargyriou, "Analytical Calculation and Stochastic Assessment of Voltage Sags", IEEE Trans. on Power Delivery, vol. 21, no. 3, pp. 1727–1734, July 2006.
4. M. Moschakis, S. Loutridis, V. Dafopoulos, A. Anastasiadis, T. Tomtsi, E. Karapidakis, and A. Tsikalakis, "Prediction of Voltage Sags Applying the Method of Critical Distances to Meshed Power Networks", in Proc. of IEEE PMAPS (Probabilistic Methods Applied to Power Systems) Conference, pp. 570-575, Istanbul, Turkey, June 10-14, 2012.
5. M. Bollen, Understanding Power Quality Problems: Voltage Sags and Interruptions, Anderson P.M., 2000, pp. 190-198.
6. Moschakis M. N., Hatziargyriou N. D., "Influence of Power Transformer's Phase Shift and R/X ratio of power line conductors on during-fault voltage", MEDPOWER Conference Proceedings, Athens, Greece, November 2008.

A Genetic Proportional Integral Derivative Controlled Hydrothermal Automatic Generation Control with Superconducting Magnetic Energy Storage

Rajesh Joseph Abraham and Aju Thomas

Abstract In this work, the Automatic Generation Control of an interconnected hydrothermal power system with Superconducting Magnetic Energy Storage (SMES) has been investigated. The gain settings of integral controller as well as Proportional Integral Derivative (PID) controller are tuned by Integral Time Squared Error (ITSE) criterion using Genetic Algorithm. Simulation, comparison and analysis of dynamic performances in the presence of Generation Rate Constraints brings out the superior performance of SMES units and PID controller in suppressing frequency and inter area tie line power deviations from their nominal values followed by a step load disturbance in thermal area.

1 Introduction

The problem of keeping electric power system in its normal operating state is of prime importance in the field of power system operation and control. This has to be solved by continuous automatic closed loop control [1]. The flows of active power and reactive power in a transmission network are fairly independent of each other and are influenced by different control actions. Active power control is closely related to frequency control and reactive power control is closely related to voltage control. As constancy of frequency and voltage are important factors in determining the quality of power supply, the quality of active power and reactive power is vital to the satisfactory performance of power systems. The frequency of a system is dependent on active power balance. As frequency is a common factor throughout the system, a change in active power demand at one point is reflected throughout

R.J. Abraham (✉)
Department of Avionics, Indian Institute of Space Science and Technology,
Thiruvananthapuram, Kerala, India
e-mail: rajeshja@gmail.com

A. Thomas
Department of Electrical & Electronics Engineering, Mangalam College of Engineering,
Kottayam, Kerala, India

the system by a change in frequency. Because there are many generators supplying power into the system, some means must be provided to allocate change in demand to the generators. In an interconnected system with two or more control areas, in addition to control of frequency, the generation within each area has to be controlled so as to maintain scheduled power interchange. The control of generation and frequency is commonly referred to as Load Frequency Control/Automatic Generation Control [2]. The objectives of AGC are,

1. To hold the system frequency at or very close to a specified nominal value.
2. To maintain the correct value of interchange power between control areas.
3. To maintain each unit's generation at the most economic value [3].

The problem of active power-frequency control is as old as the power system technology itself. The first job to do is the development of a system model. Since the system is exposed to small changes in load or load perturbations for the particular study, a linearised model is sufficient for its dynamic representation. The transfer functions for each of the components of power system can be derived from basic differential equations and Laplace transforms analysis [1, 3–5]. Also one among several nonlinearity conditions, the generation rate constraint has to be considered for better understanding of the performance under practical conditions.

A two area interconnected system can be considered for the study. Being the basic representation of a multi-area system, it has the advantage of being comparatively easy and flexible to work with. Also further studies on multi-area systems with more areas will be based on the basic two area system. A multi-area multiunit Hydro-Thermal system is adapted for study [5–7].

One of the main factors contributing for performance of AGC is the supplementary control or integral control. Here the integral controller is replaced by PID controller. The tuning or selection of PID gain values is of much importance in maintaining frequency and power at nominal values. Conventional optimization methods have been employed in many studies on AGC [8]. Evolutionary programming methods can be adopted for better optimized values of PID gains. Different methods like Particle Swarm Optimization, Ant Colony System Algorithm, Genetic Algorithm, and Simulated Annealing are used in power system control studies for optimization [9–11]. Genetic algorithm technique can be used to find the best value of PID gains [12]. The GA is a stochastic global search method that mimics the metaphor of natural biological evolution. GA's operate on a population of potential solutions applying the principle of survival of the fittest to produce (hopefully) better and better approximations to a solution. It has the advantage of searching a population of points in parallel, not a single point and do not require derivative information or other auxiliary knowledge; only the objective function and corresponding fitness levels influence the directions of search. GA's use probabilistic transition rules, not deterministic ones [13–15].

Literature survey points out that incorporation of active energy storage devices or techniques to assist AGC yields better results. Performance of different sources like battery energy storage, pumped hydro, capacitive energy storage, superconducting magnetic energy storage in interconnected power systems are observed [1, 2, 16]. A variety of storage technologies are in the market but the most viable are battery energy storage systems (BESS), pumped storage hydroelectric system, superconducting magnetic energy storage (SMES) and capacitive energy storage (CES). Some of the disadvantages of BESS include limited life cycle, voltage and current limitation and environmental hazards. The disadvantages of pumped hydro electric units are larger in size, environmental and topographic limitation [17–19].

This article investigates the dynamic performance of both integral and PID controllers used in the supplementary control of AGC. Also the impact of SMES unit in an interconnected two area multiunit hydrothermal power system needs to be analysed. In view of the above, objectives of this work are:

1. To develop a small perturbation transfer function model of a two area inter-connected hydro-thermal system considering Generation Rate Constraints.
2. To incorporate an SMES coil into the power system model.
3. To optimize the gain settings of the integral and PID controllers with and without SMES using genetic algorithm method.
4. To compare the dynamic responses with and without SMES and PID controller following a step load disturbance in the thermal area.

2 Hydrothermal Power Systems Model

A two area multiunit hydrothermal power system is considered for investigation as shown in Fig. 1. Area 1 consists of two non-reheat thermal units and area 2, with two hydro units. Each thermal unit has a generation constraint of 10 % per minute and each hydro unit has 270 % per minute for rising and 360 % per minute for lowering generation as considered in [20]. The transfer function models used for this work are developed as in [13].

Figure 1 shows the linear time invariant (LTI) transfer function model of two area multiunit hydrothermal power system with PID controller and SMES block. Area participation factors (apf) are also considered as the system under investigation is a multi unit two area system. apfs are the ratios in which generating units adjust their power output. It should be noted that in area 1, $apf_{11} + apf_{22} = 1$ and in area 2, $apf_{21} + apf_{22} = 1$. Here $apf_{11} = apf_{12} = apf_{21} = apf_{22} = 0.5$ has been considered, which means all the units share the load change equally. The values of the constants in the block diagram for the areas, PID controllers and SMES unit are given in the appendices.
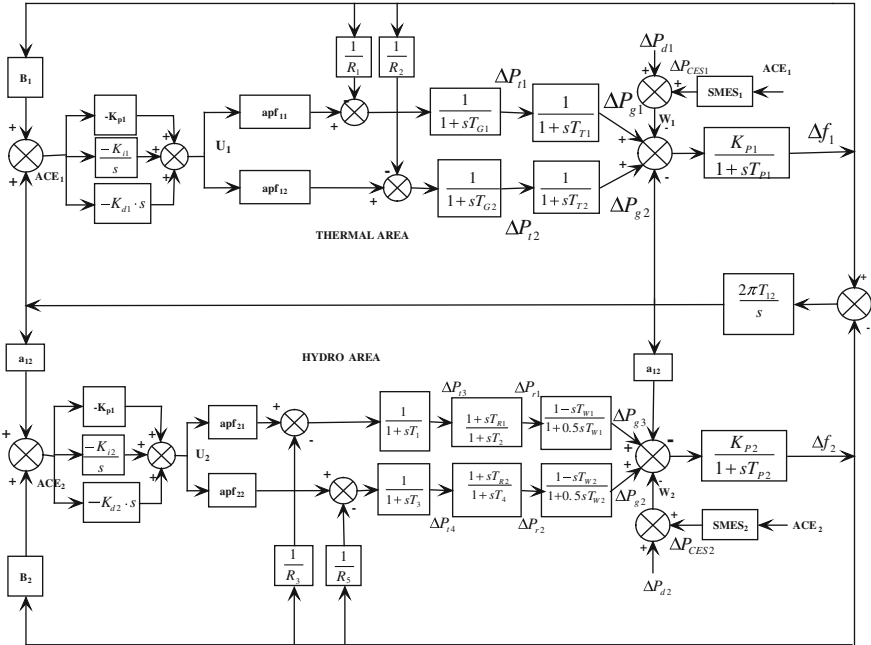
Fig. 1 LTI model of interconnected multiunit hydrothermal system with SMES and PID controller

3 Superconducting Magnetic Energy Storage

SMES is a technology based on the ability of superconductors to carry high dc currents with essentially no resistive loss in the presence of significant magnetic fields, thereby directly storing electrical energy. Independent of the application, an SMES system consists of a superconducting coil, a refrigerator, a power conversion system (PCS) and a control system. SMES systems are almost always connected to an ac power system, but the superconducting coil is inherently a dc device. Thus, some means of converting ac to dc and back is necessary. This is accomplished by the power conversion system with a 12 pulse converter and a wye delta connected transformer arrangement [21].

The electrical interface between the superconducting magnet and the electric power system is a converter, as shown in Fig. 2. The converter is an ac-to-dc rectifier and dc-to-ac inverter that changes the alternating current from the utility into the direct current that must flow continuously in the coil. To charge or discharge, the voltage across the coil is made positive or negative. When the unit is on standby, independent of storage level, the current is constant and the average voltage across the superconducting winding is zero.
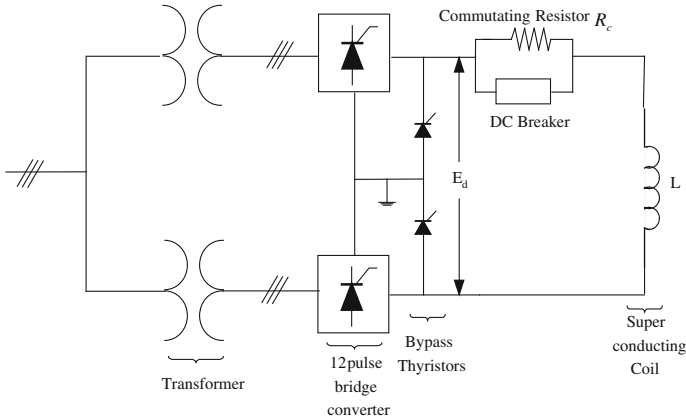
Fig. 2 SMES circuit diagram

The superconducting coil can be charged to a set value from the grid during normal operation of the power system. Once the superconducting coil gets charged, it conducts current with virtually no losses as the coil is maintained at extremely low temperatures. When there is a sudden rise in the load demand, the stored energy is almost released through the PCS to the power system as alternating current. As the governor and other control mechanisms start working to set the power system to the new equilibrium condition, the coil current changes back to its initial value. Similar action occurs during sudden release of loads. In this case, the coil immediately gets charged towards its full value, thus absorbing some portion of the excess energy in the system and as the system returns to its steady state, the excess energy absorbed is released and the coil current attains its normal value. The control of the converter firing angle α provides the dc voltage appearing across the inductor to be continuously varying within a certain range of positive and negative values. The inductor is initially charged to its rated current I_{d0} by applying a small positive voltage. Once the current reaches its rated value, it is maintained constant by reducing the voltage across the inductor to zero since the coil is superconducting [21, 22].

Neglecting the transformer and the converter losses, the dc voltage is given by

$$E_d = 2V_{do}Cos\alpha - 2I_dR_C \qquad (1)$$

where E_d is the dc voltage applied to the inductor in kV, α is the firing angle in degrees, Id is the current flowing through the inductor in kA, RC is the equivalent commutating resistance in kΩ and V_{d0} is the maximum circuit bridge voltage in kV. Charging and discharging of the SMES unit is controlled through the change of commutation angle α. If α is less than 90°, converter acts in the converter mode (charging mode) and if α is greater than 90°, the converter acts in the inverter mode (discharging mode).

In order to simulate the effect of an energy storage device on a power system, it is necessary to devise a model for the energy storage device and incorporate this model into the overall system model. When power is to be pumped back into the grid in the case of a fall in frequency due to sudden loading in the area, the control voltage E_d is to be negative since the current through the inductor and the thyristors cannot change its direction. The control input to SMES is the frequency deviations of particular control areas. The incremental change in the voltage applied to the inductor is expressed as:

$$\Delta E_d = \left[\frac{K_{SMES}}{1 + sT_{DC}}\right](\Delta f_1) \tag{2}$$

where, ΔE_d is the incremental change in converter voltage; T_{DC} is the converter time delay; K_{SMES} is the gain of the control loop and Δf_1 is the input signal to the SMES control logic. The inductor current deviation is given by:

$$\Delta I_d = \frac{\Delta E_d}{sL} \tag{3}$$

There is a possibility of the inductor current to return to its nominal value only very slowly. But the inductor current must be restored to its nominal value quickly after a system disturbance so that it can respond to the next load perturbation immediately. Hence, inductor current deviation can be sensed and used as a negative feedback signal in the SMES control loop so that the current restoration to its nominal value can be enhanced. Thus the dynamic equation for the inductor voltage deviation of the SMES unit is given by Eqn. (4) and its block diagram [19] is given in Fig. 3

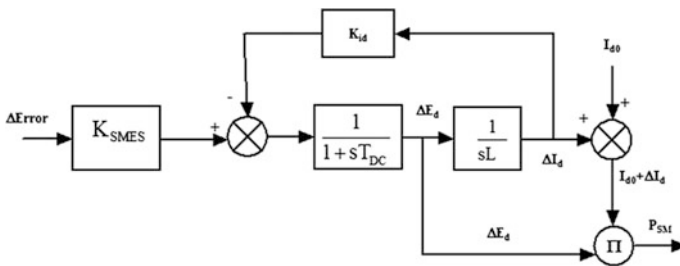$$\Delta E_d = \frac{1}{1 + sT_{DC}}[K_{SMES}(\Delta f) - K_{id}\Delta I_d] \tag{4}$$

Fig. 3 SMES Block diagram with negative inductor current deviation feedback

4 Overview of Genetic Algorithm (GA)

GA has been used for optimizing the parameters of the system that are complex and difficult to solve by using conventional optimization methods. GA maintains a set of candidates called population and repeatedly modifies them in each steps called generation. At each generation, the GA selects individuals from the current population as parents and uses them to produce the offspring's for the next generation. Candidate solutions are usually represented as strings of fixed length, called chromosomes. A fitness or objective function is used to obtain the goodness of each member of the population. For a given random initial population, GA operates in steps called generations, as follows [15]:

- Goodness of each member in the population is evaluated using a fitness function.
- The population undergoes reproduction in a number of iterations. One or more parents are chosen according to their fitness values having higher probability of contributing an offspring.
- Genetic operators, such as crossover and mutation, are applied to parents to produce offspring.
- The old population is replaced by offspring's to form new population until convergence criteria is meet.

Genetic Algorithm consists of a string representation of points in the search space, a set of genetic operators for generating new search points, a fitness function to evaluate the search points and a stochastic assignment to control the genetic operations. Simplicity of operation and power of effect are two main attractions of the GA approach. It typically consists of three phases.

(1) Initialization

Initialization is the generation of initial population of chromosomes i.e. initial search points. The population size and string length need to be judiciously selected before this job is performed. The size of the population, i.e. number of chromosomes in a population, is a direct indication of effective representation of whole search space in one population. The population size affects both the ultimate performance and efficiency of GA. If it is too small, the chance that the members of a population cover the entire search space is low. This results in difficulty in obtaining the global optimum solution and leads to a local optimum solution. It is important to note that this stagnation at local optimum is a result of premature convergence. Large population size is preferable to avoid this premature convergence and to reach a global optimum point. But a too large population size decreases the rate of convergence and in the worst case may lead to divergence. So based on the size of search space the population size needs to be selected.

The selection of "string length" depends on the accuracy requirements of the optimization problem. The higher the string length, the higher will be the resolution and accuracy. But this leads to slow convergence. Also the number of parameters in

the optimization problem will have a direct effect on the number of bits in a chromosome i.e. string length. For particular resolution and accuracy requirements, problem with more number of parameters will have large string. Keeping all the above constraints in mind, the string length is chosen appropriately.

After the selection of string length and population size, the initial population is generated as a set of strings of bits either '0' or '1'. Random number generation techniques are used to accomplish this task. These strings of bits contain the information related to the parameters of the optimization problem in encoded format. Any of the encoding techniques can be used but binary encoding is convenient and mostly used.

Now, from the initial population, chromosomes are decoded and all parameters of the optimization problem are calculated for each chromosome. This results in a set of solutions whose size is equal to population size [23, 24].

(2) Evaluation

In the evaluation phase, suitability of each of the solutions from the initial set as the solution of the optimization problem is determined. For this function called "fitness function" is defined. This is used as a deterministic tool to evaluate the fitness of each chromosome. The optimization problem may be minimization or maximization type. In the case of maximization type, the fitness function can be a function of variables that bear direct proportionality relationship with the objective function. For minimization type problems, fitness function can be function of variables that bear inverse proportionality relationship with the objective function or can be reciprocal of a function of variables with direct proportionality relationship with the objective function. In either case, fitness function is so selected that the most fit solution is the nearest to the global optimum point. On the whole for a typical optimization problem, evaluation phase consists of calculation of individual parameters, testing of any equality or inequality constraints that need to be satisfied, evaluation of objective function, and finally evaluation of fitness from fitness function.

(3) Genetic operation

In this phase, the objective is the generation of new population from the existing population with the examination of fitness values of chromosomes and application of genetic operators. These genetic operators are reproduction, crossover, and mutation. This phase is carried out if we are not satisfied with the solution obtained earlier. The GA utilizes the notion of survival of the fittest by transferring the highly fit chromosomes to the next generation of strings and combining different strings to explore new search points.

Reproduction: Reproduction is simply an operator where by an old chromosome is copied into a mating pool according to its fitness value. Highly fit chromosomes receive higher number of copies in the next generation. Copying chromosomes according to their fitness means that the chromosomes with a higher fitness value have higher probability of contributing one or more offspring in the next generation. There exist a number of reproduction operators in GA literature but the essential

idea in all of them is that the average strings are picked from the current population and their multiple copies are inserted in the mating pool in a probabilistic manner. The commonly used method for selecting chromosomes for parents to cross over is Roulette Wheel selection.

In roulette wheel selection technique, selection is usually implemented as a linear search through roulette wheel with slots weighed in proportion to string fitness values. This is achieved using the following steps.

1. Total sum of the fitness' (fit sum) of all the strings is calculated.
2. A random real number (rand-sum) between 0 and fit sum is generated.
3. Starting with the first member of existing population, for each member 'n' the fitness sum of members '1' to 'n' is compared with the randomly generated number.
4. If Σ (fitness of member n) > rand-sum, n is selected as parent. Otherwise the process is continued by incrementing n.

Crossover: The crossover is mainly responsible for the global search property of the GA. It is recombination operation. Here the gene information (information in a bit) contained in the two selected parents is utilized in certain fashion to generate two children who bear some of the useful characteristics of parents and expected to be more fit than parents. There are various techniques that are used for performing this crossover. But first of all we need to pick up two parents from the existing population to perform crossover. Crossover is carried out using any one of the following methods.

 (a) Single Point Crossover

In this a cross-site is selected randomly among the length of the mated strings and bits next to the cross-sites are exchanged. This is illustrated in the following example. Let Par1 and Par2 be the two parents selected for crossover. Assume the strings par1 and par2 as below.

Par1: 1 1 0 0 0 1 0 1
Par2: 1 0 1 1 0 1 1 1

Now, a crossover site is selected randomly as an integer between 1 and string length. For illustration the string length is taken as 8. Let this crossover site is 4. Then children Chld1 and Chld2 are generated as below.

Chld1: 1 1 0 0 0 1 1 1

<- Par1- > |<-Par2->

Chld2: 1 0 1 1 0 1 0 1

<- Par2- > |<-Par1->

 (b) Multi Point Crossover

In this method, crossover is performed over the entire length of string of bits. For this a "mask" is generated randomly. This mask is nothing but a string of bits of

value '0' or '1' and sizes same as the chromosome string length. Mask acts temporary locations with randomly bits of value '0' or '1' with random information in the mask; we generate the children as below.

Par 1 : 1 1 0 0 1 0 1 1
Par 2 : 0 1 0 0 0 1 0 0
Mask : 0 0 1 0 1 1 0 1
Chld 1 : 1 1 0 0 0 1 1 0 (If mask = 0, Chld 1 = Par1 & Chld 2 = Par2)
Chld 2 : 0 1 0 0 1 0 0 1 (If mask = 1, Chld 1 = Par2 & Chld 2 = Par1)

 (c) Uniform Crossover

In this method, crossover is performed over the entire length of the string of bits. For this a mask is generated randomly. A mask is nothing but a string of bits of value '0' or '1' and sizes same as string length. With the information in the mask we generate the children as below.

Par1 : 1 1 0 0 1 0 1 1
Par2 : 0 1 0 0 0 1 0 0
Mask : 0 0 1 0 1 1 0 1
Child1 : 1 1 0 0 0 1 1 0 (If mask = 0, Child1 = Par1 & Child2 = Par2)
Child2 : 0 1 0 0 1 0 0 1 (If mask = 1, Child1 = Par2 & Child2 = Par1)

Here we need to generate a mask for each, so number of masks needed is equal to the no of crossover need to be performed. We generate them as and when required and discard them thereafter.

Thus we have seen that each crossover resulted in two children. So the number of crossovers required to be performed for next generation depends on the number of children we need. Usually it is a general practice to copy some of the best parents as it is into the next generation the required strings as children. This phenomenon of copying best parents into the next generation is called "Elitism" and the number of parents so copied is indicated by a parameter of GA called "Percentage of Elitism (P_e)". This is nothing but the percentage of parents so copied out of the total number of parents. This Elitism is basically carried out to not to lose the best strings obtained so far which otherwise may be lost. In order to control crossover also there is a parameter called "Crossover Probability (P_c)". This probability is used as a decision variable before performing the crossover. This is done as follows. A random number between '0' and '1' is generated and if that number is less then P_c, crossover is performed. If the randomly generated number is greater than P_c, Par1 and Par2 are directly selected as Chld1 and Chld2. This is equivalent to the case of crossover where crossover site is equal to the string length. There are various other techniques too for implementing the P_c and the programmer of GA is given freedom to choose any one.

Mutation: This operator is capable of creation new genetic material in the population to maintain the population diversity. It is nothing but random alteration of a bit value at a particular bit position in the chromosome. The following example illustrates the mutation operation.

Original String: 1011001 Mutation site: 4 (say)
String after mutation: 1010001

Some programmers prefer to choose random mutation 'or' alternate bit mutation. "Mutation Probability (P_m)" is a parameter used to control the mutation. For each string a random number between '0' and '1' is generated and compared with the P_m. If it is less than P_m mutation is performed on the string. Sometimes mutation is performed bit-by-bit also instead of strings. These results in substantial increase in CPU time but performance of GA will not increase to the recognizable extent. So this is usually not preferred. Thus obviously mutation brings in some points from the regions of search space which otherwise may not be explored. Generally mutation probability will be in the range of 0.001 to 0.01.
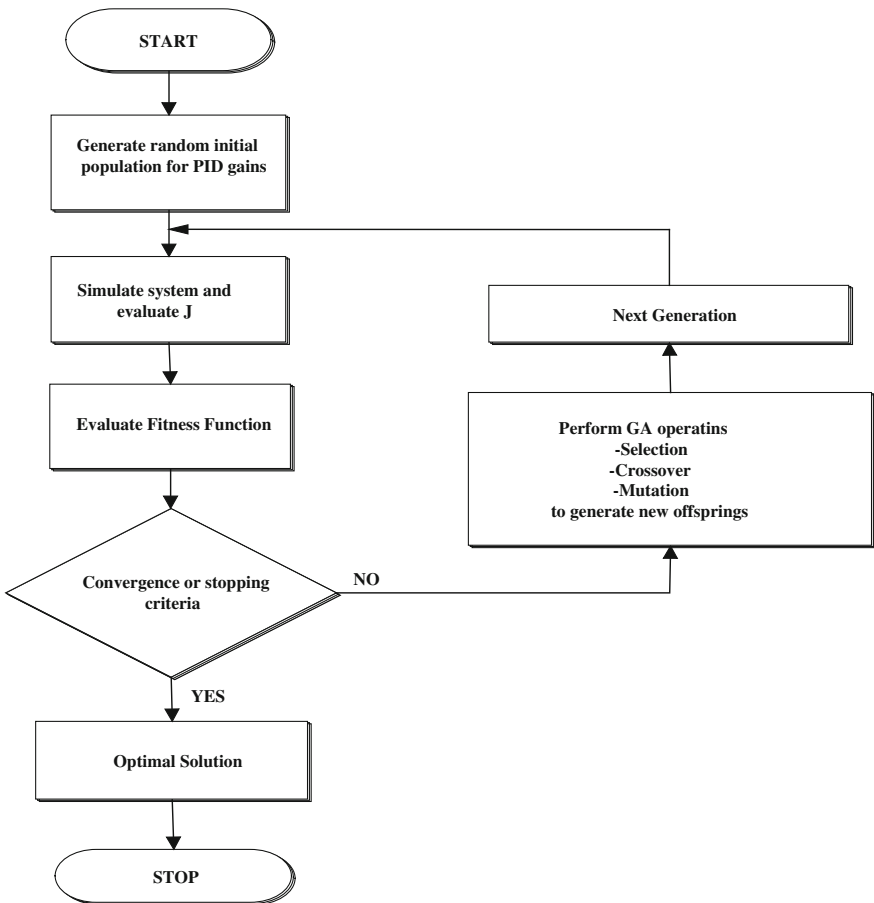

Fig. 4 Flowchart of the genetic algorithm

Termination of GA

Because the GA is a stochastic search method, it is difficult to formally specify convergence criteria. As the fitness of a population may remain static for a number of generations before a superior individual is found, the application of conventional termination criteria becomes problematic. A common practice is to terminate the GA after a pre-specified number of generations and then test the quality of the best members of the population against the problem definition. If no acceptable solutions are found, the GA may be restarted or a fresh search initiated. The flow chart of the GA optimization approach followed in the present paper is shown in Fig. 4.

5 Optimization of PID Gain Settings

Integral Square Error (ITSE) technique [22] is used for tuning optimum integral and PID gain settings. A performance index (J) is minimized using Genetic Algorithm in the presence of GRC to obtain gain values of K_{i1} and K_{i2} for integral controller, K_{p1}, K_{i1}, K_{d1} and K_{p2}, K_{i2}, K_{d2} for PID controller. Optimum values of Integral and PID controller gains of both areas are given below. Figure 5 shows the convergence of the GA with the number of generations.

$$J = \int\limits_{0}^{t} (\Delta f_1^2 + \Delta f_2^2 + \Delta P_{tie12}^2).t.dt \tag{5}$$
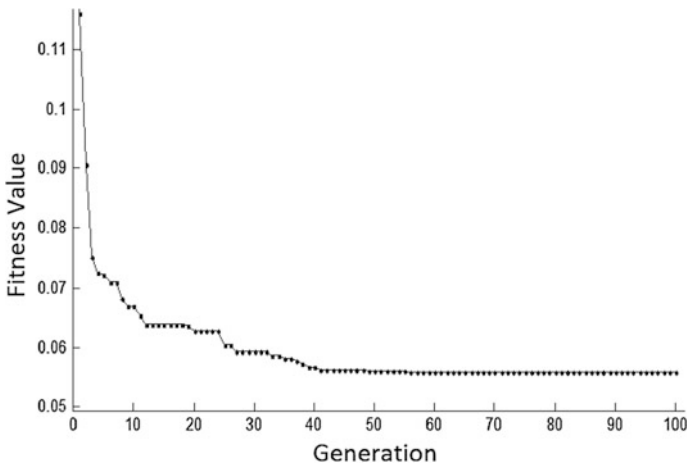

Fig. 5 Fitness value versus Generation plot for GA

Parameters for Genetic Algorithm:

Population Size: 80 Number of Iterations: 100
Selection: Roulette Wheel Crossover: Uniform Crossover
Crossover Probability Pc: 0.8 Mutation Probability Pm : 0.01
Initial Population Range: [−1; 1]

Figure 5 shows the GA convergence plot for system with CES and PID controller. It is clear from Fig. 5 that fitness value reduces as the number of generation increases and reaches a constant value once the optimum value is attained.
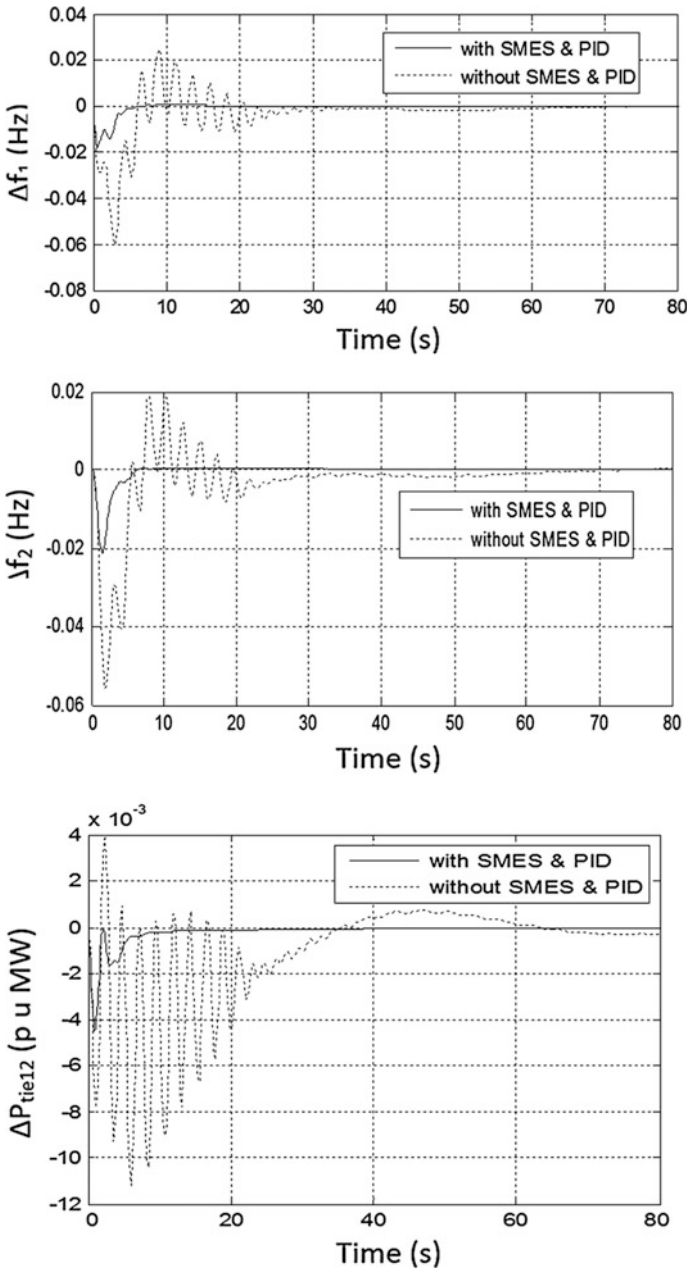
6 Dynamic Responses

With the presence pf GRCs, simulation studies are done using MATLAB/Simulink to obtain the performance of two-area multiunit hydrothermal system with and without SMES and PID controller with 1 % step load perturbation in area1. Table 1 shows the optimum values of Integral and PID gains obtained using GA technique. It is evident that there is an overall improvement in the dynamic responses with SMES and PID controller. Figure 6 shows the dynamic responses of frequency deviations and tie line power deviations for 1 % step load perturbation in area 1 with and without SMES and PID controller. From Fig. 6 it is evident that the dynamic responses have improved significantly with the use of SMES units and PID controller.

Figure 7 shows the dynamic responses of change in power generation in both the areas. Here $apf_{11} = apf_{12} = apf_{21} = apf_{22} = 0.5$ has been considered, which means all the units share the load change equally. As the load disturbance has occurred in area 1, at steady state, the power generated by generating units in area 1 are in proportion to the ACE participation factors. Therefore, as in Fig. 7, at steady state, $\Delta P_{g1ss} = \Delta P_{d1} \times apf_{11} = 0.01 \times 0.5 = 0.005$ p.u. MW and $\Delta P_{g2ss} = \Delta P_{d2} \times apf_{12} = 0.01 \times 0.5 = 0.005$ p.u. MW. Similarly $\Delta P_{g3ss} = \Delta P_{d2} \times apf_{21} = 0 \times 0.5 = 0$ p.u. MW and $\Delta P_{g4ss} = \Delta P_{d2} \times apf_{21} = 0 \times 0.5 = 0$ p.u. MW at steady state. So it is clear that ΔP_{g1} and ΔP_{g2} will settle down at 0.005 p.u MW and ΔP_{g3} and ΔP_{g4} will

Table 1 Optimum values of integral and PID gain settings

Area	With integral controller and without SMES	Optimal state feedback regulator
Thermal	$K_{i1} = 0.1877$	$K_{p1} = 01046$
		$K_{i1} = 1.3958$
		$K_{d1} = 0.0196$
Hydro	$K_{i2} = 0.2437$	$K_{p2} = 0.0663$
		$K_{i2} = -0.0488$
		$K_{d2} = -0.6042$

Fig. 6 Dynamic responses of frequency deviations and tie line power deviations for 1 % step load perturbation in area 1
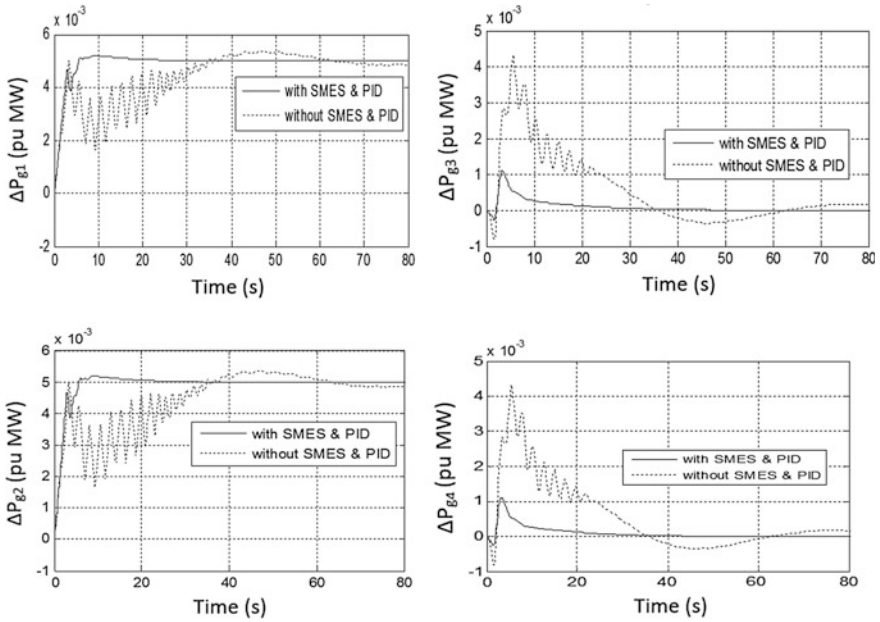
Fig. 7 Dynamic responses of change in power generation in both the areas following a 1 % step load perturbation in area

Table 2 Settling time comparison

	Settling time (s)	
	Without CES and PID controller	With CES and PID controller
Δf_1	75	45
Δf_2	75	45
ΔP_{tie12}	>100	45
ΔP_{g1}	>100	45
ΔP_{g2}	>100	48
ΔP_{g3}	>100	48
ΔP_{g4}	>100	48

settle down at 0 p.u MW. The dynamic responses of change in power generation in both the areas were also much improved.

Table 2 shows the settling time comparison for the Dynamic responses. It is clear from the table that the settling time is much reduced after the application of SMES units and PID controller.

7 Conclusion

In this work a LTI mathematical model of two area multi-unit hydro thermal power system with and without SMES and PID controllers has been studied. As per IEEE Committee report on power plant response to load change have also been considered in the simulation.

The Analysis seems to have revealed that the use of SMES and PID controller in AGC is capable of damping oscillations and also the amplitudes of the deviations in frequency and tie-line power are reduced significantly. Because of the inherent characteristics of changing loads, the operating point of a power system may change very much during a daily cycle. Thus fixed gain controllers designed at nominal operation point may fail to give better control performance over a wide range of operating conditions. Therefore the Integral and PID controller gains are optimized using genetic algorithm technique. Simulation, comparison and analysis of dynamic performances without and with SMES unit and PID controller in the presence of GRC brings out the superior performance of SMES units and PID controller in suppressing frequency and inter area tie line power deviations from their nominal values followed by a step load disturbance.

As a future work different evolutionary programming methods can be adopted for tuning of PID gains. Different methods like Particle Swarm Optimization, Ant Colony System Algorithm and Simulated Annealing can be used in power system control studies for optimization. Also the system can be simulated in Deregulated environment.

Also FACTS devices like UPFC, SSSC, TCSC, TCPS, STSTCOM etc. can be modelled and incorporated into the system for better performance.

Appendix

(A) Nomenclature

H = inertia constant (MW/sec); DPD = Incremental load change (p.u)

$D = \Delta P_d/\Delta f$ (p.u/Hz); ΔP_g = Incremental generation change (p.u)

R = Governor Speed regulation parameter. (Hz/puMW)

T_g = Steam governor time constant(s); T_t = Steam turbine time constant (s)

B = Frequency bias factor pu MW/Hz; f = Nominal system frequency (Hz)

K_{Ii} = Integral gain of PID controller in area i

K_{di} = Derivative gain of PID controller in area i

K_{pi} = Proportional gain of PID controller in area i

$B = (D + 1/R)$ (i.e. Frequency response characteristics)

ACE = Area Control Error

Δf = Incremental change in frequency (Hz)

ΔP_{tie12} = Incremental change in tie-line power (p.u MW)

T_{12} = Synchronizing coefficients; T_W = hydraulic turbine time constant (s).

$T_1 = T_2 = T_3 = T_4 = T_{R1} = T_{R2}$ = Hydraulic governor time constant.

ΔP_{g1ss}, ΔP_{g2ss}, ΔP_{g3ss} and ΔP_{g4ss}-steady state values for change in power generation of different units.

P_{d1}-step load disturbance in area1.

P_{d2}-step load disturbance in area2.

(B) System Data

$P_{R1} = P_{R2}$ = 1200 MW; $T_{P1} = T_{P2}$ = 20 s; $K_{P1} = K_{P2}$ = 120 Hz/p.u MW

$T_{R1} = T_{R2}$ = 10 s; $K_{R1} = K_{R2}$ = 0.5; $T_{TI} = T_{T2} = T_{T3} = T_{T4}$ = 0.3 s;

T_{12} = 0.0866 s

$T_{G1} = T_{G2} = T_{G3} = T_{G4}$ = 0.08 s; $R_1 = R_2 = R_3 = R_4$ = 2.4 Hz/p.u MW

$D_1 = D_2 = 8.33 \times 10\text{-}3$ p.u MW/Hz; $B_1 = B_2$ = 0.425 p.u MW/Hz

P_{d1} = 0.01 p.u MW; P_{D2} = 0 p.u MW; $T_1 = T_3$ = 41.6 s; $T_2 = T_4$ = 0.513 s;

$T_{w1} = T_{w2}$ = 1 s

(C) Superconducting Magnetic Energy Storage Data

L = 2.65 H; T_{DC} = 0.03 s; K_{ACE} = 100 kA/unit MW; K_{id} = 0.2 kV/kA;

I_{do} = 4.5 kA.

References

1. P. Kundur, Power System Stability and Control. New York: McGraw-Hill, 1994.
2. O.I. Elgerd, Electric energy system theory: An Introduction, 2007,Tata Mc-Graw hill.
3. Allen J Wood, Bruce F Wollenberg, "Power Generation Operation and Control", Wiley India Publications.
4. C. E. Fosha, O. I. Elgerd, "The megawatt-frequency control problem: A new approach via optimal control theory," IEEE Transactions on Power Apparatus and Systems, vol.PAS-89, no.4, pp.563-577, April 1970.
5. O. I. Elgerd, C. E. Fosha, "Optimum megawatt-frequency control of multiarea electric energy systems," IEEE Transactions on Power Apparatus and Systems, vol.PAS-89, no.4 pp.556-563, April 1970.
6. R. J. Abraham, D. Das, A. Patra, "Automatic generation control of an interconnected power system with capacitive energy storage," International Journal of Electrical Power and Energy Systems Engineering, vol.3, pp.41-46, 2010.
7. R. J. Abraham, D. Das, A. Patra, "Automatic generation control of an interconnected hydrothermal power system considering superconducting magnetic storage," Journal of Electrical Power and Energy Systems, vol.29, pp.571-579, 2007.
8. Y. L. Karnavas, D. P. Papadopoulos, "AGC for autonomous power system using combined intelligent techniques," Electric Power System Research, vol.62, pp.225-239, 2002.
9. C. Srinivasa Rao, S. Siva Naga Raju, P. Sangameswara Raju, "Ant colony system algorithm for automatic generation control of hydrothermal system under open market scenario," IET-UK International Conference on Information and Communication Technology in Electrical Sciences(ICTES 2007), pp.112-119, Dec 2007.
10. Ibraheem and Omveer Singh, "Hybrid GA-SA based optimal AGC of a multiarea interconnected power system," International Journal of Electrical and Power Engineering, vol.4, no.2, pp.78-84, 2010.
11. S. K. Sinha, R. N. Patel, R. Prasad, "Application of GA and PSO tuned fuzzy controller for AGC of three area thermal-thermal-hydro power system," International Journal of Computer Theory and Engineering, vol.2, no.2, pp.1793-8201, April 2010.

12. L. PinKang, Z. Hengjun, L. Yuyun, "Genetic algorithm optimization for AGC of multiarea power systems," Proceedings of IEEE TENCON, pp.1818-1821, 2002.
13. The Genetic Algorithm and Direct Search Toolbox Documentation. www.mathworks.com/access/helpdesk/help/toolbox/gads/
14. F, Verdegay J L, Genetic algorithms and soft computing, Physica-Verlag Heidelberg 1996.
15. Demiroren A, Zeynelgil H L, GA Application to optimisation of AGC in three-area power system after Deregulation, Electrical Power and Energy Systems 2007, 230-240.
16. I.J. Nagrath and D.P. Kothari, Power system engineering, Tata Mc-Graw Hill Publishing Company Limited, 1994, New Delhi (India).
17. P.F Riberiro, B K Johnson, M.L Crow, A Arsoy & Y. Liu, "Energy Storage Systems for Advanced Power Applications," IEEE Proc. C. vol 89, no 12, pp. 1744-1756, December 2001.
18. Mohd. H. Ali, B. Wu, R. A. Dougal, "An overview of SMES applications in power and energy systems," IEEE Transactions on Sustainable Energy, vol.1, no.1, April 2010, pp.38-47.
19. S. Banerjee, J. K. Chatterjee, S. C. Tripathy, "Application of magnetic energy storage unit as load-frequency stabilizer," IEEE Transactions on Energy Conversion, vol.5, no.1, March 1990, pp.46-51.
20. R. J. Abraham, D. Das, A. Patra, "Automatic generation control of an interconnected hydrothermal power system considering superconducting magnetic storage," Journal of Electrical Power and Energy Systems, vol.29, 2007, pp.571-579.
21. IEEE Committee Report: 'Dynamic models for steam and hydro turbines in power system studies', IEEE Trans. Power Appar. Syst., 1973, 92, (6), pp. 1904–1915
22. M.L. Kothari P.S. Satsangi and J. Nanda, "Automatic Generation Control of an interconnected hydrothermal system in continuous and Discrete mode considering generation rate constraints," Proc. IEE, vol. 130, 1983, pp. 17–21.
23. David E Goldberg, "Genetic Algorithms in search, optimization & machine learning", Pearson Education India, 2005.
24. Andrew Chipperfield, Peter Fleming, Hartmut Pohlheim, Carlos Fonseca; "Genetic Algorithm Toolbox for use with Matlab" Version 1.2 Users guide, Department of Automatic Control and Systems Engineering, University of Sheffield.

Linguistic Representation of Power System Signals

C. Pavlatos and V. Vita

Abstract This chapter presents an Attribute Grammar capable of modelling power system signals. Primitive pattern selection, linguistic representation, and pattern grammar formulation are the sub problems of tackled. The recognition of power system waveforms and to the measurement of its parameters is proven to easily be handled using syntactic pattern recognition techniques. Attribute grammars are used as the model for the pattern grammar because of their descriptive power, which is due to their ability to handle syntactic as well as semantic information. In order the functionality of the proposed system to be tested, a software implementation has been developed using waveforms and data provided by the Independent Power Transmission Operator (IPTO) in Greece. The proposed methodology will be applied to the implementation of an efficient protective relay that would efficiently prevent safety problems and economic losses caused by faults presented in power systems.

1 Introduction

Power systems are large and complex systems where faults frequently occur that may cause personnel and equipment safety problems, and result in substantial economic losses. An efficient protective relay would efficiently prevent these problems and losses. Microprocessor-based digital protective relays bring unquestionable improvements of the protection relays since: (i) criteria signals are

C. Pavlatos (✉)
Department of Computer Science, Hellenic Air Force Academy,
Dekelia Air Base, Tatoi 14451, Greece
e-mail: pavlatos@cslab.ece.ntua.gr

V. Vita
Department of Electrical and Electronic Engineering, School of Mathematics,
Computer Science and Engineering, City University London,
Northampton Square, London EC1V 0HB, UK
e-mail: vasiliki.vita.1@city.ac.uk

estimated in a shorter time, (ii) input signals are filtered-out more precisely, (iii) sophisticated corrections are applicable, (iv) the hardware is standardized and may communicate with other protection and control systems, and (v) relays are capable of self-monitoring. However, digital relays did not make a major break-through in power system protection as far as security, dependability and speed of operation are considered. The key reason behind this is that the principles used by digital relays blindly reproduce the criteria known for decades. In addition, prob-lems result mainly from the trade-off between the security demand (no false trip-pings), and the speed of operation and the dependability (no missing operations) requirements. The more secure is the relay (both the algorithm and its particular settings), the more it tends to misoperate or operate slowly, while the faster is the relay, the more it tends to operate falsely. There are basically two ways to mitigate the problem of limited recognition power of the classical relaying principles. One of them is to improve the recognition process itself, while the second way is to increase the performance of the implementation. Previous approaches [1] in facing the problem of improving protective relays in power systems were mainly software implementations based on artificial neural networks.

In this chapter, for the first time in the literature the recognition of power system signals is presented based on Syntactic Pattern Recognition techniques. The underlying model of implementing a system for the aforementioned application can be that of an Attribute Grammar parser. In [1] the Artificial Intelligence (AI) approaches to power system protection are reviewed and the application of artificial neural networks and fuzzy logic techniques is presented. A number of novel applications and concepts have been presented including fuzzy logic approach to differential transformer protection and artificial neural networks application to the transformer protection, CT (current transformer) and CVT (ca-pacitor voltage transformer) transients correction, and fault-type classification. However, the implementations presented are software approaches and do not achieve the maximum possible speed-up.

In [2] a real-time system implemented on an FPGA board is presented that tracks time—varying waveforms distortions in power systems based mainly on a proposed amplitude tracking algorithm derived from amplitude demodulation. However, the frequency of the fundamental signal is assumed constant but in power systems, the fundamental frequency of the current and voltage is not always exactly the nominal value.

Although the syntactic method seems suitable to the problem of protection relays and parameter measurement, not much progress has been made to date. The pro-posed project will present the application of the syntactic pattern recognition method to recognition of power systems waveforms and to the measurement of power system parameters. In syntactic pattern recognition, the task of recognition is essentially reduced to that of parsing a linguistic representation of the patterns to be recognized with a parser that utilizes a certain grammar, called pattern grammar. The pattern grammar describes the patterns to be recognized in a formal way, and the formulation of the pattern grammar is always the crucial sub problem in any pattern recognition application that is to be tackled by the syntactic approach. The

proposed project aims to give solutions to the sub problems of primitive pattern selection, linguistic representation, and pattern grammar formulation for the waveforms received by a protection relay. In the case of power systems waveforms where added morphologies can be found due to noise, and where measurements of the various parameters have to be performed, powerful grammars capable of describing syntax as well as semantics are needed as a model for the formulation of a pattern grammar. The contribution of this chapter is summarized at the following: (a) Define the linguistic representation of waveforms received by a protection relay and (b) define an attribute grammar capable of modelling the behaviour of the abovementioned linguistic representation.

The above items are novel and have not been addressed in the literature before. Our future plans is to design a hardware parser for power system signals that will be based on a proposed extension of Earley's [3] parallel parsing algorithm using the architecture proposed in [14], which given an input string, generates the parse trees in the form of an And-Or parse tree. This And-Or parse tree will be then traversed using a proposed tree traversal technique in order to execute the corresponding actions in the correct order, so as to compute the necessary attributes and define the relay's action. The proposed system will be described in Verilog hardware description language (HDL), simulated for validation, synthesized and tested on an XILINX [5] FPGA board.

2 Theoretical Background

A significant part of computer science is language theory, which copes with both theoretical and practical issues. Grammars can be found in many applications and especially Context-Free Grammars (CFG) [6] are well known for their necessity in the field of compilers and interpreters. CFGs combine expressive power and simplicity; consequently they are powerful enough to describe the syntax of programming languages (almost all programming languages are defined via CFGs) and simple enough to allow the construction of efficient parsing algorithms. Furthermore, general context-free methods and their augmentation are exploited today in various application domains.

Two well-known parsing algorithms for general CFGs are the Earley's algorithm [3] and the Cocke-Younger-Kassami (CYK) algorithm [7]. Both of them are basically dynamic programming procedures and have a time complexity $O(n^3|G|)$, where n is the length of the input string and $|G|$ is the size of the grammar. In order to increase the expression capability and usability of CFG, they may be augmented with either attributes or probabilities, forming Attribute Grammars (AG) [8] and Stochastic Context-Free Grammars (SCFG) [9] respectively. A CFG can be defined as a quadruple G = (N, T, P, S), where N is the set of non-terminal symbols, T is the set of terminal symbols, P is the set of grammar rules and S is the start symbol of the grammar. V = N ∪ T is defined as the vocabulary of the grammar. Grammar rules are written in the form B → γ, where B ∈ N and γ ∈ V*.

After the introduction of Earley's and CYK algorithms, several modifications and improvements via parallelization have been proposed for these algorithms. Chiang and Fu [10] and Cheng and Fu [11] have presented designs using VLSI (very large scale integration) arrays for the hardware implementation of the aforementioned parsing algorithms, although they do not propose an efficient implementation for the operator they use. These approaches are not implemented in reconfigurable hardware and the scale of the hardware is input string length dependent. The hardware oriented approach was reinvigorated by presenting implementations in reconfigurable FPGA boards of the CYK algorithm [12, 13]. In order to relax the hardware complexity, most of the proposed architectures implement the CYK algorithm, whose basic operations are much simpler than those of Earley's. The first FPGA implementation of Earley's algorithm was given in [14]. The approach proposed in [15] uses a combinatorial circuit for the fundamental operator of Earley's algorithm.

A CFG may be extended by associating attributes to each symbol $X \in V$. Each attribute represents a specific context-sensitive property of the corresponding symbol. The augmented CFG is called Attribute Grammar (AG) and is also defined as a quadruple AG = (G, A, SR, d), where G is a CFG, A = $\cup$ A(X) where A(X) is a finite set of attributes. The notation X.z is used to indicate that attribute z is an element of A(X). A(X) is partitioned into two disjoint sets; the set of synthesized attributes AS(X) and the set of inherited attributes AI(X). Synthesized attributes X.s are those whose values are defined in terms of attributes at descendant nodes of node X of the corresponding decorated parse tree. Inherited attributes X.i are those whose values are defined in terms of attributes at the parent and (possibly) the left sibling nodes of node X of the corresponding decorated parse tree. Finally d is a function that gives for each attribute a its domain d(a). The primary field of AG usage is in computer languages but they are also convenient in fields such as Artificial Intelligence, Pattern Recognition, or even Biomedicine. An efficient Attribute Grammar evaluator was presented in [4].

Our future goal is to design a hardware parser for power system signals on an XILINX FPGA board that will be based on a proposed extension of Earley's [3] parallel parsing algorithm, using the architecture propose on [4].

3 The Syntactic Approach in Power Systems Signals

3.1 Primitive Pattern Selection

Various segments have mainly been proposed in the past as primitive such as lines and triangles. The first are low level while the second are difficult to extract. In regards to the linguistic representation of power system signals we have chosen the peak as primitive pattern. Peaks have also been used during recognition of a considerable number of signals such as ECG (ElectroCardioGram) in [16]. This choice seems to be a natural one because power system signal are mainly
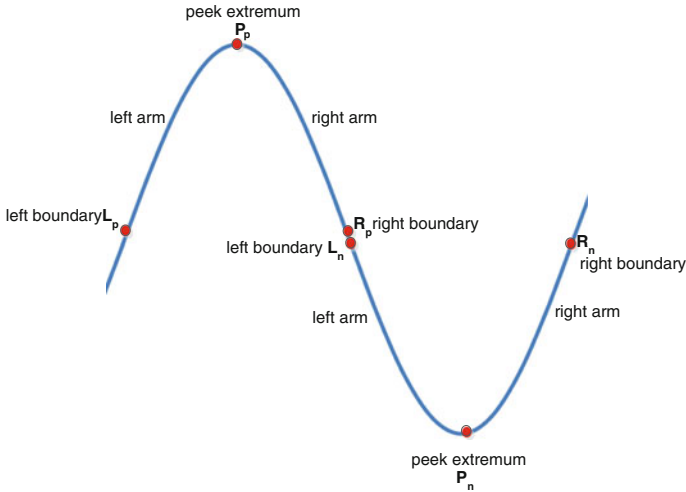
Fig. 1 Positive and negative peak patterns

sinusoidal. The peak pattern is shown in Fig. 1. This pattern is that part of a signal which is demarcated by three characteristic points. The first point is called left peak boundary, the second peak extremum, and the third right peak boundary. The sample points between the left peak boundary and the peak extremum form the left arm of the peak. The sample points between the peak extremum and the right peak boundary form the right arm of the peak. In what follows peaks will be symbolized as Π_1, Π_2,… where Π_i is the name of peak i. A peak can be other positive or negative and an index p or n is used to define if peak is positive or negative.

Each sample point of a power system signal is presented as a couple (x_i, y_i), where y_i is the amplitude in volts or amperes of the sample point i and x_i is the corresponding time. A set of attributes is assigned to each primitive pattern. The values of these attributes are calculated during the primitive extraction phase and they are utilized during the recognition process. They contribute both to the recognition of the patterns and to the measurement of their parameters. That is, they are used in a quantitative way for qualitative and quantitative purposes. A set of seven attributes is assigned to each peak Π_i. This set is symbolized as $\{x_{li}, y_{li}, x_{mi}, y_{mi}, x_{ri}, y_{li}, e_i\}$, where:

x_{li}, y_{li} is the left boundary of the peak Π_i
x_{mi}, y_{mi} is the peak extremum of the peak Π_i
x_{ri}, y_{li} is the right boundary of the peak Π_i
e_i is the energy of the peak Π_i defined as:

$$e_i = \sum_{i=p}^{q} (y_i - y_{i-1})^2 \quad where: \; p = x_{li} + 1 \; and \; q = x_{ri} \tag{1}$$

For example, the normal e i.e. e_{normal} for a sinusoidal, when frequency is equal to 50 Hz and amplitude is 230 V, is 64428.36 V^2.

3.2 Linguistic Representation

The alphabet of terminal symbols T = {p, n} has been adopted for encoding the power system waveforms, where p denotes positive peak and n a negative peak. Thus, a power system waveform is linguistically represented as a string of symbols from the set T such as *pnpnpn* or *npnpnp*. Each symbol is associated with the values of the corresponding attributes.

3.3 Pattern Grammar AG$_{PS}$

In syntactic pattern recognition, the task of recognition is essentially reduced to that of parsing a linguistic representation of the patterns to be recognized with a parser that utilizes a certain grammar, called pattern grammar. The pattern grammar describes the patterns to be recognized in a formal way, and the formulation of the pattern grammar is always the crucial sub problem in any pattern recognition application that is to be tackled by the syntactic approach. The proposed methodology aims to give solutions to the sub problems of primitive pattern selection, linguistic representation, and pattern grammar formulation for the waveforms received by a protection relay.

In the case of power systems waveforms, where added morphologies can be found due to noise, and where measurements of the various parameters have to be performed, powerful grammars capable of describing syntax as well as semantics are needed as a model for the formulation of a pattern grammar. Due to their power in describing structural and statistical features and their ability to handle syntactic and semantic information Attribute Grammars has been selected. Attribute Grammar AG$_{PS}$ presented in Table 1 is proposed for the recognition of power systems waveforms.

AG$_{PS}$ is consisted of the non-terminal symbols belonging in set N = {S, WAVE, FP, FN} where S is the start symbol; the terminal symbols belonging in set T = {n, p} where n denotes positive peak and n denotes negative peak; vocabulary of the grammar is equal to V = N ∪ T. The syntactic rules of the grammar are shown in the second column of Table 1, while the semantic rules in the third column of the same table.

Non terminal symbols p, n have the attributes presented in section "Primitive Pattern Selection", while the terminal symbols have the attributes c, s, f and: c attribute is used as a counter in order to store the number of peaks recognized till that point; s attribute is used to store the start point of the recognized substring; f attribute is used to store the last point of the recognized substring; and e attribute is used to store the sum of the energy e of peaks recognized till that point. In addition,

Table 1 Syntactic and semantic rules of AG_{PS}

Rule #	Syntactic rules	Semantic rules
1	S → WAVE	S.fr = (WAVE.c/2) * (1/(WAVE.f − WAVE.s)); S.noise = 1 − (e_{normal} * WAVE.c)/(WAVE.e)
2	WAVE → FP	WAVE.c = FP.c; WAVE.s = FP.s; WAVE.f = FP.f; WAVE.e = FP.e;
3	WAVE → FN	WAVE.c = FN.c; WAVE.s = FN.s; WAVE.f = FN.f; WAVE.e = FN.e;
4	FP → FP_1 FP_2	FP.c = FP_1.c + FP_2.c; FP.s = FP_1.s; FP.f = FP_2.f; FP.e = FP_1.e + FP_2.e
5	FN → FN_1 FN_2	FN.c = FN_1.c + FN_2.c; FN.s = FN_1.s; FN.f = FN_2.f; FN.e = FN_1.e + FN_2.e
6	FP → p	FP.c = 1; FP.s = p.xl; FP.f = p.xr; FP.e = p.e;
7	FP → p n	FP.c = 2; P.s = p.xl; P.f = n.xr; FP.e = p.e + n.e;
8	FN → n	FN.c = 1; FN.s = n.xl; FN.f = n.xr; FN.e = n.e;
9	FN → n p	FN.c = 2; FN.s = n.xl; FN.f = p.xr; FN.e = n.e + p.e;

start symbol S has two additional attributes called fr and noise so as to calculate the frequency of the recognized waveform and the ratio of the normal energy e (e_{normal}) the waveform should have over the actual energy e the waveform has. It should be noted that all attributes are synthesized.

4 An Illustrative Example

A software implementation has been developed in order the functionality of the proposed system to be tested using various waveforms and data provided by the Independent Power Transmission Operator (IPTO) [17] in Greece. Part of the data provided by IPTO is shown in Fig. 2. In this subsection, as a demonstration, a toy-scale example of the recognition of seven peaks will be presented shown in red rectangular of Fig. 2.
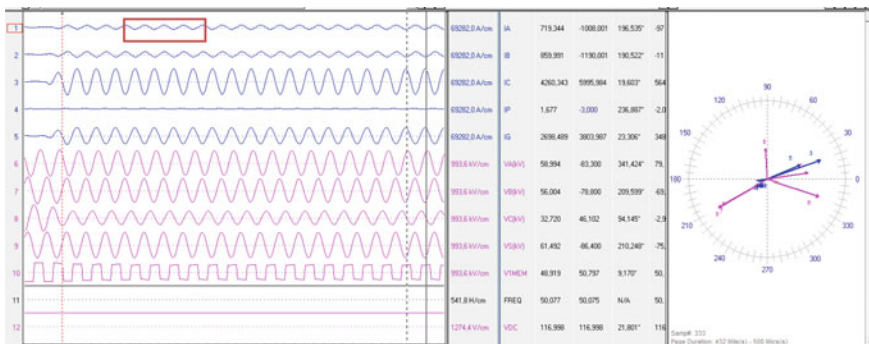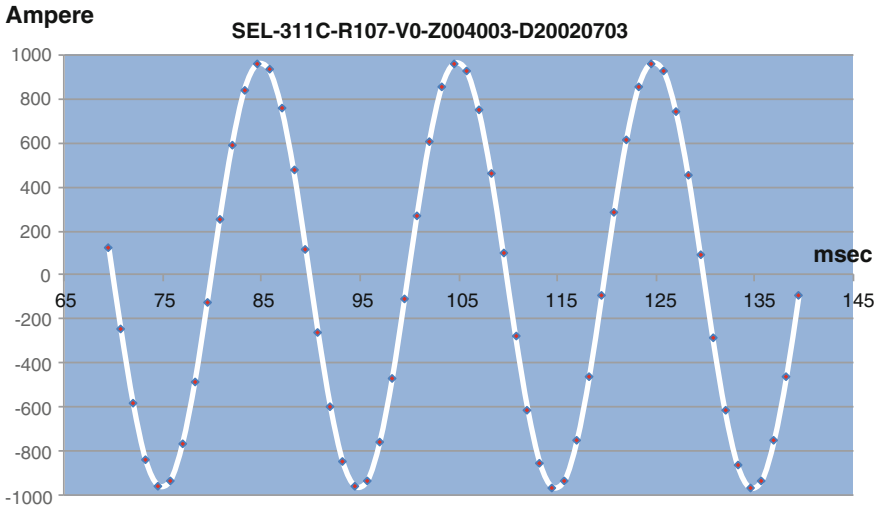

Fig. 2 Sample of data provided by IPT0

Ampere

SEL-311C-R107-V0-Z004003-D20020703

Fig. 3 Seven examined peaks of current waveform

Fig. 4 Parse tree of the input string *npnpnpn*
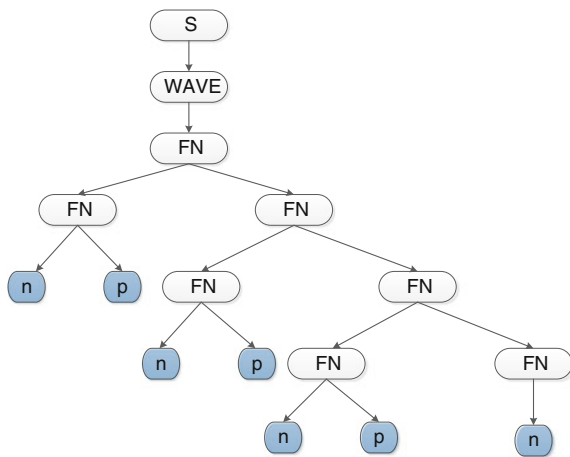
The seven peaks are part of a current waveform IA measured by IPTO in November of 2008 and presented in Fig. 3. The sampling frequency is 800 Hz; consequently, there is one sample every 0.00125 s. In this toy scale example 56 samples are presented.

After the pattern extraction, the input string to be recognized is *npnpnpn*, and the corresponding parse tree generated by the attribute evaluator is shown in Fig. 4.

Table 2 Values of peaks' attributes of input string "*npnpnpn*"

Peak #	Positive/negative	Attributes
Π_1	Negative	$x_{l1} = 69.5$ ms, $y_{l1} = 172$ A
		$x_{m1} = 74.5$ ms, $y_{m1} = -956$ A
		$x_{r1} = 79.5$ ms, $y_{r1} = -124$ A
		$e_1 = 586{,}570$ A^2
Π_2	Positive	$x_{l2} = 79.5$ ms, $y_{l2} = -124$ A
		$x_{m2} = 84.5$ ms, $y_{m2} = 956$ A
		$x_{r2} = 89.5$ ms, $y_{r2} = 114$ A
		$e_2 = 703{,}033$ A^2
Π_3	Negative	$x_{l3} = 89.5$ ms, $y_{l3} = 114$ A
		$x_{m3} = 94.5$ ms, $y_{m3} = -961$ A
		$x_{r3} = 99.5$ ms, $y_{r3} = -110$ A
		$e_3 = 707{,}473$ A^2
Π_4	Positive	$x_{l4} = 99.5$ ms, $y_{l4} = -110$ A
		$x_{m4} = 104.5$ ms, $y_{m4} = 961$ A
		$x_{r4} = 109.5$ ms, $y_{r4} = 101$ A
		$e_4 = 707{,}323$ A^2
Π_5	Negative	$x_{l5} = 109.5$ ms, $y_{l5} = 101$ A
		$x_{m5} = 114.5$ ms, $y_{m5} = -965$ A
		$x_{r5} = 119.5$ ms, $y_{r5} = -96$ A
		$e_5 = 709{,}137$ A^2
Π_6	Positive	$x_{l6} = 119.5$ ms, $y_{l6} = -96$ A
		$x_{m6} = 124.5$ ms, $y_{m6} = 962$ A
		$x_{r6} = 129.5$ ms, $y_{r6} = 92$ A
		$e_6 = 707{,}347$ A^2
Π_7	Negative	$x_{l7} = 129.5$ ms, $y_{r7} = 92$ A
		$x_{m7} = 134.5$ ms, $y_{m7} = -967$ A
		$x_{r7} = 139.5$ ms, $y_{r7} = -94$ A
		$e_7 = 708{,}622$ A^2

The values of peaks' attributes after the task of pattern extraction are shown in Table 2. For this waveform e_{normal} is equal to $658{,}000$ A^2. After the recognition process and the attribute evaluation, the frequency of the waveform i.e. the value of S.fr attribute was found really close to the frequency that IPTO has measured and was equal to 50,16 Hz and noise was found 4.63 %.

5 Conclusions and Future Work

This chapter presents an application of the syntactic pattern recognition theory to the recognition of power system signals and to the measurement of its parameters. A software implementation has been developed in order the functionality of the

proposed system to be tested using waveforms and data provided by the Independent Power Transmission Operator (IPTO) in Greece. The proposed methodology may be applied to the implementation of an efficient protective relay that would efficiently prevent safety problems and economic losses caused by faults presented in power systems. Our future plans are to design a hardware parser for power system signals that will be based on the architecture proposed in [4]. This system will be described in Verilog hardware description language (HDL), simulated for validation, synthesized and tested on an XILINX [7] FPGA board.

References

1. Saha MM, Rosolowski E, Izykowski J, Artificial Intelligent Application to Power System Protection, Proceedings of the Eleventh National Power Systems Conference (NPSC`2000), Bangalore, New Delhi, Allied Publishers 2000, 2:797-600, 2000.
2. Jinglin Xu,Uwe Meyer-Baese, Real Time Digital Signal Processing in Power Systems using FPGAs: An Analysis of Time-Varying Waveform Distortions and Power Disturbances, April 3, 2011, ISBN-13: 978-3844321722.
3. Earley J, An efficient context-free parsing algorithm, Communications of the ACM, 13(2) 94-102, 1970. doi:http://doi.acm.org/10.1147/362007.362037.
4. Dimopoulos AC, Pavlatos C, Papakonstantinou G, A platform for the automatic generation of attribute evaluation hardware systems, Computer Languages, Systems & Structures, 36 (2):203-222, 2010.
5. Xilinx Inc., www.xilinx.com.
6. Aho V, Ullman JD, The Theory of Parsing, Translation, and Compiling, Vol. I: Parsing of Series in Automatic Computation, Prentice Hall, Englewood Cliffs, New Jersey, 1972.
7. Younger DH, Recognition and parsing of context-free languages in n 3, Information and Control, 10:189-208, 1967.
8. Graham SL, Harrison MA, Ruzzo WL, An improved context-free recognizer, ACM Trans. Program. Lang. Syst., 2(3):417-462, 1980.
9. Stolcke A, An efficient probabilistic context-free parsing algorithm that computes prefix probabilities, Computational Linguistics, 21(2):167-201, 1997.
10. Chiang Y, Fu K, Parallel parsing algorithms and VLSI implementations for syntactic pattern recognition, IEEE Transactions on Pattern Analysis and Machine Intelligence, 6:302-314, 1984.
11. Cheng HD, Fu K, Algorithm partition and parallel recognition of general contextfree languages using fixed-size VLSI architecture, Pattern Recognition, 19(7):361-372, 1986.
12. Ciressan A, Sanchez E, Rajman M, Chappelier JC, An fpga-based coprocessor for the parsing of context-free grammars, Proceedings of the 2000 IEEE Symposium on Field-Programmable Custom Computing Machines (FCCM '00), IEEE Computer Society, Washington, DC, USA, pp. 236-247, 2000.
13. Bordim J, Ito Y, Nakano K, Accelerating the CKY parsing using FPGAs, IEICE Transactions Information & Systems, E-86D(7):803-810, 2003.
14. Pavlatos C, Panagopoulos I, Papakonstantinou G, A programmable pipelined coprocessor for parsing applications, in: Workshop on Application Specific Processors (WASP) CODES, Stockholm, 2004.

15. Pavlatos C, Dimopoulos AC, Koulouris A, Andronikos T, Panagopoulos I, Papakonstantinou G, Efficient reconfigurable embedded parsers, Comput. Lang. Syst. Struct., 37(2):196-217, 2009.
16. Trahanias P, Skordalakis E., Syntactic pattern recognition of the ECG. IEEE Transantions on Pattern Analysis and Machine Intelligence (PAMI), vol. 12, no. 7, July.
17. http://www.admie.gr/nc/en/home/.

Levenberg-Marquardt Algorithm Based ANN for Nodal Price Prediction in Restructured Power System

Kirti Pal, Laxmi Srivastava and Manjaree Pandit

Abstract In this chapter, a multi-layer perceptron neural network has been developed for prediction of nodal prices at various buses of power system under restructured environment. Levenberg-Marquardt algorithm has been applied to speed up the training of the multi-layer feed-forward neural network. To select the effective inputs for the Levenberg-Marquardt algorithm based artificial neural network (LMANN), an unsupervised vector quantization based clustering technique has been applied. Effectiveness of the proposed LMANN based approach for nodal price prediction has been demonstrated on benchmark 6-bus system and RTS 24-bus system. Since the training of artificial neural network is extremely fast and test results are accurate, they can be directly floated to OASIS (open access same time information system) web site. The Market Participants willing to make transactions can access this information instantly.

1 Introduction

In recent years, the electricity industry has been undergoing restructuring all over the world. A main feature of electric power industry deregulation is that the delivery of electric power (a service) must be decoupled from the purchase of the power itself (a product) and priced and contracted separately. In this price based competition, a fair, transparent and predictable transmission pricing framework of electricity is one of the major issues. The nodal price prediction based on artificial

K. Pal
Radha Govind Group of Institution, Meerut, UP, India
e-mail: kirtiglory@yahoo.co.in

L. Srivastava (✉) · M. Pandit
Madhav Institute of Technology and Science, Gwalior, MP, India
e-mail: srivastaval@hotmail.com

M. Pandit
e-mail: manjaree_p@hotmail.com

neural network (ANN) has a good potential for providing economic signals for system operation.

With the advent of Artificial Intelligence in past decade a new era has been evolved towards solving various non-linear and complicated problems of power system operation and control using various ANN models [1–4]. Reference [5] Suggested Neural Networks (NNs) and fuzzy-c-means approach to forecast locational marginal prices (LMPs), while Ref. [6] presented a wavelet transform (WT) based NN model to forecast price to improve the forecasting accuracy. Reference [7] proposed feed-forward NNs for short-term electricity prices. Fan et al. [8] proposed self organized map and support-vector machine for forecasting next-day electricity price. Reference [9] employed fuzzy inference system and least-squares estimation for short-term price forecasting in wholesale electricity markets. In Ref. [10], Georgilakis proposed the use of two ANNs: the first to predict the day-ahead load and second to forecast the day ahead market clearing price (MCP). Rodriguez [11] suggested NNs and fuzzy logic modeling for forecasting energy prices.

In Ref. [12] Bayesian framework was developed to analyze the uncertainties involved in a MCP prediction. Zhang et al. [13] applied NNs extended Kalman filter to predict market clearing price (MCP) and confidence interval in a deregulated power market. A sensitivity analysis of similar day parameters is used to increase the accuracy of NNs and to forecast hourly electricity prices [14]. The ANN based approach does not require modeling the system. During training phase, artificial neural networks learn from examples and find an appropriate mapping between inputs and the output. During testing phase, a properly trained ANN provides accurate results almost instantly, even though some incomplete information is fed to it.

Soft computing based ANN approach is significant for fast and precise prediction of nodal prices in spot power market due to its increased generalization ability in learning and inference. The application of ANNs is worth particularly where the input-output relationship is neither well defined nor easily computable. Artificial neural networks are able to approximate any nonlinear function and are data-driven. Different artificial neural network models have been proposed for solving the nodal price forecasting problem [13, 15]. In addition to this, various ANN models have been proposed for various problems of power system operation and control.

In this chapter, a multi-layer perceptron (MLP) model of neural network has been developed for prediction of nodal prices in spot power market. The MLP neural network can be trained by using any numerical optimization technique like conjugate gradient, quasi-Newton and Levenberg Marquardt algorithms [16, 17]. Levenberg Marquardt (LM) algorithm is an iterative technique that is able to locate global minimum of non-linear mathematical squared functions. Levenberg-Marquardt algorithm interpolates between Gauss-Newton algorithm and a method of gradient descent using advantage of both methods as per the situation.

LM algorithm is especially advantageous for training of the medium sized neural network. In this chapter, the MLP model has been trained using Levenberg-Marquardt algorithm. Effectiveness of the proposed LM algorithm based ANN approach has

been demonstrated on 6-bus system [18] and RTS 24-bus system [19]. For prediction of nodal prices in RTS 24-bus power system, an unsupervised vector quantization based clustering technique has been applied for feature selection so that the dimension i.e. the number of neurons, number of interconnection weights in neural network and hence the training time of ANN can be reduced [20, 21].

2 Optimal Power Flow Based Nodal Price

With the restructuring of the electric power industry, the price of electricity has become the focus of all activities in the power market. Uniform price used in conventional power system has been replaced by location-dependent marginal prices, called as nodal prices, in the emerging deregulated power market. These nodal prices are contributed by the marginal cost of generation to supply load and transmission losses and charges due to congestion at each node in the system.

The volatility of the price of electricity in a spot power market makes it necessary to facilitate the prediction of these prices accurately and instantly. Nodal price or Locational price of electricity is the combination of two components viz. locational marginal price (LMP) and nodal congestion price (NCP). LMP at a particular bus location denotes the minimal cost for supplying an additional increment of load at that bus without violating power system equality constraints. On the other hand NCP denoted the shadow prices associated with power transmission inequality constraints i.e. cost component due to congestion. This congestion component is always considered as zero at reference bus. Thus nodal or locational price depicts the optimal power dispatch with system security constraints [22]. Differences of prices between nodes reflect the costs of transmission.

In the present restructured power system scenario, nodal prices are derived using Optimal Power Flow (OPF) with objective function as minimization of total social cost (i.e. total generation cost minus total consumer benefit), subject to various constraints like power balance equation, power flow equations, supply and demand bid limits, thermal stability limits, reactive power generation limits and voltage security limits etc.

2.1 Formulation of Nodal Price

Nodal prices are the price of power, which the suppliers are paid and the price which consumers are billed. In order to compute these prices, the pool operator receives bid plots from the market participants for both the supply and the demand. Figure 1 shows bid plots for both the demand and the supply. As shown in Fig. 1, G_m and H_m are market clearing price and market clearing volume of electric power respectively in \$/MWh and in MW. The prices shown on y-axis are in \$/MWh.

Fig. 1 Supply and demand bid plots
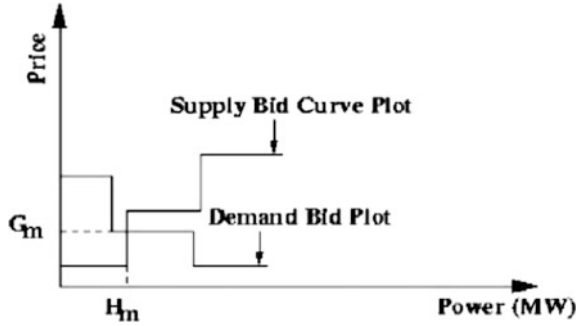
The supply bid plot shows the minimum price at which a generator is willing to produce a certain amount of power, while demand bid plot shows the maximum price that is accepted by the customers to buy a certain amount of power. For the sake of simplicity, it is assumed that the supply and demand bid is a single price not complete plot.

For a n bus system, let $P = (P_1, P_2, P_k..., P_n)$ and $Q = (Q_1, Q_2, Q_k...., Q_n)$. Here P_k and Q_k represent real and reactive power demands at bus k, respectively. Define the variables in power system operation to be $X = (x_1, ..., x_n)$, such as real and imaginary parts of each bus voltage (or voltage magnitude and its angle).

Therefore, the operation problem of a power system for the given loads (P, Q) can be formulated as an OPF problem [23–25]

$$Min f(X, P, Q) \text{ for } X \tag{1}$$

$$\text{Such that } G(X, P, Q) = 0 \tag{2}$$

$$H(X, P, Q) \leq 0 \tag{3}$$

where $G(X) = (g1(X, P, Q), ..., g_{n1}(X, P, Q))^T$ and $H(X) = (h_1(X, P, Q), ..., h_{n2}(X, P, Q))^T$ have $n1$ and $n2$ equations, respectively and are column vectors while A^T stands for the transpose of a vector A.

$f(X, P, Q)$: short-term operating cost, such as fuel cost;

$G(X, P, Q)$: vector, equality constraints, such as bus power flow balances (Kirchoff's laws);

$H(X, P, Q)$: vector, inequality constraints including limits of all variables

where $H(X, P, Q)$ includes all variable limits and function limits, such as upper and lower bounds of transmission lines, generation outputs, stability or security limits [11].

When f is a fuel cost function of the system, f can be expressed as $f(X, P, Q) = \sum_{i=1}^{n} f_i(X, P, Q)$ where f_i is the fuel cost of the ith generator. This is to be noticed that f can also be a benefit function although this paper considers f as a cost function. Certainly, Eqs. (1)–(3) form a typical OPF problem as far as the demands (P, Q) are given.

Define the Lagrangian function (or system cost) of (1)–(3) as L, then

$$L(X, \lambda, \rho, P, Q) = f(X, P, Q) + \lambda G(X, P, Q) + \rho H(X, P, Q) \tag{4}$$

where $\lambda = (\lambda_1, \ldots, \lambda_{n1})$ and $\rho = (\rho_1, \ldots, \rho_{n2})$ are the Lagrangian multipliers (or dual variables) associated to (2) and (3), respectively, and are usually explained as shadow prices from the viewpoint of economics. Hence, $\lambda G(X, P, Q) = \sum_{i=1}^{n1} \lambda_i$, $g_i(X, P, Q)$ and $\rho H(X, P, Q) = \sum_{i=1}^{n2} \rho_i, h_i(X, P, Q)$. Actually, the Lagrangian function can also be considered as an equivalent system cost. At an optimal solution (X, λ, ρ) and for a set of given load (P, Q), the nodal prices of real and reactive power for each bus are expressed below for k = 1,.., n.

$$\prod_{p,k} = \frac{\partial L(X, \lambda, \rho, P, Q)}{\partial p_k} = \frac{\partial f}{\partial_{pk}} + \lambda \frac{\partial G}{\partial_{pk}} + \rho \frac{\partial H}{\partial_{pk}} \tag{5}$$

where $\Pi_{p,k}$ are nodal prices of real power at bus k. Thus, according to (5), $\Pi_{p,k}$ the nodal price of real power at bus-k can be viewed as the system marginal cost (the sum of a marginal generation cost plus a set of premiums corresponding to their respective constraints) created by an increment of real power load at bus k. An important property for nodal prices is that each nodal price can be defined simply as a linear summation of all factors according to (5) because each nodal price, e.g., $\Pi_{p,k}$ can be rewritten as

$$\prod_{p,k} = \sum_i \frac{\partial f_i}{\partial_{p,k}} + \sum_i \lambda_i \frac{\partial g_i}{\partial_{p,k}} + \sum_i \rho_i \frac{\partial h_i}{\partial_{p,k}} \tag{6}$$

2.2 Artificial Neural Network for Nodal Price Prediction

Figure 2 shows the architecture of the proposed multi-layer feed-forward neural network trained by Levenberg-Marquardt algorithm. A large number of loading patterns were generated in wide range and for each value of total real and reactive power demand; the classical optimal power flow program was run to obtain the optimal value of nodal prices at various buses (nodes). As nodal prices are quite dependent on system's erratic loading condition, the real and reactive power load at various load (PQ) buses are considered as inputs to the LMANN for predicting the nodal prices. The non-zero real and reactive loads at various buses and the total real and reactive power demand in the power system are taken as the input variable for the proposed neural network.

Fig. 2 Neural network
architecture
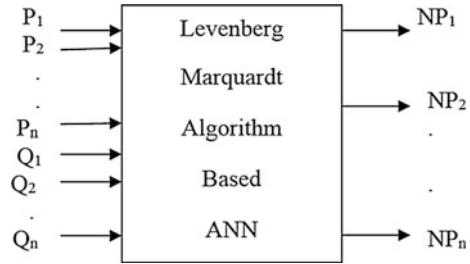
Out of all the randomly generated loading patterns, about four fifth of them are taken as training set and remaining one fifth as test set. The training and testing patterns consist of input-output pairs.

The inputs selected for the proposed artificial neural network are real and reactive loads at PQ buses (i.e. P_1, P_2,...P_n and Q_1, Q_2,...Q_n) and the outputs are the nodal prices at bus 1,2,...n. Here, n is the total number of buses. The output of the neural network provides the value of nodal price at each node of the system. In order to speed up the neural network training, Levenberg-Marquardt algorithm has been applied for the training of ANN. This algorithm has a very efficient Matlab implementation. Various architectures of LM algorithm based artificial neural network models, having different numbers of hidden layer neurons have been trained to achieve the same performance goal (mean square error). The optimal structure has been selected on the basis of the least training time taken by the LMANN. Once the LMANN is trained, its performance has been tested for the unknown testing patterns.

The Levenberg-Marquardt algorithm is a variation of Newton's method [14, 15]. This algorithm is very well suited to the artificial neural network training, where the performance index is the mean squared error. Newton's update for optimizing a performance index $F(x)$ is

$$x_{k+1} = x_k - A_k^{-1} g_k \tag{7}$$

$$\text{Where } A_k = \nabla^2 F(x)|_{x=x_k} \text{ and } g_k = \nabla F(x)|_{x=x_k} \tag{8}$$

Assuming that $F(x)$ is a sum of square function.

$$F(x) = \sum_{i=1}^{N} \in^T (x) \in (x) \tag{9}$$

Then the jth element of the gradient would be

$$[\nabla F(x)] = \frac{\partial F(x)}{\partial x_j} = 2 \sum_{i=1}^{N} \in_i (x) \frac{\partial \in_i (x)}{\partial x_j} \tag{10}$$

The gradient can therefore be written in matrix form

$$\nabla F(x) = 2J^T(x) \in (x) \tag{11}$$

Here $J(x)$ is the Jacobean matrix. The hessian matrix can be expressed in matrix form as follows:

$$\nabla^2 F(x) = 2J^T(x)J(x) + 2S(x) \tag{12}$$

where $S(x) = \sum \in_i(x)\nabla^2 \in_i (x)$

If here $S(x)$ is assumed to be small, then the hessian matrix can be approximated as

$$\nabla^2 F(x) = 2J^T(x)J(x) \tag{13}$$

Substituting (11) and (13) in (7), the Gauss-Newton method is obtained as

$$x_{k+1} = x_k - [2J^T(x_k)J(x_k)]^{-1}2J^T(x_k) \in (x_k) \tag{14}$$

$$x_{k+1} = x_k - [J^T(x_k)J(x_k)]^{-1}J^T(x_k) \in (x_k) \tag{15}$$

From this, it can be observed that the advantage of Gauss-Newton method over the standard method is that it does not require calculation of second order derivatives. One problem with the Gauss-Newton method is that the Hessian matrix $H = J^T J$ sometimes may not be invertible. This can be overcome by approaching the following modification to the Hessian matrix

$$G = H + \mu I \tag{16}$$

To make this matrix invertible, suppose that the Eigen values and Eigen vectors of Hessian matrix H are $\{\lambda_1, \lambda_2, ..., \lambda_n\}$ and $\{z_1, z_2, ..., z_n\}$. Then

$$G_{zi} = [H + \mu I]z_i = (\lambda_i + \mu)z_i$$

Therefore the Eigen vectors of G are the same as Eigen vectors of H and the Eigen values of G are $(\lambda_i + \mu)$. G can be made positive definite by increasing μ until $(\lambda_i + \mu) > 0$ for all i, and then the matrix will be invertible. This modification leads to the Levenberg-Marquardt algorithm [15].

$$x_{k+1} = x_k - [J^T(x_k)J(x_k) + \mu_k I]^{-1}J^T(x_k) \in (x_k)$$

or

$$\nabla x_k = -[J^T(x_k)J(x_k) + \mu_k I]^{-1}J^T(x_k) \in (x_k) \tag{17}$$

A useful feature of this algorithm is that as µk is increased it approaches the steepest descent algorithm with small learning rate

$$x_{k+1} \cong x_k - \frac{1}{\mu_k} J^T(x_k) \in (x_k) \tag{18}$$

$$\cong x_k - \frac{1}{2\mu_k} \nabla F(x) \text{ for large } \mu_k \tag{19}$$

And if μ_k is decreased to zero the algorithm becomes Gauss-Newton. The algorithm begins with μ_k set to some small value like $\mu_k = 0.01$ or so.

2.3   *Vector Quantization Clustering Technique*

Clustering methods are a part of pattern recognition methods. They provide a popular approach to unsupervised classification in which the pattern is assigned to a hitherto unknown class. In the pattern recognition literature, different types of clustering algorithms, such as self-organizing maps (SOMs), hierarchical clustering (HC), Vector quantization clustering technique etc., can be found, each having its own advantages and limitations. In this study, the Vector quantization clustering algorithm was selected, and it is briefly summarized here. In vector quantization clustering [20], the first vector from input patterns creates a starting cluster. Subsequent clusters are formed on the basis of Euclidean distance between input vectors and existing cluster centers.

Euclidean distance between input vector and any allocated cluster center is calculated as:

$$d = \left\| a^p - K_j \right\| = \left[\sum_{i=1}^{n} \left(a_i^p - K_j \right)^2 \right]^{1/2} \tag{20}$$

where a^p is pth input vector of ith input pattern, K_j is jth cluster and d is Euclidean distance. If the Euclidean distance of any input vector a^p from cluster K_c is less than the Euclidean distance of a^p from cluster K_j, then K_c is selected as closest cluster to the input vector a^p. The cluster K_c can be selected as closest cluster using (21)

$$\left\| a^p - K_c \right\| < \left\| a^p - K_j \right\| \{ j = 1...M, j \neq C \tag{21}$$

where M is the number of allocated clusters. Once the closest cluster K_c for the input vector a^p has been determined, the distance $\left\| a^p - K_c \right\|$ must be tested against a pre-specified threshold distance σ, such as:

If $\left\| a^p - K_c \right\| < \sigma$, the pth input vector is assigned to cth cluster i.e. K_c. Otherwise if $\left\| a^p - K_c \right\| > \sigma$, then a new cluster is allocated to pth input vector. Every time the

closest cluster center selected on the basis of comparison with threshold σ is updated as:

$$K_a = \frac{1}{n} \sum_{X \in S_n} a \qquad (22)$$

where S_n denotes the set of input vectors, 'a' denotes an input vector and n is number of input vectors in a cluster. The process of finding closest cluster is repeated for all the system variables $S_j\{j = 1,2,3,...n\}$.

3   Development of LMANN for Nodal Price Prediction

Neural Network models are the trainable analytic tools that attempt to mimic the information-processing pattern in human brain [17]. It performs desired job after training or learning. Training of a neural network is a slow intelligent process. To speed up its training, optimization is required at various steps i.e. in deciding neural network architecture, the number and type of training/testing patterns, the learning rate, and number of neurons in hidden layer [14].

3.1   Methodology Used for Training an ANN

The schematic block diagram of the work carried out in this chapter is given in Fig. 3. A large number of patterns are generated by perturbing the load randomly at each bus in a wide range. With the help of a classical optimal power flow method, nodal prices are computed at all the buses of a power system. The nodal price (NP) values obtained with an OPF solution method are heterogeneous in nature, i.e. fall in a wide range. To obtain better prediction accuracy of ANN, the whole database comprising NPs values at all the buses of the large size power system (RTS 24-Bus test system) has been divided into various data clusters (price zones), as can be seen from Fig. 3. Vector quantization clustering technique [20, 21] is used in this chapter for grouping similar NP values in one cluster. Separate ANNs have been developed for each cluster (price zone).

The training and testing patterns consist of input and output pairs. The ANN developed in this chapter for providing NPs has real and reactive power demand at PQ buses as its input, while Nodal Prices at each node are the required output of the neural network. The proposed network has single hidden layer. The optimum number of hidden layer neurons is selected on the basis of various trials. The neural network requiring least training time to achieve the same error goal has been considered as the most efficient one.
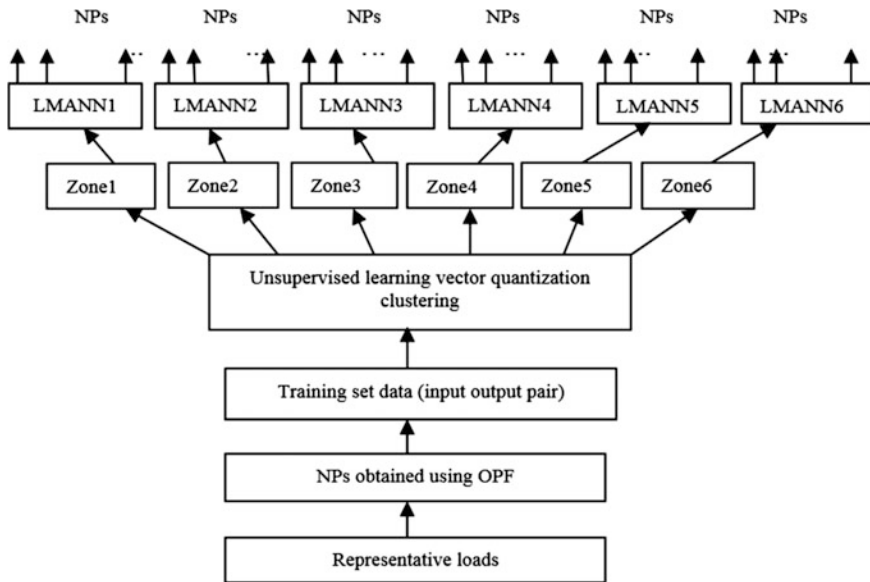
Fig. 3 Schematic block diagram for nodal price prediction

For 6-bus test system, the non-zero real and reactive loads at various buses has been taken as input in addition to the total real and reactive power loads to the proposed LMANN, while Nodal Prices at all the 6 buses are the outputs of the developed LMANN. As this is small size power system, the clustering for its partitioning into various price zones has not been carried out in this test system.

3.2 Feature Selection

Feature selection is an effective data reduction technique for handling the problem of high dimensionality. In this chapter, vector quantization based clustering algorithm [30] as discussed in Sect. 2.3, has been applied for selecting input features from the non-zero real and reactive loads at all the buses of the 24-bus test power system. An unsupervised learning has been used to discover similarities among the large number of variables and to group the total 'Y' system variables (S1, S2,......., SY) into 'Z' clusters such that the variables in a cluster are having similar characteristics. Thus, the number of variables will be reduced from 'Y' to 'Z' (Z < Y). Clustering of the variables is performed on the basis of Euclidean distance between them and a threshold called vigilance parameter ρ. First, the N dimensional system variable S1 is selected as the center of the first cluster. The next system variable is compared to the first cluster center. If its Euclidean distance from the first cluster center is smaller than the pre-specified vigilance parameter, it is included in the first

cluster. Otherwise, it will be considered as the center of a new cluster. This process is repeated for all the system variables S_j. Once all the system variables are considered, the algorithm is re-iterated until stable clusters are formed. The variable nearest to the cluster center in a group is selected as the representative variable for that cluster. These representative variables are used as input features for the proposed ANN.

4   Results and Discussion

For the prediction of Nodal Prices in real-time spot power market, the continuously varying load condition has been taken as input to the proposed ANN. To experience such a realistic power system of varying loading condition, 300 load patterns have been created by randomly perturbing the load at each bus in a wide range (±30 % of base case load). Out of these, 240 patterns have been used for training and the remaining 60 patterns have been used for testing of the proposed LM based ANN model. For each pattern, NPs values are obtained by running OPF program. All the programming modules have been developed in Matlab.

Due to dynamic uncertainties under deregulated power market scenario, the NPs are highly volatile and mainly dependent on system loading conditions. To consider this fact into account, the real and reactive loads at all the buses of the system are considered as input variables for LMANN to be developed. During training it is found that number of hidden nodes has affected the convergence rate by increasing or decreasing the complexity of the neural network architecture. Hence hidden nodes are selected in the present work by having several trials. Proposed methodology for Nodal Price prediction in deregulated spot power market has been demonstrated on two sample power systems; a 6- bus system and RTS 24-bus test system.

4.1   6-Bus Power System

6-bus test system [18] comprises of 3 generating units and 3 loads. Real and reactive power at each of the 3 load buses and total real and reactive power demand has been taken as input to the proposed LMANN, while Nodal Prices at all the 6 buses are the output of the developed LMANN. Optimal ANN architecture as obtained after several trials during training is (8-9-6). During testing phase the trained MLP model provided RMS error of 0.06192 p.u. and maximum percentage error as 1.54046.

Although the trained LMANN (8-9-6) has provided the accurate results for all the 60 testing patterns, testing results for only ten testing patterns are given in Table 1. This Table shows the target (NPs values computed by classical OPF

Table 1 Testing performance of ANN for 6-bus power system

TP	Method	NP_1	NP_2	NP_3	NP_4	NP_5	NP_6
1	Classical	8.800	8.800	8.963	9.319	9.411	9.247
	By LMANN	8.793	8.793	8.961	9.325	9.428	9.250
	Per. Error	0.134	0.079	0.017	0.070	0.185	0.030
2	Classical	8.800	8.800	8.964	9.320	9.413	9.249
	By LMANN	8.822	8.822	8.970	9.345	9.414	9.260
	Per. Error	0.015	0.250	0.068	0.271	0.015	0.119
3	Classical	8.800	8.800	8.970	9.328	9.422	9.256
	By LMANN	8.873	8.873	9.057	9.415	9.519	9.347
	Per. Error	0.943	0.830	0.971	0.931	1.030	0.985
4	Classical	8.800	8.800	8.976	9.336	9.434	9.264
	By LMANN	8.851	8.851	9.023	9.383	9.478	9.311
	Per Error	0.440	0.577	0.523	0.505	0.462	0.507
5	Classical	8.800	8.800	8.973	9.332	9.428	9.261
	By LMANN	8.885	8.885	9.070	9.430	9.535	9.362
	Per. Error	1.061	0.961	1.085	1.054	1.131	1.086
6	Classical	8.800	8.800	8.978	9.339	9.437	9.267
	By LMANN	8.883	8.883	9.062	9.422	9.519	9.352
	Per. Error	0.844	0.941	0.936	0.890	0.865	0.921
7	Classical	8.952	8.952	9.134	9.508	9.607	9.428
	By LMANN	8.909	8.909	9.086	9.457	9.548	9.378
	Per. Error	0.600	0.480	0.523	0.533	0.617	0.526
8	Classical	8.950	8.950	9.133	9.504	9.604	9.428
	By LMANN	8.921	8.921	9.104	9.485	9.579	9.401
	Per. Error	0.218	0.324	0.323	0.198	0.258	0.287
9	Classical	8.956	8.956	9.135	9.514	9.613	9.428
	By LMANN	8.909	8.909	9.086	9.457	9.548	9.378
	Per. Error	0.656	0.524	0.534	0.595	0.679	0.526
10	Classical	6.885	6.885	7.000	7.244	7.309	7.204
	By LMANN	6.881	6.881	7.008	7.254	7.331	7.211
	Per. Error	0.323	0.064	0.120	0.137	0.300	0.094

TP Testing Pattern, *Per. Error* Percentage Error, *Classical* Classical OPF

method) and actual NPs values (NPs predicted by developed LMANN) with percentage error during testing. NP1 is the nodal price at bus number 1 and so on.

The actual and target outputs for all the 60 testing patterns are shown in Figs. 4, 5, 6, 7, 8 and 9. It can be seen from these Figures, the Nodal Prices predicted by the trained LM based ANN closely follow the nodal prices as obtained by the conventional OPF method.

Figure 10 shown the plot of percentage testing error obtained during prediction of nodal prices at all the six buses, for all the 60 testing patterns. It can be observed
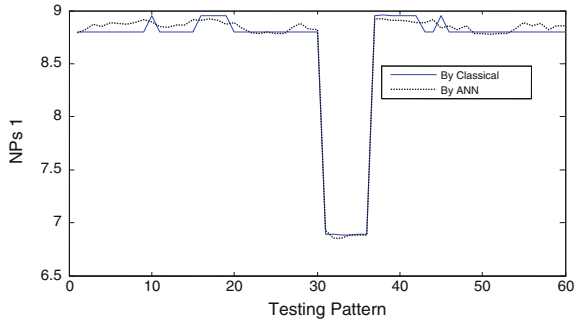
Fig. 4 Nodal price at bus1
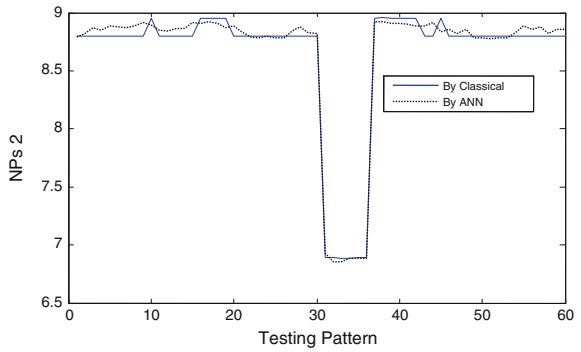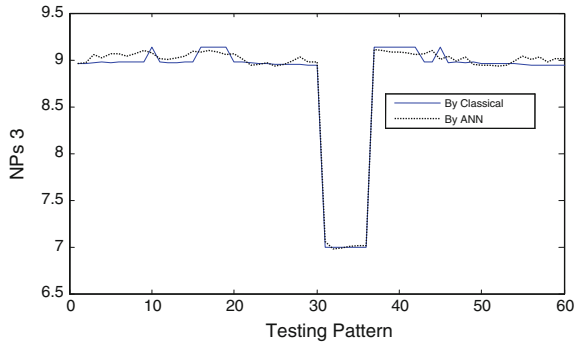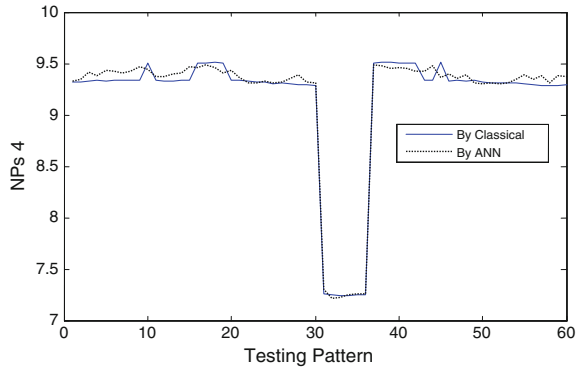

Fig. 5 Nodal price at bus2
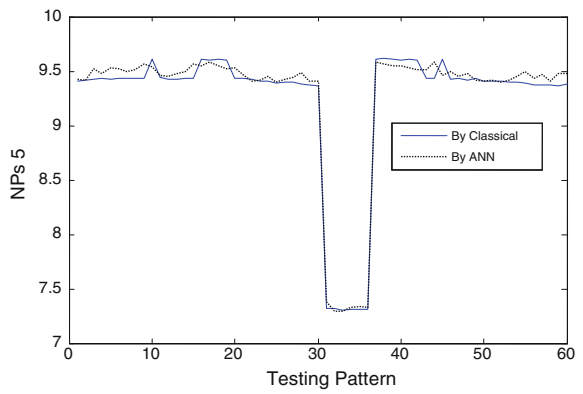

Fig. 6 Nodal price at bus3

from Fig. 10, that the maximum error for predicting NPs obtained by developed LMANN for six nodes are 1.527 %, 1.33 %, 1.398 %, 1.513 %, 1.54 % and 1.445 % respectively.
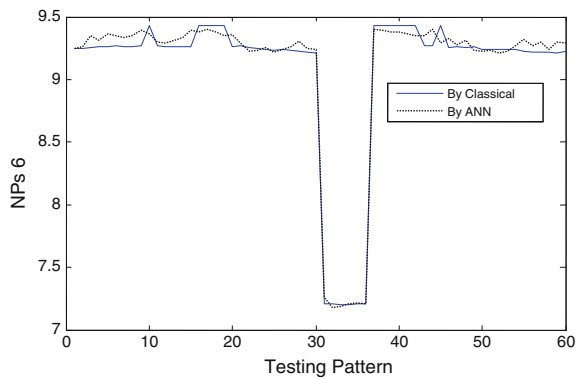
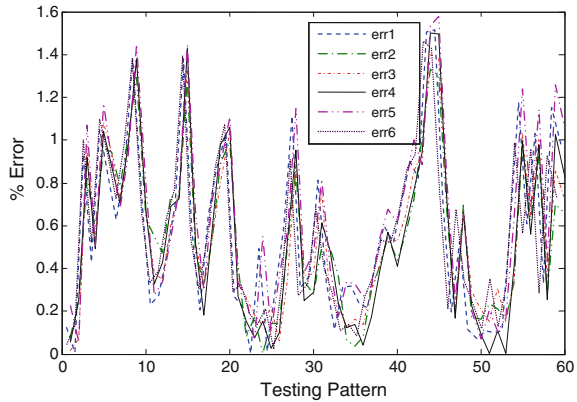**Fig. 7** Nodal price at bus4

Fig. 8 Nodal price at bus5

Fig. 9 Nodal price at bus6

Fig. 10 Plot of percentage
testing errors obtained by
ANN

4.2 RTS 24-Bus System

To establish the effectiveness of proposed neural network for predicting nodal
prices, the neural network model has been trained for 24-bus Reliability Test
System [19] comprises of total 32 generating units connected at 11 buses, 38
transmission lines and 5 transformers (132 kV/230 kV). The system is having
4783.7133 MW as a total transaction level and Independent Market Operator pays
40108.5736 $/h for this total transaction. In RTS 24-bus system, loads are con-
nected at 17 buses. Thus, this system comprises of total 34 number of non-zero real
and reactive loads (17 real power loads and 17 reactive power loads). As many as
300 load patterns were generated by varying load at each bus of the power system
randomly in a wide range (±30 % of base case).

The conventional OPF based method is applied for each load pattern to obtain
nodal prices for each node. Out of these 300 patterns, 240 patterns have been used
for training of the ANN, while the remaining 60 patterns have been used to test the
performance of the trained ANN. For reducing the size of the proposed ANN,
vector quantization based clustering was also employed in input data of dimension
34 to select representative input vectors from various clusters. Consequently by
having a threshold value of, $\rho = 0.128$, 11 clusters were formed. The 11 selected
input vectors are real loads at bus number 5, 9, 10, 13, 15, 16, 18 and 20 and
reactive loads at bus number 1, 3 and 13. Thus input dimension was reduced from
34 to 11. In addition to these 11 features, total real and reactive loads are also
considered as inputs to the LMANNs, thus making the total number of inputs as 13.

The number of outputs in this case is 24, which vary in wide range, so one ANN
was not able to estimate nodal price for all the 24 buses accurately. Hence the
division of power system (24 buses) into various price zones having different price
levels was carried out using vector quantization technique such that in each zone
nodal prices lie in a closed range. For each price zone a separate LMANN was
developed, so that fast and accurate prediction of nodal prices could be achieved.

Using an unsupervised vector quantization clustering, with the threshold value of, ρ = 0.283, the 24-bus system has been divided into six zones. A total of 6 LMANNs were developed for nodal price prediction in these 6 price zones. Optimal architectures for the 6 LMANNs developed for nodal price prediction in 6 zones were obtained after several trials during training and found to be as (13-11-7), (13-5-4), (13-19-7), (13-14-2), (13-12-3) and (13-10-1) respectively. The division of 24-bus power system with range of nodal prices in each zone is given in Table 2. The testing performance of all the 6 LMANNs developed for nodal price prediction of 6 clusters (price zones) have also been summarized in Table 2. Table 2 shows that zone 6 is comprising of lowest NP range, hence supposed to be the most suitable zone for making transactions. For each price zone an individual LMANN has been developed for predicting NPs within that price zone. Maximum percentage error and per unit rms error for all the six price zones are also indicated in Table 2. These results show the well acceptable performance of the developed LMANNs for Nodal Price prediction.

The performance of LMANN in terms of nodal prices computed by classical OPF method and those predicted by LM based ANN along with percentage testing error at each bus for zone 3 where prices are in higher range and for zones 4, 5, 6 where prices are in lower range are shown in Tables 3 and 4 respectively. Negative NP values as can be seen in Table 4, shows the reward for not creating congestion in any of the line terminating at this bus, while positive NP values indicate the penalty on the buses, which are creating congestion in the lines connected at those buses. Thus NP prediction is an effective way of finding congestion management through imposing penalty and rewards on electricity consumers.

However, plots of percentage testing errors obtained during prediction of NPs for all the six zones, for all the 60 testing patterns are shown in Figs. 11, 12, 13, 14, 15 and 16. These figures clearly depict the maximum and minimum percentage error obtained during testing at each node of each zone.

Table 2 Partitioning of IEEE RTS 24-bus system into various price zones

Zones	No. of buses	Bus numbers	NPs range ($/MWh)	Max. per error (%)	Max. RMS error (p.u.)
1	7	1, 2, 7, 12 13, 16, and 24	38.2790 to 29.6030	2.1813	0.2997
2	4	3, 4, 5 and 20	53.1250 to 43.0700	2.1848	0.3736
3	7	6, 8, 9, 10, 11, 14 and 19	65.4970 to 52.8740	2.3396	0.4979
4	2	15 and 17	22.9810 to 14.4190	2.875	0.2008
5	3	18, 21 and 22	13.2310 to 6.5070	2.6019	0.0874
6	1	23	1.6930 to −2.2660	2.7692	0.0178

Table 3 Testing performance of ANN for 6-bus power system

TP	Method	NP₁	NP₂	NP₃	NP₄	NP₅	NP₆	NP₆
1	Classical	54.661	54.661	58.222	62.966	56.414	58.411	53.534
	By LMANN	55.585	55.585	59.201	63.409	57.073	59.184	54.103
	Per. Error	−1.694	−1.691	−1.681	−0.703	−1.167	−1.323	−1.063
2	Classical	55.167	55.167	58.832	63.542	56.989	59.118	53.961
	By LMANN	56.017	56.017	59.549	63.951	57.453	59.489	54.085
	Per. Error	−1.668	−1.540	−1.218	−0.644	−0.814	−0.628	−0.230
3	Classical	55.179	55.179	58.840	63.562	56.982	59.098	53.939
	By LMANN	56.017	56.017	59.549	63.951	57.453	59.489	54.085
	Per. Error	−1.622	−1.518	−1.204	−0.612	−0.826	−0.662	−0.271
4	Classical	55.179	55.179	58.840	63.562	56.982	59.098	53.939
	By LMANN	56.047	56.047	59.638	64.041	57.431	59.594	54.060
	Per Error	−1.916	−1.573	−1.356	−0.753	−0.788	−0.839	−0.224
5	Classical	55.171	55.171	58.835	63.550	56.986	59.109	53.951
	By LMANN	55.528	55.528	59.038	63.421	57.021	58.912	53.956
	Per. Error	−0.459	−0.647	−0.345	0.202	−0.062	0.333	−0.009
6	Classical	57.021	57.021	60.458	65.487	58.244	60.399	54.548
	By LMANN	56.596	56.595	59.966	64.528	57.881	59.614	54.086
	Per. Error	0.652	0.747	0.813	1.464	0.624	1.300	0.847
7	Classical	57.029	57.029	60.466	65.497	58.248	60.400	54.546
	By LMANN	56.353	56.353	59.764	64.455	57.722	59.469	54.085
	Per. Error	1.220	1.186	1.161	1.592	0.902	1.541	0.845
8	Classical	56.290	56.290	59.730	64.692	57.747	57.649	54.224
	By LMANN	56.111	56.111	59.617	64.160	57.554	59.483	53.962
	Per. Error	0.145	0.318	0.189	0.823	0.164	0.442	0.484
9	Classical	56.912	56.912	60.354	65.377	58.150	60.287	54.479
	By LMANN	56.759	56.759	60.174	64.863	58.123	59.730	54.188
	Per. Error	0.139	0.268	0.299	0.786	0.047	0.924	0.534
10	Classical	57.022	57.022	60.459	65.488	58.245	60.399	54.548
	By LMANN	56.208	56.208	59.679	64.307	57.724	59.327	54.036
	Per. Error	1.304	1.427	1.291	1.804	0.895	1.776	0.939

Table 4 Testing performance of LMANN for cluster 4, 5 and 6

| TP	Method	Cluster 4		Cluster 5			Cluster 6
		NP$_1$	NP$_2$	NP$_1$	NP$_2$	NP$_3$	NP$_1$
1	Classical	22.240	15.202	12.739	10.435	7.308	−1.578
	By LMANN	22.345	14.980	12.761	10.423	7.185	−1.578
	Per. Error	−0.474	1.460	0.172	0.116	1.682	0.0211
2	Classical	22.445	14.954	12.728	10.424	7.305	−1.602
	By LMANN	22.491	15.357	12.757	10.427	7.219	−1.602
	Per. Error	−0.206	−2.696	0.227	0.032	1.184	−0.000
3	Classical	22.422	14.928	12.732	10.428	7.305	−1.593
	By LMANN	22.491	15.357	12.775	10.462	7.304	−1.593
	Per. Error	−0.309	−2.875	0.335	0.328	0.011	0.000
4	Classical	22.422	14.928	12.724	10.420	7.304	−1.586
	By LMANN	22.425	15.236	12.602	10.251	7.341	−1.579
	Per Error	−0.015	−2.060	0.962	1.620	−0.507	0.420
5	Classical	22.435	14.943	12.627	10.229	6.867	−1.580
	By LMANN	22.181	15.057	12.602	10.251	7.041	−1.578
	Per. Error	1.131	−0.761	0.201	0.217	2.533	0.105
6	Classical	22.223	15.189	12.461	10.025	6.619	−1.592
	By LMANN	22.214	15.012	12.390	9.978	6.654	0.001
	Per. Error	0.040	1.164	0.567	0.466	0.527	0.0628
7	Classical	22.458	14.968	12.437	9.994	6.582	0.938
	By LMANN	22.410	15.068	12.390	9.978	6.654	0.940
	Per. Error	0.214	0.670	0.375	0.157	1.093	0.213
8	Classical	22.492	15.007	12.437	9.995	6.583	0.934
	By LMANN	22.324	15.020	12.321	9.895	6.551	0.942
	Per. Error	0.746	0.089	0.935	1.002	0.486	0.829
9	Classical	22.565	15.091	12.597	10.299	7.259	0.934
	By LMANN	22.432	15.139	12.678	10.341	7.155	0.932
	Per. Error	0.590	0.315	0.645	0.409	1.430	0.000
10	Classical	22.546	15.069	12.422	9.976	6.559	0.944
	By LMANN	22.458	15.194	12.390	9.978	6.654	0.942
	Per. Error	0.392	0.827	0.254	0.023	1.447	0.238

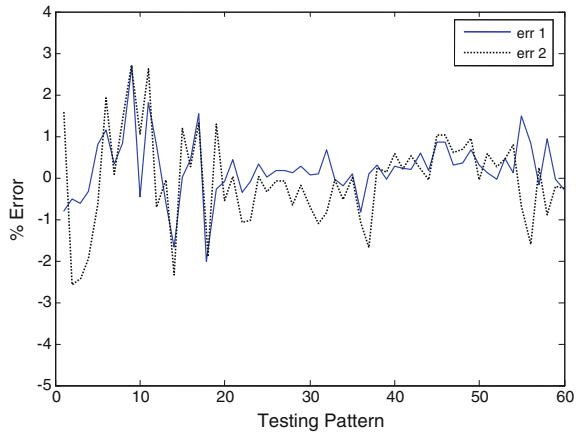**Fig. 11** Plot of percentage error for cluster 1
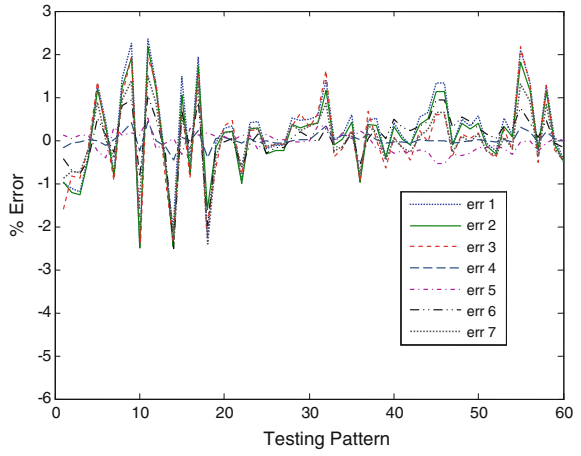
Fig. 12 Plot of percentage error for cluster 2
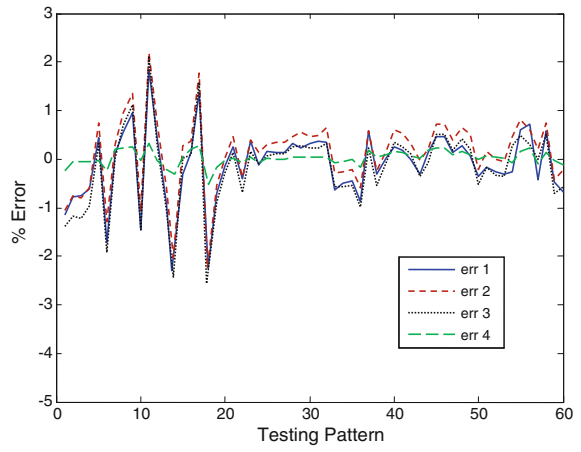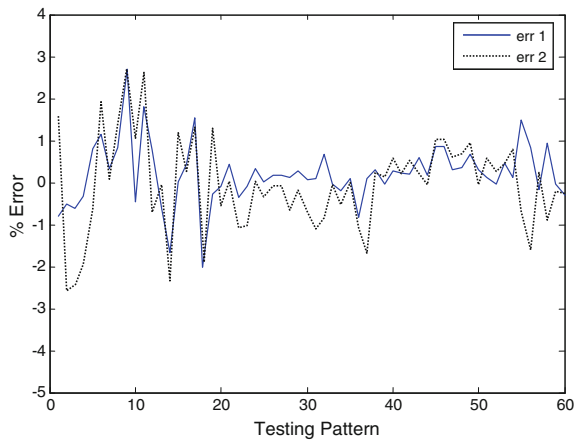

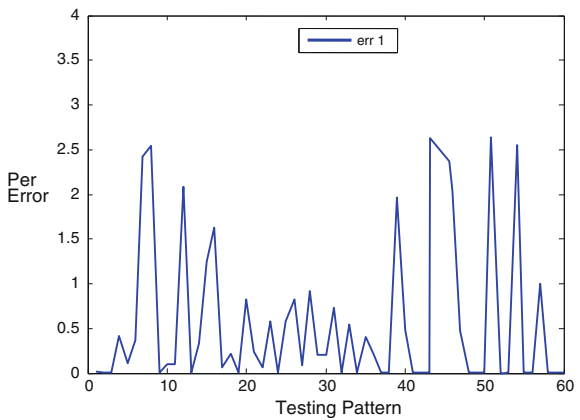**Fig. 13** Plot of percentage error for cluster 3
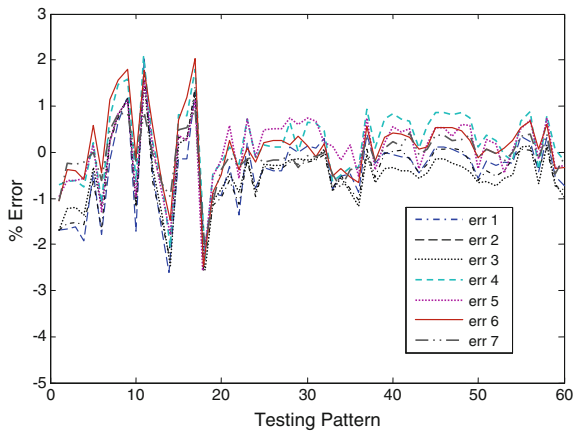
Fig. 14 Plot of percentage error for cluster 4

Fig. 15 Plot of percentage error for cluster 5

Fig. 16 Plot of percentage error for cluster 6

5   Conclusion

In this chapter, an artificial neural network based approach for prediction of nodal prices at each bus of power system under restructured environment has been presented. Levenberg-Marquardt algorithm has been applied to speed up the training of the multi-layer feed-forward neural network.

During testing phase, the trained neural network furnished results within acceptable accuracy limits for previously unseen load patterns almost instantaneously. Since the training of the ANN using LM algorithm is quite fast, these results can be directly floated to Open Access Same-Time Information System (OASIS) web-site, to be assessed by market participants before trading their required transactions.

As nodal prices provide the appropriate economic signals location-wise to the market participants, this LMANN based technique can be proved to be of great importance in enhancing the theme of spot power market. The aim of providing nodal prices directly online using artificial neural network approach is, to provide a platform for the market participants to improve their bidding strategies so that in the time-ahead market, their transaction can be fulfilled. This may be useful for motivating them for managing congestion by rescheduling their transactions. This will certainly improve the power system security and reliability in the Deregulated Power Market scenario.

References

1. Yuan-Kang Wu, Comparison of Pricing Schemes of Several Deregulated Electricity Markets in The World, IEEE/PES, Transmission and Distribution Conference and Exhibition: Asia and Pacific (2005) 1-6.
2. M. Pandit, L. Srivastava and J. Sharma, Voltage Security Assessment Employing Coherency Based Feature Selection for Neural Network, 14 (1) (2006) 25-37.
3. K.T. Chaturvedi, L. Srivastava and M. Pandit, Levenberg Merquardt Algorithm Based Economic Load Dispatch, Presented in 2006 IEEE Power India Conference, held at New Delhi (2006).
4. S. N. Pandey, S. Tapaswi, and L. Srivastava, Nodal congestion price estimation in spot power market using artificial neural network, IET Gener. Transm. and distrib., 1 (2008) 280-290.
5. Y. Y. Hong, C. Y. Hsiao, C.Y., Locational Marginal Price Forecasting in Deregulated Electricity Markets Using Artificial Intelligence, IEE Proc.-Generation, Transmission and Distribution, 149 (5) (2002) 621-626.
6. S. Aggarwal, L. Saini, Ashwani Kumar, Electricity Price Forecasting in Ontario Electricity Market Using Wavelet Transform in Artificial Neural Network Based Model, International Journal of Control, Automation, and Systems, 6 (5) (2008) 639-650.
7. J. P. S. Catalao, S. J. P. S. Mariano, V. M. F. Mendesb, and L. A. F. M. Ferreira, Short-Term Electricity Prices Forecasting in a Competitive Market: A Neural Network Approach, Electric Power Systems Research, 77 (2007) 1297–1304.
8. S. Fan, S., C. Mao, C. and L. Chen, Next-Day Electricity Price Forecasting Using a Hybrid Network, IET Generation, Transmission and Distribution, 1 (1) (2007) 176-182.

9. G. Li, C. C. Liu, C. Mattson, and J. Lawarrée, Day- Ahead Electricity Price Forecasting in a Grid Environment, IEEE Transactions on Power Systems, 22 (1) (2007) 266–274.
10. P. S. Georgilakis, Artificial Intelligence Solution to Electricity Price Forecasting Problem, Journal of Applied Artificial Intelligence,21 (8) (2007) 707-727.
11. C. P. Rodriguez, and G. J. Anders, Energy Price Forecasting in The Ontario Competitive Power System Market, IEEE Transactions on Power Systems,19 (1) (2004) 366–374.
12. L. Zhang, P. B. Luh and K. Kasiviswanathan, Energy Clearing Price Prediction and Confidence Interval Estimation With Cascaded Neural Networks, IEEE Power Engineering Review, 22 (12) (2002) 1-60.
13. L. Zhang, and P. B. Luh, Neural Network-Based Market Clearing Price Prediction and Confidence Interval Estimation With an Improved Extended Kalman Filter Method, IEEE Transactions on Power Systems, 20 (1) (2005) 59–66.
14. P. Mandal, A. K. Srivastava, and J. W. Park, An Effort to Optimize Similar Days Parameters for ANN-Based Electricity Price Forecasting, IEEE Transactions on Industry Applications, 45 (5) (2009) 1888–1896.
15. Y.Y. Hong, C. F. Lee, A Neuro Fuzzy Price Forecasting Approach in Deregulated Electricity Markets, Electrical Power and Energy System, 73 (2) (2005) 151-157.
16. M.T. Hagan and M.H. Mehnaj, Training Feed Forward Neural Networks with Marquardt Algorithm, IEEE Transaction on Neural Network, 5 (6) (1994) 989-993.
17. L.M. Saini and M.K. Soni, Artificial Neural Network Based Peak Load Forecasting using Levenberg Marquardt and Quasi- Newton Method, IET Proceeding Generation, Transmission and Distribution (2002) 578-584.
18. F. Milano, An Open Source Power System Analysis Toolbox, IEEE Transactions on Power Systems, 20 (3) (2005) 1199-1206.
19. F. Milano, C. A. Canizares, and A. J. Conejo, Sensitivity Based Security Constrained OPF Market Clearing Model, IEEE Transactions on Power Systems, 20 (4) (2005) 2051–2060.
20. S. Rajasekaran and G.A.V. Pai, Neural Networks, Fuzzy Logic and Genetic Algorithms: Synthesis and Applications, Prentice-Hall Press, New Delhi, India, 2006.
21. S.N. Pandey, S. Tapaswi and L. Srivastava, Growing RBFNN Based Soft Computing Approach for Congestion Management, Neural Computing and Applications, 18 (8) (2009) 945-955.
22. H.A. Gil, F.D. Galiana, and E.L.D. Silva, Nodal Price Control: A Mechanism for Transmission Network Cost Allocation, IEEE Transactions on Power Systems, 21 (1) (2006) 3-10.
23. L. Chen et al., Mean Field Theory For Optimal Power Flow, IEEE Transactions on Power Systems, 12 (4) (1997) 1481–1486.
24. L. Chen et al., Surrogate Constraint Method for Optimal Power Flow, IEEE Transactions on Power Systems, 13 (3) (1998) 1084–1089.
25. L. Chen, Y. Tada, H. Okamoto, R. Tanabe, and A. Ono, Optimal Operation Solutions of Power Systems With transient Stability Constraints, IEEE Transactions On Circuits Syst. I, 48 (3) (2001) 327–339.